FILTERED AND SEMI-CONTINUOUS SINGLE EPOCH GPS FOR DEFORMATION MONITORING

AHMED E RAGHEB

School of Civil Engineering and Geosciences,

Newcastle University

Thesis submitted for the degree of

Doctor of Philosophy

NOVEMBER 2007

ABSTRACT

Multipath is a major sidereally-repeating error affecting GPS. The repetition of satellite-receiver geometry approximately every sidereal day enables filtering to minimize multipath. Computing the exact error repeat interval using the day-to-day autocorrelation with a 10-hour window yields a consistent and steady value of 23h 55m 54s. A 2-hour window gives fluctuating lag values with >97% of the optimal lag's correlation, suggesting little advantage in using a satellite-specific or time-varying lag in double-difference processing.

GPS data are filtered by stacking at the optimum lag, and applying, either coordinate residuals ("coordinate filtering"), or double-difference carrier phase residuals ("observation filtering"). Coordinate filtering yields better coordinate repeatability than observation filtering, but with similar hour-to-hour consistency. The variance reduction in a high multipath environment over a 24-hour dataset reaches 73%, using a 3-day coordinate-filter in a high multipath environment. However, observation filtering requires less processing time to generate and apply the filter.

As the time gap between the days generating the filter and the applied day increases, the variance reduction worsens gradually, reaching zero at a gap of ~30 days. The optimal variance reduction (61% in a low multipath environment) is achieved by

stacking seven days immediately before the applied day, but a stack of 3–9 days is acceptable.

A switched-antenna array system may be adopted instead of continuous GPS for cost minimization. According to the used receivers' hardware, the optimum session interval to use is 119 seconds, which provides sufficient usable epochs per switch interval and is synchronized with the "sidereal" lag. Semi-continuous sidereally-filtered GPS is efficient in detecting horizontal and vertical deformations in near-static environments with high multipath to the millimetre level. In addition, the precision of the deforming stations improved, reaching to a precision better than 5 mm and 8 mm in the horizontal and vertical plane respectively. Hence, this provides the capability of monitoring slow moving deformations using a quick, cost-effective and precise GPS technique.

TABLE OF CONTENTS

ABSTRACT i
TABLE OF CONTENTS iii
LIST OF FIGURES vii
LIST OF TABLES xv
LIST OF ACRONYMS xviii
ACKNOWLEDGEMENT xxi

CHAPTER 1 INTRODUCTION 1
1.1 Sensors for Deformation Monitoring 2
1.2 State of the Art in GNSS 7
1.3 Research Motivation 9
1.4 Other Multipath Mitigation Techniques 12
1.5 Research Objectives and Methodology 14
1.6 Thesis Outline 18

CHAPTER 2 GPS OVERVIEW AND PROCESSING SOFTWARE 20
2.1 Introduction 20
2.2 GPS Constellation 20
2.3 GPS Errors 23
2.3.1 Satellite Errors 24
2.3.2 Receiver/Antenna Errors 26
2.3.3 Atmospheric Errors 30
2.4 GPS Observation Equations and Differencing 33
2.4.1 Code Pseudorange Observable 34
2.4.2 Carrier Phase Observable 35

2.4.3 GPS Differencing Techniques....36
2.5 Ambiguity Resolution Techniques....38
2.6 GPS Ambiguity Search Program (GASP)....42
2.6.1 Initialization and Antenna Phase Centre Variation....43
2.6.2 Reading RINEX Observation and Navigation Data....44
2.6.3 Application of Tropospheric Model....45
2.6.4 Determination of Initial Position and Search Volume Construction....47
2.6.5 Calculation of Ambiguity Function Value....48
2.6.6 Least Squares Adjustment and Statistical Testing....50
2.6.7 Results Output and Miscellaneous Information....51

CHAPTER 3 SIDEREAL FILTERING SOFTWARE AND GEOMETRY REPEAT INTERVAL....54
3.1 Introduction....54
3.2 Sidereal Filtering Software....55
3.2.1 GPS Autocorrelation Sidereal Filtering (GASF)....55
3.2.1.1 Initialization and Reading of Epochs....56
3.2.1.2 Averaging and Weighting....57
3.2.1.3 Autocorrelation and Sidereal Lag Determination....58
3.2.2 Filter Application Program (FAP)....60
3.2.2.1 Initialization and Weighting....61
3.2.2.2 Stacking Methodology....61
3.2.2.3 Application of Filter....62
3.3 Sidereal Filter Strategies Data Collection....64
3.3.1 April_05 Data set....66
3.3.2 December 05 Data set....66
3.3.3 Environment Characterization....67
3.4 Data Handling....67
3.5 Sidereal Lag Investigation....70
3.5.1 Data Processing....70
3.5.2 Sidereal Lag Analysis....72
3.6 Lag Investigation Conclusions....80

CHAPTER 4 SIDEREAL FILTER STRATEGIES, PERFORMANCE AND LIFETIME 81

4.1 Introduction 81

4.2 Sidereal Filter Application Methodology 81

4.3 Coordinate v. Observation Filtering 82

4.3.1 Coordinate Filter Methodology 84

4.3.2 Observation Filter Methodology 91

4.3.3 Comparison of Computational Efficiency 96

4.3.4 Effect of Sidereal Lag Variation 102

4.4 Sidereal Filter Performance 103

4.4.1 Filter Performance Data Collection and Processing 103

4.4.2 Sidereal Filter Optimum Days Stacking 104

4.4.3 Optimum Sidereal Filter Lifetime 106

4.5 Sidereal Filter Conclusions 108

CHAPTER 5 GPS SWITCHED ANTENNA ARRAY 111

5.1 Introduction 111

5.2 Mechanism of Multi-Antenna Array 112

5.3 Previous Multi-Antenna Array Investigations 113

5.4 Development of Dual Antenna Switch Device 116

5.5 Investigation of Antenna Switching Interval 118

5.5.1 Data Collection 118

5.5.2 Optimum Session Observation Interval 121

5.6 Switched Antenna Sidereal Filter Application 129

5.7 Switched Antenna Array Conclusions 142

CHAPTER 6 DEFORMATION MONITORING USING SIDEREAL FILTER DUAL ARRAY GPS 144

6.1 Introduction 144

6.2 Displacement Simulation Platform 145

6.3 Switched Data Collection 146

6.4 GPS Processing and Switch Array Analysis 147

6.5 Sidereal Filter Application with Displacement Implementation 151

6.6 Deformation Monitoring Conclusions 166

CHAPTER 7 SUMMARY, CONCLUSIONS AND RECOMMENDATIONS 169

7.1 Summary 169

7.2 Conclusions 171

7.3 Recommendations and Future Work 176

REFERENCES 181

APPENDIX A GASP INITIAL FILE 194

APPENDIX B GASF INITIAL FILE 195

APPENDIX C SIDEREAL FILTER TABLES 196

APPENDIX D SIDEREAL FILTER FIGURES 197

APPENDIX E WEB RESOURCES 203

LIST OF FIGURES

Figure 2.1 Good and poor geometric configuration of satellites. 25
Figure 2.2 Multipath error.....27
Figure 2.3 Layers of the Earth's atmosphere. 31
Figure 2.4 Integer phase ambiguity. 35
Figure 2.5 GPS differencing techniques. 38
Figure 2.6 GASP software flowchart.....53
Figure 3.1 GASF software flowchart.....60
Figure 3.2 FAP software flowchart.....63
Figure 3.3 Relative location of the two Drummond stations (DRMS and DRMN). ...64
Figure 3.4 Relative location of the two Bedson stations (SN02 and NEWC). 65
Figure 3.5 Relative location of the Drummond and Bedson buildings.....65
Figure 3.6 Multipath (MP1 and MP2) RMS for all four stations with a 5° elevation mask.....68
Figure 3.7 Multipath (MP1 and MP2) RMS for all four stations with a 15° elevation mask.....69
Figure 3.8 Up coordinate times series over a 24-hour period. Left for SN02, middle for DRMS and right for NEWC. Lower raw time series are one sidereal day (86164 seconds) later than the upper raw (Y-axis major tick marks are at 1 cm intervals).....71
Figure 3.9 Optimum sidereal lag for different window sizes over a 3-day period (SN02). Dashed line indicate nominal lag of 86164 seconds.....72
Figure 3.10 Optimum sidereal lag for different window sizes over a 3-day period (DRMS). Line attributes as before. 73

Figure 3.11 Optimum sidereal lag for different window sizes over a 3-day period (NEWC). Line attributes as before. 73
Figure 3.12 2-hour window autocorrelation over a 3-day period (SN02). 74
Figure 3.13 10-hour window autocorrelation over a 3-day period (SN02). 74
Figure 3.14 2-hour window autocorrelation over a 3-day period (DRMS). 75
Figure 3.15 10-hour window autocorrelation over a 3-day period (DRMS). 75
Figure 3.16 2-hour window autocorrelation over a 3-day period (NEWC). 75
Figure 3.17 10-hour window autocorrelation over a 3-day period (NEWC). 75
Figure 3.18 2-hour window thresholds (SN02). Values are expressed as a percentage of the maximum autocorrelation. The solid line shows the optimal lag for a 10-hour window. 76
Figure 3.19 10-hour window thresholds (SN02). Values are expressed as a percentage of the maximum autocorrelation. The solid line shows the optimal lag for a 2-hour window. 76
Figure 3.20 2-hour window thresholds (DRMS). Shading as before. 76
Figure 3.21 10-hour window thresholds (DRMS). Shading as before. 76
Figure 3.22 2-hour window thresholds (NEWC). Shading as before 76
Figure 3.23 10-hour window thresholds (NEWC). Shading as before 76
Figure 3.24 Optimum 2- and 10-h window sidereal lag for December_05 data set over a 3-day period (SN02). Dashed line indicate nominal lag of 86164 seconds 77
Figure 3.25 Optimum 2- and 10-h window sidereal lag for December_05 data set over a 3-day period (DRMS). Line attributes as before. 77
Figure 3.26 Optimum 2- and 10-h window sidereal lag for December_05 data set over a 3-day period (NEWC). Line attributes as before. 78
Figure 3.27 2-hour window thresholds (SN02, December_05 data set). Shading as before. 79
Figure 3.28 10-hour window thresholds (SN02, December_05 data set). Shading as before. 79
Figure 3.29 2-hour window thresholds (DRMS, December_05 data set). Shading as before. 79
Figure 3.30 10-hour window thresholds (DRMS, December_05 data set). Shading as before. 79

Figure 3.31 2-hour window thresholds (NEWC, December_05 data set). Shading as before.....79

Figure 3.32 10-hour window thresholds (NEWC, December_05 data set). Shading as before.....79

Figure 4.1 NEWC Easting, Northing and Up coordinate time series. Left for unfiltered, middle for coordinate filter and right for observation filter. Note that the coordinate scale of E and N differ from that of U by a factor of 1.5. (Y-axis tick marks are at 1 cm intervals). 83

Figure 4.2 Hourly Easting coordinate standard deviations for all six cases based on the coordinate filter. Dotted lines are for the standard deviations of unfiltered coordinates. Solid lines represent the standard deviations of filtered coordinates. 85

Figure 4.3 Hourly Northing coordinate standard deviations for all six cases based on coordinate filter. Line attributes as before.....86

Figure 4.4 Hourly Up coordinate standard deviations for all six cases based on coordinate filter. Line attributes as before.....87

Figure 4.5 3D hourly coordinate standard deviations for all six cases based on the coordinate filter for the December_05 data set. Line attributes as before. 90

Figure 4.6 Hourly Easting coordinate standard deviations for all six cases based on the observation filter. Line attributes as before.....92

Figure 4.7 Hourly Northing coordinate standard deviations for all six cases based on the observation filter. Line attributes as before.....93

Figure 4.8 Hourly Up coordinate standard deviations for all six cases based on the observation filter. Line attributes as before.....94

Figure 4.9 Hourly χ^2 mean values for all six cases based on the observation filter. Line attributes as before. 97

Figure 4.10 Hourly χ^2 standard deviations for all six cases based on the observation filter. Line attributes as before. 98

Figure 4.11 3D hourly coordinate standard deviations for all six cases based on the observation filter for the December_05 data set. Line attributes as before.....99

Figure 4.12 A bar chart showing GASP processing times on a Linux workstation for each step of both filtering methods for all three stations. 101
Figure 4.13 Percentage of 24-hour variance reduction of the applied day for both filtering methodologies (optimum stacked filter).....105
Figure 4.14 Time scale of all used data sets for the sidereal filter lifetime. The filter applied day is marked with a larger symbol. Zero days is set at 4th of April 2005. 106
Figure 4.15 Percentage of 24-hour variance reduction of the applied day for both filtering methodologies (different satellites processing). Numbers indicate age of filters.....107
Figure 4.16 Percentage of 24-hour variance reduction of the applied day for both stacking methodologies (common satellites processing). 109
Figure 5.1 The employed switch box.....116
Figure 5.2 Schematic diagram of switch antenna array connections.....116
Figure 5.3 Main interface of Tardis 95. 117
Figure 5.4 Main interface of DASP program.....118
Figure 5.5 Relative location of the three Drummond building stations.....119
Figure 5.6 Multipath RMS with a 5° elevation mask. 120
Figure 5.7 Multipath RMS with a 15° elevation mask. 120
Figure 5.8 3D discrepancies for all switch intervals. Upper for one minute switch session, then two, five and ten minute. Left for DRME while right for DRMS.123
Figure 5.9 3D discrepancy percentiles for all switch intervals. Order as before. 124
Figure 5.10 Percentage of passing good epochs (less than 50 cm) and total observed epochs for two minute switch interval. Observed epochs in red. Good epochs in blue. 126
Figure 5.11 3D discrepancies for all two minute switch sessions after removing epochs > 50 cm.....126
Figure 5.12 3D discrepancy percentiles for two minute switch interval after removing bad epochs > 50 cm. 126
Figure 5.13 Percentage of passing good epochs (less than 50 cm) and total observed epochs for five minute switch interval. Line attributes as before. 127

Figure 5.14 3D discrepancies for all five minute switch sessions after removing epochs > 50 cm. 127
Figure 5.15 3D discrepancy percentiles for five minute switch interval after removing bad epochs > 50 cm. 127
Figure 5.16 Percentage of passing good epochs (less than 50 cm) and total observed epochs for ten minute switch interval. Line attributes as before. 128
Figure 5.17 3D discrepancies for all ten minute switch sessions after removing epochs > 50 cm. 128
Figure 5.18 3D discrepancy percentiles for ten minute switch interval after removing bad epochs > 50 cm. 128
Figure 5.19 Hourly coordinate standard deviations using 50 cm limit for accepting epochs. Solid lines for filtered standard deviations. Dashed lines for unfiltered standard deviations. 130
Figure 5.20 Hourly coordinate standard deviations using 40 cm limit for accepting epochs. Line attributes as before. 131
Figure 5.21 Hourly coordinate standard deviations using 30 cm limit for accepting epochs. Line attributes as before. 131
Figure 5.22 Hourly coordinate standard deviations using 20 cm limit for accepting epochs. Line attributes as before. 131
Figure 5.23 Hourly coordinate standard deviations using 10 cm limit for accepting epochs. Line attributes as before. 132
Figure 5.24 Hourly coordinate standard deviations using 50 cm limit for accepting epochs and removing the first 30 seconds of each switch interval. Line attributes as before. 132
Figure 5.25 Hourly coordinate standard deviations using 40 cm limit for accepting epochs and removing the first 30 seconds of each switch interval. Line attributes as before. 133
Figure 5.26 Hourly coordinate standard deviations using 30cm limit for accepting epochs and removing the first 30 seconds of each switch interval. Line attributes as before. 133

Figure 5.27 Hourly coordinate standard deviations using 20 cm limit for accepting epochs and removing the first 30 seconds of each switch interval. Line attributes as before. 133
Figure 5.28 Hourly coordinate standard deviations using 10 cm limit for accepting epochs and removing the first 30 seconds of each switch interval. Line attributes as before. 134
Figure 5.29 DRME filtered and unfiltered 24-hr 3D coordinate standard deviations for all accepting limits. a) without removing any epochs from the switch session, and b) removing the first 30 seconds from the switch session.....137
Figure 5.30 DRMS filtered and unfiltered 24-hr 3D coordinate standard deviations for all accepting limits. a) without removing any epochs from the switch session, and b) removing the first 30 seconds from the switch session.....138
Figure 5.31 Filtered coordinate cumulative histogram for both stations using 50 cm acceptance limit in three directional components. Lower dashed line indicates 5 % frequency. Upper dashed line indicates 95 % frequency. 140
Figure 5.32 Unfiltered coordinate cumulative histogram for both stations using 50 cm acceptance limit in three directional components. Line attributes as before.....141
Figure 6.1 Displacement simulation platform. 145
Figure 6.2 Digital vernier calliper used for displacement measurements.....146
Figure 6.3 DRME A and B antennae mounted on the displacement simulation platform. 146
Figure 6.4 3D discrepancy percentiles.....148
Figure 6.5 3D discrepancy percentiles after removing epochs of discrepancies greater than 30 cm. 148
Figure 6.6 DRME_A coordinate time series while applying horizontal displacements. Black dashed lines indicate time of these displacements of different magnitude. Red line shows a 119 seconds box-car filter. Coordinates are plotted relative to a false origin. (GPS week = 1445) 149
Figure 6.7 DRME_B coordinate time series while applying horizontal displacements. Line attributes, coordinates origin and GPS week as before.....150
Figure 6.8 DRME_A coordinate time series while applying vertical displacements. Line attributes, coordinates origin and GPS week as before.....152

Figure 6.9 DRME_B coordinate time series while applying vertical displacements. Line attributes, coordinates origin and GPS week as before.....153
Figure 6.10 DRME_A filtered coordinate time series while applying horizontal displacements. Line attributes, coordinates origin and GPS week as before.....154
Figure 6.11 DRME_B filtered coordinate time series while applying horizontal displacements. Line attributes, coordinates origin and GPS week as before.....155
Figure 6.12 DRME_A filtered coordinate time series while applying vertical displacements. Line attributes, coordinates origin and GPS week as before.....156
Figure 6.13 DRME_B filtered coordinate time series while applying vertical displacements. Line attributes, coordinates origin and GPS week as before.....157
Figure 6.14 DRME_A unfiltered and filtered average hourly coordinates, while applying horizontal displacements. Solid lines and right error bars for filtered coordinates. Dotted lines and left error bars for unfiltered coordinates. Coordinates are plotted relative to a false origin. Error bars show 3σ standard deviation limits. GPS week as before.....159
Figure 6.15 DRME_B unfiltered and filtered average hourly coordinates, while applying horizontal displacements. Line attributes, error bars, coordinates origin and GPS week as before.....159
Figure 6.16 DRME_A unfiltered and filtered average hourly coordinates, while applying vertical displacements. Line attributes, error bars, coordinates origin and GPS week as before.....160
Figure 6.17 DRME_B unfiltered and filtered average hourly coordinates, while applying vertical displacements. Line attributes, error bars, coordinates origin and GPS week as before.....160
Figure 6.18 DRME_A unfiltered and filtered true versus observed coordinates. Easting and Northing coordinates while applying horizontal displacements on 18/09/2007 and Up coordinates while applying vertical displacements on 19/09/2007. Minor tick marks = 1 cm. Easting scale is double Northing and Up scale. Black line indicates ideal relation. 163
Figure 6.19 DRME_B unfiltered and filtered true versus observed coordinates. Coordinates, tick marks, scale and line attributes as before.....164

Figure D.1 Hourly Easting coordinate standard deviations for all six cases based on the coordinate filter for the December_05 data set. Line attributes as before....197

Figure D.2 Hourly Northing coordinate standard deviations for all six cases based on the coordinate filter for the December_05 data set. Line attributes as before....198

Figure D.3 Hourly Up coordinate standard deviations for all six cases based on the coordinate filter for the December_05 data set. Line attributes as before. 199

Figure D.4 Hourly Easting coordinate standard deviations for all six cases based on the observation filter for the December_05 data set. Line attributes as before..200

Figure D.5 Hourly Northing coordinate standard deviations for all six cases based on the observation filter for the December_05 data set. Line attributes as before..201

Figure D.6 Hourly Up coordinate standard deviations for all six cases based on the observation filter for the December_05 data set. Line attributes as before.....202

LIST OF TABLES

Table 3.1 Data collection parameters of the April_05 data set for all four stations. (GPS Week = 1317) (star (*) indicates actual processsing start and end times).66

Table 3.2 Data collection parameters of the December_05 data set for all four stations. (GPS Week = 1353) (star (*) as before).....66

Table 3.3 Multipath parameters for all four stations for both 5° and 15° elevation masks.....70

Table 4.1 24-hour coordinate standard deviations in three directions for all six cases based on the coordinate filter for the April_05 data set.....89

Table 4.2 24-hour variance reduction in three directions for all six cases based on the coordinate filter for the April_05 data set.....89

Table 4.3 3D coordinate standard deviations over a 24-hour period for all six cases based on the coordinate filter.....89

Table 4.4 3D 24-hour standard deviations for all six cases based on the coordinate filter for the December_05 data set.....91

Table 4.5 3D 24-hour standard deviation over a 24-hour period for all six cases based on the observation filter.....95

Table 4.6 3D 24-hour standard deviations for all six cases based on the observation filter for the December_05 data set.....100

Table 4.7 GASP processing times for each step of both filtering methods for all three stations on a Linux workstation.....101

Table 4.8 3D coordinate standard deviations over a 24-hour period, for both methodologies over different lags for the December_05 data set (3-day filter stacking).....102

Table 4.9 24-hour standard deviations and variance reductions for the optimum 7-day filter for both filtering methodologies..... 105

Table 4.10 24-hour standard deviations and variance reductions for the case of optimum filter age for both filtering methodologies..... 109

Table 5.1 Observation criteria for all four observed data sets..... 121

Table 5.2 24-hr Easting, Northing, Up and 3D coordinate standard deviations for all cases of acceptance limits and after removing epochs for DRME. (δ) stands for variance reduction, (UF) stands for unfiltered values while (F) stands for filtered values. 135

Table 5.3 24-hr Easting, Northing, Up and 3D coordinate standard deviations for all cases of acceptance limits and after removing epochs for DRMS. Abbreviations as before. 136

Table 6.1 DRME_A hourly unfiltered and filtered true versus observed Easting coordinates along with hourly raw data and switch sessions RMS, while applying horizontal displacements on 18/09/2007..... 165

Table 6.2 DRME_A hourly unfiltered and filtered true versus observed Northing coordinates along with hourly raw data and switch sessions RMS, while applying horizontal displacements on 18/09/2007..... 165

Table 6.3 DRME_A hourly unfiltered and filtered true versus observed Up coordinates along with hourly raw data and switch sessions RMS, while applying vertical displacements on 19/09/2007..... 165

Table 6.4 DRME_B hourly unfiltered and filtered true versus observed Easting coordinates along with hourly raw data and switch sessions RMS, while applying horizontal displacements on 18/09/2007..... 167

Table 6.5 DRME_B hourly unfiltered and filtered true versus observed Northing coordinates along with hourly raw data and switch sessions RMS, while applying horizontal displacements on 18/09/2007..... 167

Table 6.6 DRME_B hourly unfiltered and filtered true versus observed Up coordinates along with hourly raw data and switch sessions RMS, while applying vertical displacements on 19/09/2007..... 167

Table C.1 24-hour coordinate standard deviations in three directions for all six cases based on the coordinate filter for the December_05 data set. 196

Table C.2 24-hour coordinate standard deviations in three directions for all six cases based on the observation filter for the April_05 data set. 196

Table C.3 24-hour coordinate standard deviation in three directions for all six cases based on the observation filter for the December_05 data set. 196

LIST OF ACRONYMS

3D	Three-Dimension
AEP	Architecture Evolution Plan
AFM	Ambiguity Function Method
AFT	Ambiguity Function Technique
AFV	Ambiguity Function Value
bps	bit per second
BST	British Summer Time
C/A	Coarse/Acquisition GPS Signal
CGSIC	Civil GPS Service Interface Committee
DBX	Direct Branch eXchange
DOP	Dilution Of Precision
DOT	Department Of Transportation
DOY	Day Of Year
EDM	Electronic Distance Measurement
FAP	Filter Application Program
FARA	Fast Ambiguity Resolution Approach
FASF	Fast Ambiguity Search Filter
F-Test	Fisher Test
FTP	File Transfer Protocol
GASF	GPS Autocorrelation Sidereal Filter program
GASP	GPS Ambiguity Searching Program
GLONASS	GLObal NAvigation Satellite System
GMAS/GMS	GPS Multi Antenna System
GNSS	Global Navigation Satellite System

GPS	Global Positioning System
Hz	Hertz
IGS	International GNSS Service
ION	Institute of Navigation
InSAR	Interferometric Synthetic Aperture Radar
L1	GPS L-band signal 1 (1575.45 MHz)
L2	GPS L-band signal 2 (1226.60 MHz)
LAMBDA	Least squares AMBiguity Decorrelation Adjustment
LSA	Least Squares Adjustment
LSAST	Least Squares Ambiguity Search Technique
MAFV	Maximum Ambiguity Function Value
MASS	Multi Antenna Switch Script
MCD	Modified Cholesky Decomposition
MHz	Mega Hertz
NASA	National Aeronautics and Space Administration
NGA	National Geospatial-intelligence Agency
NGS	National Geodetic Survey
NXF	Newcastle eXchange Format
OS	Ordnance Survey
OTF	On The Fly
P-code	Precision Code
PC	Personal Computer
PCV	Phase Centre Variation
PDOP	Position Dilution of Precision
ppm	part per million
PRN	Pseudo-Random Noise
QZSS	Quazi-Zenith Satellite System
RASP	Rinex Antenna Switch Program
RINEX	Receiver INdependent EXchange format
RINTONXF	RINex TO NXF
RMS	Root Mean Square
SA	Selective Availability

SD	Standard Deviation
SNR	Signal-to-Noise Ratio
STD	Slant Total Delay
SV	Space Vehicle
TEC	Total Electron Content
TEQC	Translating, Editing and Quality Checking
UHF	Ultra High Frequency
UK	United Kingdom
US	United States
USA	United States of America
UTC	Coordinated Universal Time
WGS84	World Geodetic System 1984
ZHD	Zenith Hydrostatic Delay
ZWD	Zenith Wet Delay

ACKNOWLEDGEMENT

First, I would like to thank and glorify GOD for his protection on myself and my family.

I would like to express my deep gratitude to my supervisors Prof. Peter Clarke and Dr Stuart Edwards for their help and assistance they offered throughout my study. Their guidance and distinguished knowledge played a major role in the accomplishment of the current research. I consider myself lucky being one of their students.

Many sincere thanks go to Martin Robertson for his technical support during data collection, Fred Beadle and David Dick for their help with the displacement platform, Mark Greaves and the colleagues at the geodetic section of the Ordnance Survey for timely provision of the 1s data for NEWC station, Alison Ford and Pauline Miller for updating the Visual Basic software and Henny Mills for facilitating data collection. I also would not forget precious one to one conversations, help and discussions with Dr Nigel Penna, Dr David Lavallee and Dr Matt King which provided very useful ideas and information. Appreciation also to the Universities UK organization for partially funding my research.

I also appreciate all the help and friendly treatment I got from my colleagues in the Geomatics Department, Peter, Sofia, Ian, Talaq, Mohammed and Nadim. It was a

pleasure working with you all. Very special thanks go to my desk mate friend Roghailan Al-Shammari and dearest friend Saad Al-Hamlan. They both made life easier and helped me settle well in my early days here. I also would like to remember my professors in Egypt, Prof. Ibrahim Shaker, Prof. Mohamed El-Tokhey, Dr Mohamed El-Maghraby, Dr Atef Fayad and especially Prof. Mohamed Nassar, to whom I am indebted for their fruitful advice and ideas in my early research years.

A big thank you goes to my dad for his total moral and financial support during my study here. I also thank my mother, step father and sister for their continuous encouragement, and last but not least, I thank my wife Rabab for her incessant support, patience and homey environment she always provided. I have to admit that without her nothing would have been accomplished and to her, my daughter Hana and my son Omar, I dedicate this thesis. Finally, for all my friends and colleagues in Cairo, Newcastle, anywhere in the world and anyone whom I did not mention above, THANKS!

INTRODUCTION

Monitoring of natural and structural deformations is a vital procedure with many benefits, starting with assuring the performance of any structure against its design criteria, identifying any abnormalities in the structure's behaviour, or warning against geohazards and natural displacements. Also it could be useful for calibration purposes to be used later for structural design codes (Ogaja et al. 2001). Structural deformations occur either rapidly due to wind or seismic forces, or in the form of long-term deformations due to overloading or change in water levels, etc., as in deformation of buildings, bridges, dams, reservoirs and embankments.

Of course, regardless the type of structure, deformation monitoring is often required to be carried out as quickly as possible, that is in real time or near real time, for safety and stability purposes. This is to avoid collapse of defective structures causing high financial liabilities and severe environmental damage (Rutledge et al. 2001). Sudden failure of engineering structures will cause major catastrophes, whether economic or death of civilians.

In most cases, the nature of the monitored structure, required accuracy and environmental conditions will define the deformation methodology as well as the instrumentation used. Several factors have to be taken into consideration regarding instrumentation, starting with the required equipment and material, dealing with monumentation and how to protect it, in addition to the locating, operation and maintenance of the monitoring points (Ali 2003).

1.1 Sensors for Deformation Monitoring

A wide range of sensors are used for monitoring deformations, which could vary according to the scale of the project, density of test stations, cost, manpower required, etc. Generally, deformation monitoring sensors can be characterized as meteorological, geotechnical and surveying (geodetic) sensors (Hill and Sippel 2002). Meteorological sensors are the kind used mainly for the calibration of the other two kinds of sensors and not for monitoring structural deformation itself. They are also used to monitor atmospheric change, such as temperature, pressure, humidity, etc. Geotechnical sensors provide deformation monitoring in one dimension only, e.g. tilt meters, accelerometers, micrometers and plumb lines. The main focus here is on the third type of sensor, namely geodetic sensors. These sensors could be categorized by their measurement type such as angle, distance and angle-distance, or by the adopted technique such as levelling, photogrammetry, laser scanning, Interferometric Synthetic Aperture Radar (InSAR), Pseudolites or the Global Positioning System (GPS).

Comparing the efficiency of geotechnical and geodetic sensors, the former are easy to adapt for automatic and continuous monitoring. However, they provide localized information that needs to be compared to other independent measurements, resulting in relative deformation measurements within the deformable object and its surroundings. On the other hand, geodetic sensors provide sufficient redundancy required for quality statistical evaluation and detection of errors. They can be used to determine absolute displacements relative to a stable reference station or network (Erol et al. 2004).

Angular sensors are mainly electronic theodolites measuring horizontal and vertical circle reading (directions) leading to the calculation of horizontal and vertical angles. The accuracy here depends on the accuracy of the horizontal and vertical circles, which could reach 0.5–1 second. Distance sensors used for monitoring deformations are the Electronic Distance Measurement (EDM) devices transmitting visible or near infrared radiation to calculate slope distances. The accuracy of the EDM may reach 1 mm + 1 ppm for short baselines. Lower accuracy is achieved for longer baselines,

mainly due to the difficulty in determining the refractive index of the travelling media. On the other hand, one type of EDM used to monitor crustal deformations and called the two colour (blue and red) EDM, reaches a precision of 0.5–1 mm. The difference in travel time between both wavelengths is used to calculate the refractive index, which can then be used to calculate the distance from the travel time of one of the colours (US Geological Survey 2007).

The most common type of angle-distance sensor is the total station, which is in principle an electronic theodolite and an EDM combined together, fitted with a computer, with internal and external memory. The measured horizontal and vertical directions, as well as the slope distances, are transformed into three dimensional coordinates, which could be related to pre-deformation coordinates and thus produce an interpretation of the deforming structure. Another type of these sensors is the survey robot, which is generally a total station programmed for continuous deformation monitoring. The observed directions and distances are transmitted to an office computer through a telemetry link. These sensors are beneficial near high walls in open pit mining and slope stability studies, but possess lower accuracy when compared to regular total stations. Principally, this is due to the lower accuracy of the self-pointing of the device and lack of observation time tagging, which causes problems during processing (Radovanovic and Teskey 2001).

Note that these kinds of angle and/or distance sensors require the formation of some sort of frame or reference network, in addition to the test points. These networks provide redundant observations leading to a more reliable least squares adjustment and hence achieve high accuracy for monitored points. However, in contrast, these sensors are skill and labour intensive with a limited observation rate, and are affected by atmospheric refraction. Most importantly, they require intervisibilty between reference and monitored test points for pointing purposes. This will confine the distribution criteria upon which the choice of reference and monitored points are based. In addition, as the use of these conventional sensors generally requires intensive post-observation calculations, they are inappropriate for real time deformation monitoring applications, which is considered a major drawback. Finally,

these sensors require good weather and sometimes daylight to perform properly and thus are not suitable for all seasons or even every-day purposes.

Another type of geodetic sensor is the precise level, which is the most common example of a levelling sensor, measuring height differences for deformation test points relative to a known elevation benchmark. There are two types of precise level used for deformation monitoring, namely the optical and digital levels. The former is the old-fashioned type of level but still the most reliable and accurate method, observing staff readings relative to a horizontal plane. For approximately 20 m setups between the instrument and the staff, an accuracy of 0.01 mm can be achieved (Schofield 2001), depending on the minimum division of the staff used and the magnification of the parallel glass plate of the micrometer. This accuracy degrades for longer levelling loops and distance between level and staff. Another helpful factor in increasing the reliability of the solution is the material used for the staff, having high temperature resistant coefficient, e.g. invar. Recent types of precise level perform an automatic levelling process through height and distance readings from encoded levelling rods. This, of course, boosts the speed of the process and reduces the need for manpower; however there still exists some debate about the obtained accuracy due to systematic deviations of the levelling components (Ali 2003).

Photogrammetric techniques are cost effective in deformation monitoring when large areas are to be observed. Aerial photogrammetry is widely used in detecting ground subsidence, while terrestrial photogrammetry is used for monitoring the deformation of large structures. These techniques have the advantage of monitoring an unlimited number of points, providing high density coverage — as is the case with laser scanning — in addition to a significant reduction in fieldwork time, along with high accuracy (US Army Corps of Engineers 2002). Nevertheless, these sensors are not suitable for small-scale (limited area) projects, as they will produce a major financial burden due to the high cost of the flight mission in the case of aerial photogrammetry or even the production of photos. New photogrammetric digital cameras now have a GPS receiver fitted, and thus provide coordinated imagery of monitored points in real time without the need of photographing ground stations for coordinate referencing.

This will decrease the overall cost of the process, due to the reduction in the number of photos produced (RICOH 2007).

InSAR is now a common cost-effective technique used for monitoring deformations. It is a remote sensing technique utilizing radar satellite images, used mainly for measuring ground movements. The main methodology is to compare the variation of the radar signal phases of two epochs covering the same portion of the Earth. This will reveal any terrain surface subsidence in the direction of the line of sight occurring in this period of time, providing centimetre level of accuracy (Crosetto et al. 2003).

In brief, GPS is a Global Navigation Satellite System (GNSS) consisting at the moment of 31 Space Vehicles (SV) (satellites) transmitting microwave radio signals to be observed by GPS receivers (sensors). The main advantage of GPS sensors is that station-station intervisibilty is unnecessary and thus there is more flexibility, especially in the location of reference stations that need to be in the most stable areas. GPS sensors also have the ability to continuously observe night and day, all year long, under any weather conditions. In addition, GPS sensors provide three-dimensional coordinates with respect to a global reference frame, achieved in real time or near real time with less labour. In consequence, GPS can provide fast and continuous automated deformation monitoring, in addition to the ability of full integration with other sensors.

Unfortunately, GPS has its drawbacks in deformation monitoring, as false movements are detected from time to time due to GPS noise, as well as the resistance facing continuous high precision monitoring due to the major sources of errors in GPS in the form of cycle slip and multipath error (Roberts et al. 2001 a, b). Slope deformation monitoring, e.g. in landslides or open pit mines, is challenged by cycle slips and multipath in achieving centimetre level accuracy. This is due to the existence of reflecting surfaces near to the monitoring area causing multiple paths for the reflected GPS signals, as well as frequent loss of lock on satellites. In addition, sometimes long or high rate continuous GPS sessions are required to monitor movements such as settlement of buildings, which will lead to higher operational cost.

Accordingly, several applications have investigated how to overcome those drawbacks, as in Rutledge et al. (2001) where adaptive Kalman filtering was used to decrease random noise attributed to GPS observations to monitor landslides, while providing a comprehensive internet enabled automatic monitoring system. Teferle et al. (2003) investigated the effect of radio frequency interference and multipath on the monitoring of land movements at tide gauges in UK harbours. Forward et al. (2001) used a multi-antenna array system (connecting multiple antennae to one receiver) to monitor steep wall deformations while reducing the overall running cost.

In general, the GPS monitoring methods differ depending on the monitored structure. For bridge monitoring, dual frequency receivers combined with high speed processing and Ultra High Frequency (UHF) data links provide real time processing and navigation, reaching centimetre accuracy, as in the case of cable suspension bridges. Gen-you et al. (2005) applies a single epoch GPS technique, utilizing low cost single frequency receivers for monitoring large landslide displacements, reaching centimetre level coordinate accuracy as well. Concerning dam monitoring, several studies, as in Bock et al. (2001) and De Jonge et al. (2000), were performed, possessing high precision but with high cost. The feasibility of the use of GPS for dam deformation monitoring will depend on the budget, scale and importance of the project. On the other hand, monitoring building deformations is often investigated using geotechnical sensors such as accelerometers or terrestrial photogrammetry for large-scale structures.

Lately, the extensive use of GPS in daily life has tempted GPS users and geodesists to utilize GPS sensors either as a stand-alone tool or in conjunction with other sensors to monitor different types of deformations, e.g. tall buildings under rapid or vibrating forces such as wind or earthquakes for long time periods (Ogaja et al. 2000). GPS usually provides lower accuracy in vertical positioning than horizontal, although it can be efficiently utilized when integrated with other sensors, such as precise levels, Pseudo-satellites (Pseudolites) or precise accelerometers. This will enhance the deformation monitoring process due to the omission of different types of errors.

Pseudolites are ground based transmitters of GPS-like signals, with their location being carefully selected. They are used to enhance the satellite geometry constellation required to improve the integrity of monitoring deformations where visibility of satellites is poor or the satellite geometry is weak, especially in the case of monitoring in valleys or deep open-cut mines. Barnes et al. (2003) augmented GPS with Pseudolites in order to improve geometrically weak satellite constellations for the purpose of monitoring bridge deformations to the sub-centimetre level in both the horizontal and vertical components. Erol et al. (2004) used GPS with precise levelling measurements to monitor and analyse deformations of a large viaduct. Meng (2002) used an integrated sensor system comprising GPS and triaxial accelerometers to monitor long term and short-term dynamic deformations, achieving centimetre level accuracy.

The new invention in modern surveying is the smart station, which is simply a GPS receiver mounted on a total station. The advantage of using this station is that there is no need for terrestrial reference stations to observe and relate the measurements to, or even the formation of any kind of network or traverse, as the GNSS/GPS receiver provides instantaneous coordinates for all monitored points. Accordingly, the monitoring process becomes easier with fewer instrument setups, reducing the time of field observations by up to 50%, while reaching sub centimetre or even millimetre relative accuracy. However, it must be kept in mind that this station combines the characteristics of the total station and GPS along with their attributed advantages and disadvantages (Leica Geosystems 2007).

1.2 State of the Art in GNSS

GPS is a promising and widely used tool in many engineering projects, mainly due to its reliability, accuracy and 24-hour availability. GPS is now a famous utility among geodesists and often users, utilizing the non-precise form in navigation and day-to-day activities, especially in-car navigation. GPS is highly automatic and not labour intensive (Chen et al. 2000). The accuracy of GPS depends upon many factors, e.g. the resolution of the unknown integer phase ambiguities (N), in order to obtain accurate and reliable phase measurements. Of course, these measurements will still

contain various kinds of systematic and random errors (Leick 2004). On the other hand, the main disadvantage of GPS is its high cost and low accuracy in real time positioning, although nowadays several investigations are being undertaken in order to overcome this latter drawback.

Due to the continuous need for precision and reliability improvement, frequent updates are being introduced in GPS in particular and the Global Navigation Satellite System (GNSS) as a whole, aimed at easing the use and improving the accuracy of the system. In GPS, new signals are being introduced and codes are being modernized. In addition, the new European Galileo system, expected to be fully operational by the year 2012, will offer an increase in the number of satellites and new frequencies. The Russian GLObal NAvigation Satellite System (GLONASS) is also continuously updating with new satellites, leading to more satellites being available for the user (Kaplan and Hegarty 2006).

A recent newcomer to the GNSS family is China, which launched its new satellite navigation system, called Beidou/Compass, in 2000. China is currently developing its system to be called Beidou 2 or Compass Navigation Satellite System (CNSS), which is expected to be fully operational by 2008. Recently, the first Compass M-1 satellite was launched, having similar characteristics to GPS and Galileo satellites in terms of frequency bands (Chen et al. 2007). The Quasi-Zenith Satellite System (QZSS) is a new GNSS system developed by the Japanese, covering East Asia and centred on Japan. It is mainly designed to enhance GPS services regarding satellite availability and accuracy. The first QZSS satellite is scheduled to be launched in 2009 (GPS-QZSS Technical Working Group 2007). Lately, India has revealed it may launch its own satellite navigation system as well.

All these modifications and updates will definitely enrich the satellite navigation system in different aspects, which will in turn bring increased benefit to the civilian user in particular (Lavrakas 2007). Lavrakas recently looked into the future of GNSS in 2017 by setting different predictive scenarios. Under the most pessimistic scenario, the hybrid user (using all available systems) will not rely permanently on GPS. A rich

global capability for positioning, navigation and timing will be available, having about 20 satellites in view at any time over all the Earth.

1.3 Research Motivation

One of the major uses of GPS is its application in deformation monitoring in various aspects, adopting several GPS observation methods. The traditional method is continuous static GPS, in which GPS receivers occupy all monitoring stations, while logging data continuously for long periods of time. A special case of continuous static GPS is episodic GPS, where data is logged per station for a certain time interval e.g. few minutes. Then this process is repeated every short time gap, thus ending up with semi-continuous GPS data per station. Campaign GPS is also a popular technique utilized in monitoring structural deformations, where by the data collection and the monitoring process for the site area is undertaken for a specific time interval e.g. few hours, and repeated every long period of time e.g. yearly. This is to detect any movements or deformations occurring with time, in order to asses on the behaviour of the structure. On the other hand, kinematic GPS allows logging of data while moving the receiver to different stations, and thus maintaining instantaneous GPS positioning at each station.

In order to accurately monitor deformations, many factors must be considered. The first is to use a quick ambiguity resolution technique for instantaneous resolution at the desired test deformation points. A single epoch ambiguity resolution technique is preferable. Some other previous investigations utilized epoch-by-epoch positioning to provide viable alternative to traditional GPS batch processing with a better insight in to GPS error sources. Bock et al. (2000) used instantaneous positioning through the Geodetics Real Time Dynamic Network software (RTDNet) to resolve the integer phase ambiguities using a single epoch of data every 30 seconds, with the ability to be used with higher sampling rates reaching to 10 Hz. Thus three-dimensional relative coordinates as well as atmospheric zenith delay parameters are estimated over a 12-week period for various baseline lengths (50m, 14 km and 37 km). A precision of about 10 mm and 75 mm in the horizontal and vertical direction respectively is

reached for the 50 m baseline, while the corresponding counterparts are 15 mm and 110 mm for the longest baseline i.e. 37 km.

De Jonge et al. (2000) further augmented the previous investigation with 1 Hz GPS data achieving similar horizontal and vertical precision. Bock et al. (2001) used a more robust epoch-by-epoch software called Continuous Reference Network (CRNet) with a 2 second sampling interval to reach a horizontal precision of 10 mm and vertical precision of 50 mm over an 8 km baseline. This precision can be further improved to 4 mm horizontally and 10 mm vertically for baselines less than 1 km. The approach used in the current research builds on previous studies and uses, like RTDNet and CRNet, the double difference observable. The approach applies a technique that forms a search volume of possible trial positions, seeking for the correct ambiguity set at each epoch independently from any previous epochs. All mathematical procedures and methodologies are executed through a previously prepared ambiguity software called **GPS Ambiguity Search Program (GASP)** (Corbett 1994; Al-Haifi 1996; Gunasingam 2003) (see Section 2.6).

Secondly, although most of the errors affecting short-baseline GPS are eliminated or minimized by differencing techniques (Leick 2004), multipath error will remain due to the highly site-specific nature of the reflection of GPS signals from nearby surfaces. Hence, multipath is often considered the most limiting factor in precise GPS positioning, especially in deformation monitoring (e.g. Lau and Mok 1999; Axelrad et al. 1996). Short-term positions will be subject to quasi-periodic errors with characteristic timescales varying from seconds to minutes depending on the satellite-reflector geometry (e.g. Barnes 2000). Long-term position monitoring is also affected: if GPS data are processed in 24-hour batches, as is often the case, multipath error occurring at the satellite geometry repeat interval can alias into periodic errors close to annual and semi-annual periods (Penna and Stewart 2003).

Fortunately, due to the nearly exact repetition of satellite geometry in the sky above a site every sidereal day (nominally 23h 56m 04s), multipath and many other geometry repeating errors are highly correlated across subsequent days. This is, of course, valid providing the same antenna and reflector environment are maintained. Consequently,

it is possible to apply "sidereal filtering" techniques to mitigate this error (Genrich and Bock 1992; Nikolaidis et al. 2001). Essentially, these methods subtract a filter value from the site coordinates at each epoch. The filter at a given epoch is composed from the coordinate residuals of the long-term mean position, at an epoch separated by a multiple of the near-sidereal error repeat interval (a multiple of the nominal lag 86164s). To improve the precision and robustness of the filter, residuals may be stacked (averaged) over several sidereal days.

Recent investigations based on satellite orbit analysis (Choi et al. 2004) have shown that the actual satellite geometry repeat interval ("sidereal lag") is slightly less than the nominal sidereal period used in earlier sidereal filtering studies. In addition, Larson et al. (2007) have discussed the use of cross-correlation within the coordinate residuals to determine the overall multipath-repeat lag, which was confirmed to match the actual satellite geometry repeat interval. Agnew and Larson (2007) computed the GPS satellite constellation repeat time using the orbital period or the topocentric positions of satellites. The former utilizes the semi major axis parameter and the correction to the mean motion in the broadcast ephemerides to calculate the orbital repeat time. The latter calculates the period at which the satellite has nearly the same direction vector with the observing station using polynomial interpolation. Both techniques confirmed, with slight differences, the average sidereal lag being less than the known nominal one, fluctuating at the few seconds' level across the constellation, with polar observing stations showing greater inter-satellite variability than equatorial ones. Interestingly, this work suggested that the multipath signal is most similar only on adjacent sidereal days, tending to differ as the time separation increases, and thus not repeating endlessly. This criterion is investigated and confirmed later in the current study as part of the filter lifetime analysis (Chapter 4).

Finally, using GPS for monitoring deformations, especially continuous GPS, is of high cost, which is basically due to the capital cost of the GPS equipment. Accordingly, this was the main motive behind the desire to utilize an alternative technique with moderate expense, which could be achieved using episodic GPS in the form of a switched multi-antenna array. This procedure has the advantage of combining some characteristics of both the static and rapid static techniques. GPS

data are not collected continuously at previously fixed points, but for a certain time interval at fixed antennae connected to one receiver, without the need to move a rover receiver through the monitoring points.

1.4 Other Multipath Mitigation Techniques

Several algorithms have been used for the reduction of multipath. At the point of measurement, the use of choke ring antennas or special architecture receivers with built-in multipath mitigation techniques eliminate much of the code multipath. However, carrier phase multipath will still be dominant, as it is more embedded and a harder-to-mitigate source of error (Philippov et al. 1999; Van Dierendonck and Braasch 1997). Other mitigation techniques reduce the multipath error at the post-processing stage. Both code and phase multipath can be minimized through the preparation of multipath maps of the GPS antenna environment, provided that this environment remains unaltered. These maps contain the multipath corrections for each satellite signal depending upon its elevation and azimuth (Cohen and Parkinson 1991; Haji 1990). Recently, some other techniques have been developed to reduce multipath using either wavelet analysis (Satirapod and Rizos 2005), a Vondrak filter with cross-validation (Zheng et al. 2005), or weighting the data using the observed signal-to-noise ratio (SNR) (Lau and Mok 1999).

The first technique (Satirapod and Rizos 2005) applies wavelet decomposition to GPS double difference residuals in order to extract multipath from GPS carrier phase observations. Such multipath signatures are then directly applied to GPS observations in subsequent days to correct for the multipath effect, thus giving the best unbiased least squares solution. The basic concept is the multi resolution analysis of GPS signals at different scales by using filters of different cut-off frequencies. Through setting a zero baseline (two receivers and one antenna), double difference residuals are produced for all satellite pairs representing true GPS observation noise. Such residuals are decomposed into low frequency bias and high frequency noise through wavelet transformation using three levels of decomposition. Then, the F-test is used to compare the standard deviation of real GPS observation noise and those calculated from extracted noise components at each decomposition level. The first level of

wavelet decomposition produces the best fit to the multipath disturbance signal, reducing carrier phase multipath and leaving behind GPS noise.

The second methodology (Zheng et al. 2005) separates signals from noise at different noise levels wherever the noise level is lower than the magnitude of the signal. The Vondrak filter produces filter values based on different smoothing factors, while cross validation determines the optimal smoothing factor. This removes noise properly from useful signals giving the least variances among Easting, Northing and Up station coordinates. Both techniques together give a balance between data fitting and smoothing. Actual and simulated GPS data are used in the filtering process. The larger the smoothing factor, the rougher the filtered curve will be and thus more high frequency signals remain in the filtered curve. Reliable GPS multipath models are produced to reduce multipath effects in subsequent days through day-to-day sidereal filtering, resulting in an improvement in the accuracy of about 20–40% of RMS values. This technique has the disadvantage in the case of high noise level, where high frequency signals tend to be filtered out.

The main idea of the third technique (Lau and Mok 1999) is to **C**ombine the **A**mbiguity Function Method (AFM) with **S**ignal-to-noise ratio in a **L**east squares **M**ethod called **CALMS** in order to model noise in each observation for multipath mitigation. The use of SNR is due to the fact that it determines how well the carrier tracking loop in the GPS receiver can track the signals and hence determines the precision of carrier phase measurements. Double difference L1 and L2 phase residuals are obtained through the AFM, in which the correct position obtained, will act as an a priori position for SNR weighted least squares of carrier phase measurements. SNR weighting is applied to each receiver and satellite, thus producing the so-called SNR cofactor matrix, which is the Variance-Covariance (V-C) matrix of double difference SNRs. From such a matrix, the SNR weighted double differences are obtained to be used as the weight matrix in the least squares adjustment. A certain shift in the Z-direction is embedded to simulate deformation monitoring and calibration of the technique, and thus the results of CALMS are tested and compared, as well as its integrity through sidereal day-to-day repeatability. CALMS improves the accuracy even with a small data set without any averaging or smoothing of the multipath error.

However, some differences occurred during results comparison, and it was suspected these were either due to weather or the actual lag not being exactly what was used (86160s). The main disadvantage here is that the SNR information is not always present in a RINEX observation file, which makes it practically inapplicable in all cases. In addition, this technique is only suitable for static platforms in severe multipath environments, observing short baselines.

1.5 Research Objectives and Methodology

Although previous applications used for deformation monitoring were successful and accomplished certain goals, most of the results were achieved in a post-processing batch mode, where a solution is obtained every certain time period. Thus, these techniques required relatively long observational periods (24 hours) in order to obtain the results and assess them, only after which any action could be taken. Keeping in mind the main disadvantages of GPS sensors, the research aim in this thesis will focus on using a fast, and more importantly accurate, GPS technique, utilizing a single epoch processing approach (cycle slip free), along with sidereal filtering (trying to minimize the most limiting factor of multipath error), through which the switched antenna array procedure is adapted (reduction of cost with reliable precision), for the sake of monitoring structural deformations. This combined methodology could lead to the optimum criteria of using GPS in a reliable, precise and cost effective manner for monitoring deformations. Accordingly, the current research aims to improve the precision as well as reduce the cost of semi-static monitoring of engineering structures.

The first objective arises from the high effect of sidereally repeating errors (mainly multipath) on GPS observations. Such consideration of signal multipath is essential, especially near buildings, as it is one of the major errors attributed to GPS measurements, affecting coordinate precision. At first, it is important to assure the value and consistency of the sidereal lag by analysing the periodicity of the coordinate and phase residuals in single epoch positioning. Secondly, one must establish whether filtering at the coordinate or carrier phase observation level is the most beneficial. It is also necessary to check the validity of applying previously obtained sidereal filters in

enhancing the coordinate precision of any data set some days later, as well as identifying the optimum number of days to stack and apply, in order to produce the highest coordinate precision. In deciding the optimal filtering method, one must consider not only the improvement in short-term coordinate precision, but also the consistency of improvement and the processing time necessary to achieve final filtered coordinates. For near-real-time applications, such as landslides, geohazards and monitoring of civil engineering structures, these additional criteria are important.

In addition, one aims to merge both the single epoch processing and sidereal filtering technique, in conjunction with a switched antenna array, for monitoring deformations, aiming to reduce the overall monitoring cost while achieving reliable precision. The switched antenna array technique provides periodic GPS observations from multiple GPS antennae. Through a manual or automated switch, one could control (switch) the GPS data stream from each antenna every specified time interval. Thus, a reliable solution could be obtained using this technique with relatively low cost, satisfying both applicability and effectiveness. Accordingly, the switched antenna array can be easily adopted for monitoring deformations through the fixation of the required test points, upon which multiple GPS antennae — connected to one receiver — are mounted. This of course can be efficiently utilized for the assessment of the stability of the applied structure (Forward et al. 2001).

The GPS processing software GASP (Corbett 1994; Al-Haifi 1996; Gunasingam 2003) operates in a single-epoch mode, unlike the batch mode, and thus would be very useful in near real time applications. Each epoch is treated as an entirely independent measurement, while conducting a search in ambiguity space for the optimal integer values of the ambiguity parameters, using the L1 and L2 phase observables. As each epoch is treated separately, there is no possibility for common parameters to affect the level of multipath error. GASP processes baselines, either in the fully-kinematic mode in which the coordinates of the "fixed" site are determined by a code pseudorange solution at each epoch, or in the fixed-base mode in which the coordinates of the "fixed" site are specified a priori. The latter mode of operation is the one used in the current research. Of course, such a program is updated from an older version with certain modifications in order to cope with the nature and objective

of this thesis. This single epoch ambiguity resolution technique utilized in GASP has the advantage of not requiring long GPS sessions or initialization, as well as eliminating the effect of cycle slips and the necessity of continuous lock on satellites (Corbett 1994; Al-Haifi 1996; Gunasingam 2003).

It should be mentioned here that in order to fulfil these objectives efficiently some modifications needed to be made to the GPS processing GASP software. The first and major modification was the conversion of the program to read RINEX (**R**eceiver **IN**dependent **EX**change format) data directly instead of reading NXF (**N**ewcastle e**X**change **F**ormat) data. This in turn required the running of a certain previously made utility program called RINTONXF (**RIN**ex **TO NXF**) to transform the observational data file from the RINEX version to the NXF version, which consumes time. Nowadays, RINEX observational data is the most commonly used among a wide variety of receiver manufacturers.

As a further modification, Phase Centre Variation (PCV) corrections are applied optionally to all the antennae used, whether these corrections are applied as a fixed value to the antenna offset or a variable correction to be subtracted from the phase observations depending upon the elevation angle of each satellite. Such variations are modelled using the US National Geodetic Survey calibration values (National Geodetic Survey 2005). More details on antenna PCV correction can be found in Section 2.6.1. In addition, a more precise tropospheric model using the updated Saastamoinen model with Niell's mapping functions is inserted, in order to minimize the tropospheric error as much as possible. Mathematical expressions and detailed explanation about this model can be found in Section 2.6.3. Other modifications were applied to the GASP software in order to utilize the single epoch processing methodology with the sidereal filtering technique. Detailed explanation of such updated software is given in Section 2.6.

Accordingly, the current research investigates two main topics. The first considers sidereal filtering of data, in order to help in the mitigation of the multipath error, which will eventually increase the precision of the final obtained point coordinates. Thus, instead of comparing the coordinates of successive epochs, it is possible to

compare and study the autocorrelation of point coordinates in each processed epoch with its counterpart one sidereal day before. But, of course, this will be done after several investigations are undertaken in order to determine first the optimum value of the sidereal lag period. Thus, various trial lags are considered ranging around the known nominal value of 23 hours and 56 minutes. As closure to this part, the ageing of any sidereal filter is investigated using different batches of multiple days, as well as the determination of the best possible combination of days to use and form the filter, in order to obtain maximum precision for the filtered coordinates.

For this purpose, two newly established programs are introduced. The first is the **GPS Autocorrelation Sidereal Filtering (GASF)**, which is used to determine the optimum sidereal lag period based on the maximum value of autocorrelation between subsequent epochs. The second program, called **Filter Application Program (FAP)**, uses the optimum sidereal lag period obtained from the first program in order to filter the coordinates from the multipath error and obtain the final accurate coordinates. In addition, the sidereal filtering process is also discussed, while comparing the raw phase data of GPS observations between epochs separated by one sidereal day, rather than comparing the coordinates themselves.

The second part of the research deals with the switched antenna array. The investigation concerned here is to determine the most appropriate observation session length per each fixed antenna before switching to the next one. This is employed while considering three main factors. The first is efficiency; that is using a short but still reliable session length. The second is how to implement sidereal filtering with switched antennae; that is synchronizing the used session length with the optimum sidereal lag obtained; and thirdly, to acquire at the end the best possible precision for station coordinates. This specific investigation of switch session length is vital, in order not to confuse structural deformation with observational errors, which will lead to inaccurate interpretation of the obtained results. In the end, after the accomplishment of the previous two main research objectives, the reliability and efficiency of sidereal filtering was investigated for improving the coordinate precision while detecting simulated deformations, using a dual antenna switch array, processing 1 Hz GPS data.

Note that due to the high precision required, the use of the navigation message broadcast along with GPS signals will be inapplicable, and thus more precise orbits must be used. In this case, final precise orbits could be used with an orbital accuracy less than 0.05 m but with 13 days latency or even the quicker rapid precise orbits with similar accuracy but only 17 hours latency. In addition, half observed ultra rapid precise orbits are available with similar accuracy within only three hours, which could definitely be regarded as a near real time application. Half predicted ultra rapid precise orbits could be also used for real time applications with 0.1 m orbital accuracy (Gledan 2004). For the current study, we use the International GNSS Service (IGS) precise orbits, which can be easily downloaded from the IGS website (International GNSS Service 2007; Neilan et al. 1997).

Finally, the current research will adopt several methodologies in order to assess the obtained results, such as (i) the obtained coordinate accuracy relative to previously known static coordinates; (ii) the repeatability (precision) of station coordinates over a certain time interval; (iii) the F-test statistic applied to the goodness of fit of the residuals to the phase observations (χ^2); and (iv) the efficiency of the used technique from the precision and processing time point of view.

1.6 Thesis Outline

This thesis consists of seven chapters and five appendices, briefly detailed as follows:

Chapter one introduces first the different sensors used for monitoring deformations, followed by the current situation of GNSS. The motivation behind the current research is outlined, and then pursued by the different techniques used for multipath mitigation. The chapter concludes with the main research objectives and adopted methodology.

Chapter two gives a brief introduction to GPS and its constellation, error sources and observables. Differencing GPS techniques and ambiguity resolution techniques are given next, ending with a detailed description of the utilized GPS software and adopted ambiguity resolution technique in the current research.

Chapter three provides a full illustration of the two programs used for sidereal lag determination and filter application and conclude with the actual geometry repeat lag investigations.

Chapter four introduces the main concept behind sidereal filtering using coordinate or carrier phase residual stacking. The actual application of the filter is fully illustrated together with a comparison of the two filtering techniques used, as well as an investigation into the effect of sidereal lag variations. Finally, investigations into the optimum number of days to stack and the sidereal filter lifetime are given.

In Chapter five, the mechanism of the multi-antenna array system is described. Various multi-antenna array system applications are briefly outlined, and then the development of the dual antenna switching device is explained. This is followed by the optimum session observation interval investigations. The Chapter ends with sidereal filter application on periodic GPS data, while considering various precision limits.

Chapter six involves the practical application of the single epoch sidereally filtered GPS utilizing a dual antenna switch array for monitoring deformations. The used simulating deformation platform is shown first. After that, the application of sidereal filtering on periodic GPS data sets, while considering implemented deformations, is fully described.

Chapter seven summarizes the work done throughout the research and the conclusions extracted from the results, in addition to the suggestions and recommendations for future research in the subject area.

GASP and GASF initial files are given in Appendix A and B, respectively. Additional sidereal filter analysis tables and plots are illustrated in Appendix C and D, respectively, while web resources are outlined in Appendix E.

GPS OVERVIEW AND PROCESSING SOFTWARE

2.1 Introduction

Currently, GPS is the dominant fully operational GNSS used for engineering surveying and geodetic applications. Although detailed explanations of GPS can be found in many publications, this chapter gives a brief background to GPS. At the start, a brief introduction to the GPS constellation and its various segments is given, followed by an outline of all major attributed errors in GPS positioning. The two main GPS observables are explained next, namely the code and carrier phase observables, accompanied by their mathematical expressions, after which the three GPS differencing techniques are illustrated. A concise overview of the different ambiguity techniques is presented. Most importantly at the end, the main GPS processing software used in the current research is fully described.

2.2 GPS Constellation

GPS consists of three segments: the space segment, control segment and user segment. The space segment includes the space vehicles (satellites) and the rockets used for launching the satellites. The constellation of GPS satellites today consists of 31 satellites (block II/IIA, IIR and IIR-M satellites), of which some are spare, to be used in the case of malfunction of any of the operational satellites. All satellites orbit the earth at a nominal altitude ≈ 20,200 km, distributed in six near-circular orbits, each inclined at 55^{o} to the equatorial plane, having the earth's centre at one of its foci. This inclination is chosen to ensure that the constellation of satellites covers the polar

regions. The satellites orbit the earth twice a day, that is, one complete revolution approximately every 12 hours (Leick 2004).

The current satellites transmit radio signals on two carrier frequencies L1 and L2, having frequencies of 1575.42 MHz and 1227.60 MHz respectively. The wavelength of L1 ≈ 19 cm, while for L2 ≈ 24 cm. Dual frequency receivers receive both L1 and L2 frequencies, while single frequency receivers deal with L1 only. These two carrier frequencies are modulated with Pseudo-Random Noise (PRN) codes and navigation messages. The first code is the Coarse/Acquisition code (C/A-code), which is unique for every satellite, encoding the transmission time of the signal according to the satellite atomic clock. This code is modulated on the L1 frequency only, and repeats itself every 0.001 second.

The second code is the Precise code (P-code), modulating both frequencies, so that it can be used for ionospheric corrections, repeating every week. This code length is 38 weeks, divided into seven day segments, where each week segment is given a PRN number, which is then designated to one of the GPS satellites. Consequently, the P-code is unique for every satellite (Hofmann-Wellenhof et al. 2001). The P-code has the same information as provided by the C/A-code but with ten times the resolution (Johnson 1997). However, due to anti-spoofing (Section 2.3.1), the P-code is encrypted with the W-code (a special encryption sequence), generating what satellites actually transmit which is the Y-code (or sometimes referred to as P(Y)-code), modulated also on L1 and L2 frequencies. Finally, both carrier frequencies are modulated with the navigation broadcast message containing satellite information, such as orbital elements, clock error correction, etc.

Note that since late 2005, a programme of modernizing GPS has been taking place called GPS III. All GPS III satellites will not carry the degradation capability, known as Selective Availability (SA). Although, this degradation was stopped back in May 2000, this new action eliminates a source of uncertainty in GPS performance concerning civil GPS users worldwide (Partyka 2007). Currently, block IIR-M satellites (and all future block IIR-M and IIF satellites) transmit the new L2 civil signal called L2C, aimed at eliminating the need for semi-codeless tracking

techniques to acquire L2 measurements. The L2C signal is easier to track than the P-code and thus improves the accuracy of navigation. This signal could become the most widely used GPS signal, used for indoor positioning, low cost consumer applications and in forest areas (Fontana et al. 2001). This signal has two PRN codes imposed on it: the first is the Civil Moderate (CM) code modulated with the Civil Navigation message CNAV and the second is the dataless Civil Long (CL) code. The CNAV message is an upgraded, more compact and flexible version of the NAV message. It has higher precision representation enabling extended week number calculation as well as the capability of supporting double the number of satellites than the current NAV message. The former message has a new flag to distinguish untrusted satellites, important for safety of life applications.

In addition, since the end of 2006, the new military code (M-code) has been transmitted on both L1 and L2 frequencies of block IIR-M satellites, modulating the Military Navigation message MNAV. The purpose of this code is to provide better performance and flexibility than the Y-code, while protecting the military utility of GPS (Barker et al. 2000). It is expected that by 2008 the safety of life civil signal LC5 will be transmitted on the newly launched block IIF satellites with a new third frequency of 1176.5 MHz. This signal is imposed by two PRN codes, the in-phase code (I5-code) and the Quadra-phase code (Q5-code). It has an improved noise performance at the receiver level as well as signal structure of higher power and wider bandwidth with an aeronautical radio navigation service band (Pullen and Enge 2004). Also, the L1 civil signal L1C will be transmitted on the L1 frequency in the future. Certainly, this multiplicity of signals will allow a new level of accuracy e.g. offering new techniques in removing the ionospheric delay (Enge 2003). However, it is expected that not until 2011 will manufacturers' receivers be able to track the L2C signal and the M-code in full on all available satellites, while it is anticipated that LC5 signals will be transmitted on all satellites by 2015.

The second segment of the GPS system is the control segment. Recently in September 2007, the US Air Force underwent a major upgrade of the GPS control segment, referred to as the Architecture Evolution Plan (AEP). This is aimed to modernize the control stations with new technology, in order to implement new capabilities, such as

the next generation of block IIF satellites (US Coast Guard 2007). The control segment consists of one master control station, four monitor stations and ground antennae, as well as six newly installed National Geospatial-intelligence Agency (NGA) monitor stations. The master station is located at Falcon Air Force Base in Colorado Springs, Colorado. It is mainly responsible for the overall management of the whole system, maintaining the functionality of the system and transmission of data to satellites. Other monitoring stations are located at Hawaii, Ascension Island in the Atlantic Ocean, Diego Garcia Atoll in the Indian Ocean and Kwajalein Island in the South Pacific Ocean. The role of these monitoring stations is to determine the position and health of all satellites in their respective orbits. Then all this information is sent to the master control station, to calculate the orbital elements and clock corrections and upload the data to the satellites.

Finally, the third GPS segment is the user segment. This segment is considered as the most influential segment because it is user interactive. It consists of either fixed or moving GPS antennae connected to receivers, utilized by the user and located at desired points for position determination. The term user includes both military and civilian users, where military users have the advantage of accessing higher accuracy than their civilian counterparts. That is to say, military users have full access to the C/A-code and the highly accurate P-code, while civilian users can fully access the C/A-code only, while accessing the P-code with degraded signal to noise ratio. Interaction between the user segment in terms of the civil user and the control segment in terms of the United States (US) GPS authorities is possible through the Civil GPS Service Interface Committee (CGSIC). This is a recognized worldwide forum, part of the US Department of Transportation (DOT), comprising members from the civil sector, government, and industry. The responsibility of this committee is to exchange GPS information with the civil GPS user community, concerning navigation, timing, and positioning (US Coast Guard 2006).

2.3 GPS Errors

The journey of the GPS signal, starting from the satellite and ending at the GPS receiver, is subject to different kinds of errors. The main sources of GPS errors may

be due to the control segment (such as: anti-spoofing), the space segment, (such as: satellite clock errors, orbital errors, system delays, etc.), the user segment, (such as: receiver clock error, phase centre variation, measurement noise, receiver delays, etc.). Errors can also result due to the atmosphere through which the signal propagates, (e.g. troposphere and ionosphere). In addition, the observing environment will also affect the GPS signals (e.g. multipath). Some of those errors can be eliminated by mathematical models. Others can be eliminated or at least minimized by using certain observation techniques such as relative positioning. However, some errors will still remain and propagate into the observations. The following three subsections will give an explanation of the types and sources of errors in GPS observations, which are classified as satellite, receiver and atmospheric errors.

2.3.1 Satellite Errors

Anti spoofing was implemented on 31st of January 1994, whereby the characteristics of the P-code are changed by mixing it with the 50 bit per second (bps) encrypted W-code, resulting in the Y-code. This security encryption denies receivers full access to the P-code measurements. However, many receiver manufacturers have developed proprietary techniques, providing GPS receivers with special decryption circuitry to make P-code measurements possible with only a small addition of noise (Leick 2004).

Orbital errors are basically the differences between the predicted broadcast satellite orbits and the actual perturbed orbits. Those errors are caused by the non-spherecity of the Earth (i.e. oblateness), additional gravitational forces by the sun and the moon, solar radiation pressure, etc., causing the deviation of the satellite from its orbit (Leick 2004). This error cannot be entirely eliminated by relative positioning and its effect depends mainly on the baseline length. The reason behind this fact is that a different component of the orbital error will be embedded in the measurement at each end of the baseline. Accordingly, the difference between these components increases as the baseline increases, causing a greater effect from this error source. An error of 1 m in the satellite's estimated position produces an approximate error of 0.05 ppm in the baseline (Leick 2004). Note that the precise orbits are the ones used in the current research, which are similar in principle to the broadcast orbits but with higher

accuracy, where this error — although existing — is negligible, for applications discussed here.

Satellite clock error is due to the imperfection of the atomic clock in the satellite, causing error in the calculated time and consequently in the obtained range. In GPS point positioning, this kind of error can be modelled to within one nanosecond using the clock parameters included in the broadcast ephemerides (Leick 2004). In addition, this error can be almost eliminated by adopting differencing techniques.

The satellite configuration error, or in other words, the geometric configuration of satellites with respect to the GPS antenna, is measured by the Dilution of Precision (DOP). In general, the smaller the value of DOP, the better the configuration of satellites, leading to higher observational accuracy, and vice versa. One aspect of DOP is the Geometric Dilution of Precision (GDOP), which is a measure of the geometric configuration (Figure 2.1).

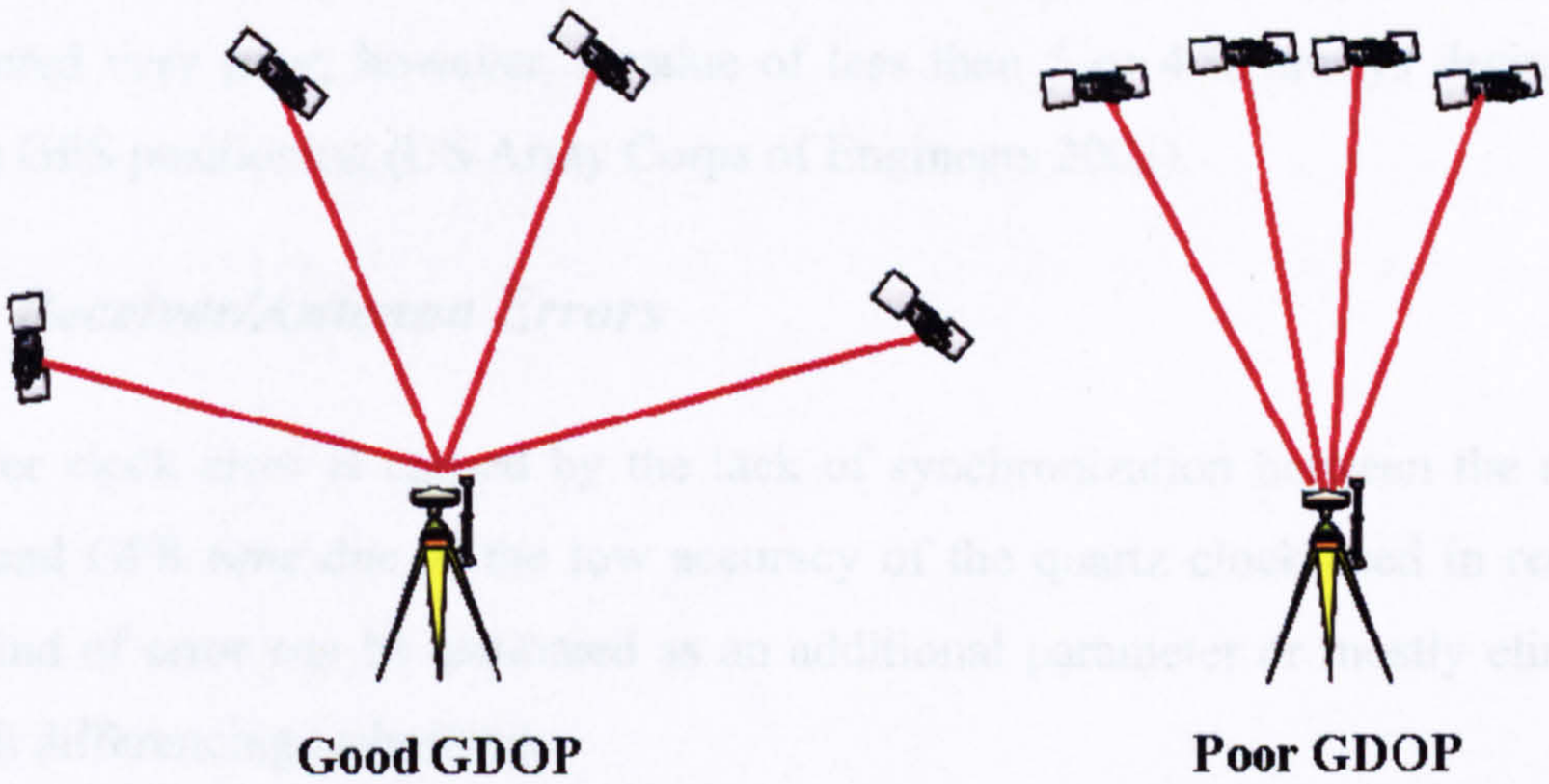

Figure 2.1 Good and poor geometric configuration of satellites.

By definition, GDOP is the ratio between the positional accuracy and the measurement accuracy, i.e. the accuracy in the geometrical position (3D position and time), and is given through the following expression:

$$GDOP(\sigma) = \sqrt{\sigma_e^2 + \sigma_n^2 + \sigma_u^2 + c^2\sigma_t^2} \,/\, \sigma_\rho \,, \qquad 2.1$$

where σ_e, σ_n, σ_u are the formal errors of the receiver coordinates in the local system e,n,u, respectively, and is calculated through mathematical manipulation from the

actual receiver coordinates x, y, z and time t. c is the speed of light in vacuum, which is equal to 299792458 m/s, while σ_t and σ_ρ are the formal errors of the receiver clock bias estimate and measured range.

Another measure of the quality of the geometry of satellites surrounding the antenna is the Positional Dilution of Precision (PDOP), defined as the accuracy of the three dimensional position, and is given by the following equation:

$$PDOP(\sigma) = \sqrt{\sigma_e^2 + \sigma_n^2 + \sigma_u^2} \Big/ \sigma_\rho \qquad 2.2$$

As the value of the PDOP decreases, the positional formal errors also decrease, which means an improvement in the positional accuracy. It should be mentioned here that the impact of the satellite geometry is of more concern in navigation and kinematic surveying than in static positioning. These geometry effects could be mininized by averaging in static positioning. In most GPS receiver manuals, satellite geometry having a GDOP or PDOP value of less than 6 is acceptable while greater than 10 is considered very poor; however, a value of less than 5 or 4 is always desirable for precise GPS positioning (US Army Corps of Engineers 2003).

2.3.2 Receiver/Antenna Errors

Receiver clock error is caused by the lack of synchronization between the receiver clock and GPS time due to the low accuracy of the quartz clock used in receivers. This kind of error can be estimated as an additional parameter or mostly eliminated through differencing techniques.

The reason for the antenna phase centre variation is the non-coincidence of the electrical phase centre of the receiver antenna to which the radio signal is referred and the actual physical antenna centre due to the non-spherical pattern of the antenna, reaching as much as several centimetres (Leick 2004). This offset is not constant, as the antenna's sensing point location will vary according to the direction of the incident signal depending on the azimuth and elevation of the observed satellite. This error can be modelled by applying certain satellite elevation dependent corrections to

the observed phases, and varies according to the type of antenna used (National Geodetic Survey 2005).

Electronic measurement noise results from imperfect generating and recording mechanisms in the receiver. The value of the measurement noise error ranges between 1–3 m for C/A-code, 10–20 cm for P(Y)-code and 3–10 mm for the carrier phase noise (Lachapelle et al. 1992). These errors are random and thus can be estimated through various tests, such as the zero baseline test (two receivers and one antenna).

Multipath error (Figure 2.2) occurs due to the existence of reflecting surfaces near the receiver causing the arrival of the signal via more than one path. The resulting signal will be a combination of the direct signal from the satellite and the signal reflected from nearby surfaces (Pratt 1991). The reflected signal arrives at the antenna with a phase delay relative to the direct signal, due to the extra path travelled, causing distortion of the signal's amplitude and phase, depending on the wavelength of the signal. The reflected signal is always weaker due to the attenuation at the reflector. This attenuation will depend upon the nature of the observing environment, in terms of the height of the antenna above the ground or its distance from any vertical barrier, material of the reflector, the incident angle of reflection, polarization and the receiver hardware and firmware (Lau and Cross 2007).

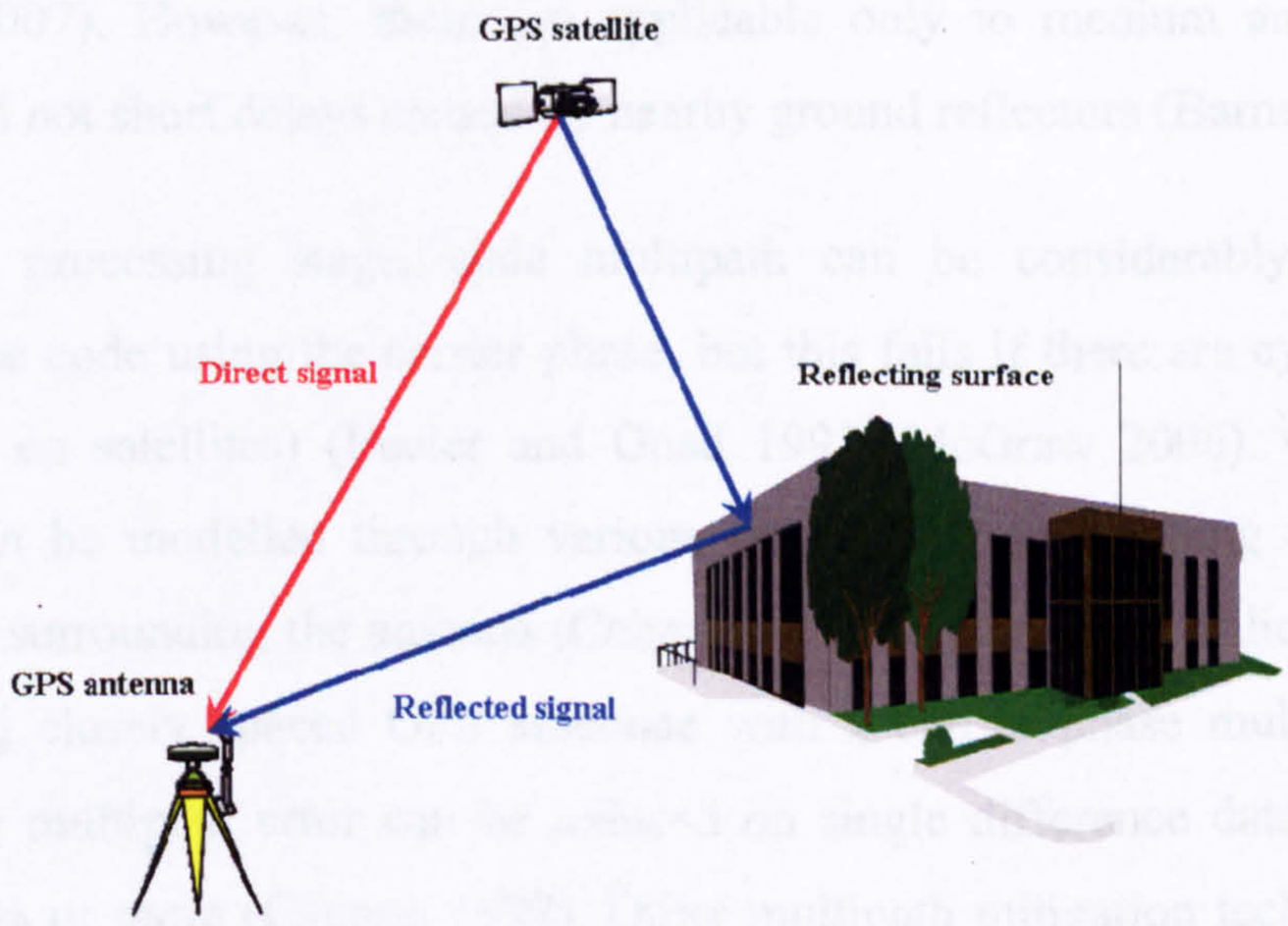

Figure 2.2 Multipath error.

In general, reflections of signals from satellites with low incident angles are less attenuated at the reflector, which explains the well known fact that low elevation satellites produce higher multipath because they generate stronger reflected signal (Leick 2004). Reflections from smooth surfaces are called specular multipath, producing highly correlated, slowly varying errors that are difficult to deal with. On the other hand, reflections from rough surfaces produce diffuse multipath, having a more random property, which could be filtered out (Barnes 2000).

Numerous techniques are used to reduce code and carrier phase multipath, keeping in mind that the latter is small when compared to code multipath error (Ray 2000). At the measurement stage, using antennae with special ground plates, such as choke ring antennae, will reduce the pseudorange multipath error (Philippov et al. 1999). Also, given the nature of the GPS signal being right-hand circularly polarized (RHCP), which in theory becomes left-hand circularly polarized (LHCP) after reflection from an ideal conducting surface, provides some protection against multipath signals. GPS antennae are designed to accommodate for RHCP signals with much lower sensitivity to LHCP signals and therefore attenuate signals of the opposite polarization (Schupler and Clark 1991). In addition, several receiver technologies were developed to reduce the code and carrier phase multipath, e.g. filtering out multipath having large additional path length caused by the reflection of signals from distant reflectors (Lau and Cross 2007). However, these are applicable only to medium and long-delay multipath and not short delays caused by nearby ground reflectors (Barnes 2000).

At the post processing stage, code multipath can be considerably reduced by smoothing the code using the carrier phase, but this fails if there are cycle slips (i.e. loss of lock on satellites) (Eueler and Goad 1991; McGraw 2006). Carrier phase multipath can be modelled through various ways, such as mapping the multipath environment surrounding the antenna (Cohen and Parkinson 1991; Bilich and Larson 2007). Using closely spaced GPS antennae with a carrier phase multipath model, carrier phase multipath error can be reduced on single difference data in the static mode by 70% or more (Cannon 1998). Other multipath mitigation techniques at the post processing stage are explained in more detail in Section 1.4.

Assuming a single horizontal large reflector located at a distance H beneath the antenna phase centre and a plane wave GPS signal having an angle of incidence equal to the angle of reflection ε, the direct carrier phase signal voltage Sd_A^j from point A to satellite j is given by the following expression (Georgiadou and Kleusberg 1988):

$$Sd_A^j = V_A^j \cos\phi_A^j, \qquad 2.3$$

while the reflected signal voltage Sr_A^j is given by:

$$Sr_A^j = \alpha_A^j V_A^j(\cos\phi_A^j + \theta_A^j), \qquad 2.4$$

where V_A^j is the signal voltage amplitude, ϕ_A^j is the carrier phase signal, α_A^j is the antenna gain pattern or, in other words, the factor of attenuation of the signal after reflection ($0 \le \alpha \le 1$) and θ_A^j is the phase shift between the direct and reflected signal given as follows:

$$\theta_A^j = \frac{4\pi H \sin\varepsilon}{\lambda} \qquad 2.5$$

Note that the extra atmospheric propagation delay due to the reflected path is ignored as well as the phase and polarization changes which might occur on reflection (Elósegui et al. 1995). Accordingly, the signal received at the antenna is the sum of the direct and reflected signal given by the following equation:

$$S_A^j = Sd_A^j + Sr_A^j = \beta V_A^j(\cos\phi_A^j + \psi_A^j), \qquad 2.6$$

in which β is the change in the signal voltage and is given by:

$$\beta = \left(1 + 2\alpha_A^j \cos\theta_A^j + \alpha_A^{j\,2}\right)^{1/2}, \qquad 2.7$$

and ψ_A^j is the amplitude of the carrier phase multipath error (the dominant multipath error in the current research) given in radians by the following equation:

$$\psi_A^j = \tan^{-1}\left(\frac{\alpha_A^j \sin\theta_A^j}{1 + \alpha_A^j \cos\theta_A^j}\right) \qquad 2.8$$

Considering $\alpha_A^j <<< 1$ and neglecting squares of α_A^j, Equation 2.8 can be approximated as follows:

$$\psi_A^j \approx \alpha_A^j \sin\theta_A^j \qquad 2.9$$

Thus, the amplitude of the carrier phase multipath depends mainly on the signal strength of the reflected signal, having maximum value when the reflected signal is not attenuated, that is α_A^j=1 and θ_A^j=90° or 270°. Accordingly, the maximum carrier phase multipath error is equal to quarter of the wavelength of the signal, reaching about 4.8 cm and 6.1 cm for the L1 and L2 frequency respectively (Georgiadou and Kleusberg 1988).

As long as the GPS receiver remains static in the same environment, the multipath effect will mainly depend upon the position of the satellite in the sky, i.e. its azimuth and elevation angle. The multipath error increases as the satellite elevation decreases. This effect cannot be eliminated by adopting any kind of differencing technique even at short distances, although it will repeat itself over time. Thus, temporal filtering could result in the reduction of multipath as well as any other geometry repeating errors. This is one of the main objectives of this research.

2.3.3 Atmospheric Errors

Neutral atmospheric delay is due to the refraction of the GPS signal as it passes through the neutral atmosphere (troposphere, tropopause and stratosphere), extending from the earth's surface to a height of about 50 km. This delay is often referred to as the tropospheric delay. Figure 2.3 illustrates the different layers of the Earth's atmosphere. The troposphere contains 75% of the mass of the neutral atmosphere, in which the meteorological parameters such as temperature, humidity and pressure are the dominant factors. The velocity of the GPS signal passing through the troposphere is affected by two main factors. The first will be the atmospheric conditions surrounding the observing point, as well as the height of the point above mean sea level.

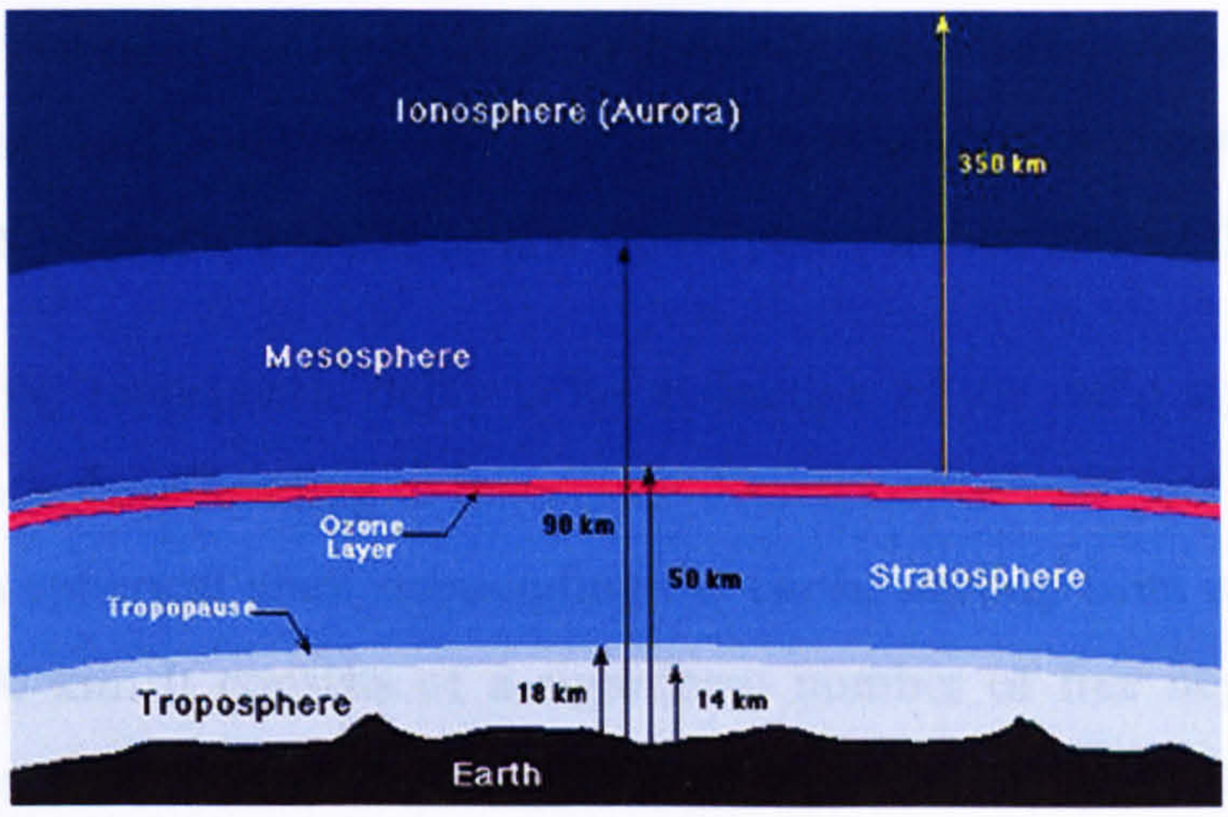

Figure 2.3 Layers of the Earth's atmosphere.

(http://www.fas.org/irp/imint/docs/rst/Sect14/atmosphere.jpg)

The second is the direction of propagation of these signals through the troposphere. Consequently, GPS signals transmitted from highly elevated satellites are less affected by the tropospheric delay than those signals from low elevated satellites near the horizon (Leick 2004), because the distance travelled by the signal through the troposphere is reduced. This distance is approximately given by the following expression:

$$d(\theta) \approx D / \cos\theta , \qquad 2.10$$

where d is the distance travelled by the signal in the troposphere layer, D is the thickness of the troposphere and θ is the incident angle of the satellite signal ($\theta = 90 - Z$). Z is the elevation angle of the satellite.

Tropospheric delay is modelled in this research through the application of the empirical Saastamoinen model to calculate the zenith tropospheric dry (90%) and wet delay (Saastamoinen 1973; Saastamoinen 1972). Niell's mapping functions are used to relate the tropospheric delays at the zenith to its values at different elevation angles (Niell 1996). Consequently, the computed tropospheric delays correct the observables of each satellite depending on its elevation angle (see Section 2.6.3). However, in order to apply this model, the meteorological data at the receiver should be known, either through standard models or ground observations. An error of 1 mm in relative zenith delay creates an error of about 3 mm in the height component (Santerre and

Beutler 1993). Fortunately, this kind of error can be minimized through relative GPS positioning over short baselines, with a small height difference between the two end points, as the atmospheric conditions and signal paths will be almost the same.

The source of the ionospheric delay is the refraction of the radio signal as it passes through the ionosphere, leading to inaccurate determination of signal travel time. The ionosphere is a spherical shell surrounding the earth, starting from a height of about 40 km to 1,500 km. It consists of a significant number of free negatively charged electrons generated through the impact of solar ultraviolet radiation on the atmospheric gases. Positively charged atoms also exist. Both cause delay of the propagating GPS signals (Leick 2004). Although it is called a delay, the ionosphere delays the arrival of the code modulation while, on the other hand, it advances the carrier phase by the same amount for the same frequency.

The main factors affecting this error are the frequency of the radio signal and the ionospheric refractive index. This index is a function of the number of free electrons in a square metre column along the signal path (also known as the Total Electron Content, TEC). The ionospheric delay is given by the following approximate expression (Hoffman-Wellenhof et al. 2001):

$$\delta_{ion} \approx \pm 40.3 \frac{TEC}{f^2}, \qquad 2.11$$

where δ_{ion} is the ionospheric delay in meters, which is added in the case of the pseudorange or subtracted in the case of the carrier phase. f is the frequency of the signal in Hz. From the previous equation, the code delay and the phase advance are proportional to the inverse of the frequency squared. Therefore, the code delay or phase advance on the L2 frequency is greater than its counterpart on the L1 frequency. Typically, the TEC values range from 10^{16} to 10^{18} electrons per square metres at the zenith, and thus considering for example the L1 frequency, the ionospheric delay for satellites at the zenith, ranges between 0.16 m to 16.24 m respectively (Leick 2004).

Accordingly, the ionospheric delay is one of the major error sources in GPS observations, and must be eliminated or at least reduced. This could be done through one of the following three methodologies. The first is by using the broadcast coefficients in the navigation message to compute the ionospheric delay. This is widely used when employing broadcast orbits or single frequency receivers. The second methodology uses differencing techniques, reliable for baseline lengths of less than 10 km, in which the remaining ionospheric errors will be negligible. The last methodology is to use linear combinations of L1 and L2 phase observables, especially for baseline length greater than 10 km. The general expression for the linearized phase combination is given as follows:

$$\Phi_{L1,L2} = n_1\Phi_{L1} + n_2\Phi_{L2}, \qquad 2.12$$

$\Phi_{L1,L2}$ is the linear phase combination, while n_1 and n_2 are arbitrary factors to be determined according to the type of linear combination. For the wide-lane combination, $n_1 = 1$ and $n_2 = -1$, while for the ionosphere-free, $n_1 = 1$ and $n_2 = -\frac{f_{L2}}{f_{L1}}$. Note that f_{L1} and f_{L2} are the frequencies of the L1 and L2 carrier waves respectively.

2.4 GPS Observation Equations and Differencing

GPS observables are actually ranges, which are calculated either from the measured travel time of GPS signals called code pseudoranges or from phase differences called carrier phases. The pseudorange is obtained by comparing the actual satellite signal and the receiver generated signal. Consequently, it is calculated from the time difference between transmitting the signal and receiving it using two clocks, one atomic clock in the satellite, and a quartz clock in the receiver, which is less accurate.

For the carrier phase, the satellite signal is mixed with the receiver's replica carrier signal, producing the carrier beat phase, which is equal to the difference in phase between the two signals. Nevertheless, recording the fractional phase difference is still not sufficient, as the initial ambiguous integer number of cycles from the satellite to the receiver has to be solved for, by adopting what is called ambiguity resolution techniques. While tracking the satellite, this integer number remains constant and

added to the measured fractional and complete cycles, providing continuous lock on the satellite (no cycle slips).

However, these ranges and phase differences are biased by the inherent existing errors during GPS positioning. Many biases existing in these two types of observables are correlated over short baselines. Therefore, most of these errors can be eliminated or at least reduced by adopting certain differencing strategies. The two observables used in GPS positioning are described first, each with its observation equation, followed by a brief discussion of the three GPS differencing techniques.

2.4.1 Code Pseudorange Observable

The measured quantity here is the time difference between the emission of the signal from the satellite and the reception of this signal at the receiver. The mathematical model defining the relationship between the observed pseudorange at any epoch t, and the 3D unknown receiver Cartesian coordinates, as well as accompanied errors, can be expressed as follows (Hofmann-Wellenhof et al. 2001):

$$R_i^j(t) = \rho_i^j(t) + c.(\delta_i(t_r) - \delta^j(t^t)) + \delta_{trop}(t) + \delta_{ion}(t) + \delta_{orb}^j(t) + \delta_i^{hardware} + \delta_{hardware}^j + \delta_{p_{multi}}(t) + \delta_{p_{noise}}(t), \quad 2.13$$

in which $R_i^j(t)$ is the measured code pseudorange between the observing unknown point i (more accurately its antenna) and the satellite j at epoch t. $\rho_i^j(t)$ is the geometric distance between points i and j, represented as:

$$\rho_i^j(t) = \sqrt{\left(X^j(t^t) - X_i(t_r)\right)^2 + \left(Y^j(t^t) - Y_i(t_r)\right)^2 + \left(Z^j(t^t) - Z_i(t_r)\right)^2}, \quad 2.14$$

where $X^j(t^t), Y^j(t^t), Z^j(t^t)$ are the known 3D coordinates of the satellite position at transmission time t^t according to the satellite clock when the signal was transmitted, while $X_i(t_r), Y(t_r)_i, Z_i(t_r)$ are the unknown 3D coordinates of the observing point at received time t_r according to the receiver clock when the signal was received. $\delta_i(t_r)$ and $\delta^j(t^t)$ are the receiver and satellite clock offset with respect to GPS time, respectively. The latter is determined from the broadcast navigation message and

enables the minimization of this error, but does not eliminate it totally. $\delta_{trop}(t)$ is the tropospheric error, $\delta_{ion}(t)$ is the ionospheric delay, $\delta^{j}_{orb}(t)$ is the orbital error for satellite j. $\delta_{i}^{hardware}$ and $\delta^{j}_{hardware}$ are the receiver and satellite hardware delays respectively, $\delta_{p_{multi}}(t)$ is the code multipath effect, while $\delta_{p_{noise}}(t)$ is the receiver noise. Note that epoch time (t) is somewhere between transmission time (t^{t}) and received time (t_{r}).

2.4.2 Carrier Phase Observable

The carrier phase is the difference between the phase of the received satellite carrier signal and the phase of the reference carrier generated in the receiver. Ideally, the carrier phase observable would be the total number of full carrier cycles and fractional cycles between the satellite and the receiver at any instant. This is determined by measuring the fractional phase and tracking the changes in the full number of cycles. Unfortunately, the initial integer number of cycles between the satellite and the receiver at the instant of locking onto the satellite cannot be determined during the observation process. The number of unknown cycles is known as the integer phase ambiguity N, and shall be considered as an additional parameter to be determined (see Figure 2.4).

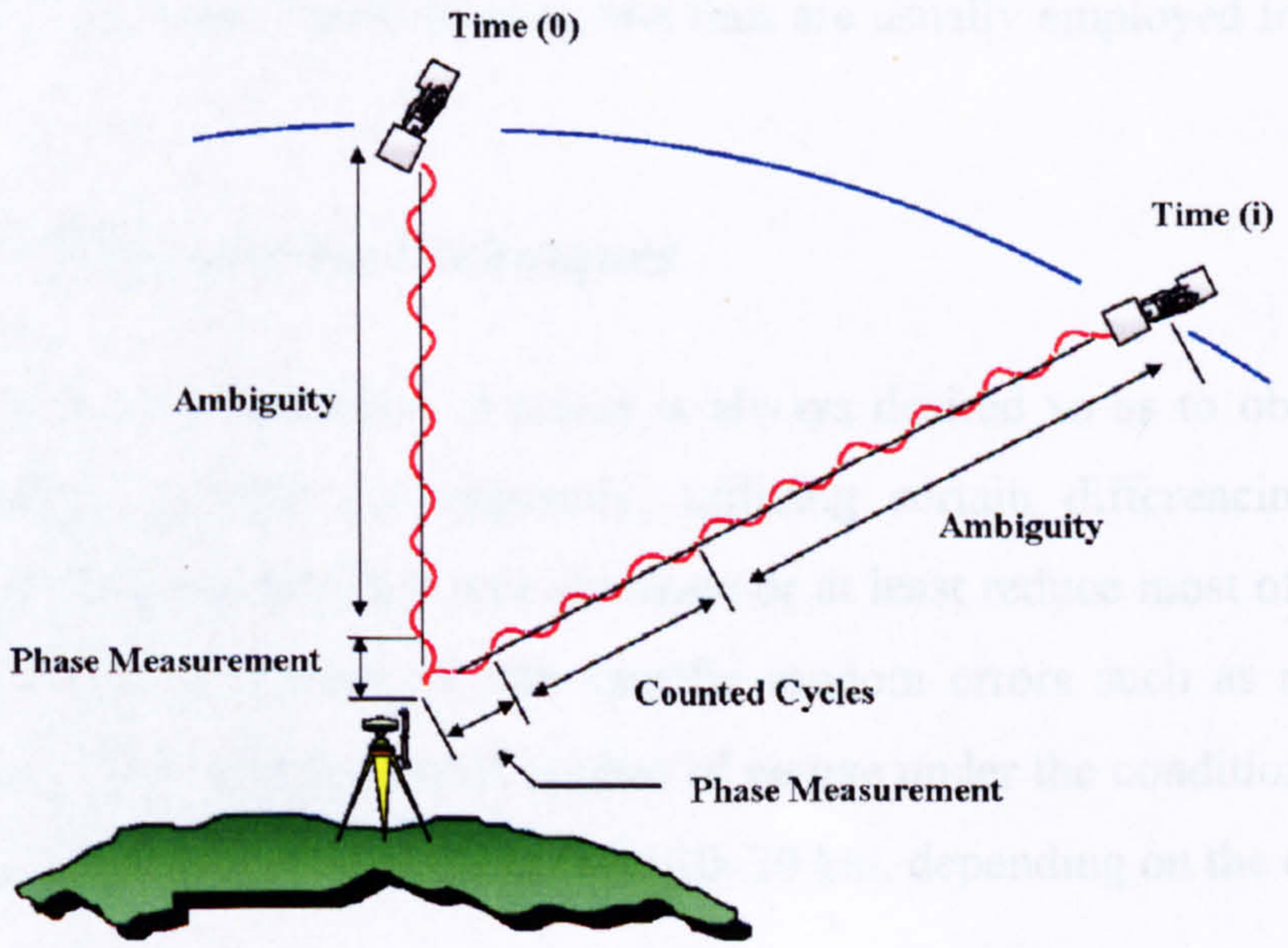

Figure 2.4 Integer phase ambiguity.

The mathematical model expressing the relationship between the carrier phase observed quantity and the unknown point 3D Cartesian coordinates is given in units of length by the following expression:

$$\lambda.\Phi_i^j(t) = \rho_i^j(t) + c.(\delta_i(t_r) - \delta^j(t^t)) + \lambda\, N_i^j + \delta_{trop}(t) - \delta_{ion}(t) + \delta_{orb}^j(t) + \delta_i^{hardware} + \delta_{hardware}^j + \delta_{\Phi_{multi}}(t) + \delta_{\Phi_{noise}}(t) \quad 2.15$$

$\Phi_i^j(t)$ is the measured carrier phase observable between the observing point i and the satellite j at epoch t in cycles, λ is the carrier signal wavelength, and N_i^j is the integer phase ambiguity. All other terms are as previously defined.

The precision of the pseudorange measurements depends on the precision of correlating the incoming satellite signal with the generated receiver signal. In other words, it is the precision of determining the difference between the transmission time of the signal relative to the satellite clock, and the signal received time relative to the receiver clock. This time difference precision is about one nanosecond. On the other hand, the precision of carrier phase measurements depends on the precision of determining the phase difference between received and generated signal, that is the precision of the carrier beat phase. This measurement precision is about 1/100 of a wavelength, leading to an accuracy of about 1.9 mm for L1 and 2.4 mm for L2 (Hofmann-Wellenhof et al. 2001). Accordingly, carrier phase measurements are more precise than code range measurements, and thus are usually employed in precise GPS positioning.

2.4.3 GPS Differencing Techniques

In GPS geodesy, the reduction of errors is always desired so as to obtain the most accurate results possible. Consequently, utilizing certain differencing techniques between receivers and satellites will eliminate or at least reduce most of the common errors at both points, except for site specific random errors such as multipath and receiver noise. This error reduction applies of course under the condition of moderate separation between receivers ranging from 10–20 km, depending on the error source.

The first case of receiver-to-receiver differencing is the ***single difference***. Two GPS observations taken simultaneously from two ground receivers i and m, to the same satellite j at epoch t, are differenced. Using Equation 2.15, the new single difference observation equation will be as follows (Hofmann-Wellenhof et al. 2001):

$$\lambda.\Phi_{im}^{j}(t) = \rho_{im}^{j}(t) + c(\delta_m(t_r) - \delta_i(t_r)) + \lambda.N_{im}^{j} + \delta_{\Phi_{multi}}(t) + \delta_{\Phi_{noise}}(t), \qquad 2.16$$

where $\Phi_{im}^{j}(t)$, $\rho_{im}^{j}(t)$ and N_{im}^{j} are respectively the difference between the measured carrier phase observable, geometric distance and integer ambiguity at points i and m. From Equation 2.16 it can be seen that single differencing has the advantage of almost eliminating the satellite clock error and reducing satellite orbital error and hardware biases, assuming the signal transmitted from the satellite to each of stations i and m at the same transmission time t^{j} and position $X^{j}(t^{j}), Y^{j}(t^{j}), Z^{j}(t^{j})$. In addition, atmospheric errors at both stations are considered similar, and thus cancel out each other, providing reasonable short baseline length (less than 10 km).

The second kind of differencing is the ***double difference*** technique, which is adopted in this research. It is simply differencing two single difference equations to two satellites j and k at epoch t. Accordingly, the equation for double difference is given by the following expression:

$$\lambda.\Phi_{im}^{jk}(t) = \rho_{im}^{jk}(t) + \lambda.N_{im}^{jk} + \delta_{\Phi_{multi}}(t) + \delta_{\Phi_{noise}}(t) \qquad 2.17$$

This leads to the cancellation of the receiver clock errors as well, assuming the signal arrived at both stations at the same received time t_r. This verifies the importance of this differencing technique and the reason behind its regular use in differential GPS. The last technique is the ***triple difference***, where two double difference equations are differenced, with GPS observations collected at two different epochs t_1 and t_2. The triple difference equation is expressed as follows:

$$\lambda.\Phi_{im}^{jk}(t_{12}) = \rho_{im}^{jk}(t_{12}) + \delta_{\Phi_{multi}}(t) + \delta_{\Phi_{noise}}(t), \qquad 2.18$$

in which $t_{12} = t_2 - t_1$. One can see that, in addition to the elimination of both receiver and satellite clock offsets, the involved ambiguities will also disappear, providing

continuous lock on satellites between epoch t_1 and t_2. This technique has the disadvantage of being noisier and thus less accurate, due to the accumulation of errors, and therefore is not frequently used in practice; however, it is mainly used for cycle slip detection. Figure 2.5 illustrates all three differencing techniques.

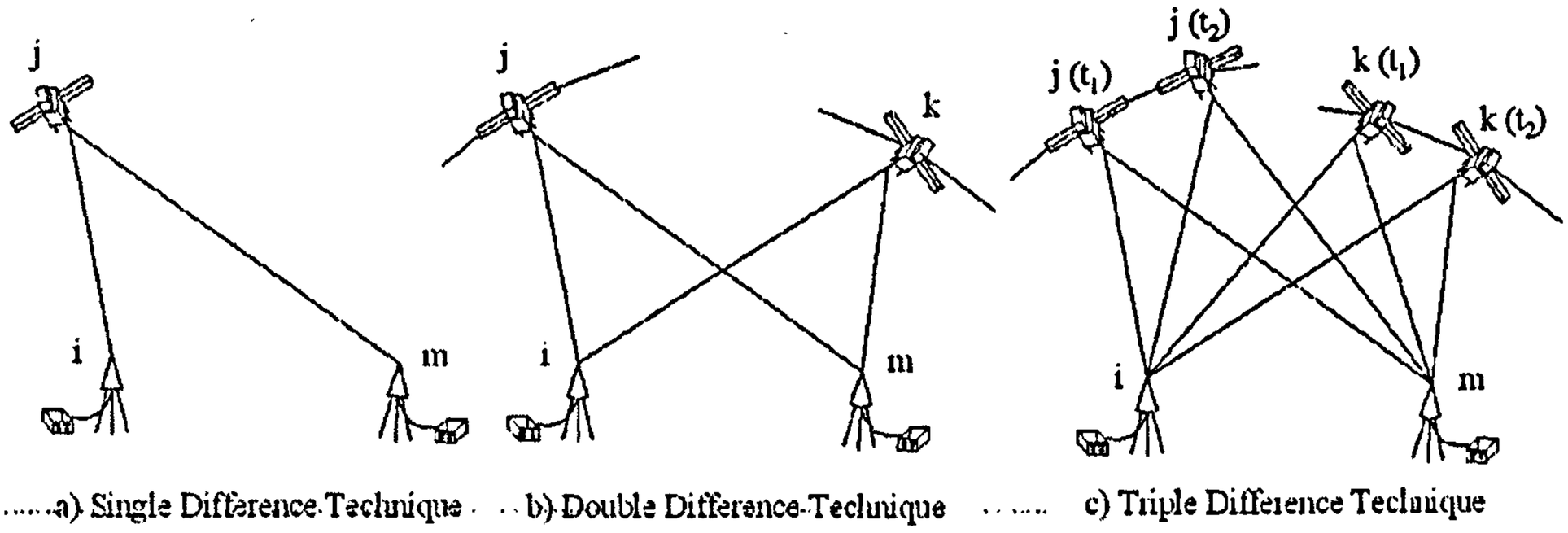

Figure 2.5 GPS differencing techniques.

2.5 Ambiguity Resolution Techniques

As mentioned earlier, carrier phase measurements are commonly used for GPS positioning, usually adopting double differencing for the cancellation of many of the various errors previously discussed. One of the major problems in carrier phase double differencing is the estimation of the integer phase ambiguity. This estimation is essential for instantaneous accurate positioning using phase data. Several techniques could be used to recover the ambiguity, whether static or kinematic. Static techniques include static initialization of baselines over a short time period, occupation of a known baseline, antenna swapping, etc.

Static occupation of baselines requires simultaneous observations at both end stations of the baseline (one fixed and the other unknown) for a certain time interval depending on the length of the baseline. This allows for the geometry of the satellite constellation to change significantly so that the ambiguities can be correctly estimated (Rizos 2007). However, the disadvantage of this technique is that it requires long time to solve for the ambiguity, i.e. 5–20 minutes. Similar methodology is adopted for the technique of occupying a known baseline, where both end stations' coordinates are fixed. Accordingly, a shorter observation period is required to solve for the ambiguity

by comparing the obtained coordinates of one of the stations with its already known fixed coordinates. The basic idea behind antenna swapping is to force a change in the geometry of the satellites, instead of waiting for a long observation period. This is performed by collecting data on two stations separated by 5–10 meters for about 1–5 minutes. Then the receivers are swapped between the two stations without losing lock on satellites and another data set is collected. Then at the end, the receivers are placed back to their initial position for the last data set, after which the ambiguity is resolved (El-Rabbany 2006).

Note that, all previous techniques are suitable to be used preceding any static, rapid static or kinematic GPS surveying. However, if loss of lock occurs during any of these techniques, the solution for the ambiguity fails, which is considered a major disadvantage in these static techniques. Accordingly, those static techniques require relatively long observation periods, and thus they are not considered suitable for kinematic positioning or in our case here of monitoring deformations, where the test point is assumed to be moving. In addition, the occurrence of loss of lock during observations will require re-initialization. Consequently, in such a case, On The Fly (OTF) ambiguity resolution techniques may offer a solution (e.g. Hatch 1990; Remondi 1991).

Ambiguity resolution techniques especially OTF resolution provides centimetre level accuracy in real time positioning. This accuracy is affected by many factors; geometric configuration of satellites measured through PDOP value, number of satellites in view, as well as the search algorithm itself. The more satellites, reference stations and better geometry, the greater the reliability of the OTF ambiguity resolution, resolving the ambiguity successfully using only a single epoch or a few epochs. OTF techniques should maintain the following properties: fast computations and successful operation with a small number of epochs to be suitable for real time applications; high reliability for correct ambiguity resolution; and quality control for unmodelled biases and cycle slips.

Any OTF ambiguity resolution technique will adopt two main procedures in order to solve for the unknown ambiguities. The first will be the determination of an initial

approximate solution for the unknown receiver, which should lie close to the actual true value within a certain range of search volume. This is considered a vital step for phase ambiguity resolution and improves the processing efficiency (Hatch 1990). The second step will include a least squares estimation of the correct real valued ambiguity combination, having a minimal estimated variance factor calculated using the adjusted carrier phase residuals. Nowadays, many OTF techniques are being used for the resolution of integer phase ambiguity. The most common resolution techniques are: the Fast Ambiguity Resolution Approach (FARA), Least Squares Ambiguity Search Technique (LSAST), Fast Ambiguity Search Filter (FASF), Modified Cholesky Decomposition (MCD), Ambiguity Function Technique (AFT) and Least squares AMBiguity Decorrelation Adjustment (LAMBDA).

In FARA, the algorithm used to obtain the final set of ambiguities can be divided into four main steps (Frei and Beutler 1990; Erickson 1992). The first involves a float carrier phase adjustment to obtain real values for the double difference ambiguities, as well as some statistical information. These statistics are used in the second step to form a search range of different ambiguity sets. The third step performs a Least Squares Adjustment (LSA) process using fixed ambiguities for each chosen ambiguity set. Thus, for each set, the adjusted baseline component and the a posteriori variance factor are known. In the last step, the solution with the smallest variance factor is statistically tested for the null hypothesis using the F-test, to ensure its significance over all tested ambiguity sets. This multi-epoch technique has two main disadvantages, one of which is that it is affected by cycle slips, and the other being the small number of tested ambiguity sets, which will affect the outcome of the final solution.

The LSAST was developed by Hatch (1990) based upon the idea that ambiguities of two groups of satellites are correlated. At first, the search size is determined from the standard deviation of an approximate code solution. Then, the observed satellites are divided into primary and secondary satellites. The primary satellites consist of four satellites of highest elevation angle and good geometry, which are used along with the initial fixed position to calculate three primary double difference ambiguities, and then form a search volume of different ambiguity sets based on the search size. The

secondary satellites consist of all remaining satellites, which are used first to eliminate false ambiguity sets through the calculation of a phase residual vector passing a pre-defined threshold. For the remaining ambiguity sets, the solution obtained from the primary satellites is updated using the set of ambiguities and observations from the secondary satellites. Finally, the computed variance factor for each set is tested against a predefined threshold. The correct solution should be the only one passing the test, and if not, then the whole epoch is discarded. Note that the GPS processing software used in the current research utilizes a similar concept for ambiguity resolution, except for using the AFT for determining passing ambiguity sets to be tested.

FASF, developed by Chen (1993), determines the phase ambiguity through least squares adjustment with some constraints, adopting a special ambiguity search procedure called the Recursive Computation of the Search Range (RCSR) for every double difference ambiguity set. Briefly, the size of the search range decreases with time, while still containing the true solution, due to accumulation of data and change in the satellite geometry. When the ambiguities are fixed, a baseline solution is computed. If the ambiguities at any epoch cannot be fixed due to ineffective change in the satellite constellation, then they could be estimated as real values using Kalman filtering. FASF only applies to multi-epoch solutions and its efficiency depends on the environment dynamics (kinematic or static).

Eueler and Landau (1992) developed the MCD technique. Here, the effect of different ambiguity sets on the sum of the squared residuals is tested using constrained least squares adjustment, applying the mathematics of Cholesky decomposition. The search space is calculated through matrix manipulation of the least squares adjustment, producing various numbers of trial positions. The best position is accepted based on the following criteria: the ratio between the sum of squared residuals of the second best solution to its counterpart of the best solution must be greater than 2.

The ambiguity function technique (AFT) was initially developed by Counselman and Gourevitch (1981) and then updated by Remondi (1984). The principle behind this technique is to use complex numbers in order to separate the initial phase ambiguities

and the fractional phases. The derivation of the AFT algorithm can be found in many publications, such as Leick (2004). The major advantage of this technique and the reason for its wider use over other OTF techniques is that every epoch is processed independently from the previous one. In other words, if the ambiguity is not resolved in any epoch, the solution in subsequent epochs will not be affected. In addition, this technique does not require continuous lock on satellites, so it is unaffected by cycle slips and thus has no need for initialization. Special emphasis on this technique is given in Section 2.6.5.

Finally, the main idea of the LAMBDA technique is that GPS carrier phase ambiguities are highly correlated during a short time span of ineffective satellite constellation change (Teunissen 1993). An elongated integer search space defined by the covariance matrix can stretch to a considerable range of cycles as a result of low precision in each of the ambiguities. Therefore, the multi-dimensional confidence ellipsoid remains extremely elongated due to the high correlation between ambiguities states. At first, a short observational period is undertaken, and the main ambiguities are resolved through any of the OTF techniques. These ambiguities are then transformed through a Gauss transformation, so that the correlation between ambiguities is minimized (decorrelation). This transformation should maintain the integer ambiguities, preserve the volume of the multidimensional confidence ellipsoid, and reduce the number of ambiguity sets. This results from the reduction in the product of the ambiguity variances, which is considered the main advantage of the LAMBDA technique, and makes it appropriate for real-time applications (Teunissen 1993). After that, a sequential conditional least-square based search follows. However, the reliability is limited by the effectiveness of the test used to select the single correct set of integer ambiguities.

2.6 GPS Ambiguity Search Program (GASP)

The main GPS processing software used in this thesis is an in-house program called GPS Ambiguity Search Program (**GASP**), written in the C programming language. This program is a modified and updated author's version of the original used by Corbett (1994), Al-Haifi (1996) and Gunasingam (2003). The program operates with

double difference observables, resolving the integer phase ambiguities at each epoch independently. Processing involves one unknown (moving or fixed) station, one base known station (moving or fixed) and up to 9 known fixed stations. The following subsections will explain in detail the methodology of the modified GASP program developed for this research.

2.6.1 Initialization and Antenna Phase Centre Variation

At the start, some input information is necessary in order to run the program, and thus a set of initialization data is either directly input from the keyboard or read from a file. This information includes the name and location of the fixed and unknown receiver RINEX (receiver independent exchange format) files, epoch interval, etc. A sample of the initial file is given in Appendix A. If the antenna phase centre variation (PCV) correction is applied — according to the initial file — then these corrections, whether fixed or variable corrections are read from another file, depending upon the antenna model used for the unknown and fixed receivers. Fixed corrections are added to the antenna offset directly, while variable corrections depending on the elevation angle of the satellites are subtracted from the phase observations.

The fixed PCV corrections are given in topocentric format and thus should be transformed to their Cartesian counterparts, since the mathematical manipulation in the software deals with Cartesian coordinates during processing. Such transformation expressions are given as follows (Hofmann-Wellenhof et al. 2001):

$$\Delta Z = \Delta N \times \cos\phi + \Delta U \times \sin\phi \qquad 2.19$$

$$\Delta XY = \Delta U \times \cos\phi - \Delta N \times \sin\phi \qquad 2.20$$

$$\Delta Y = \Delta E \times \cos\lambda + \Delta XY \times \sin\lambda \qquad 2.21$$

$$\Delta X = \Delta XY \times \cos\lambda - \Delta E \times \sin\lambda \qquad 2.22$$

$\Delta E, \Delta N, \Delta U$ are the fixed phase centre variation corrections to the antenna offset in Easting, Northing and Up directions, respectively. $\Delta X, \Delta Y, \Delta Z$ are the fixed phase centre variation corrections to the antenna offset in the geocentric X, Y and Z directions, respectively. Elevation- and azimuth-dependent PCV corrections are

subtracted from the carrier phase observables measured from satellites to known and unknown receivers during processing. After applying phase centre variation corrections, all the initialization data are written to screen as a check, as well as in the header of the output file. Note that all the following procedures of the software are repeated for every processed epoch.

2.6.2 Reading RINEX Observation and Navigation Data

One of the major advantages of the modified and updated software is that all the older versions of the software, required the RINEX observation data format to be converted to the NXF (**N**ewcastle e**X**change **F**ormat) data format through a separate program called RINTONXF (**RIN**ex **TO NXF**). This of course was far from efficient as being time consuming, and needed to be modified. This was done and the RINEX observation files of the unknown and known receiver(s) are now read continuously, until synchronization with the start processing GPS time specified in the initial file. If any of the unknown or known receivers are static, then their fixed coordinates are given in that file. During the reading of the RINEX files, a filtering process is carried out to eliminate satellites in each epoch, either specified to be ignored in the initial file or those having zeroes in the existing code or phase observables. Consequently, only healthy satellites are processed. The number of common satellites between all receivers is checked, to ensure that this is greater than or at least equal to four, in order to be able to process the epoch. If not applicable, then GASP proceeds to the next epoch by increasing the GPS time by one interval, specified in the initial file (one second for this research).

The approximate coordinates of the unknown receiver are obtained, either from the RINEX header or directly through the initial file or from the previous epoch. As for the coordinates of the satellites, the navigation broadcast message is read, if using broadcast orbits, and thus satellite coordinates are interpolated from the broadcast Keplerian elements. The other option is to read a precise orbit file and thus the coordinates of satellites, the range rate, satellite clock error and transmission time are interpolated according to the epoch time from the precise ephemerides. As done before, bad satellites having incorrect satellite clock information are omitted. After

reading observation and navigation files, the distance and elevation angle of each satellite with respect to each receiver are calculated using the previous coordinates. Then the common satellites between unknown and known receiver(s) are sorted from higher to lower according to their elevation. During this process, satellites of elevation angle lower than the elevation mask angle, which is set in the initial file, are removed.

2.6.3 Application of Tropospheric Model

The tropospheric model used in the updated software is the modified Saastamoinen model using Niell's mapping functions. All mathematical expressions for this tropospheric model and mapping functions are given (Niell 1996; Saastamoinen 1973; Saastamoinen 1972):

$$p = p_o(1-0.0000226H)^{5.225}\,, \qquad 2.23$$

where p is the atmospheric pressure at the observing point, p_o is the standard atmospheric pressure at mean sea level (1013.25 mbar) and H is the height of the observing point above mean sea level in metres. Note that the geoid undulation value that needs to be added to the GPS ellipsoidal height in order to obtain the height above mean sea level is specified by the user in the initial file.

$$T = T_o - 0.0065H\,, \qquad 2.24$$

in which, T is the atmospheric temperature at the observing point and T_o is the standard atmospheric temperature in degrees Kelvin at mean sea level (^oC +273.15),

$$\delta(h_w,T) = \frac{h_w}{100}\exp(-37.2465+0.213166T-0.0002569085T^2)\,, \qquad 2.25$$

where δ is the water vapour pressure at the observing point, while h_w is the humidity at the observing point and is given by:

$$h_w = h_{wo}\exp(-0.0006396H)\,, \qquad 2.26$$

where h_{wo} is the standard humidity at mean sea level (50 %),

$$\mu_h(p,\phi,H) = \frac{0.0022768p_o}{1-0.00266\cos 2\phi - 0.00028\times(H/1000)}\,, \qquad 2.27$$

and,

$$\mu_w(h_w,T) = 0.0122+0.00943\times \delta(h_w,T), \qquad 2.28$$

μ_h is the zenith hydrostatic delay in metres, ϕ is the latitude of the observing point and μ_w is the zenith wet delay in metres. Finally, the total slant delay (μ_T), that is the atmospheric correction to be subtracted from the phase observables, is given by:

$$\mu_T = \mu_h \times m_h + \mu_w \times m_w, \qquad 2.29$$

such that m_h and m_w are the mapping functions for the hydrostatic and wet zenith delay, respectively, taken from Niell (1996). The hydrostatic mapping function is given by:

$$m_h(z)=\frac{1+\dfrac{a}{1+\dfrac{b}{1+c}}}{\cos z+\dfrac{a}{\cos z+\dfrac{b}{\cos z+c}}}+\frac{H}{1000}\times\left(\frac{1}{\cos z}-\frac{1+\dfrac{a_h}{1+\dfrac{b_h}{1+c_h}}}{\cos z+\dfrac{a_h}{\cos z+\dfrac{b_h}{\cos z+c_h}}}\right), \qquad 2.30$$

in which z is the zenith angle (90 – elevation angle) taken for every satellite to each receiver. The interpolated values of a,b,c are given through the following expression:

$$a = a'-a_p \times \cos\left(2\pi \times \frac{DOY - DOY_o}{365.25}\right), \qquad 2.31$$

DOY is the current day of the year and DOY_o is given as 28 for the northern hemisphere and 211 for the southern hemisphere. Similar expressions can be written for b and c. On the other hand, the wet mapping function is given as follows:

$$m_w(z)=\frac{1+\dfrac{a_w}{1+\dfrac{b_w}{1+c_w}}}{\cos z+\dfrac{a_w}{\cos z+\dfrac{b_w}{\cos z+c_w}}}, \qquad 2.32$$

where a_w, b_w, c_w are the coefficients for the wet mapping function. All coefficients $a', b', c', a_p, b_p, c_p, a_h, b_h, c_h, a_w, b_w, c_w$ can be found in tables in Niell (1996), as a function of the latitude of the observing point ϕ.

2.6.4 Determination of Initial Position and Search Volume Construction

The initial approximate coordinates of the unknown receiver can be optionally obtained by three methods: (i) given directly in the initial file, obtained from previous calculations or (ii) computed from a code double difference least squares estimation procedure (with options to choose the type of code data) (Al-Haifi 1996) or (iii) obtained from the previous processed epoch providing that the epoch is successful and the unknown point is static. Accordingly, the search size in terms of cycles is either given in the initial file or is calculated, depending on the mode through which the initial position was obtained. If the initial coordinates were given, then the search size is taken as the value given in the initial file. Alternatively, if the initial position is calculated from the code observations, then the search size is computed from the formal errors of the initial position coordinates though the following expression (Gunasingam 2003):

$$\beta = ceil\ (S \times \sqrt{\frac{\sigma_o^2 \times (\sigma_x^2 + \sigma_y^2 + \sigma_z^2)}{3}} \times \frac{f_1}{c}), \qquad 2.33$$

where β is the search size in cycles, while *ceil* is the function required to round the resultant real number to the nearest higher integer. S is a scaling factor (normally taken ≈ 1), σ_o^2 is the unit variance, $\sigma_x^2, \sigma_y^2, \sigma_z^2$ are the a posteriori variances of the initial coordinates in all three directions and f_1 is the L1 carrier frequency. On the other hand, if the initial coordinates are obtained from the previous successful epoch, then the search size is obtained from Equation 2.33, but from the formal errors of the final coordinates of the previous epoch. The latter methodology is the one mostly used in the current research, although the maximum search size is given in the initial file.

Then the highest satellite is chosen as the reference satellite and the position dilution of precision (PDOP) is calculated for the constellation containing the reference satellite and all combinations of three satellites among the available observed satellites for both receivers. This process will output the best constellation of four satellites with the best PDOP, which are used to estimate the initial ambiguities through their L1 phase observables only. These estimated initial ambiguities are then rounded to the nearest integer value, and a search volume is constructed using the obtained search size and L1 observable.

For example, a search size of 5 with three initial double difference phase ambiguities N_o, that is $N_o \pm 5$ for each double difference ambiguity, will produce 1331 ($11 \times 11 \times 11$) trial ambiguity sets. Trial positions are computed for each trial ambiguity set, implying that the search volume is constructed as a cube having the initial position in its centre. This volume has to be within ± 1.2 m of the correct final position, as previously investigated by Corbett (1993), in order to obtain correct ambiguity resolution using the software, which shows the importance of accurate determination of the initial position. Note that if the search size calculated from Equation 2.33 is greater than the default search size predefined in the initial file, then the search volume is constructed using the default search size.

2.6.5 Calculation of Ambiguity Function Value

The GASP program utilizes the ambiguity function technique (AFT) for resolving the phase integer ambiguities. The ambiguity function value (AFV) for each trial position in the search volume is calculated through the following expression (Counselman and Gourevitch 1981):

$$\mathrm{AFV}\,(x_i, y_i, z_i) = \frac{1}{2L(M-1)} \sum_{h=1}^{L} \sum_{j=1}^{M-1} \left[\cos(2\pi \nabla \Delta \Phi_{L1}) + \cos(2\pi K \nabla \Delta \Phi_{L2})\right]_i , \quad 2.34$$

where AFV is the ambiguity function value for each trial position (i). L is the number of reference fixed receivers, and M is the number of common observed satellites and $\nabla\Delta\Phi$ is the double difference phase residual at each trial position, given by the following expression:

$$\nabla\Delta\Phi = \nabla\Delta\Phi_{obs} - \nabla\Delta\Phi_{calc}, \qquad 2.35$$

K is a weighting factor applied to $L2$ phase residuals in order reduce the contribution of $L2$ residuals in the calculation of AFV (typical value $=(f_1/f_2)^2 \approx 1.7$, to account for lower power of L2, ionospheric errors and increase in tracking noise due to anti-spoofing) (e.g. Gunasingam 2003; Leick 2004). Each candidate position having an AFV greater than the ambiguity threshold specified in the initial file is passed to the least squares adjustment procedure and the F-test statistic to obtain the final correct position and accompanying ambiguity set. On the other hand, trial positions of AFV below the threshold are eliminated and not taken into further account.

Considering all trial positions, if the AFV for at least one of the trial positions does not reach a maximum ambiguity threshold, also specified in the initial file, then the search size is increased by one and a new search volume is constructed as before. This continues until either the AFV of one of the trial positions becomes greater than or equal to the maximum ambiguity threshold, or the maximum allowable search size is reached. In the latter case, the solution from this epoch is considered unreliable and the existence of the correct true position within the formed search volume is not verified. In addition, from Equation 2.34, it is clear that the accuracy of the AFT in single epoch positioning depends mainly upon the number of observed satellites and the number of total observations (e.g. if using more than one reference fixed receiver). In other words, a good solution is obtained, given a large number of observed satellites: say six satellites or more and the maximum possible number of observations.

This technique has two disadvantages. The first is its lack of any statistical information required to test the positions obtained, and therefore the F-test statistic is used here to test the candidate positions to infer the correct position. The second is that more than one candidate position can pass the statistical test. In this case, a single correct final position cannot be distinguished. This could be avoided with more satellites in view and more observational epochs. Notwithstanding, the technique has proven to be useful and efficient in reducing the computation time, as well as checking for the quality of the data. Previous trials, e.g. Corbett (1994) and Al-Haifi

(1996), showed this technique is successful in almost all circumstances for single epoch ambiguity resolution using unbiased dual frequency phase data from at least five satellites over short baselines (less than 10 km).

2.6.6 Least Squares Adjustment and Statistical Testing

A least squares estimation procedure is performed using each candidate position as the a priori position, in order to obtain the correction residuals for this position. This is done while weighting the double difference carrier phase observables according to the elevation angle of the satellites. The L1 and L2 frequencies are used independently, forming twice the number of observation equations i.e. more redundancy in least squares adjustment. The weighted residuals are calculated for each candidate position least squares adjustment — assuming independent observations — using the following expression (Cross 1990):

$$\hat{\sigma}_o^2 = \frac{\sum (V^T W V)}{n-m}, \qquad 2.36$$

where $\hat{\sigma}_o^2$ is the a posteriori variance factor and V is the vector of correction residuals of the observables. W is the weight matrix, n is the number of double difference equations in each processed epoch from L1 and L2 data and m is the number of unknown parameters (in this case here $m=3$, corresponding to the three coordinate components of the unknown receiver). Consequently, the candidate position having the minimum variance is the most likely position.

However, in order to verify this position, the F-test is performed in order to test the solution with minimum residuals against other candidate positions, through the following equation (Cross 1990):

$$F = \frac{\hat{\sigma}_{o(\min)}^2}{\hat{\sigma}_{o(i)}^2} < F_{DOF,1-\alpha}, \qquad 2.37$$

given that $\hat{\sigma}_{o(\min)}^2$ is the minimum value of the a posteriori variance factor among all candidate positions and $\hat{\sigma}_{o(i)}^2$ is the a posteriori variance factor for every other

candidate position i. $F_{DOF,1-\alpha}$ is the critical percentile extracted from the F-distribution table that corresponds to the number of degrees of freedom ($DOF = n-3$), while α is the significance level (taken here as 5%). In Equation 2.37, if the null hypothesis is rejected, that is the candidate position passes the F-test, i.e. satisfying the equation, then the candidate position of minimum residuals has come from a different population and thus corresponds to the correct ambiguity combination (Al-Haifi 1996). If more than one position passes the F-test, then the position with minimum variance is considered to be the final correct position although it is insignificantly differentiated from the other passing positions.

2.6.7 Results Output and Miscellaneous Information

The results of the processed epoch are written to the output file, in the form of the coordinates of the unknown receiver in Cartesian and/or ellipsoidal and/or topocentric format along with their formal errors, depending on the output format stated in the initial file. Also the output of each epoch includes the number of observed common satellites, PDOP value, number of positions passing the ambiguity function value test and F-test, error ellipsoid for the final position and the time taken to process this epoch.

Another simpler format of the output results is written to two different output files in the form of either X,Y,Z or N,E,U coordinates. In addition, two other output files are provided. The first includes the phase residuals accompanied by the PRN numbers of each double difference formed in each epoch, along with some miscellaneous information. The second file includes an array of indicators of all the satellite pairings existing through the whole processing campaign. All these files are used later as input files for sidereal filter investigations (see Chapters 3 and 4).

At the end of processing the epoch, the synchronized epoch time between known and unknown receivers is increased by the interval value provided through the initialization data, and the same methodology is repeated. Processing terminates either due to reaching the last common epoch between all receivers, or reaching the end processing time given in the initial file. Note that other modifications of the GASP

software include the ability to apply filtered L1 and L2 carrier phase residuals to update and correct the carrier phase residuals during GASP processing (explained in Section 4.2). In addition, GPS data can be processed across the GPS boundary week, which was not the case in the older version.

In summary, this chapter discussed the GPS constellation and its different kinds of observables. Errors affecting GPS positioning were also explained in addition to the differencing techniques, which can be adopted for the reduction of these errors. Different OTF ambiguity resolution techniques were briefly summarized. Then, the main GPS processing software (GASP) was explained in details. Figure 2.6 shows a flowchart of all steps and methodology adopted in the GASP software. The next chapter will discuss the two other programs required for geometry repeat period determination and the application of sidereal filtering, followed by the extensive investigations of the geometry repeat lag.

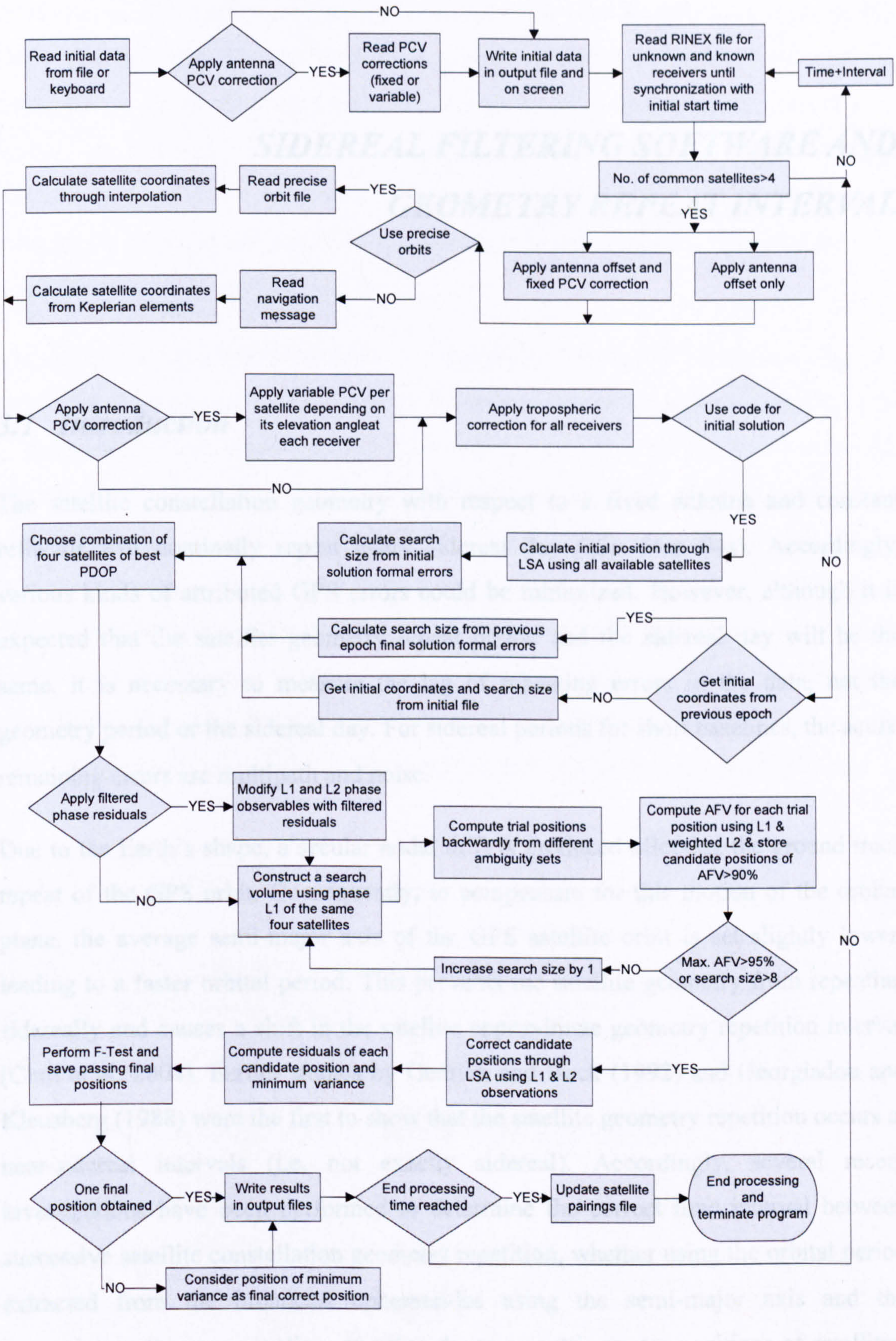

Figure 2.6 GASP software flowchart.

SIDEREAL FILTERING SOFTWARE AND GEOMETRY REPEAT INTERVAL

3.1 Introduction

The satellite constellation geometry with respect to a fixed antenna and constant reflector will nominally repeat every sidereal day (23h 56m 04s). Accordingly, various kinds of attributed GPS errors could be minimized. However, although it is expected that the satellite geometry repeat period and the sidereal day will be the same, it is necessary to measure the lag of repeating errors in the data, not the geometry period or the sidereal day. For sidereal periods for short baselines, the actual remaining errors are multipath and noise.

Due to the Earth's shape, a secular nodal drift is produced affecting the ground track repeat of the GPS orbit. Consequently, to compensate for this motion of the orbital plane, the average semi-major axis of the GPS satellite orbit is set slightly lower, leading to a faster orbital period. This prevents the satellite geometry from repeating sidereally and causes a shift in the satellite approximate geometry repetition interval (Choi et al. 2004). Earlier studies by Genrich and Bock (1992) and Georgiadou and Kleusberg (1988) were the first to show that the satellite geometry repetition occurs at near-sidereal intervals (i.e. not exactly sidereal). Accordingly, several recent investigations have been performed to determine the correct time interval between successive satellite constellation geometry repetition, whether using the orbital period extracted from the broadcast ephemerides using the semi-major axis and the correction to the mean motion, or using the topocentric vector positions of satellites, or interpolating the precise orbits to the time of equator crossing (Agnew and Larson 2007; Axelrad et al. 2005).

Accordingly, it is vital to revisit and investigate the satellite geometry repeatability, while approaching it from a different perspective compared to previous investigations, through the use of the autocorrelation technique for determining the actual error repeat lag. Sidereal filtering is then applied using two different methodologies. Essentially, filtering the data sidereally is the method of subtracting a filter residual at each epoch, which is composed of one or more residuals at epochs separated from the application epoch by multiples of the lag.

The main aim of this chapter is to test the repeat interval of multipath-dominated errors, i.e. those at near sidereal periods for short baselines, hereafter referred to as the "sidereal lag". There is also a check for the short- and long-term variability of the lag. The chapter starts with a detailed explanation of the two main programs required for sidereal filter studies that were developed by the author, starting with sidereal lag determination and followed by sidereal filter application. The process of collecting the primary and secondary data sets (April and December 2005) is described, with a brief explanation of the test stations and instruments used, the data handling and processing. The methodology adopted for the error repeat lag investigation is given next, followed by the initial analysis and results concerning the lag value and its variability.

3.2 Sidereal Filtering Software

Sidereal filter investigations were performed with the aid of two programs, both developed by the author. The next two main sections will fully describe the main ideas and methodologies of these two programs.

3.2.1 GPS Autocorrelation Sidereal Filtering (GASF)

As mentioned earlier, multipath error is one of the inevitable errors in GPS positioning that cannot be mitigated through any differencing technique. On the other hand, since this error is mainly dependent on the positions of the satellites with respect to the antenna and nearby reflectors, it should repeat whenever the same geometry of satellites occurs with respect to a static antenna and fixed reflectors. Assuming the removal of other errors through either differencing or observing short

baselines (less than 10 km), one can use the approximate geometry repetition of satellites roughly every one sidereal day to minimize the multipath error.

Unfortunately, the value of the multipath repeat interval, or the so-called sidereal lag, is not exactly predetermined because it repeats on the actual satellite orbits, although it is known to be in the region of 23 hours and 56 minutes (the sidereal day). Accordingly, the GASF program was established as a preliminary step to determine the optimum value of the "sidereal" lag before applying the sidereal filtering technique on the results from the GASP program. For this, the autocorrelation methodology is used, which is defined mathematically as the correlation of a variable with itself over successive time intervals. Autocorrelation is often calculated for time series data to determine how the correlation between data values varies with the distance or time lag between them. This will detect non-randomness in the data, as well as identifying an appropriate time series model in non-random data. In other words, for a variable Y with sample size N, the autocorrelation R at a lag value K is calculated as follows (NIST/SEMATECH 2005):

$$R(K) = \frac{\sum_{i=1}^{N-K} (Y_i - \bar{Y})(Y_{i+K} - \bar{Y})}{\sum_{i=1}^{N} (Y_i - \bar{Y})^2}, \qquad 3.1$$

This autocorrelation value is computed for all valid epochs, for a range of chosen sidereal lags and variations of window size (number of considered epochs). The maximum autocorrelation value will correspond to the optimum value of the lag. The following three subsections will examine the methodology of the GASF program.

3.2.1.1 Initialization and Reading of Epochs

The program starts by reading the initialization data from a file. This file includes the name of the input data file (the results file of the GASP program), name of the output file, time of start epoch, number of epochs considered (window size), minimum (start) value of trial sidereal lag (τ) in seconds, number of lags to be tested, approximate station coordinates, as well as the formal error and coordinate tolerance for accepting any epoch as valid. A sample of such an initial file is shown in Appendix B. After

initialization, all epochs in the input file are read; each epoch line will contain the week number, time of epoch (GPS seconds), coordinates (x, y, z), formal errors (σ_x, σ_y, σ_z), number of candidate positions passed by the ambiguity function value and F-test, number of observed satellites, PDOP, maximum ambiguity function value, minimum $V^T WV$ and number of degrees of freedom. During the reading process, all bad (unhealthy) epochs, that is with formal errors or a coordinate difference from the approximate coordinates greater than the tolerance limits (specified in the initial file), are excluded.

3.2.1.2 Averaging and Weighting

The weighted average coordinates X_o, Y_o, Z_o are calculated for all good epochs in the input file using the following expression:

$$X_o = \frac{P_{x_1} \times x_1 + P_{x_2} \times x_2 + \ldots\ldots + P_{x_i} \times x_i + \ldots\ldots + P_{x_n} \times x_n}{P_{x_1} + P_{x_2} + \ldots\ldots + P_{x_i} + \ldots\ldots + P_{x_n}}, \qquad 3.2$$

with similar expressions for the Y and Z coordinates, where n is the total number of good epochs in the input file, X_o is the weighted average coordinate in the X direction, while x_i and P_{x_i} are the coordinate and weight of the i^{th} good epoch in the input file respectively. Then, the input file is rewound in order to read the epochs one by one. According to the lag and start epoch time tag specified in the initial file, the first epoch is read from the input file. Reading of epochs continues, until reaching the epoch that is separated from the start epoch by the sidereal lag (τ) in question. When the two epochs are matched, the weight in each coordinate component of each of the two epochs is calculated through the following formula:

$$P_x = 1/\sigma_x^2, \qquad 3.3$$

and similarly for the y and z weights. Then, the combined formal error is computed according to the following expression:

$$\sigma_{xc} = \sigma_{x_i} \times \sigma_{x_{i+\tau}}, \qquad 3.4$$

where σ_{xc} is the combined formal error, σ_{x_t} is the formal error of the first epoch, and $\sigma_{x_{t+\tau}}$ is the formal error of the second epoch τ seconds later. Again, similar expressions could be written for y and z.

3.2.1.3 Autocorrelation and Sidereal Lag Determination

The final step of the program is to calculate the autocorrelation among matching epochs. At first, the autocovariance function C between those two matching epochs, defined as the measure of the degree of similarity between a time series and itself at different shifts or lags, is computed in each direction through the following expression:

$$C(x,t,\tau)=(x_t-X_o)\times(x_{t+\tau}-X_o), \qquad 3.5$$

where x_t and $x_{t+\tau}$ are the x-coordinates of the two matching first and second epochs, respectively. Also, the variance function V for each of those two epochs, defined as the autocovariance function at zero lag, is calculated as follows:

$$V(x,t)=(x_t-X_o)^2 \qquad 3.6$$

$$V(x,t,\tau)=(x_{t+\tau}-X_o)^2 \qquad 3.7$$

Again, similar expressions can be written for y and z. Then, the 3D weighted value of the autocovariance function is computed for those two epochs at time (t) and $(t+\tau)$, using the following equation:

$$C_l=\frac{P_{xc}\times C(x,t,\tau)+P_{yc}\times C(y,t,\tau)+P_{zc}\times C(z,t,\tau)}{P_{xc}+P_{yc}+P_{zc}}, \qquad 3.8$$

where P_{xc},P_{yc},P_{zc} are the weights of the combined formal errors in the x,y,z directions, respectively, computed using Equation 3.3. Similarly, the weighted value of the variance function for both epochs is calculated by:

$$V(t)=\frac{P_x^t\times V(x,t)+P_y^t\times V(y,t)+P_z^t\times V(z,t)}{P_x^t+P_y^t+P_z^t} \qquad 3.9$$

$$V(t,\tau)=\frac{P_x^{t+\tau}\times V(x,t,\tau)+P_y^{t+\tau}\times V(x,t,\tau)+P_z^{t+\tau}\times V(x,t,\tau)}{P_x^{t+\tau}+P_y^{t+\tau}+P_z^{t+\tau}}, \qquad 3.10$$

and finally, similarly for all three directions, the weighted variance function is given as follows:

$$V_i=V(t)+V(t,\tau) \qquad 3.11$$

Recalling Equations 3.8 and 3.11, the values calculated here for the autocovariance or variance function are for those two epochs only, and consequently the whole procedure should be repeated a number of times depending upon the desired window size (m), i.e. number of considered epochs stated in the initial file. At the end, the summation of autocovariance function $\sum_{i=1}^{m} C_i$ and variance function $\sum_{i=1}^{m} V_i$ for the current specified sidereal lag can be calculated. Since the value of the autocovariance or variance functions depend on the units of x, it is more useful to use the autocorrelation value over the whole window, which is computed from the following equation:

$$R(t,\tau,m)=\sum_{i=1}^{m} C_i \Big/ \sum_{i=1}^{m} V_i \quad , \qquad 3.12$$

where $R(t,\tau,m)$ is the autocorrelation, noting that it has no units and is limited $(-1\le R(t,\tau,m)\le 1)$. After calculating this value for all considered epochs, it is written on the screen and in the output file along with the sidereal lag period and the number of actual processed epochs. The program is run all over again, for all lag values to be considered. A summary is then written on-screen and in the output file, giving the time of the start epoch, the optimum sidereal lag $(\bar{\tau})$ accompanied with its maximum autocorrelation value and the number of processed epochs. Figure 3.1 shows a flowchart of all procedures of the GASF software.

It should be noted here that another version of the GASF program was established in order to perform sidereal lag determination, but dealing with the double difference carrier phase residuals instead of the output station coordinates. The methodology of

this version is the same as mentioned earlier, but instead of matching the coordinates separated by a specified sidereal lag, the program matches all double difference L1 and L2 phase residuals of the two epochs' common satellites. Then the program calculates a weighted average autocovariance and variance function, and consequently the autocorrelation value. Of course, the main output of this program's version will be the same as before, being the optimum sidereal lag having maximum autocorrelation.

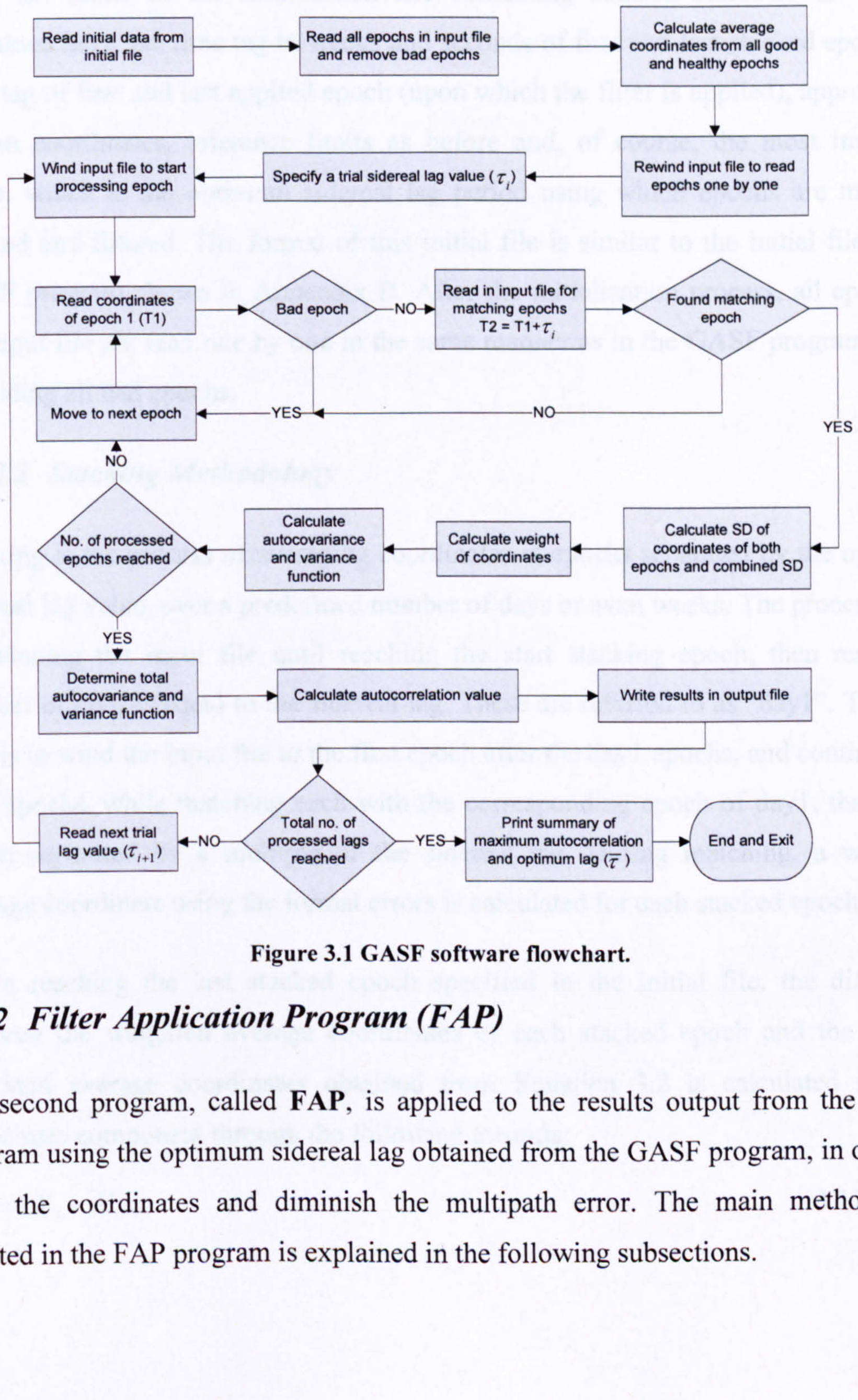

Figure 3.1 GASF software flowchart.

3.2.2 Filter Application Program (FAP)

The second program, called **FAP**, is applied to the results output from the GASP program using the optimum sidereal lag obtained from the GASF program, in order to filter the coordinates and diminish the multipath error. The main methodology adopted in the FAP program is explained in the following subsections.

3.2.2.1 Initialization and Weighting

Initially, the program reads the initialization data from a file, which contains the name of the input data file (results of GASP program), which could be either in the X,Y,Z or E,N,U format, the name of the output file containing all epochs whether processed or not, the name of the result file containing the processed healthy epochs only, the name of the information file containing stacked residuals as will be explained later, the time tag in weeks and seconds of first and last stacked epoch, the time tag of first and last applied epoch (upon which the filter is applied), approximate station coordinates, tolerance limits as before and, of course, the most important value, which is the optimum sidereal lag period using which epochs are matched, stacked and filtered. The format of this initial file is similar to the initial file of the GASF program shown in Appendix B. After the initialization process, all epochs in the input file are read one by one in the same manner as in the GASF program, again excluding all bad epochs.

3.2.2.2 Stacking Methodology

Stacking is the process of averaging coordinates at epochs separated by the optimum sidereal lag value, over a predefined number of days or even weeks. The process starts by winding the input file until reaching the start stacking epoch, then reading a number of epochs equal to the sidereal lag. These are referred to as "day1". The next step is to wind the input file to the first epoch after the day1 epochs, and continuously read epochs, while matching each with the corresponding epoch of day1, that is the epoch separated by a multiple of the sidereal lag. During matching, a weighted average coordinate using the formal errors is calculated for each stacked epoch.

When reaching the last stacked epoch specified in the initial file, the difference between the weighted average coordinates of each stacked epoch and the overall weighted average coordinates obtained from Equation 3.2 is calculated in each coordinate component through the following formula:

$$\Delta X_i = X_i - X_o, \qquad 3.13$$

where ΔX_i is the so-called correction residual at any particular stacked epoch and X_i is the weighted average coordinate of the stated epoch. Again, similar expressions can be given for the Y and Z coordinates. These correction residuals, as well as the number of stacked points for each epoch, and the time of each stacked epoch in weeks and seconds, are written to the information file, to be used by another program called **APPLY**, which will be explained later.

3.2.2.3 Application of Filter

After averaging coordinates over all stacked epochs, the final stage of the program involves the application of the filter in order to obtain accurate and reliable coordinates almost free from multipath error. The input file is wound until reaching the first applied epoch specified in the initial file, after which all following epochs are read until reaching the last applied epoch. Each read epoch is matched with its stacked counterpart of correction residuals some days or weeks ago. The corrected (filtered) coordinates of any applied epoch are computed through the following expression:

$$X^{corr}_{i+n\tau^o} = X_{i+n\tau^o} - \Delta X_i, \qquad 3.14$$

with similar expressions for the Y and Z coordinates, and where $X_{i+n\tau^o}$ is the original x-coordinate of the epoch matching with the i^{th} stacked epoch of day1 residuals n sidereal days ago, $X^{corr}_{i+n\tau^o}$ is the corrected filtered x-coordinate of such epoch, and τ^o is the optimum value of the sidereal lag used. The final step of the program includes printing out the obtained filtered coordinates to the output and result files. If the applied epoch is bad (according to the gross coordinate check or formal error limit) or if no averaged epochs were considered, then the relevant information is printed out in the output file only, indicating the situation of this epoch. On the other hand, if the epoch is good and matches one of the healthy stacked epochs, then the results, including the three dimensional filtered coordinates in terms of X,Y,Z or E,N,U coordinates, as well as the epoch time and number of stacked points at the epoch, are printed in both the output and result file.

As a final remark, another program called **APPLY** was established for efficiency purposes. This program applies any previously formed correction residuals on another part of the data or even on another data set without having to re-run the FAP program. This program has proven to be useful for investigating sidereal filter performance and lifetime, which will be discussed at a later stage in Chapter 4. Figure 3.2 shows a flowchart of all procedures of the FAP program. As was the case with the GASF program, another version of the FAP program was established that uses double difference carrier phase residuals instead of coordinate residuals. The difference is that the output of this version, being the stacked carrier phase residuals, must be applied through the GASP program while reprocessing the raw data.

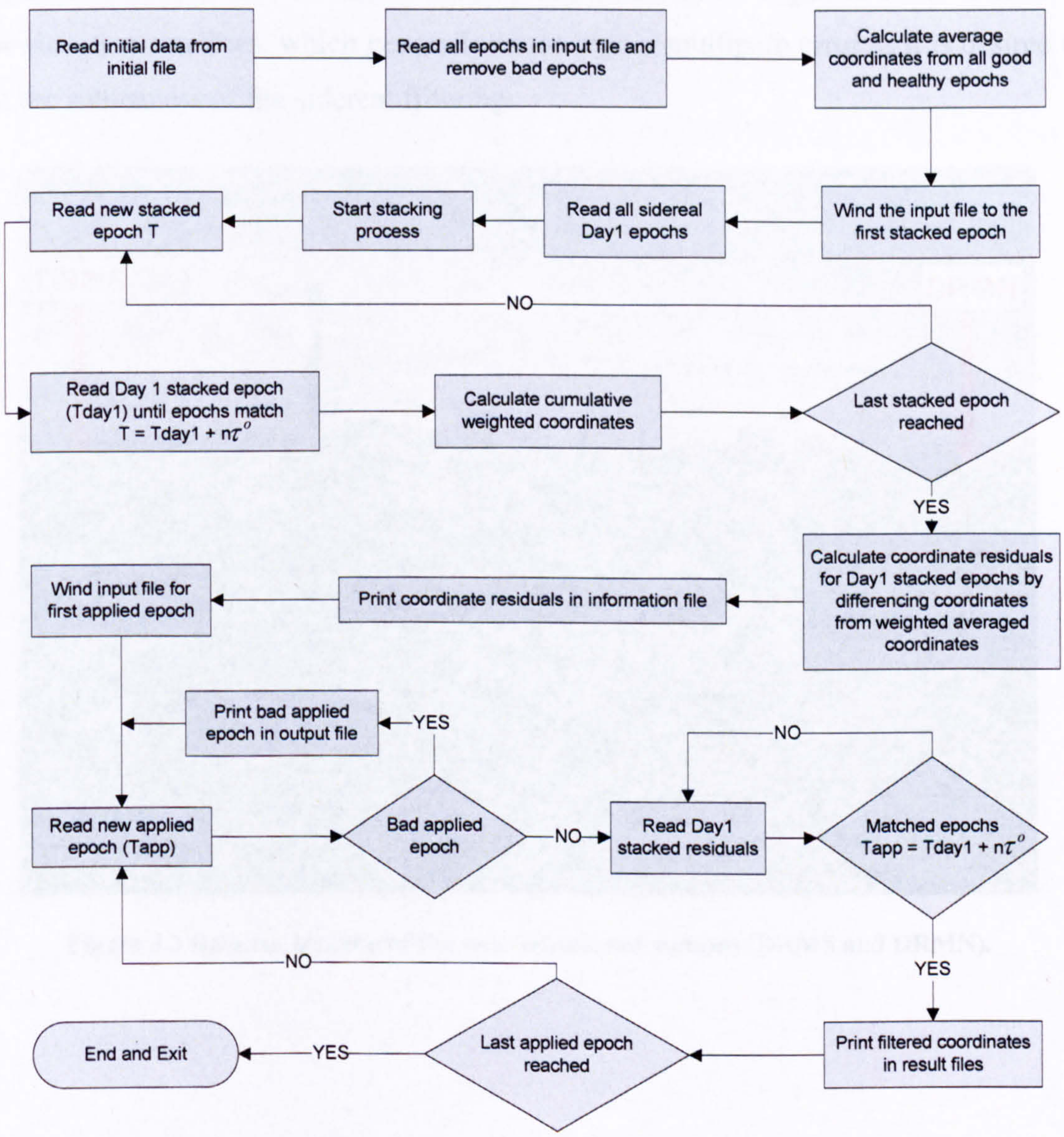

Figure 3.2 FAP software flowchart.

3.3 Sidereal Filter Strategies Data Collection

Four stations on the Newcastle University campus were chosen, two on the roof of the Drummond building, a relatively low multipath environment, named **DRMN** and **DRMS,** and two on the roof of the Bedson building, a higher multipath environment, called **SN02** and **NEWC**. The latter is part of the "Active GPS Network" of the Ordnance Survey of Great Britain (OS). Figures 3.3 and 3.4 show the locations of the stations and the environment of the Drummond and Bedson buildings respectively, while Figure 3.5 show the relative location of the Drummond and Bedson buildings on the university campus map. For sidereal lag investigation and filter application, two 1 Hz data sets were collected with a 5° elevation mask angle, in order to include low elevation satellites, which generally cause higher multipath error as it is desired to test the robustness of the sidereal filtering.

Figure 3.3 Relative location of the two Drummond stations (DRMS and DRMN).

Figure 3.4 Relative location of the two Bedson stations (SN02 and NEWC).

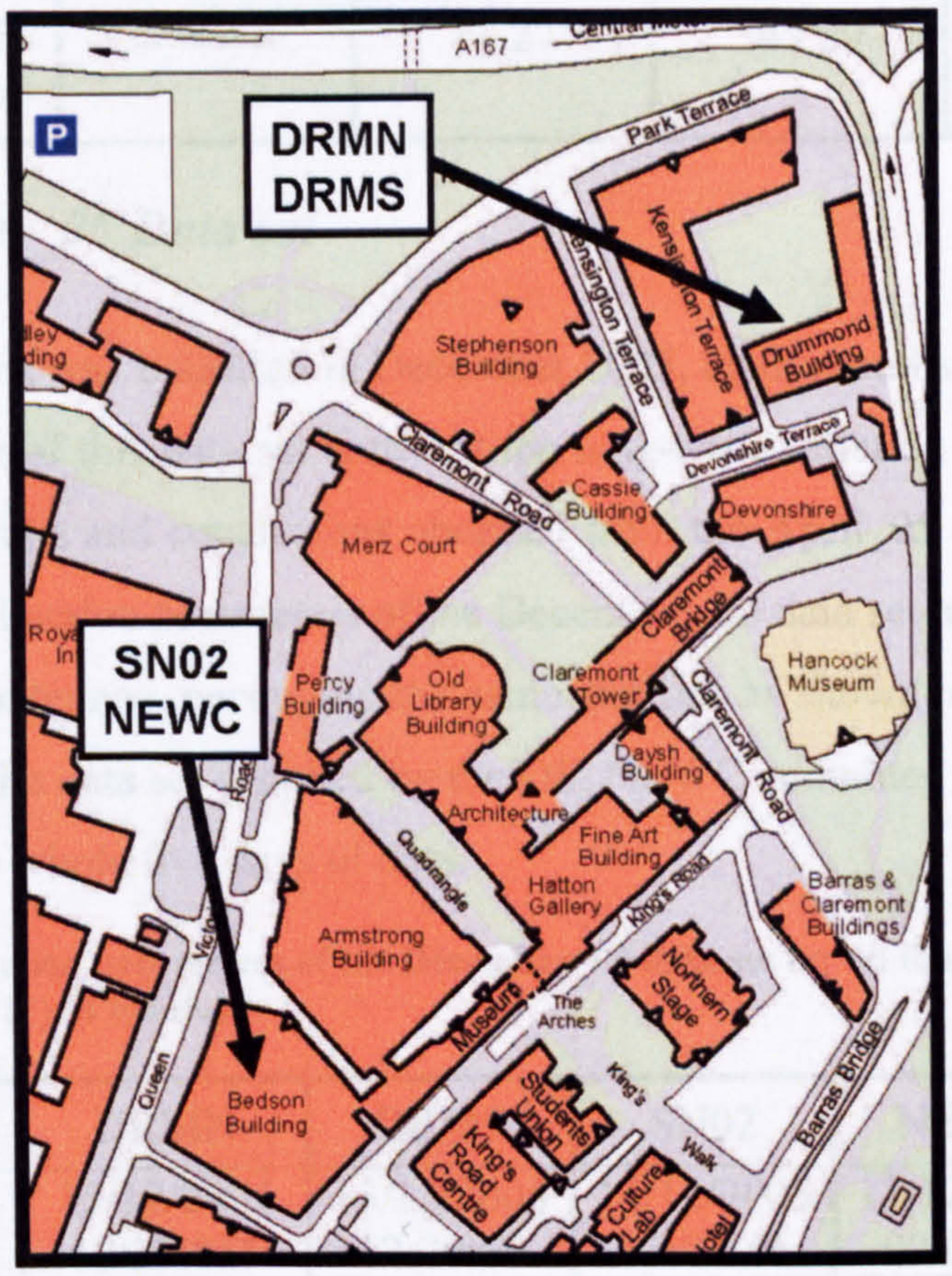

Figure 3.5 Relative location of the Drummond and Bedson buildings. (acknowledgement of the Newcastle University campus map)

3.3.1 April_05 Data set

The first data set was collected in April 2005 at all four stations for four continuous days. Table 3.1 summarizes the data collection parameters of this data set.

Table 3.1 Data collection parameters of the April_05 data set for all four stations. (GPS Week = 1317) (star (*) indicates actual processing start and end times)

Station	DRMN	DRMS	SN02	NEWC
Start Time (GPS Time)	04 Apr 2005 14:07:50*	04 Apr 2005 13:46:57	04 Apr 2005 11:16:35	04 Apr 2005 11:00:00
End Time (GPS Time)	08 Apr 2005 14:47:50	08 Apr 2005 14:43:38	08 Apr 2005 14:25:05*	08 Apr 2005 17:59:59
Receiver Type	LEICA GX1230	LEICA GX1230	LEICA GX1230	LEICA RS500
Antenna Type	LEIAX1202	LEIAX1202	LEIAX1202	ASH700936E-SNOW
Pillar Type	Concrete	Concrete	Steel	Steel
Baseline length from DRMN (m)	---------	11.27	349.29	339.59

3.3.2 December_05 Data set

The second data set was collected in December 2005, eight months after the first data set. The main aim of this data set is to test the long-term variation in the sidereal lag and verify the results and conclusions obtained from the April_05 data set. Table 3.2 shows the data collection parameters of the December_05 data set using the same type of receivers and antennae, occupying the same stations as shown previously in Table 3.1. Note that in the data set supplied by the OS, NEWC contained some missing data in each day of the whole five days of data.

Table 3.2 Data collection parameters of the December_05 data set for all four stations. (GPS Week = 1353) (star (*) as before)

Station	DRMN	DRMS	SN02	NEWC
Start Time (GPS Time)	13/12/2005 12:35:05*	13/12/2005 12:20:50	13/12/2005 11:05:44	13/12/2005 00:00:00
End Time (GPS Time)	17/12/2005 14:05:31	17/12/2005 14:16:20	17/12/2005 13:43:12*	17/12/2005 23:59:59

3.3.3 Environment Characterization

Multipath analysis was performed in order to characterize the multipath environment at each of the four stations, using the UNAVCO software TEQC (Translate, Edit and Quality Check). MP1 and MP2 code multipath proxy values (Estey and Meertens 1999) were extracted on the L1 and L2 frequencies, respectively, from the observation and navigation files of all site stations over the whole data period. Then, the Root Mean Square (RMS) errors of MP1 or MP2 within 3° bins of the sky were computed. Note that although a different receiver is used at NEWC having a different receiver smoothing factor, the MP1 and MP2 code multipath proxy values are still roughly comparable based on the performance of high elevation satellites. Figures 3.6 and 3.7 represent these RMS values for MP1 and MP2 for all four stations using 5° and 15° minimum elevation angles, respectively, laid upon the mean and RMS value over the entire sky. In addition, Table 3.3 shows the overall mean and RMS value over the entire sky for both 5° and 15° elevation mask angles. From Figures 3.6 and 3.7 and Table 3.3, it is evident that both Drummond building stations, DRMN and DRMS, sustain high multipath for very low elevated satellites only. Whereas NEWC suffers from high multipath all over much of the sky, and SN02 has high multipath for a certain part of the sky. It is suggested that this multipath is due to the high wall close to this station.

3.4 Data Handling

Data Collected from receivers at the three stations DRMN, DRMS and SN02 were downloaded to the LEICA Geo Office 2.0 software (Leica Geosystems 2005), after which files were transformed into RINEX observation format. For ease of handling, the RINEX files were concatenated into either 6- or 24-hour files and synchronized with the same start and end time for each station. A very small part of the April_05 data was missing. This is from 08:31:06 to 08:32:00 (GPS Time) on 5th of April, 2005, and from 09:14:08 to 09:14:18 and 15:11:21 to 15:11:26 (GPS Time) on 6th of April, 2005. As can be seen, it is a very small period of time and thus negligible and will not affect the assessment of the sidereal lag value or the sidereal filtering technique for multipath reduction.

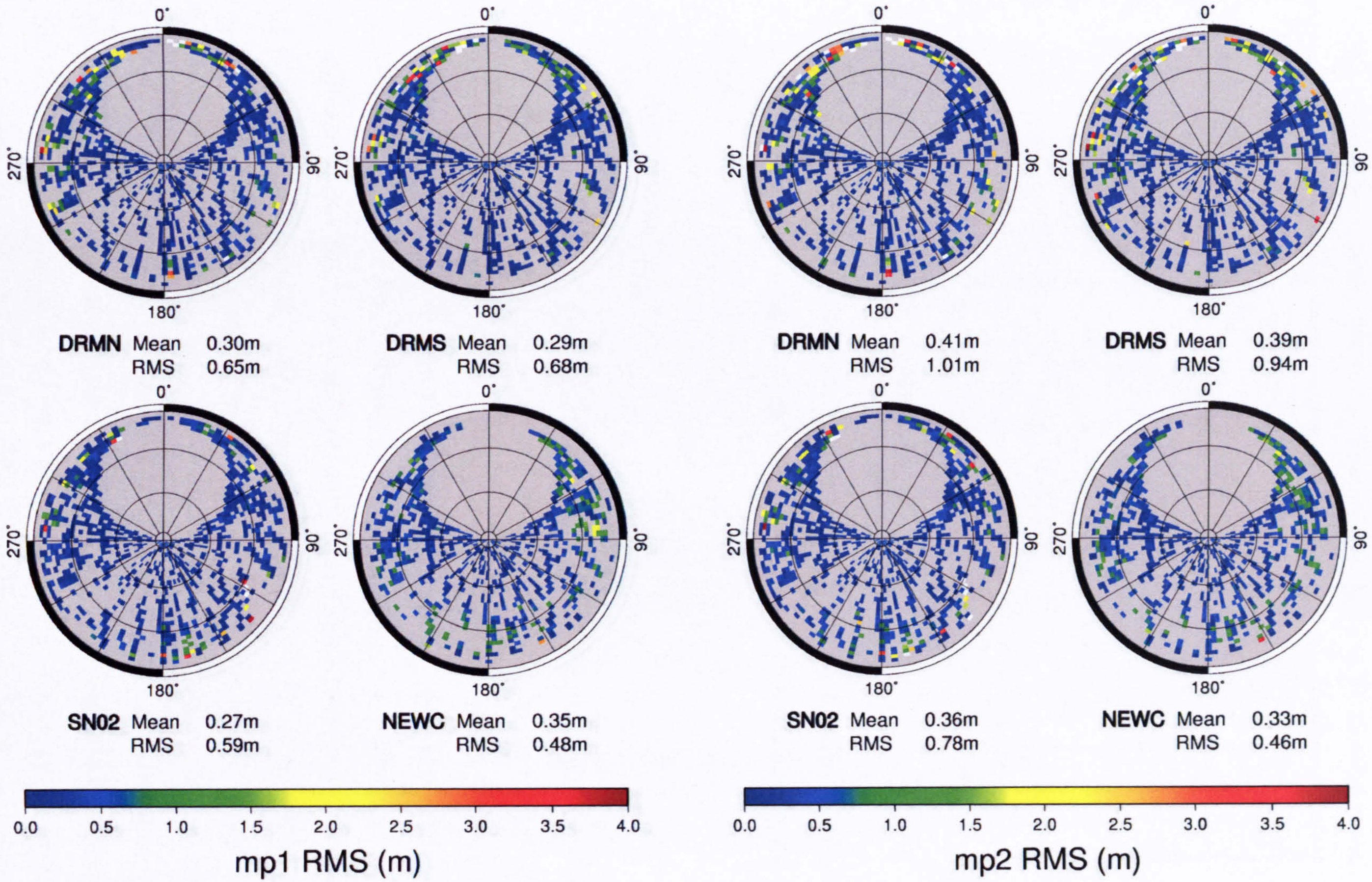

Figure 3.6 Multipath (MP1 and MP2) RMS for all four stations with a 5° elevation mask.

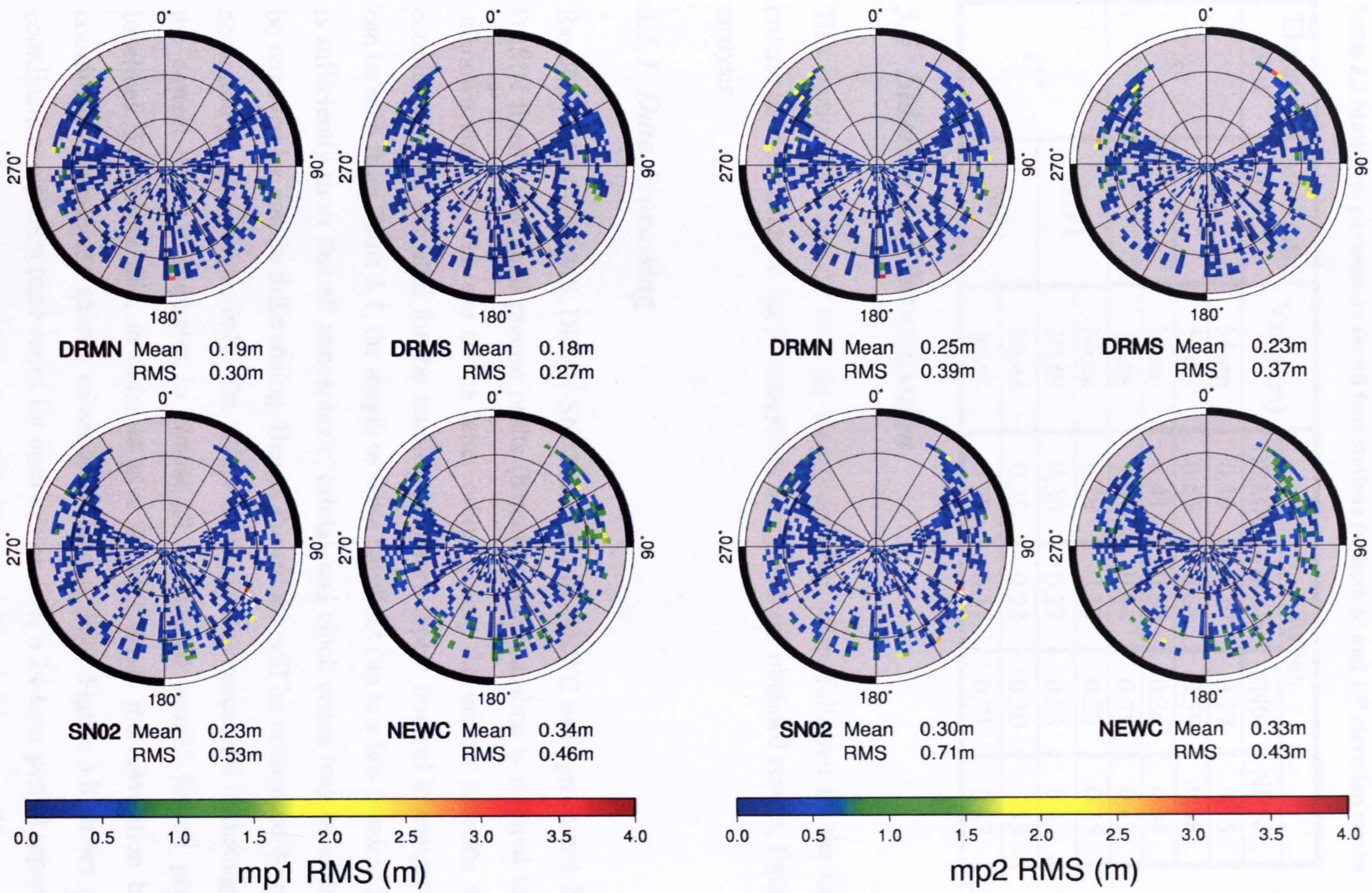

Figure 3.7 Multipath (MP1 and MP2) RMS for all four stations with a 15° elevation mask.

Table 3.3 Multipath parameters for all four stations for both 5° and 15° elevation masks.

Elevation mask	Multipath proxy	Value (m)	Station			
			DRMN	DRMS	SN02	NEWC
5°	MP1	Mean	0.30	0.29	0.27	0.35
		RMS	0.65	0.68	0.59	0.48
	MP2	Mean	0.41	0.39	0.36	0.34
		RMS	1.01	0.94	0.78	0.47
15°	MP1	Mean	0.19	0.18	0.23	0.35
		RMS	0.30	0.27	0.53	0.46
	MP2	Mean	0.25	0.23	0.30	0.33
		RMS	0.39	0.37	0.71	0.43

3.5 Sidereal Lag Investigation

This section will explain first the data processing stage, followed by the different criteria used for sidereal lag investigation, along with the obtained results, figures and analysis.

3.5.1 Data Processing

Baselines DRMN-DRMS, DRMN-SN02 and DRMN-NEWC were processed, holding DRMN fixed using final precise orbits (hereafter each baseline is referred to by its unknown station). The use of the latter orbits having the utmost accurate satellite coordinates was essential for the satellite geometry repeat interval investigation. As can be seen from Table 3.1, the length of these baselines (up to a few hundred metres) is sufficiently short that all atmospheric, orbital, and clock errors may be assumed to be removed by double differencing. Hence, the results will be influenced by receiver noise and multipath error only. The GASP software was successful in distinguishing the correct epoch coordinates in almost all considered epochs for all processed baselines. Following this, in order to give an idea about the correlation between coordinate components among subsequent sidereal days, Figure 3.8 shows two Up coordinate component time series for each station over a 24-hour period separated by one sidereal day (86164 seconds). This figure indicates the resemblance of the coordinate time series over sidereal periods as well as visualizes the higher noise and multipath of NEWC compared to SN02 and DRMS.

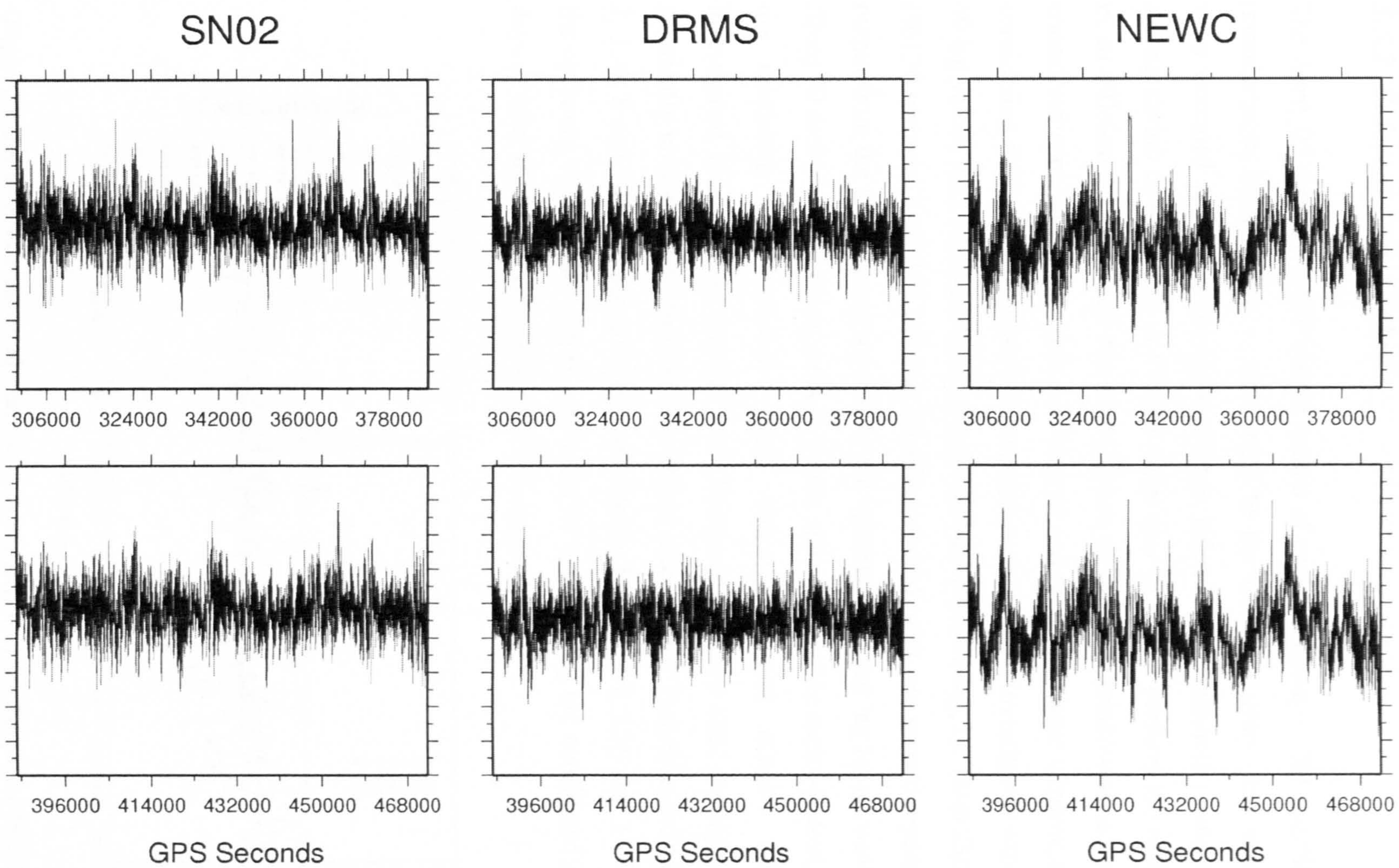

Figure 3.8 Up coordinate times series over a 24-hour period. Left for SN02, middle for DRMS and right for NEWC. Lower raw time series are one sidereal day (86164 seconds) later than the upper raw. (Y-axis major tick marks are at 1 cm intervals)

3.5.2 Sidereal Lag Analysis

The April_05 data set GASP output results of each unknown — 3D coordinates and miscellaneous information — were input to the GASF program, and several trials were executed searching for the optimum sidereal lag (maximum autocorrelation among station coordinates). A C-shell script was written to perform the required task in an efficient way, through the investigation of different window sizes (number of considered epochs) starting from a 30 second and up to a 10 hour window, as well as considering different start times at hourly intervals. In each investigated window size, 60 lag values were considered, ranging around the nominal lag, i.e. from 23h 55m 30s (86130 seconds) until 23h 56m 30s (86190 seconds), with one second separation. The output from the GASF program will be the optimum sidereal lag for all window sizes (from 30 seconds to 10 hours) at each hourly start time within each window, based on the maximum autocorrelation value. Although several window sizes were investigated, results for 30 seconds up to 30 minutes window sizes display very large, apparently random fluctuations in the optimal sidereal lag. Therefore, only the 0.5, 1, 2, 3, 4, 8 and 10 hour window sizes are shown. Figures 3.9, 3.10 and 3.11 illustrate the optimum value of the lag as a function of time among the considered first three days of data, for SN02, DRMS and NEWC, respectively.

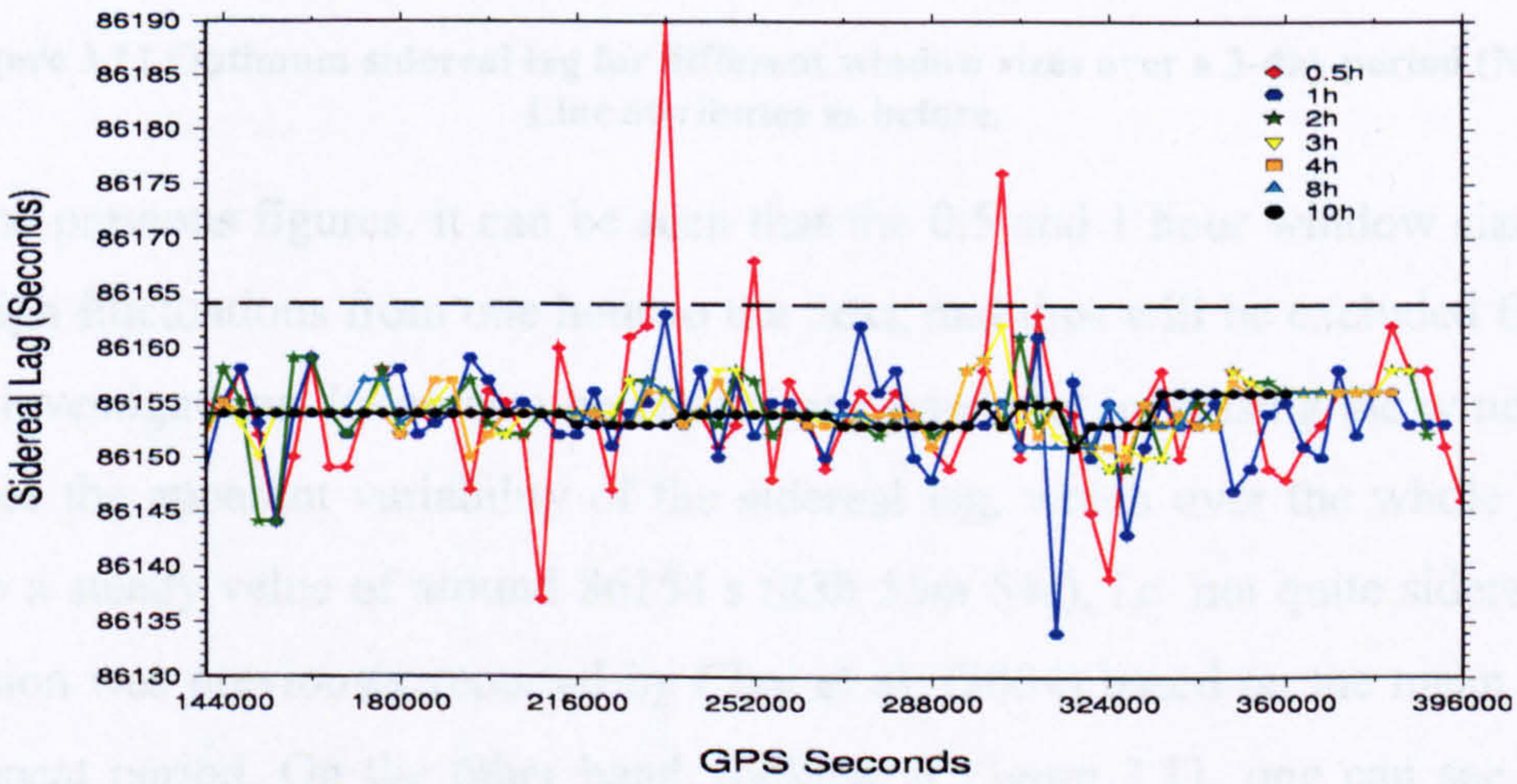

Figure 3.9 Optimum sidereal lag for different window sizes over a 3-day period (SN02). Dashed line indicate nominal lag of 86164 seconds.

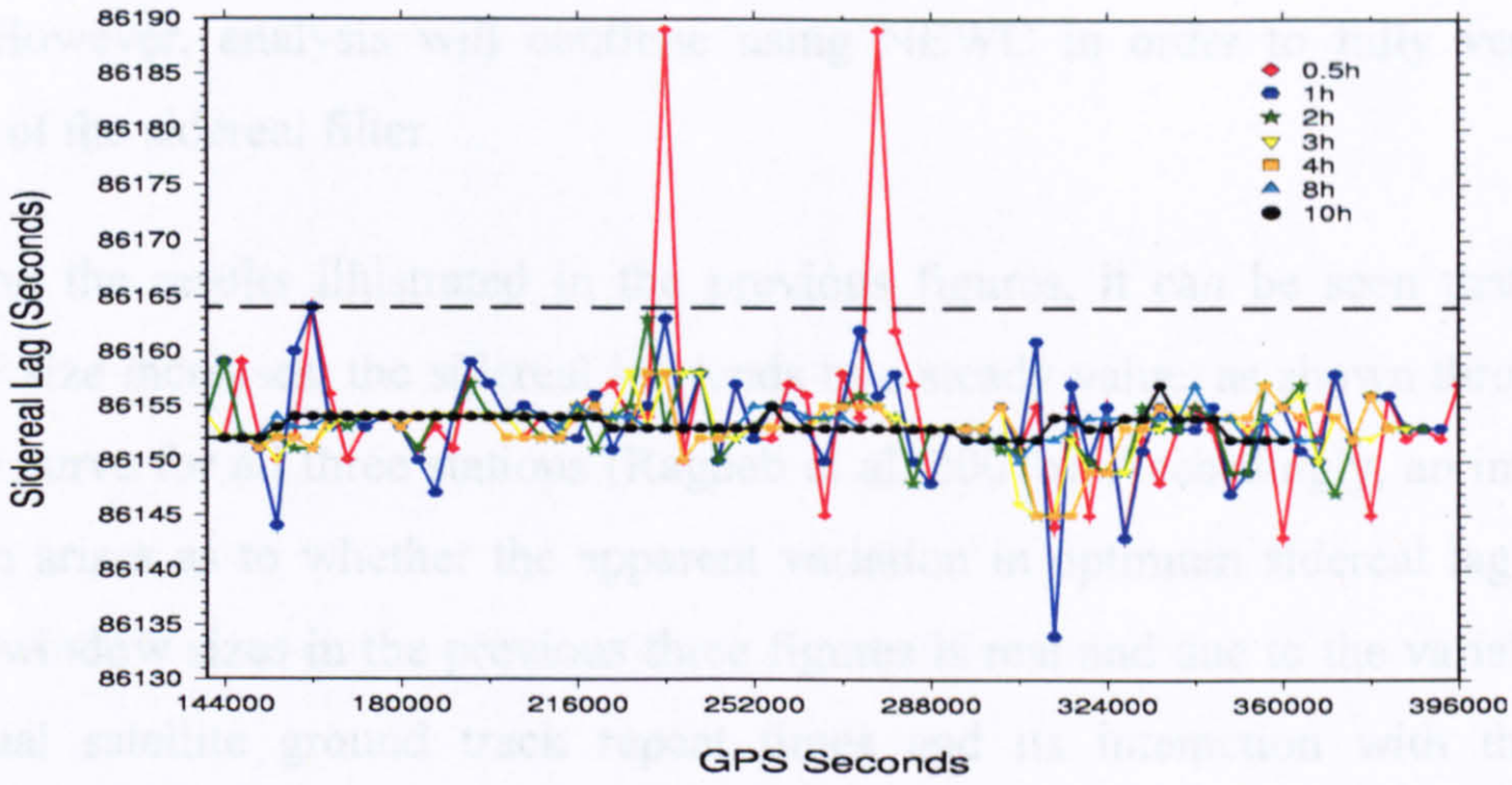

Figure 3.10 Optimum sidereal lag for different window sizes over a 3-day period (DRMS). Line attributes as before.

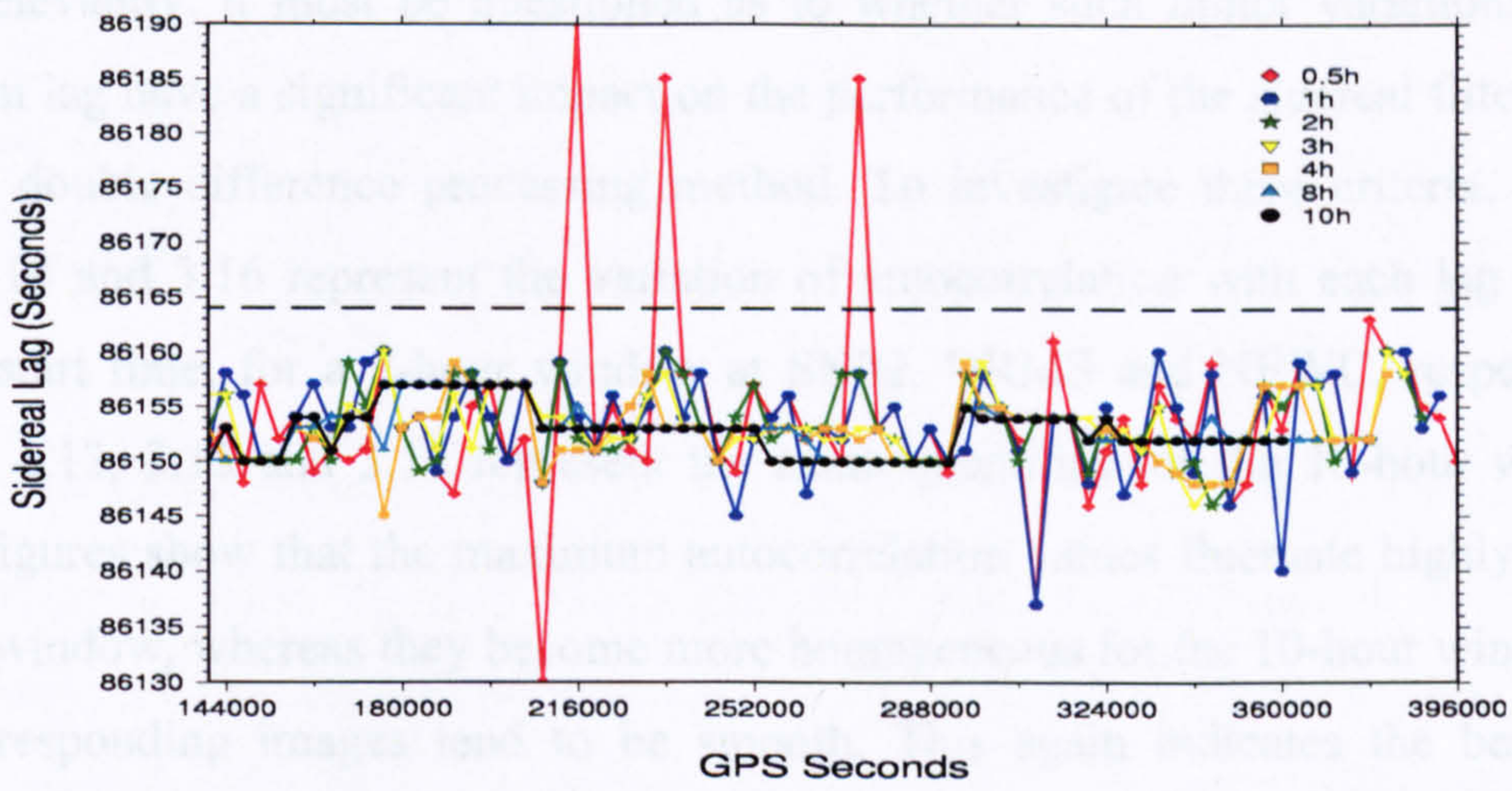

Figure 3.11 Optimum sidereal lag for different window sizes over a 3-day period (NEWC). Line attributes as before.

From the previous figures, it can be seen that the 0.5 and 1 hour window sizes again show high fluctuations from one hour to the next, and thus will be excluded from any further investigations. It can also be easily concluded that increasing the window size decreases the apparent variability of the sidereal lag, which over the whole data set tends to a steady value of around 86154 s (23h 55m 54s), i.e. not quite sidereal. This conclusion was previously reported by Choi et al. (2004) based on the mean satellite orbit repeat period. On the other hand, looking at Figure 3.11, one can see that the value of the sidereal lag does not always completely stabilize, even using a 10-hour window. This could be attributed to the higher noise and multipath environment surrounding the NEWC station as illustrated in Figures 3.6 and 3.7, which causes frequent receiver loss of lock leading to data gaps and thus increasing the random

noise. However, analysis will continue using NEWC in order to fully verify the success of the sidereal filter.

Based on the results illustrated in the previous figures, it can be seen that as the window size increases, the sidereal lag tends to a steady value, as shown through the 10 hour curve for all three stations (Ragheb et al. 2007b). Accordingly, an important question arises as to whether the apparent variation in optimum sidereal lag for the shorter window sizes in the previous three figures is real and due to the variability in individual satellite ground track repeat times and its interaction with the local multipath reflectors (Larson et al. 2007), or is an artefact of the small sample size.

More relevantly, it must be questioned as to whether such minor variations in the optimum lag have a significant impact on the performance of the sidereal filter, when using a double difference processing method. To investigate these criteria, Figures 3.12, 3.14 and 3.16 represent the variation of autocorrelation with each lag at each hourly start time, for a 2-hour window at SN02, DRMS and NEWC, respectively. Figures 3.13, 3.15 and 3.17 represent the same quantities for the 10-hour window. These figures show that the maximum autocorrelation values fluctuate highly for the 2-hour window, whereas they become more homogeneous for the 10-hour window, as the corresponding images tend to be smooth. This again indicates the benefit of increasing the window size for the determination of the optimum sidereal lag. The "striping" in Figures 3.12, 3.14 and 3.16 strongly suggests that there are times at which the sidereally-repeating signal is weak or incoherent, perhaps due to a beneficial satellite geometry for which there is temporarily little or no multipath error.

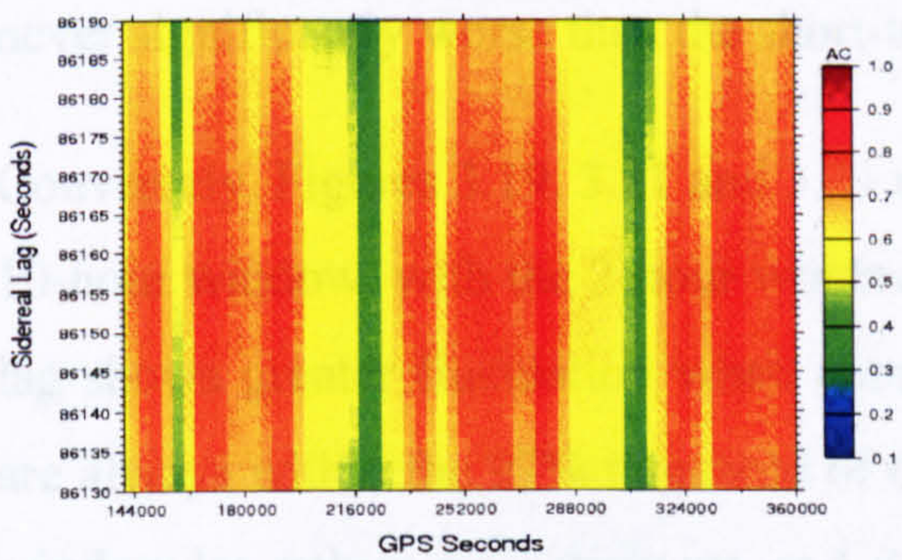

Figure 3.12 2-hour window autocorrelation over a 3-day period (SN02).

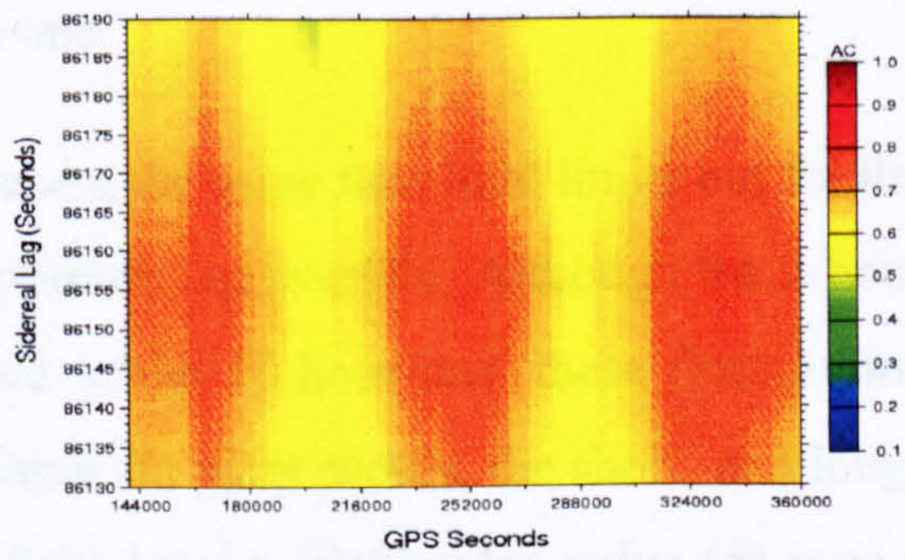

Figure 3.13 10-hour window autocorrelation over a 3-day period (SN02).

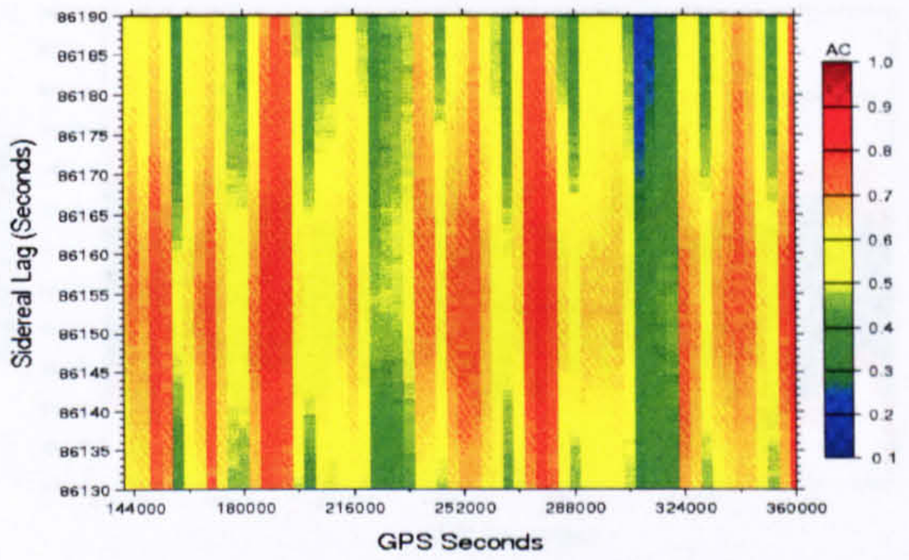

Figure 3.14 2-hour window autocorrelation over a 3-day period (DRMS).

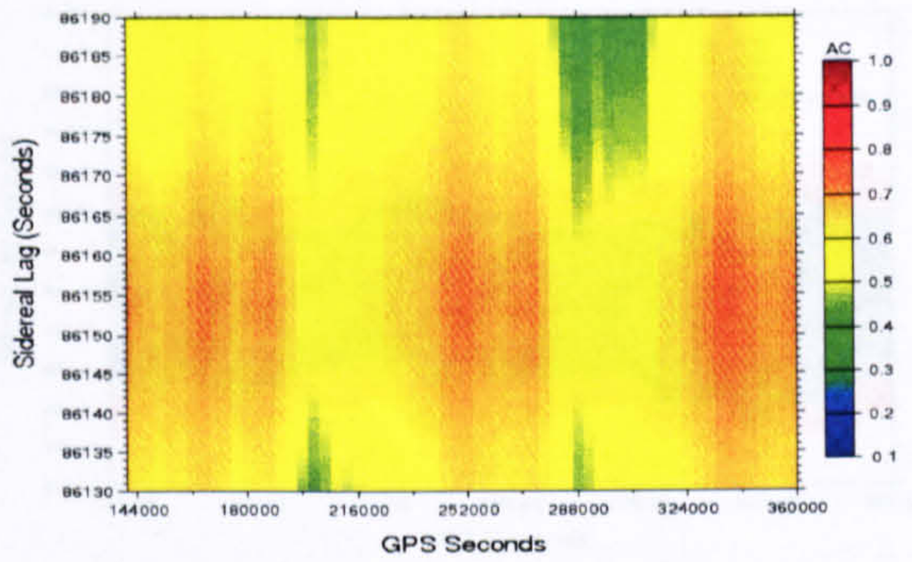

Figure 3.15 10-hour window autocorrelation over a 3-day period (DRMS).

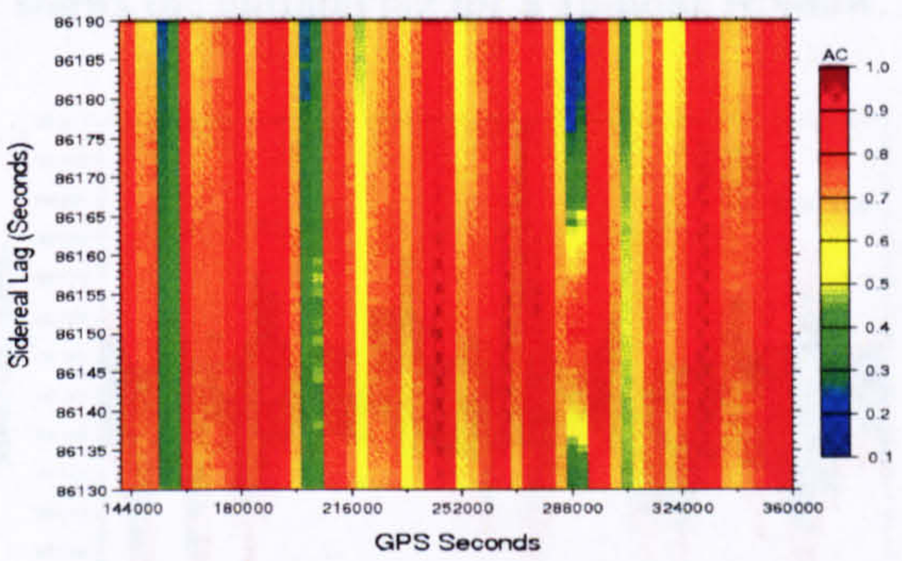

Figure 3.16 2-hour window autocorrelation over a 3-day period (NEWC).

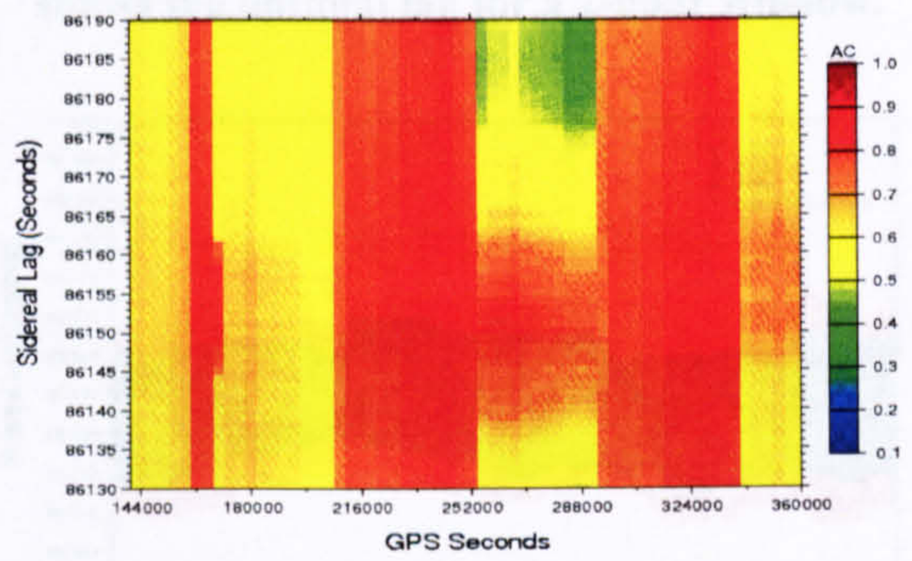

Figure 3.17 10-hour window autocorrelation over a 3-day period (NEWC).

To distinguish those epochs where the maximum autocorrelation is less well determined, as opposed to those where the autocorrelation is simply weaker, Figures 3.18, 3.20 and 3.22 show the sidereal lags having an autocorrelation equal to or greater than 95%, 97% and 99% of the maximum autocorrelation value at each hourly start time for the 2-hour window for all three stations, in which the 10-hour window optimum lag is overlaid. It can be seen that the optimal 10-hour lag nearly always lies within the 99% threshold, implying that the longer-term estimate of sidereal lag is never significantly worse than the short-term one.

Conversely, Figures 3.19, 3.21 and 3.23 represent the same threshold limits but for the 10-hour window, with the 2-hour window optimum lag overlaid. Although the 2-hour lag shows greater fluctuation when compared to the 10-hour one, these fluctuations are always within the 97% threshold of the latter. In other words, the short- and long-window lag values are consistent, and use of the longer-window lag value (or even a constant value) should not appreciably worsen the filtering, especially in double difference processing. This is mainly due to the fact that the resultant repeating

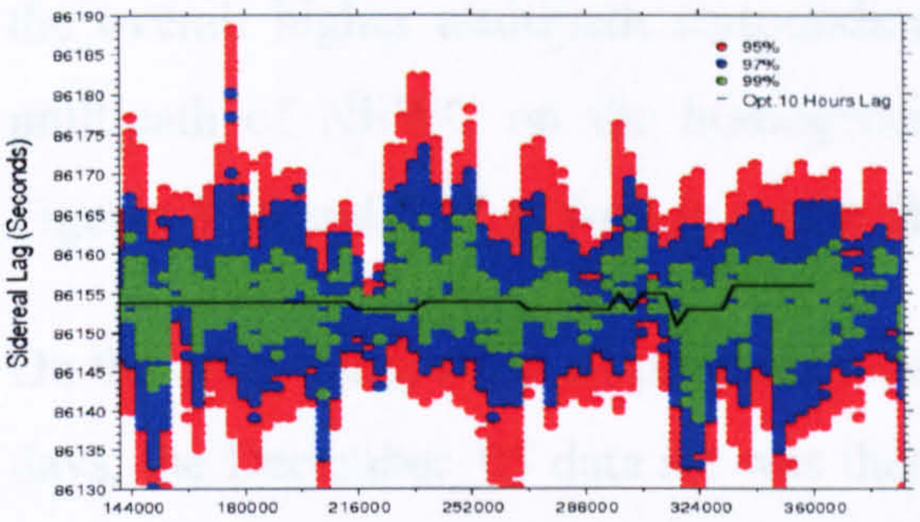

Figure 3.18 2-hour window thresholds (SN02). Values are expressed as a percentage of the maximum autocorrelation. The solid line shows the optimal lag for a 10-hour window.

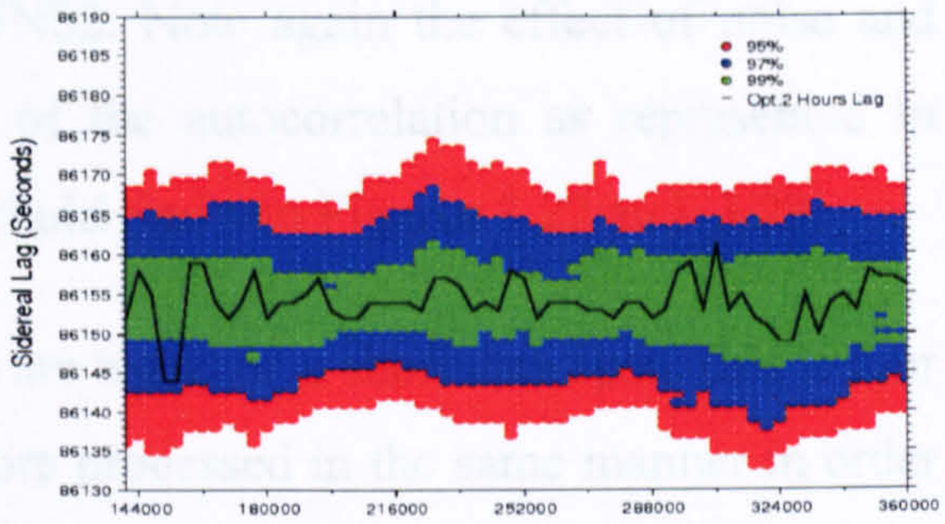

Figure 3.19 10-hour window thresholds (SN02). Values are expressed as a percentage of the maximum autocorrelation. The solid line shows the optimal lag for a 2-hour window.

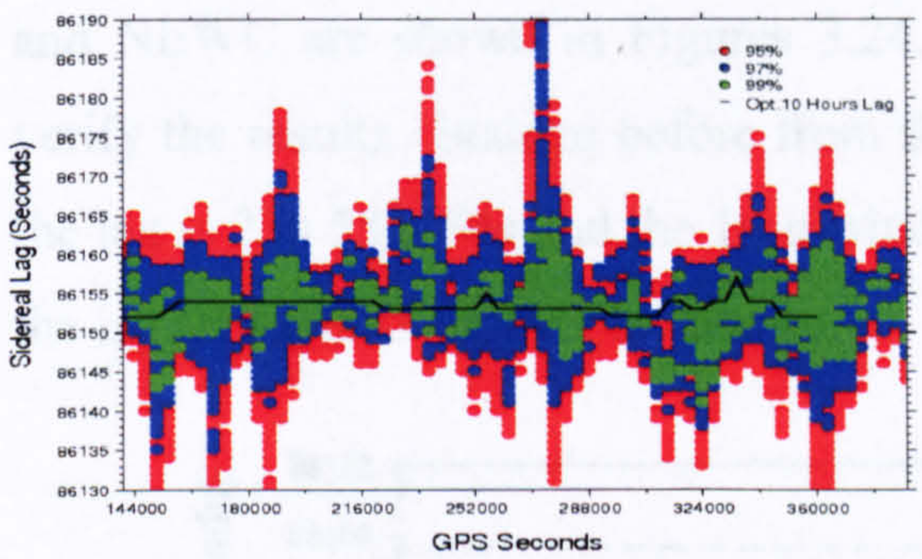

Figure 3.20 2-hour window thresholds (DRMS). Shading as before.

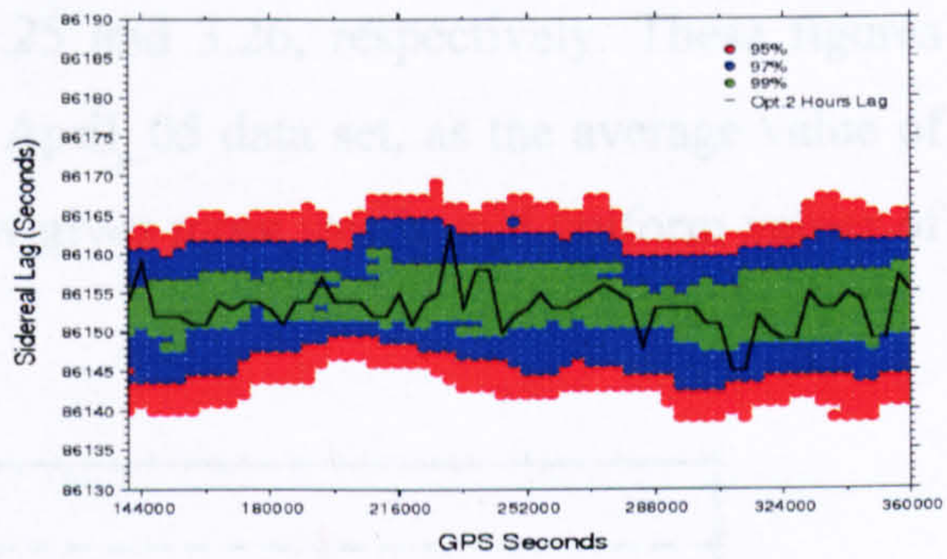

Figure 3.21 10-hour window thresholds (DRMS). Shading as before.

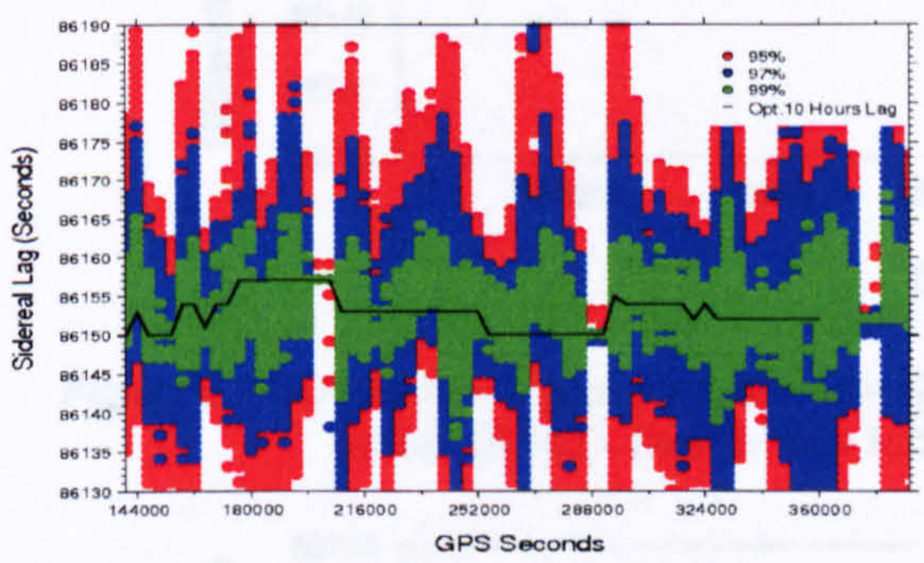

Figure 3.22 2-hour window thresholds (NEWC). Shading as before.

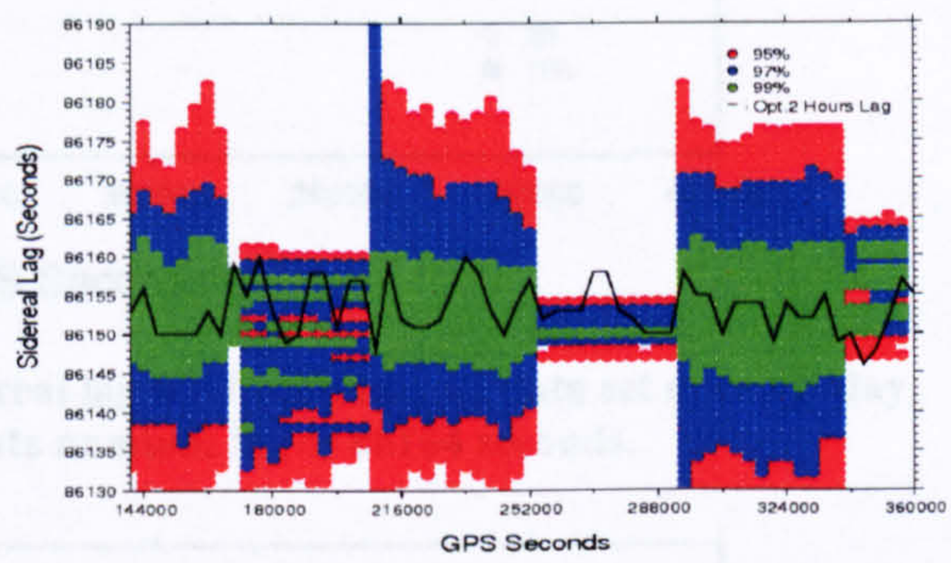

Figure 3.23 10-hour window thresholds (NEWC). Shading as before.

multipath will arise from the combination of the stations and satellites included in double differencing, which will in turn produce lower autocorrelation values with broader peaks when compared to previous investigations where a specific value of the lag is obtained for each satellite using point positioning. In addition, the effect of the multipath environment is well illustrated when comparing Figures 3.18 and 3.20 or Figures 3.19 and 3.21: the limits for SN02 are larger than the limits for DRMS, due to

the overall higher multipath surrounding SN02. Note again the effect of noise and multipath of NEWC on the homogeneity of the autocorrelation as represented in Figures 3.16 and 3.17 as well as on the threshold limits in Figures 3.22 and 3.23.

On the other hand, since all previous results are based on a short data span, that is four days, the December_05 data set was therefore processed in the same manner in order to visualize the long term variation in the sidereal lag and to confirm previous results and conclusions. The coordinate results of the GASP program were input to the GASF program, with only two window sizes for sidereal lag determination (2 and 10 hours) being investigated. The optimum hourly lag for both window sizes for SN02, DRMS and NEWC are shown in Figures 3.24, 3.25 and 3.26, respectively. These figures verify the results obtained before from the April_05 data set, as the average value of the lag is 23h 55m 54s and the 10-h window gives more steady and uniform values of the lag throughout the whole data set.

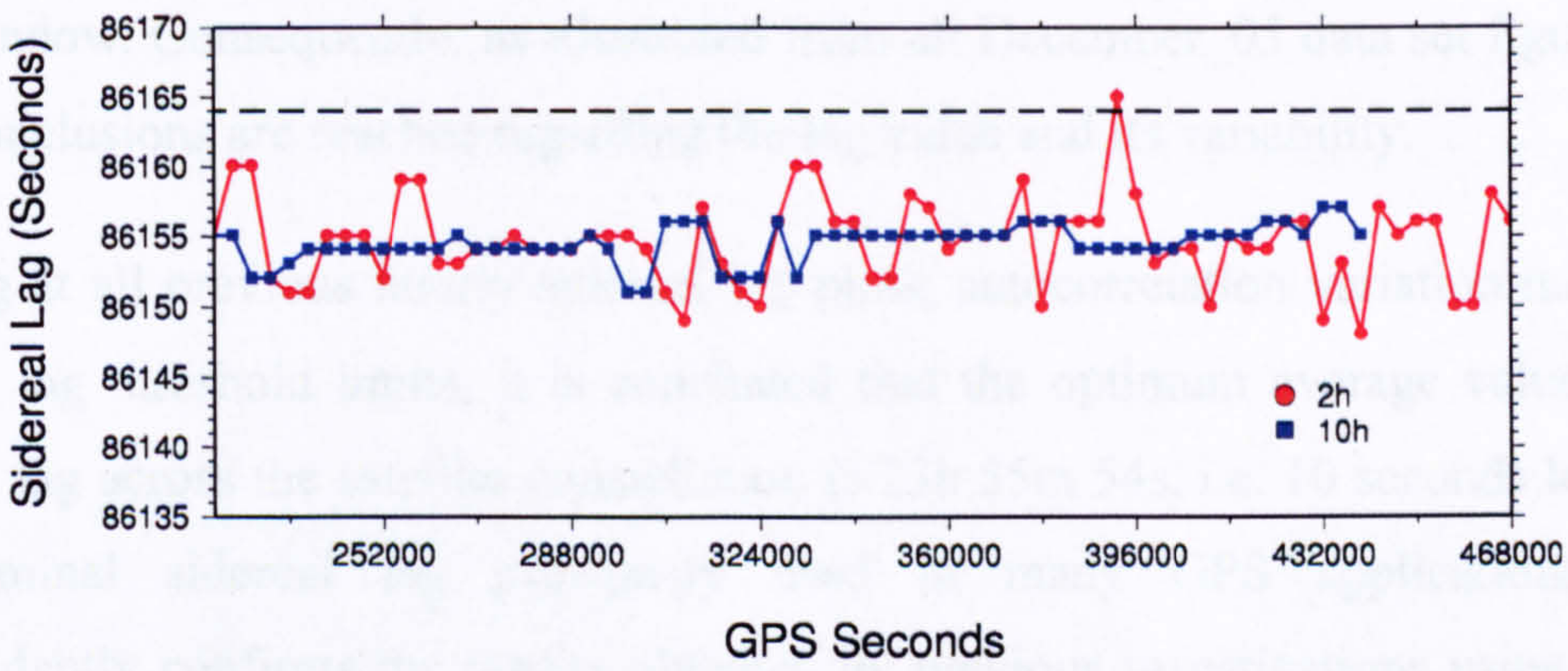

Figure 3.24 Optimum 2- and 10-h window sidereal lag for December_05 data set over a 3-day period (SN02). Dashed line indicate nominal lag of 86164 seconds.

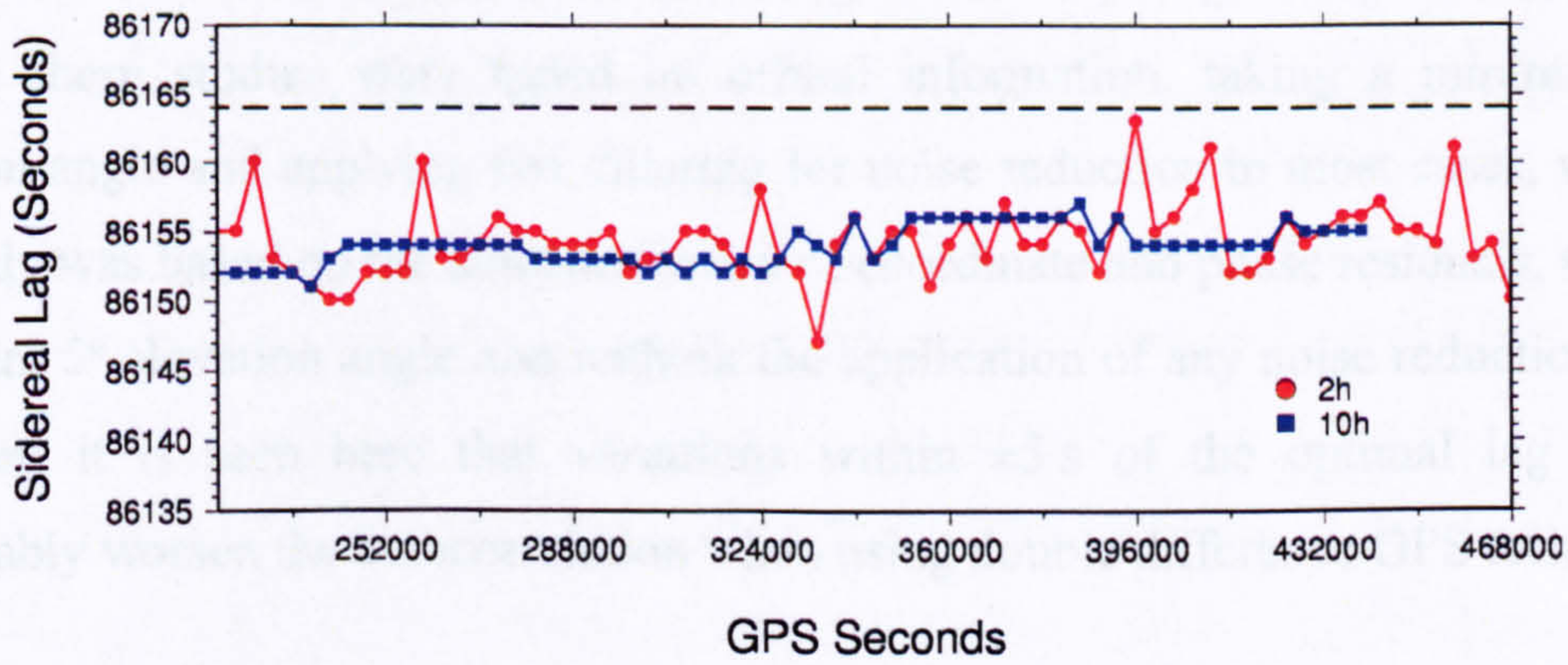

Figure 3.25 Optimum 2- and 10-h window sidereal lag for December_05 data set over a 3-day period (DRMS). Line attributes as before.

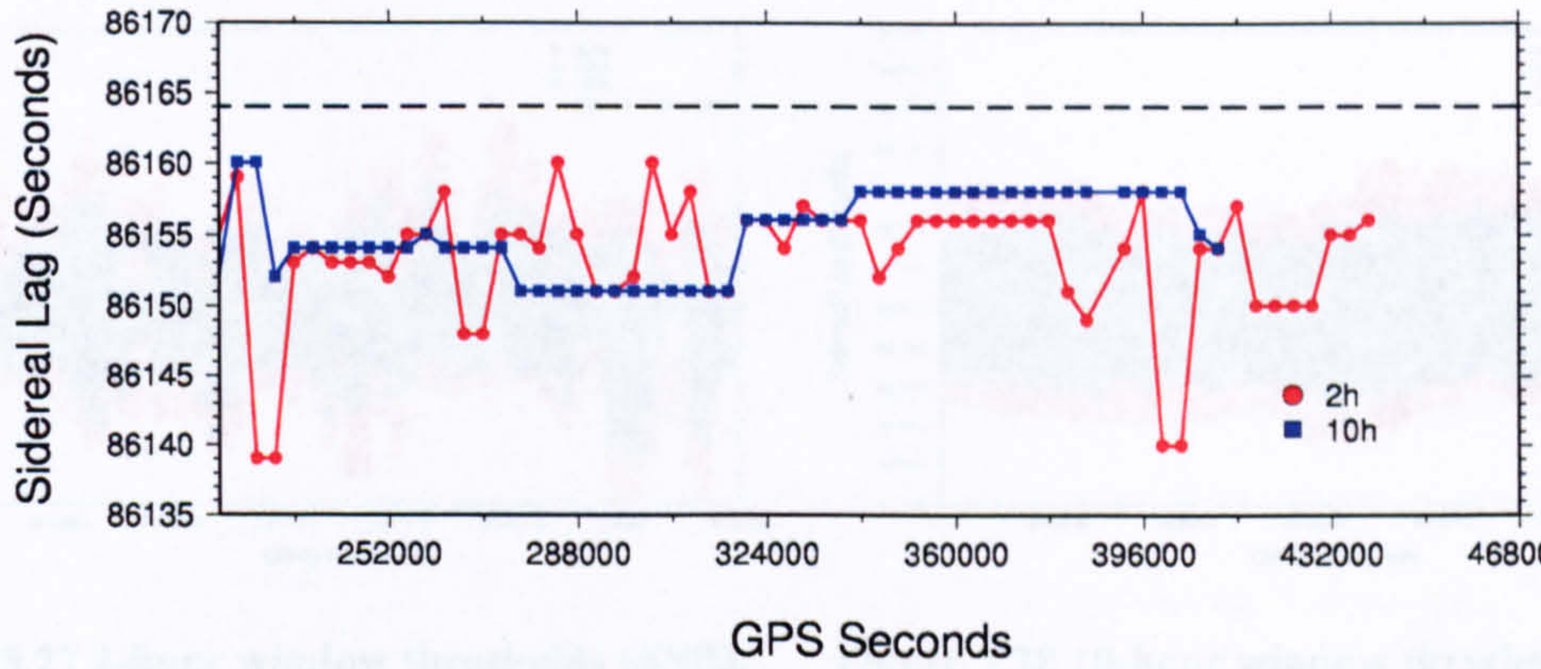

Figure 3.26 Optimum 2- and 10-h window sidereal lag for December_05 data set over a 3-day period (NEWC). Line attributes as before.

Once again, NEWC shows higher variability for the lag, caused by the higher multipath environment surrounding the NEWC station, or even perhaps due to the considerably large amount of missing data. As before, Figures 3.27, 3.29 and 3.31 show the sidereal lag threshold limits for the 2-hour window for SN02, DRMS and NEWC, respectively, while Figures 3.28, 3.30 and 3.32 show the same, but for the 10-hour window. Consequently, as illustrated from all December_05 data set figures, the same conclusions are reached regarding the lag value and its variability.

Looking at all previous hourly sidereal lag plots, autocorrelation variation maps and sidereal lag threshold limits, it is concluded that the optimum average value of the sidereal lag across the satellite constellation is 23h 55m 54s, i.e. 10 seconds less than the nominal sidereal lag previously used in many GPS applications. This independently confirms the results obtained by previous investigations using a wide range of baseline lengths and localities (e.g. Agnew and Larson 2007; Axelrad et al. 2005; Choi et al. 2004; Larson et al. 2007), with very slight differences, mainly because these studies were based on orbital information, taking a minimum 15° elevation angle and applying box filtering for noise reduction in most cases, whereas this study was based on the autocorrelation of coordinate and phase residuals, taking a minimum 5° elevation angle and without the application of any noise reduction filter. However, it is seen here that variations within ±5 s of the optimal lag do not appreciably worsen the autocorrelation when using double difference GPS techniques.

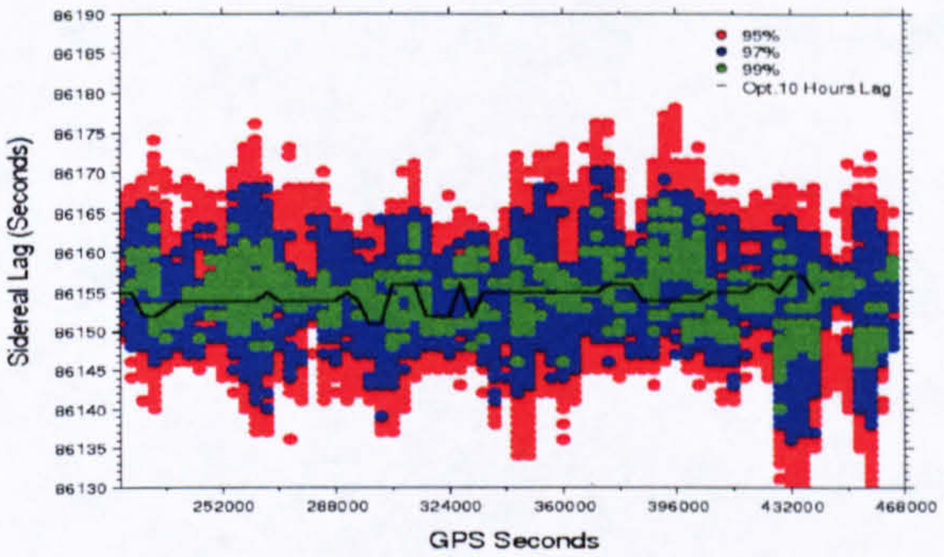

Figure 3.27 2-hour window thresholds (SN02, December_05 data set). Shading as before.

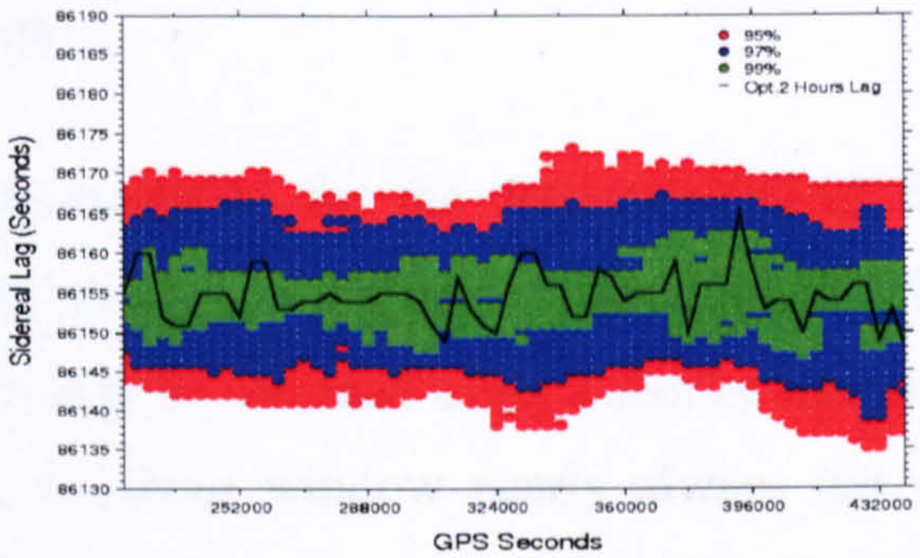

Figure 3.28 10-hour window thresholds (SN02, December_05 data set). Shading as before.

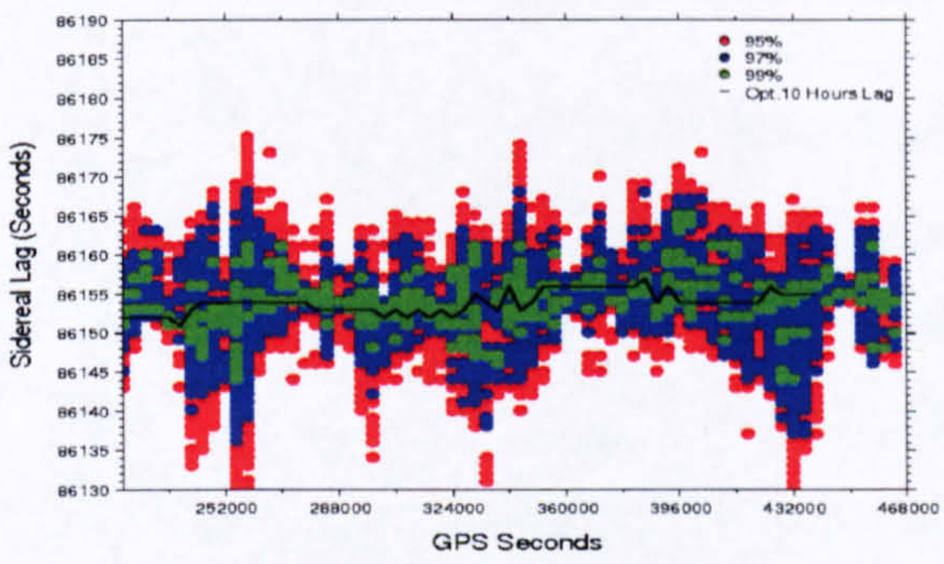

Figure 3.29 2-hour window thresholds (DRMS, December_05 data set). Shading as before.

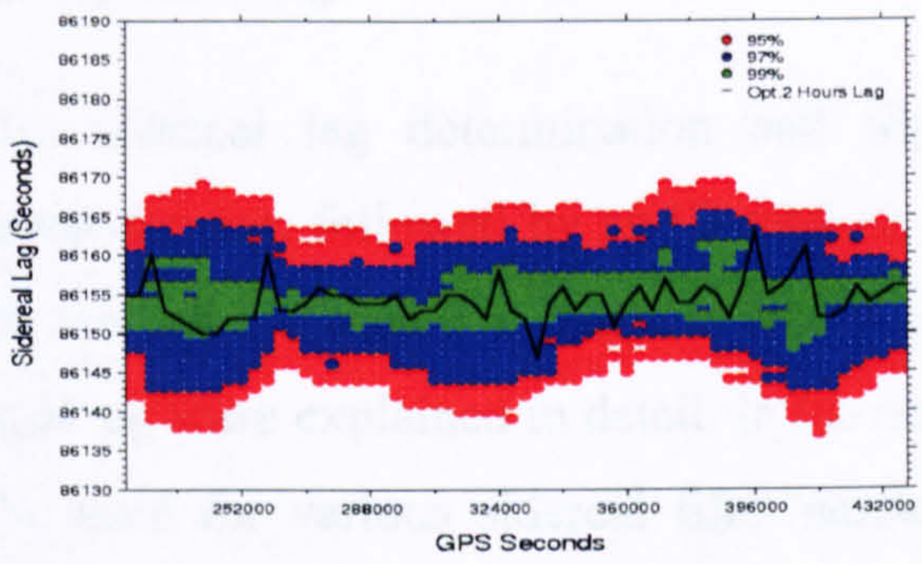

Figure 3.30 10-hour window thresholds (DRMS, December_05 data set). Shading as before.

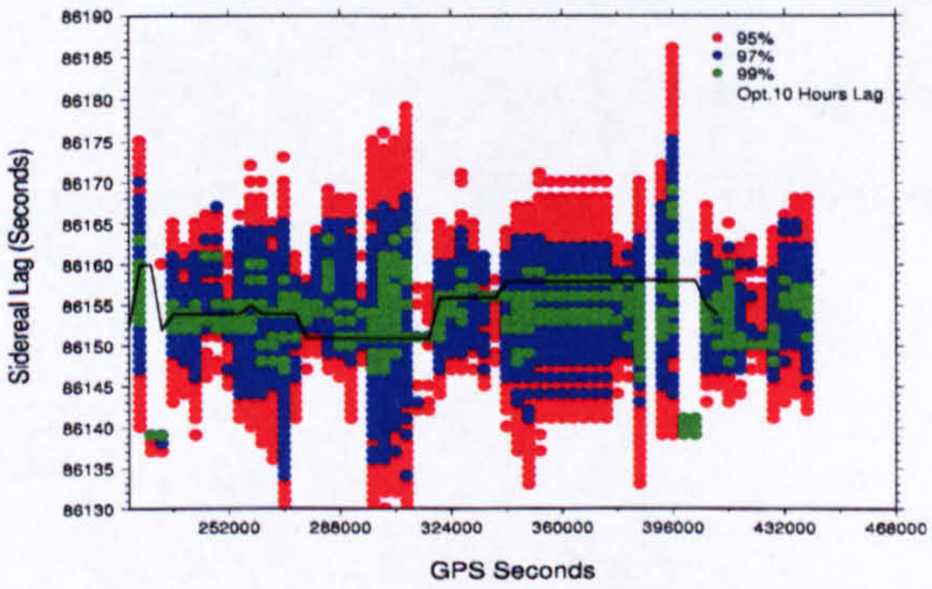

Figure 3.31 2-hour window thresholds (NEWC, December_05 data set). Shading as before.

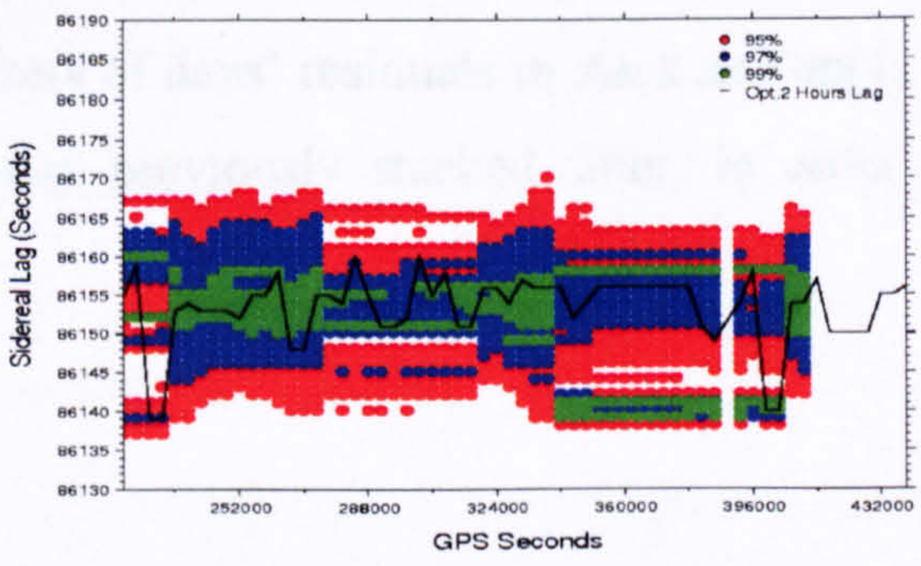

Figure 3.32 10-hour window thresholds (NEWC, December_05 data set). Shading as before.

Consequently, the sidereal lag value obtained will be used further in the filtering process, in order to obtain filtered coordinates. Also, it should be noted that NEWC shows a higher fluctuation for the lag when compared to the other two cases, for example, SN02. This indicates higher multipath, although both are located on the same building, but still the corresponding lag obtained from NEWC lies within at least 97% of the threshold limits.

3.6 Lag Investigation Conclusions

A long window size (8–12 hours) is recommended for the determination of the optimum sidereal lag, for a more consistent, steady and uniform value throughout the whole data set. Alternatively, a usable value can be obtained using a shorter window; for example, in the used data sets here, a 2-hour window nearly always has an autocorrelation with at least 97% of the optimal longer-term value, despite showing greater fluctuation. In addition, short-term variations in the optimum lag appear to have little effect, at least for double-difference processing.

In summary, the two programs used for sidereal lag determination and filter application were fully described in the current chapter, followed by an illustration of the site test stations, different collected data sets and environment characterization. At the end, all investigations concerning sidereal lag were explained in detail. In the next chapter, the obtained optimum lag will be used for various sidereal filter studies. Coordinate and observation filtering are used to filter the data from sidereally repeating errors, while comparing between these filtering techniques from the precision and efficiency point of view. The effect of sidereal lag variation is also considered. In addition, the optimum numbers of days' residuals to stack and apply is investigated, as well as the lifetime of any previously stacked filter, in order to achieve highest possible precision.

SIDEREAL FILTER STRATEGIES, PERFORMANCE AND LIFETIME

4.1 Introduction

After the determination of the "sidereal" lag and verification of its variability through different data sets, this chapter is concerned with all the practical work applied to test the methodology of sidereal filtering. At first, a more detailed overview is given of the two different filtering methodologies, namely coordinate and observation filtering. This is followed by the practical application of these two filtering techniques using the April_05 and December_05 data sets. The efficiency of both methodologies is investigated further, in terms of reliability, precision and computational time. Following this study, a deeper investigation is carried out into the competence of sidereal filtering in the case of long data sets and with different data sets. That is sidereal filter application with a varying time span between the filter and the applied day. The collected data sets for this investigation (March_06 and July_06) are discussed first. After which, two main questions are posed in terms of the performance of sidereal filtering: the optimum number of days to stack (average) and apply, and the lifetime over which any sidereal filter is valid.

4.2 Sidereal Filter Application Methodology

The fundamental idea behind applying sidereal filtering involves differencing the residuals of a station at two epochs separated by a multiple of the sidereal lag. Thus with the repeated geometry of satellites for those two epochs, any repeating error such as the multipath effect will be similar, and consequently removed, or at least greatly reduced. Regarding the type of residuals to be used, two different methodologies will

be adopted. The first, called here the coordinate filter, includes stacking the output coordinate residuals from the GASP program at the optimum sidereal lag over one or more days using epoch-by-epoch weighted coordinate residuals. These residuals are obtained with respect to the long-term weighted mean coordinate of each site. Filtering is then applied by subtracting these residuals from the processed coordinates at the corresponding epoch of the applied data in question (matching by multiple of sidereal days).

The second methodology, referred to as the observation filter, includes two main steps. The first is to run the GASP program with respect to a fully-fixed solution with fixed ambiguities rounded to the nearest integer (without ambiguity search or least squares adjustment), and thus leaving only sidereally repeating errors with multipath and noise being the dominant errors. In this solution, both ends of the baseline have coordinates fixed to their a priori or long-term mean values, outputting biased double difference phase residuals of all satellite pairings. These residuals are then passed to the FAP program, which stacks only these residuals without weighting due to the identical geometry of satellites in each double difference among sidereal days. The second step includes a re-run of the GASP program with ambiguity search on the applied data only. During this process, double difference phase L1 and L2 observables are adjusted with the stacked filtered phase residuals at the corresponding epoch in order to output final filtered coordinates.

4.3 Coordinate v. Observation Filtering

Considering the April_05 data set first, since the data available are for four days, it was decided that the filter process would be applied always on the fourth day, while stacking a combination of the previous three days: either one day, two days, or all three days together. In essence, the stacking process will include six cases, three for stacking each day of the three days individually, called Case **Day1**, Case **Day2** and Case **Day3,** respectively, two for stacking two days together, named Case **Day1,2** and Case **Day2,3** and finally stacking all three days together, called Case **Day1,2,3**. Figure 4.1 shows the coordinate time series of NEWC (the highest multipath) in the Easting, Northing and Up directions for the unfiltered case and for each of the filtering

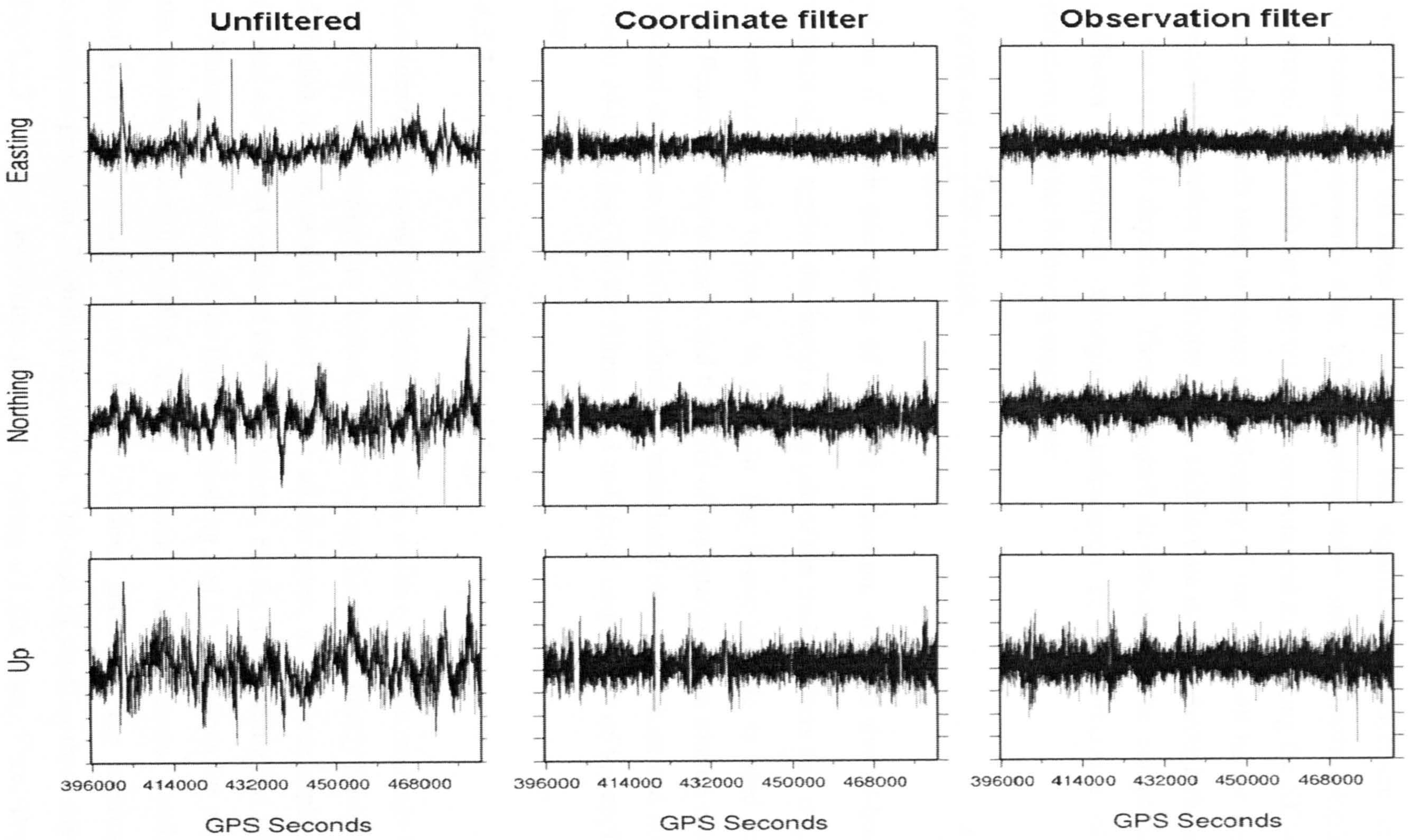

Figure 4.1 NEWC Easting, Northing and Up coordinate time series. Left for unfiltered, middle for coordinate filter and right for observation filter. Note that the coordinate scale of E and N differ from that of U by a factor of 1.5. (Y-axis tick marks are at 1 cm intervals).

methods based on three-day stacking. The significant improvement in all three directional components after filtering using either stacking methodologies is well illustrated, even with the high multipath environment surrounding the NEWC station. The main criteria used to assess the efficiency of the filter will be the repeatability (precision) of station coordinates over a certain time interval, through the calculation of the standard deviation. These standard deviations can be compared to their unfiltered counterparts, through the calculation of the percentage of variance reduction using the following expression:

$$\delta(\sigma)\% = (1 - \frac{\sigma^2_{filter}}{\sigma^2_{unfiltered}}) \times 100, \qquad 4.1$$

where δ is the percentage of variance reduction, σ^2_{filter} is the 24-hour filtered variance of the applied day based on any one of the stacked filters and $\sigma^2_{unfiltered}$ is the 24-hour unfiltered variance. In addition, the F-test statistic is used to test the significance of improvement and the level of consistency in the filtered solution. The standard deviation of the coordinates is calculated once every hour and once for the whole 24-hr of data for the filtered and unfiltered coordinates of the applied fourth day.

4.3.1 Coordinate Filter Methodology

Considering the coordinate filtering method in which coordinate residuals relative to the long term average are stacked, Figure 4.2 represents the hourly Easting standard deviation throughout the applied day for all six cases, at the three applied stations. Figures 4.3 and 4.4 represent the same statistic, but for the Northing and Up standard deviations respectively. In the Easting, Northing and Up directions for all six cases, the standard deviation after filtering becomes smaller, more consistent and homogeneous in almost every hourly window, indicating the improvement in coordinate precision (Ragheb et al. 2007b). The case of stacking three days together Day1,2,3 achieved maximum precision among all six cases. Here, the standard deviation becomes significantly smaller at the 95% confidence level, decreasing to a roughly similar value for all three stations, regardless of the unfiltered standard

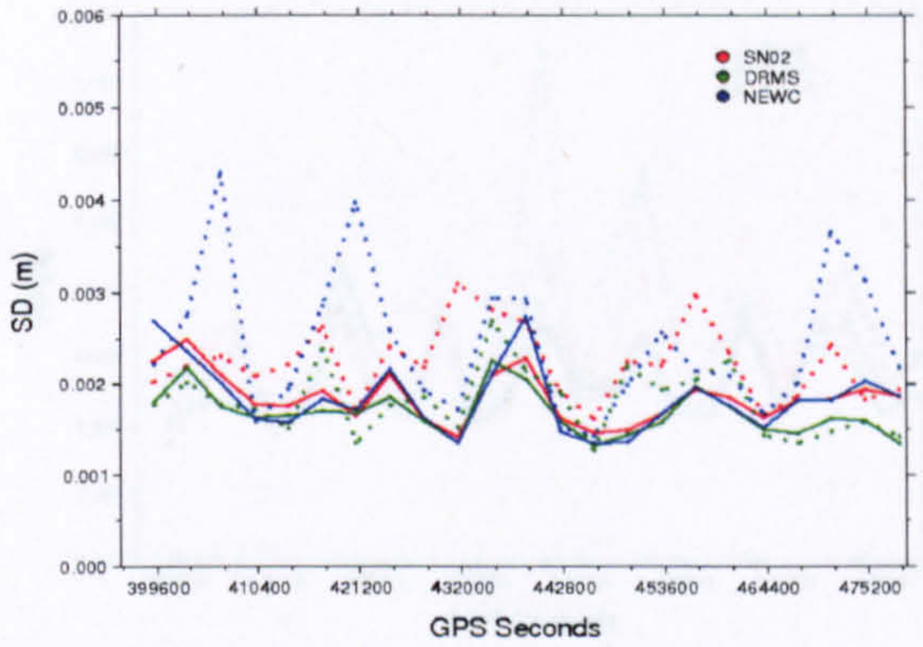

(a) Case Day1

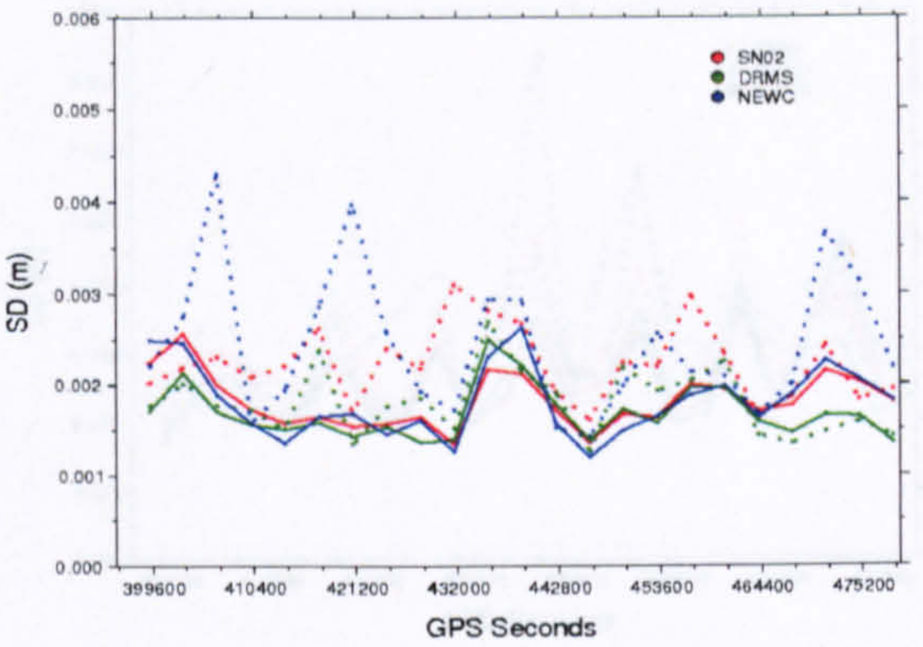

(b) Case Day2

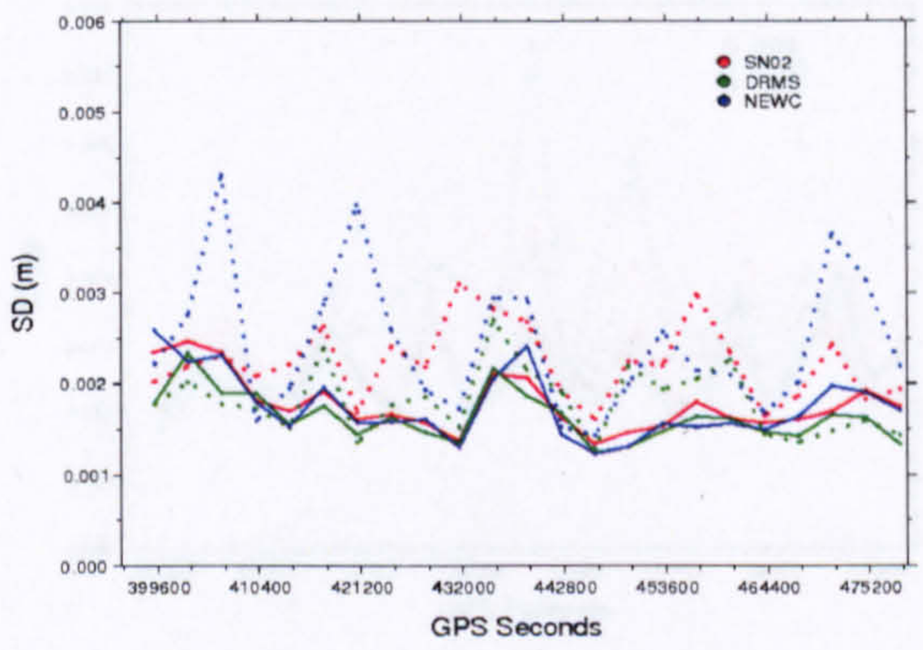

(c) Case Day3

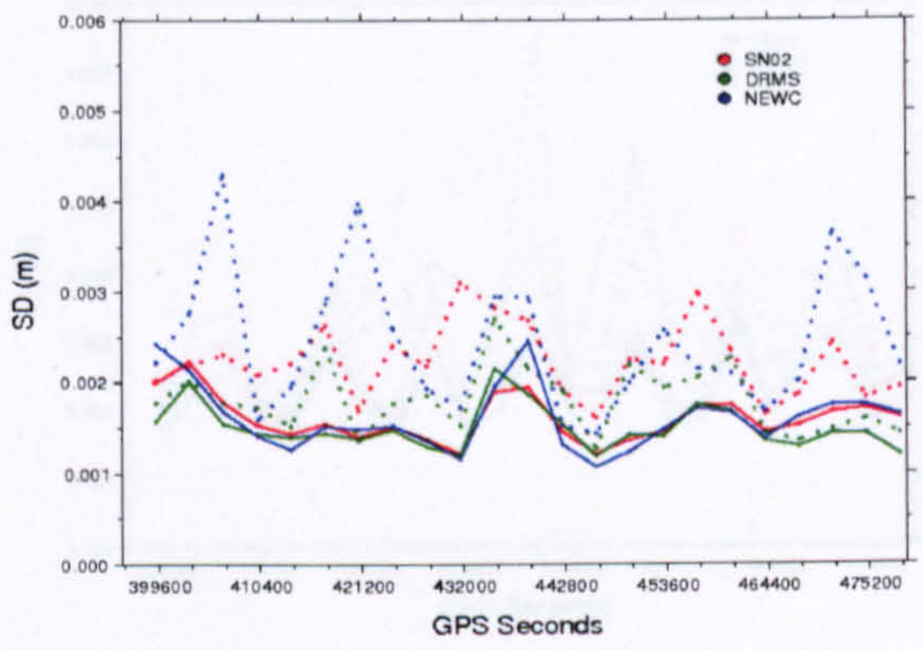

(d) Case Day1,2

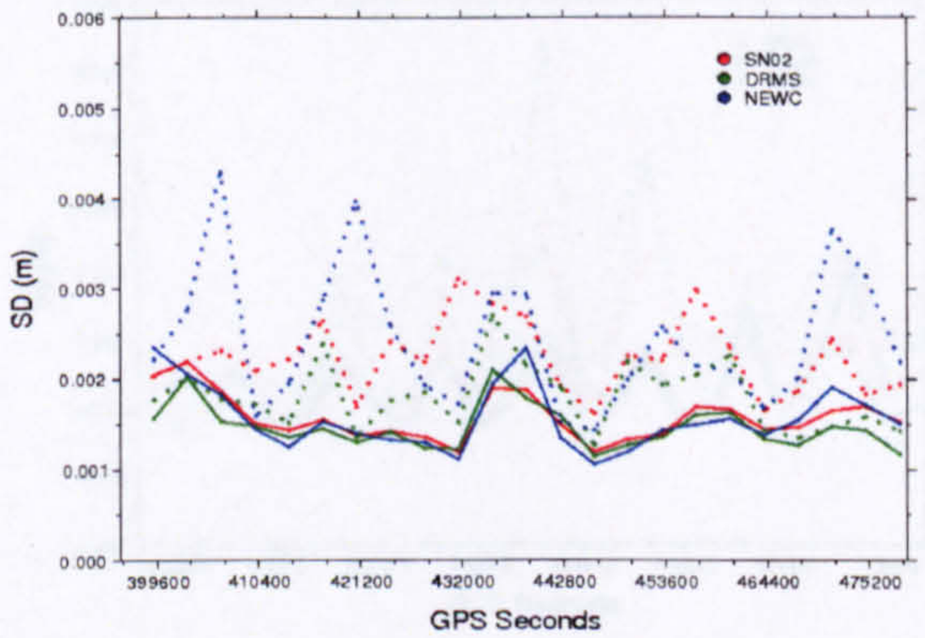

(e) Case Day2,3

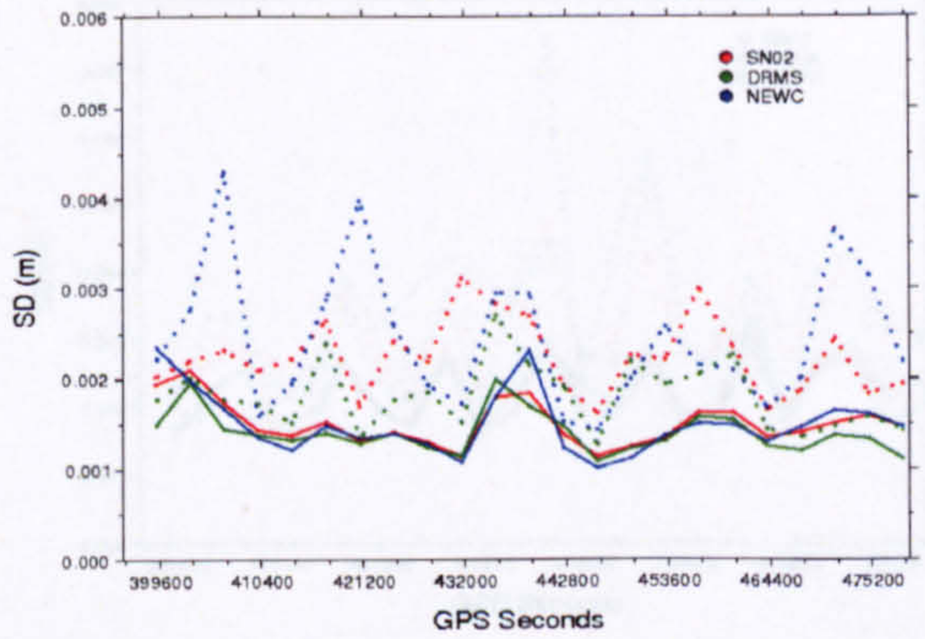

(f) Case Day1,2,3

Figure 4.2 Hourly Easting coordinate standard deviations for all six cases based on the coordinate filter. Dotted lines are for the standard deviations of unfiltered coordinates. Solid lines represent the standard deviations of filtered coordinates.

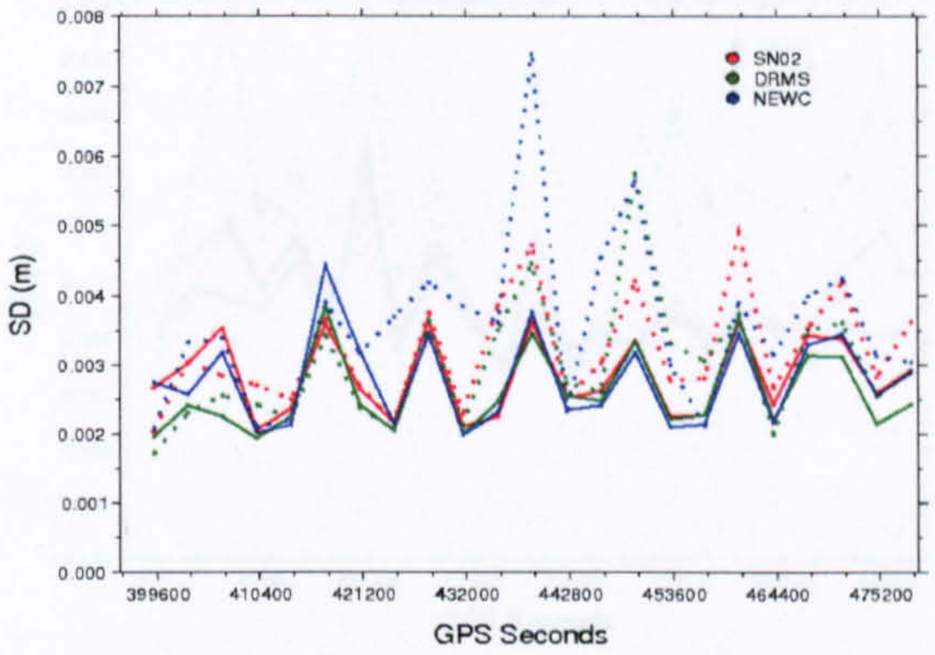

(a) Case Day1

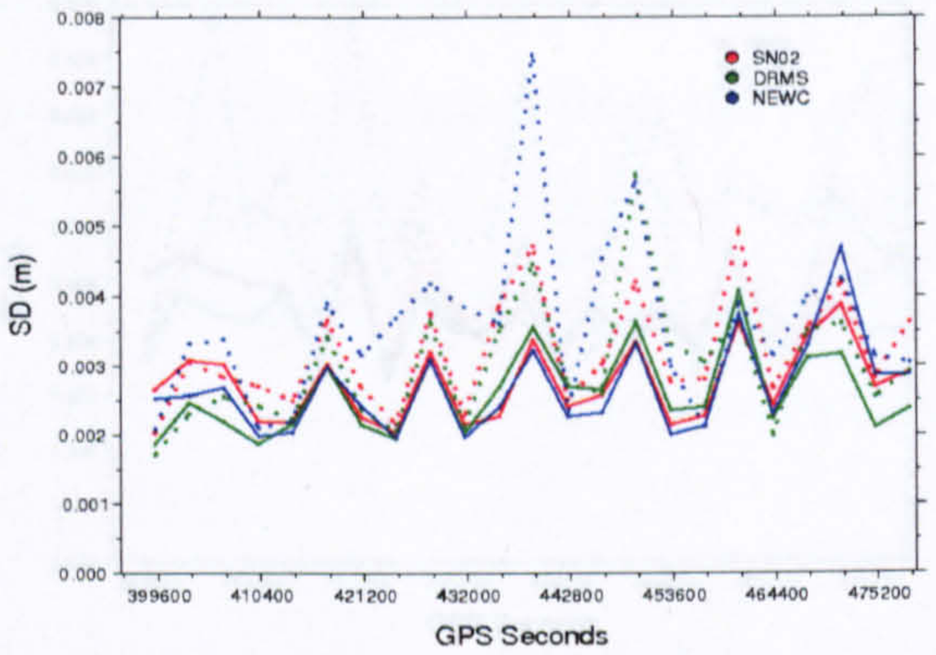

(b) Case Day2

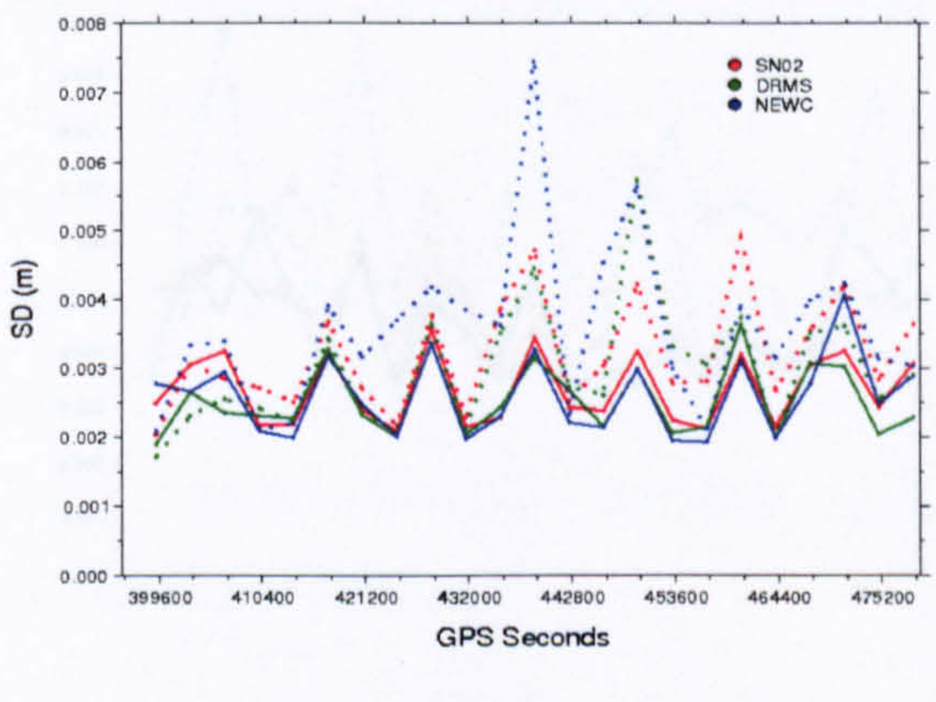

(c) Case Day3

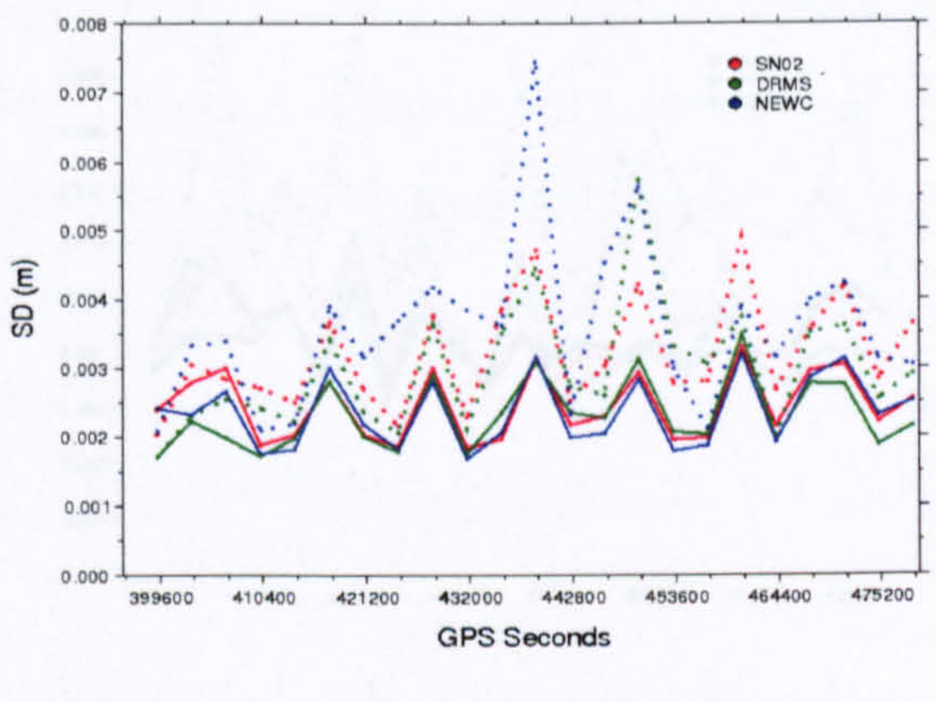

(d) Case Day1,2

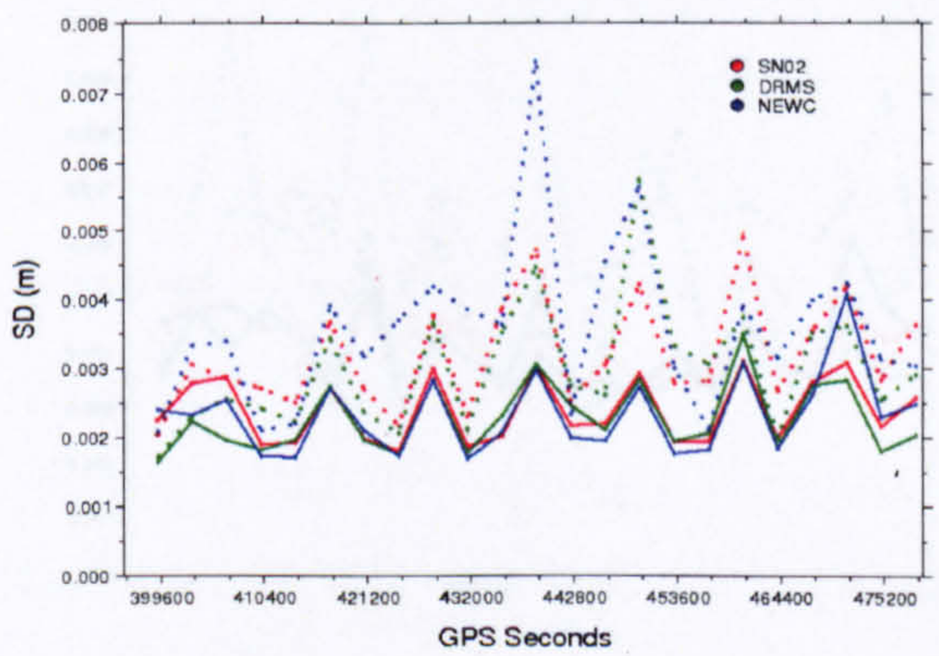

(e) Case Day2,3

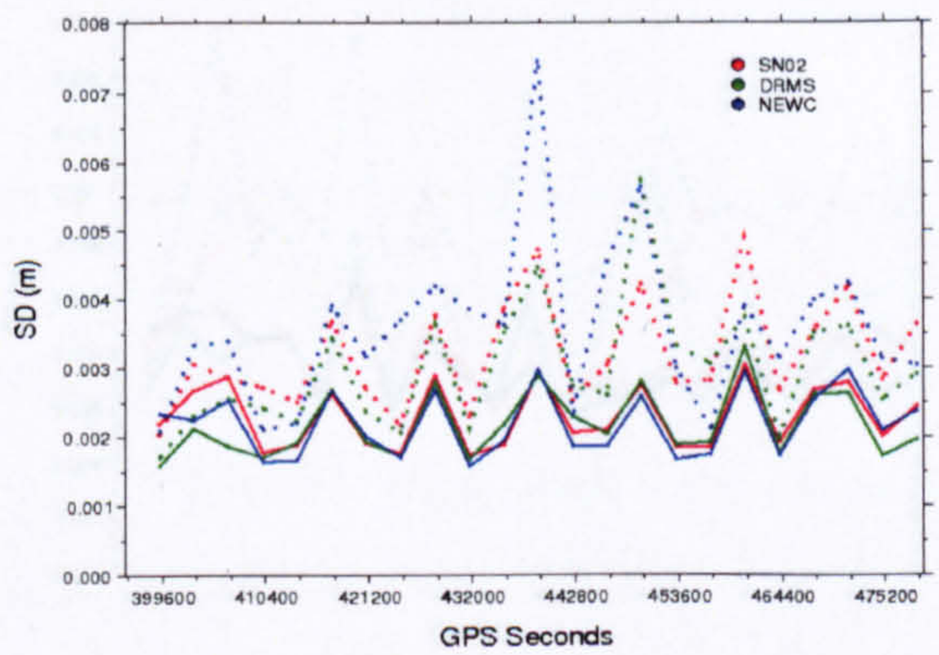

(f) Case Day1,2,3

Figure 4.3 Hourly Northing coordinate standard deviations for all six cases based on coordinate filter. Line attributes as before.

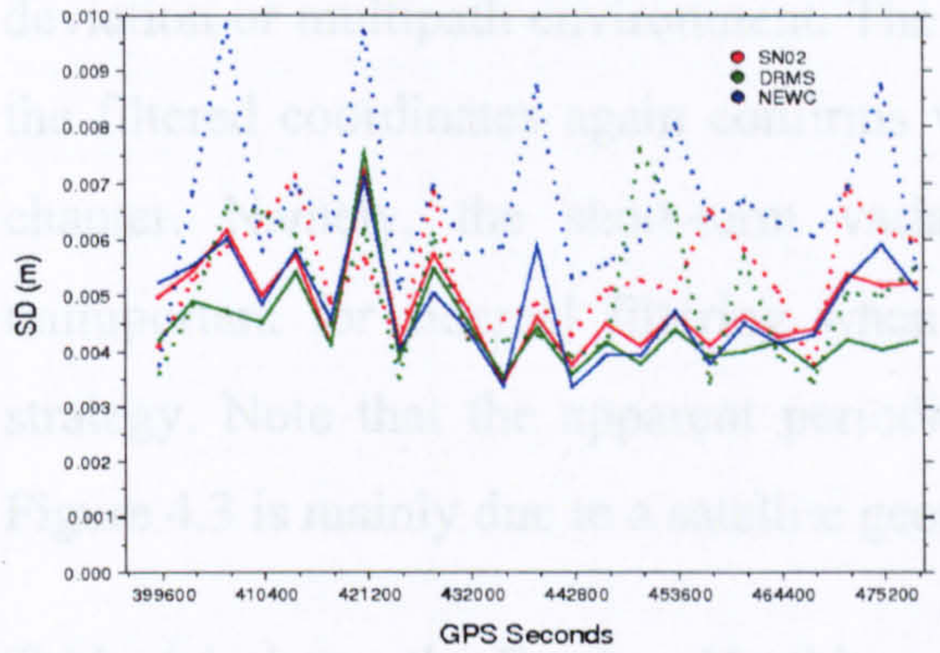

(a) Case Day1

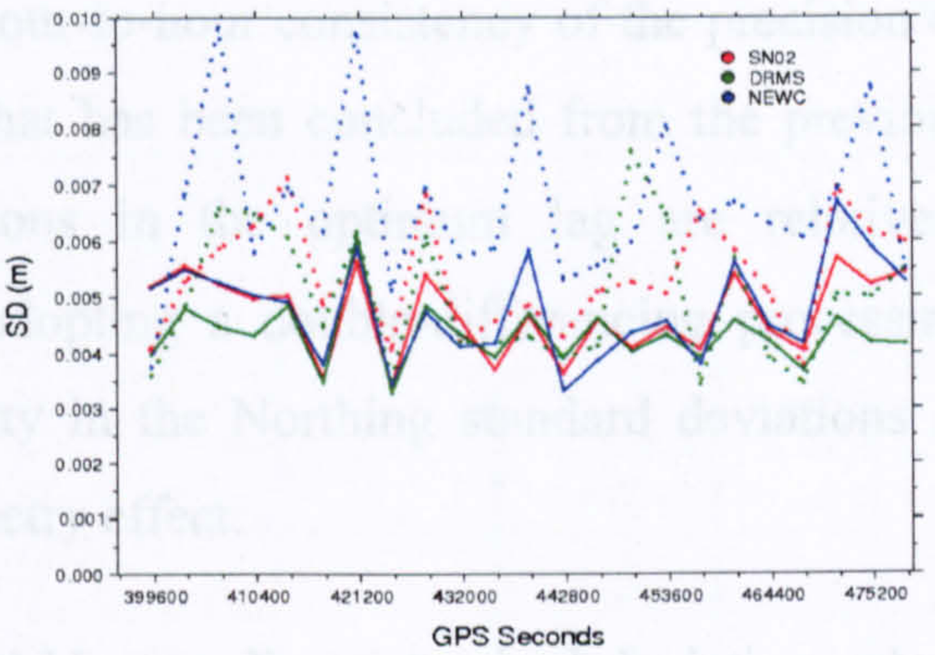

(b) Case Day2

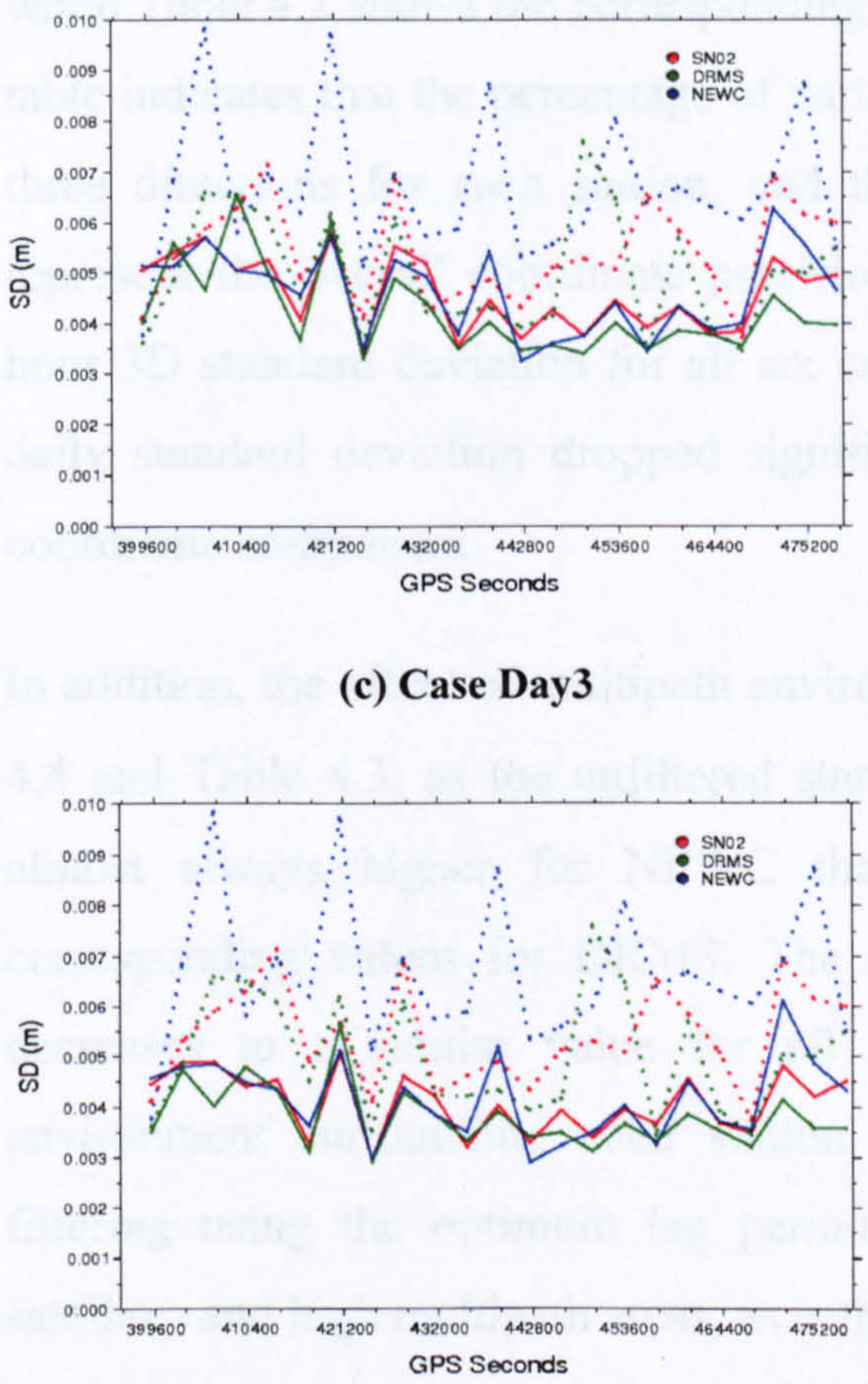

(c) Case Day3

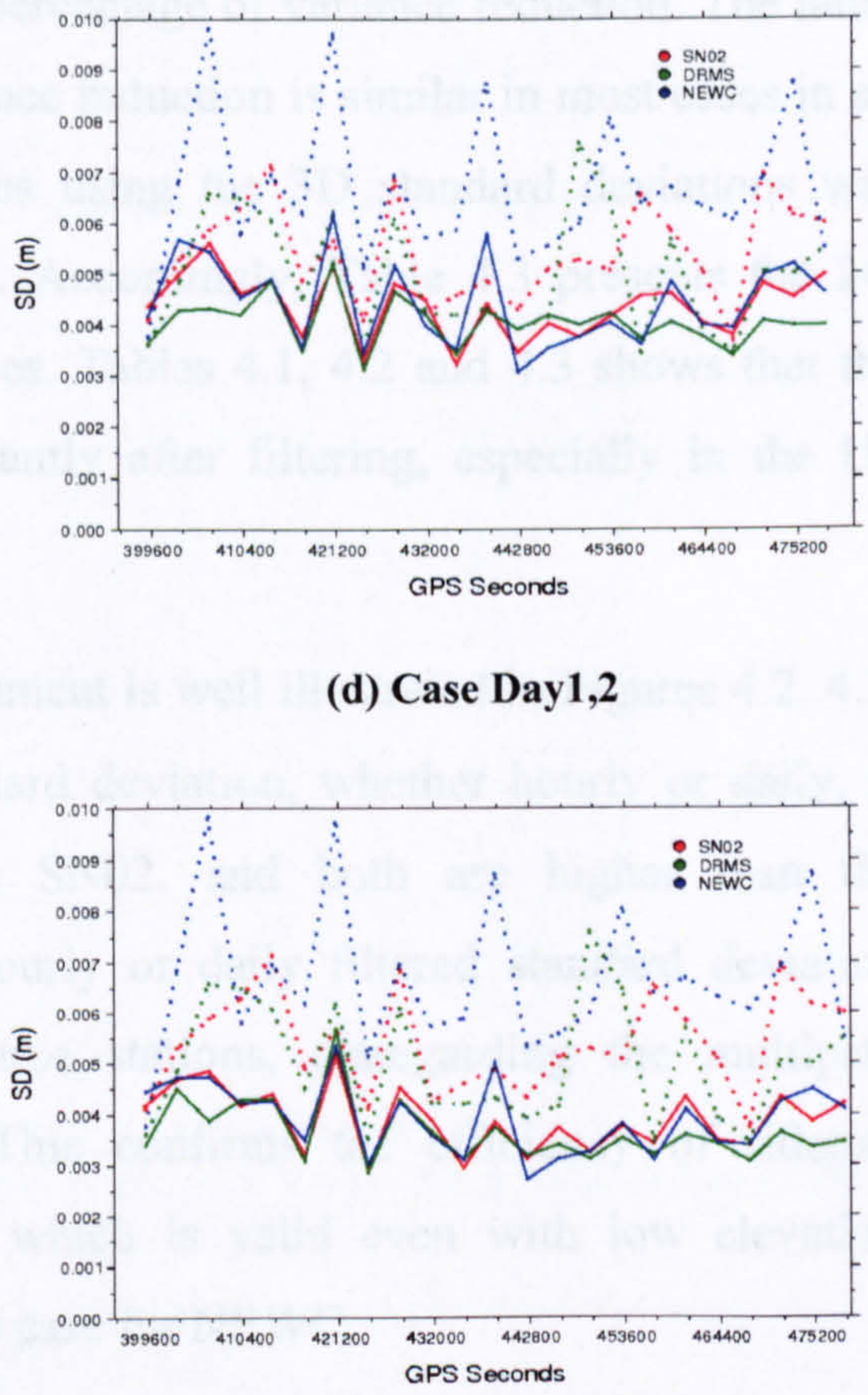

(d) Case Day1,2

(e) Case Day2,3

(f) Case Day1,2,3

Figure 4.4 Hourly Up coordinate standard deviations for all six cases based on coordinate filter. Line attributes as before.

deviation or multipath environment. The hour-to-hour consistency of the precision of the filtered coordinates again confirms what has been concluded from the previous chapter. Namely, the short-term variations in the optimum lag are relatively unimportant for sidereal filtering when adopting a double-differencing processing strategy. Note that the apparent periodicity in the Northing standard deviations in Figure 4.3 is mainly due to a satellite geometry effect.

Table 4.1 shows the Easting, Northing and Up coordinate standard deviation values over the entire applied fourth day for all six study cases against the unfiltered values, while Table 4.2 shows the corresponding percentage of variance reduction. The latter table indicates that the percentage of variance reduction is similar in most cases in all three directions for each station, and thus using the 3D standard deviations will represent the overall coordinate precision. Accordingly, Table 4.3 presents the 24-hour 3D standard deviation for all six cases. Tables 4.1, 4.2 and 4.3 shows that the daily standard deviation dropped significantly after filtering, especially in the Up coordinate component.

In addition, the effect of multipath environment is well illustrated in Figures 4.2, 4.3, 4.4 and Table 4.3, as the unfiltered standard deviation, whether hourly or daily, is almost always higher for NEWC than SN02, and both are higher than the corresponding values for DRMS. The hourly or daily filtered standard deviation decreases to a similar value for all three stations, disregarding the multipath environment surrounding each station. This confirms the efficiency of sidereal filtering using the optimum lag period, which is valid even with low elevation satellites and high multipath areas, as is the case for NEWC.

Utilizing the December_05 data set to verify the results obtained, the April_05 optimum lag value is used to stack the coordinate residuals and apply them on the fourth day of this data set for the six study cases to produce final filtered coordinates. Following this the hourly and daily standard deviations were calculated. Figure 4.5 illustrates the hourly 3D standard deviation for all six study cases, each containing the three applied stations. A more detailed hourly Easting, Northing and Up standard deviation plots are shown in Figures D.1, D.2 and D.3 respectively in Appendix D.

Table 4.1 24-hour coordinate standard deviations in three directions for all six cases based on the coordinate filter for the April_05 data set.

Station	SD (mm)	CASE						
		Unfiltered	Day1	Day2	Day3	Day1,2	Day2,3	Day1,2,3
SN02	E	2.3	1.9	1.9	1.8	1.6	.1.6	1.5
	N	3.3	3.0	2.9	2.8	2.6	2.5	2.4
	U	5.6	5.1	4.8	4.7	4.3	4.2	4.0
DRMS	E	1.9	1.7	1.7	1.6	1.5	1.5	1.4
	N	3.3	2.7	2.7	2.6	2.4	2.4	2.3
	U	5.3	4.6	4.4	4.4	4.0	3.9	3.7
NEWC	E	2.9	1.9	1.9	1.8	1.7	1.6	1.5
	N	4.3	3.0	2.9	2.7	2.5	2.5	2.3
	U	8.0	5.2	4.9	4.8	4.4	4.3	4.0

Table 4.2 24-hour variance reduction in three directions for all six cases based on the coordinate filter for the April_05 data set.

Station	δ (%)	CASE					
		Day1	Day2	Day3	Day1,2	Day2,3	Day1,2,3
SN02	E	31.8	31.8	38.8	51.6	51.6	57.5
	N	17.4	22.8	28.0	37.9	42.6	47.1
	U	17.1	26.5	29.6	41.0	43.8	49.0
DRMS	E	19.9	19.9	29.1	37.7	37.7	45.7
	N	33.1	33.1	37.9	47.1	47.1	51.4
	U	24.7	31.1	31.1	43.0	45.9	51.3
NEWC	E	57.1	57.1	61.5	65.6	69.6	73.2
	N	51.3	54.5	60.6	66.2	66.2	71.4
	U	57.8	62.5	64.0	69.8	71.1	75.0

Table 4.3 3D coordinate standard deviations over a 24-hour period for all six cases based on the coordinate filter.

Station	3D SD (mm) / CASE						
	Unfiltered	Day1	Day2	Day3	Day1,2	Day2,3	Day1,2,3
SN02	6.9	6.2	6.0	5.8	5.3	5.1	4.9
DRMS	6.5	5.6	5.4	5.3	4.9	4.8	4.6
NEWC	9.5	6.3	6.0	5.8	5.3	5.2	4.9

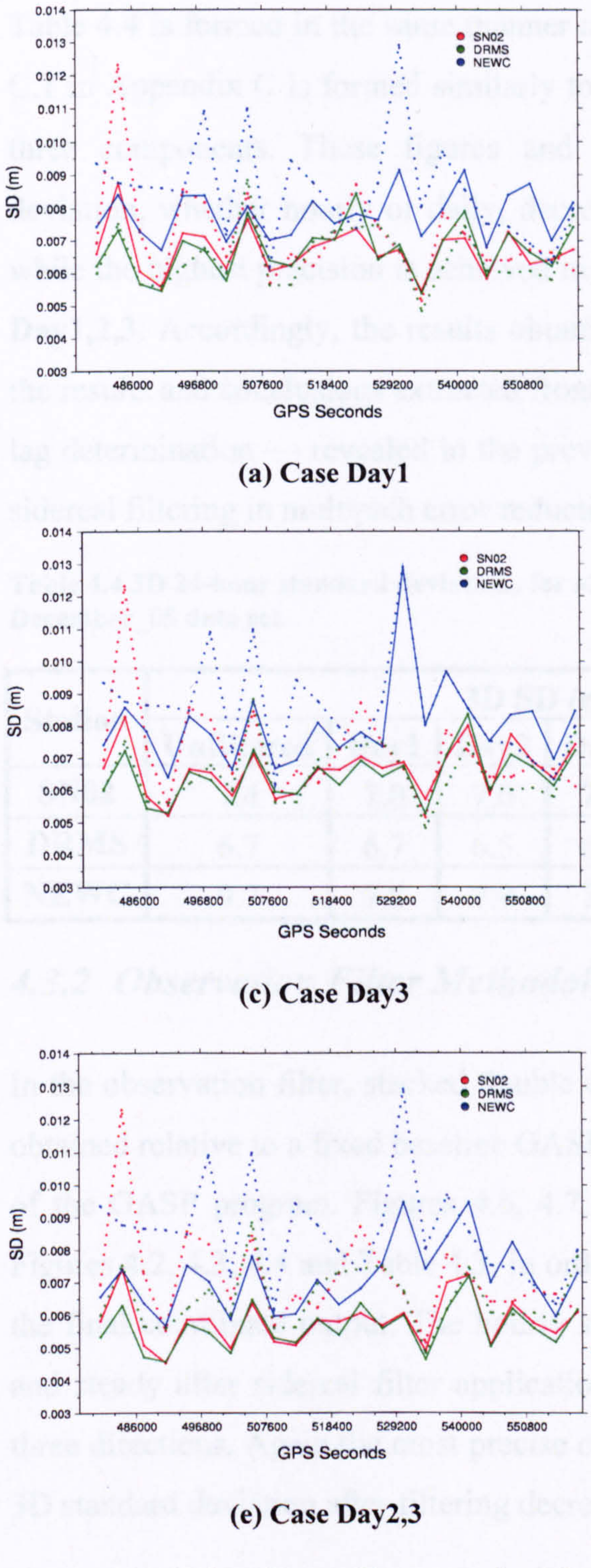

(a) Case Day1

(b) Case Day2

(c) Case Day3

(d) Case Day1,2

(e) Case Day2,3

(f) Case Day1,2,3

Figure 4.5 3D hourly coordinate standard deviations for all six cases based on the coordinate filter for the December_05 data set. Line attributes as before.

Table 4.4 is formed in the same manner as Table 4.3, while the comprehensive Table C.1 in Appendix C is formed similarly to Table 4.1 for the standard deviations of all three components. These figures and tables indicate that the filtered standard deviation, whether hourly or daily, decreases after filtering over the whole data set, while the highest precision is achieved in the case of stacking three days together, i.e. **Day1,2,3**. Accordingly, the results obtained from the December_05 data set validate the results and conclusions extracted from the April_05 data set regarding the sidereal lag determination — revealed in the previous chapter — as well as the robustness of sidereal filtering in multipath error reduction.

Table 4.4 3D 24-hour standard deviations for all six cases based on the coordinate filter for the December_05 data set.

Station	3D SD (mm) / CASE						
	Unfiltered	Day1	Day2	Day3	Day1,2	Day2,3	Day1,2,3
SN02	7.4	7.0	7.0	7.2	6.2	6.1	5.8
DRMS	6.7	6.7	6.5	6.5	5.8	5.6	5.4
NEWC	9.7	7.8	7.9	7.7	7.0	7.2	6.6

4.3.2 Observation Filter Methodology

In the observation filter, stacked double difference L1 and L2 carrier phase residuals obtained relative to a fixed baseline GASP solution are applied during a normal re-run of the GASP program. Figures 4.6, 4.7, 4.8 and Table 4.5 are formed similarly to Figures 4.2, 4.3, 4.4 and Table 4.3, in order to show the effect of this methodology on the final coordinate output. The hourly standard deviation tends to be homogeneous and steady after sidereal filter application over almost the whole applied day in all three directions. Again the most precise case is for stacking 3 days, when the 24-hour 3D standard deviation after filtering decreases significantly.

Moreover, from Figures 4.2 to 4.8, some peaks do exist in the filtered standard deviation in one or two directions. This could be attributed to the fact that the coordinates of some epochs within any hour may be off the optimum value by about 1 or 2 cm, and thus cannot be entirely excluded as outliers prior to filtering and should be taken into consideration. However, this will cause these undesirable peaks which affect the homogeneity of the standard deviation of the filtered applied day. Again,

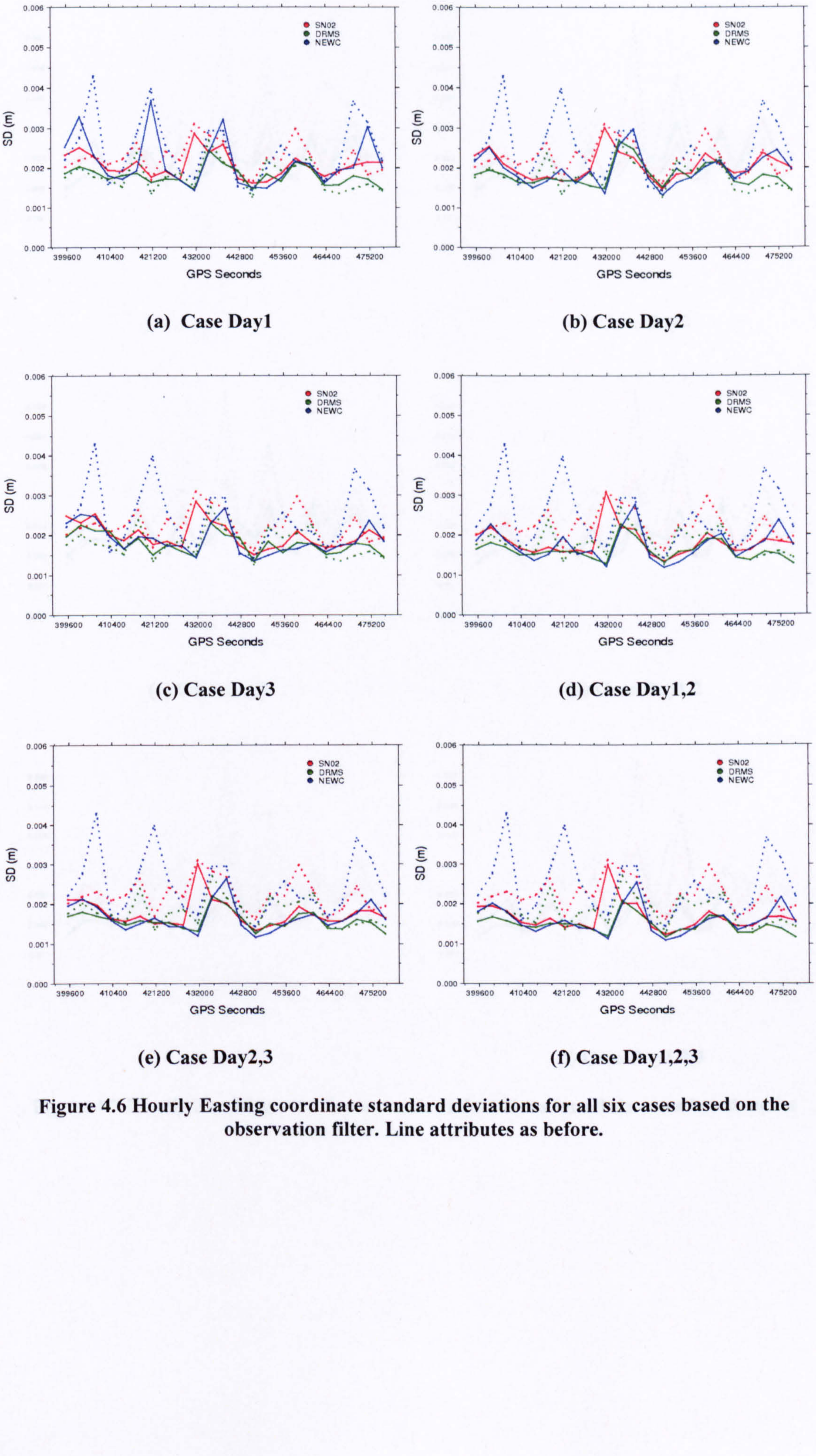

(a) Case Day1

(b) Case Day2

(c) Case Day3

(d) Case Day1,2

(e) Case Day2,3

(f) Case Day1,2,3

Figure 4.6 Hourly Easting coordinate standard deviations for all six cases based on the observation filter. Line attributes as before.

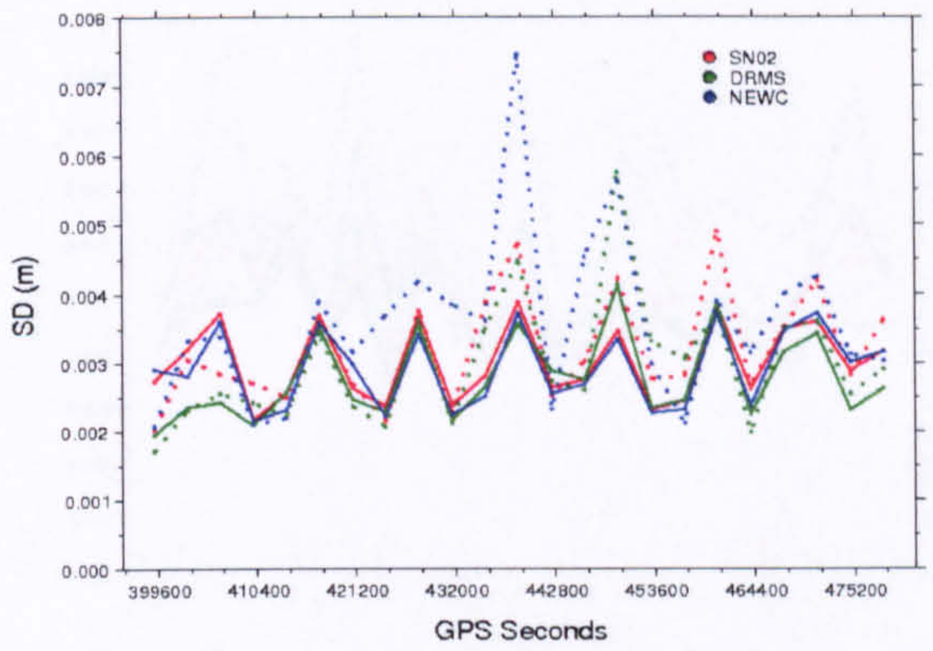

(a) Case Day1

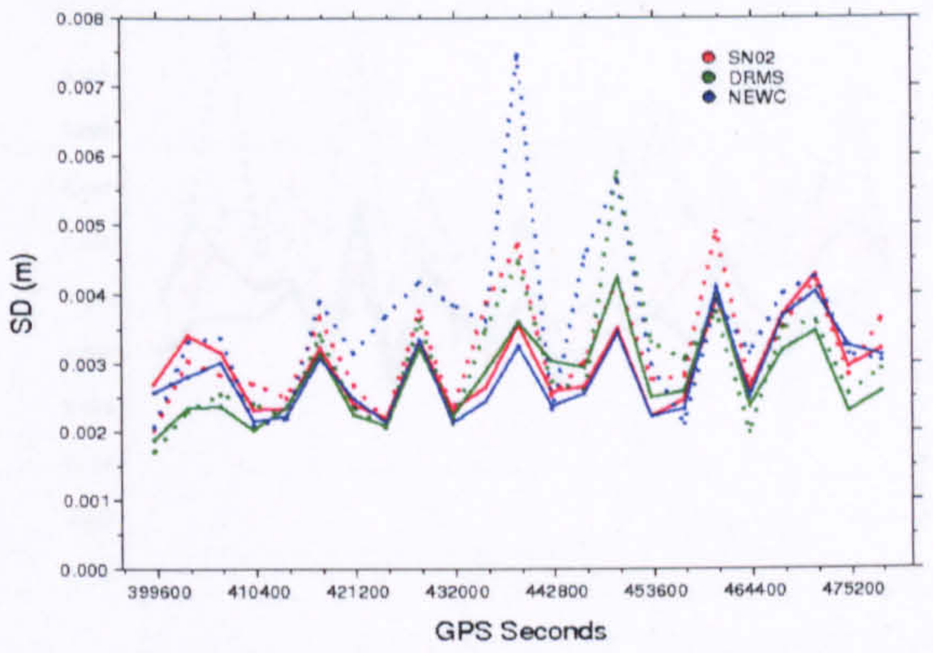

(b) Case Day2

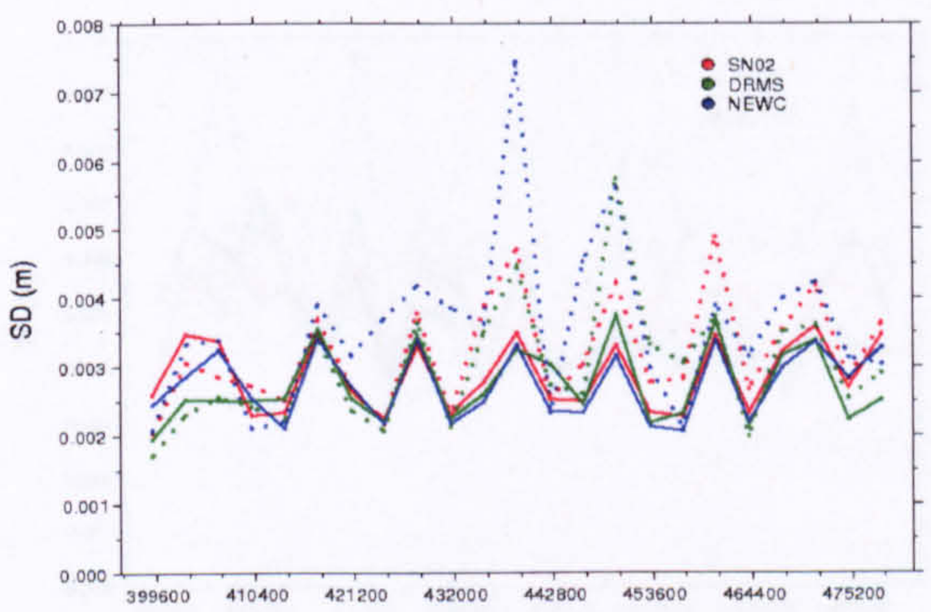

(c) Case Day3

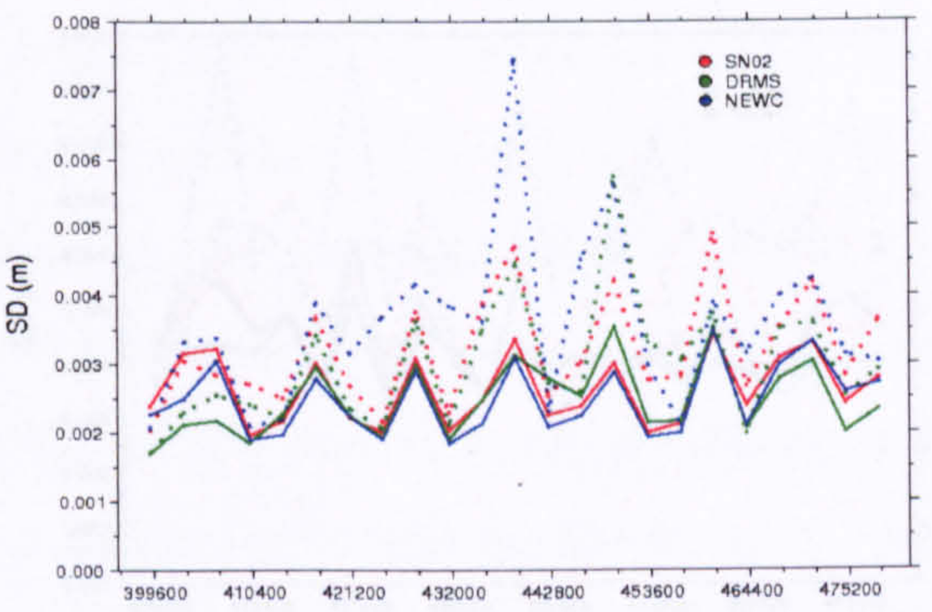

(d) Case Day1,2

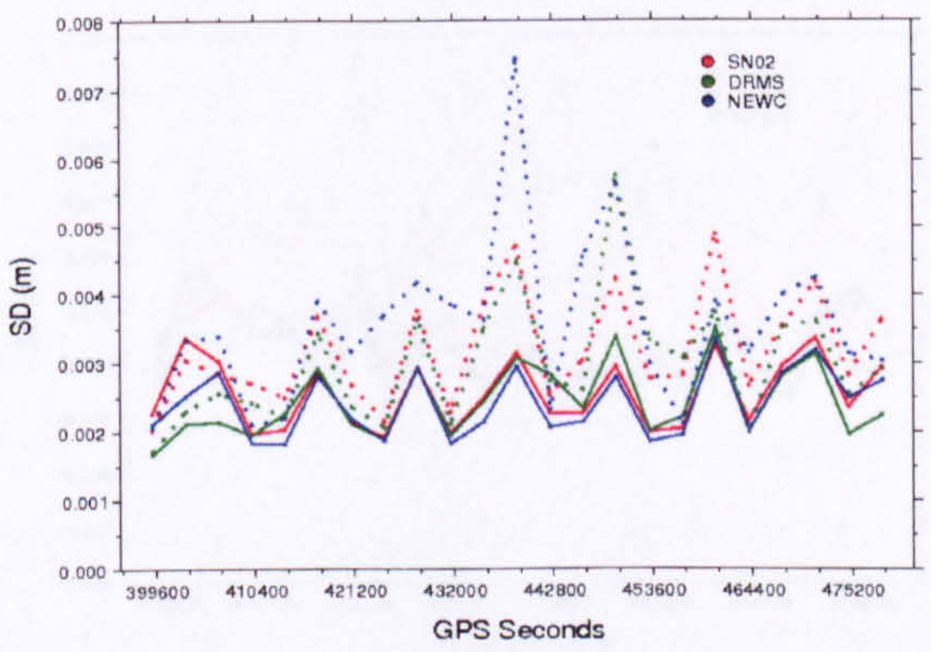

(e) Case Day2,3

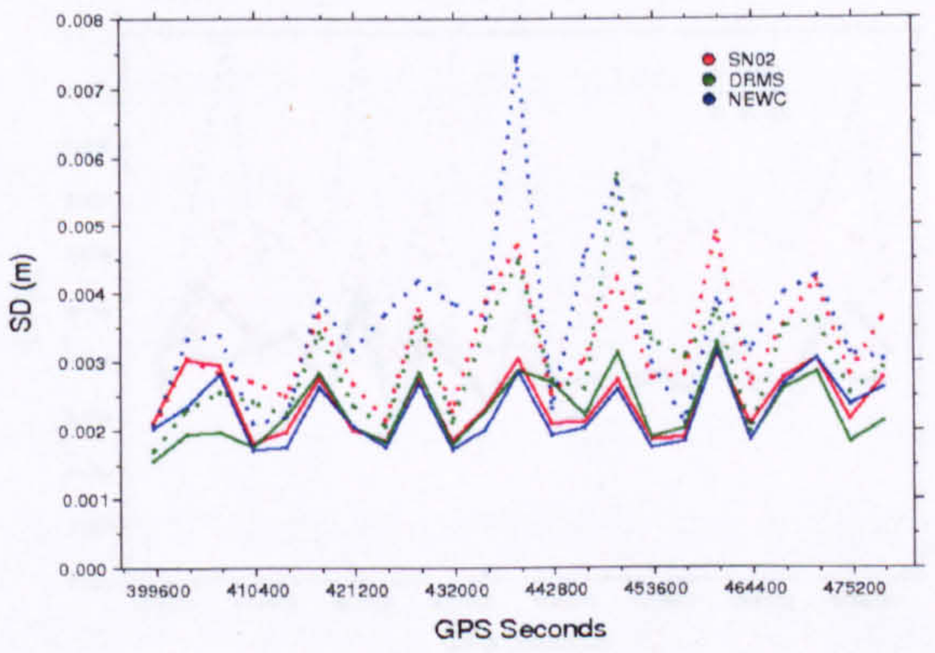

(f) Case Day1,2,3

Figure 4.7 Hourly Northing coordinate standard deviations for all six cases based on the observation filter. Line attributes as before.

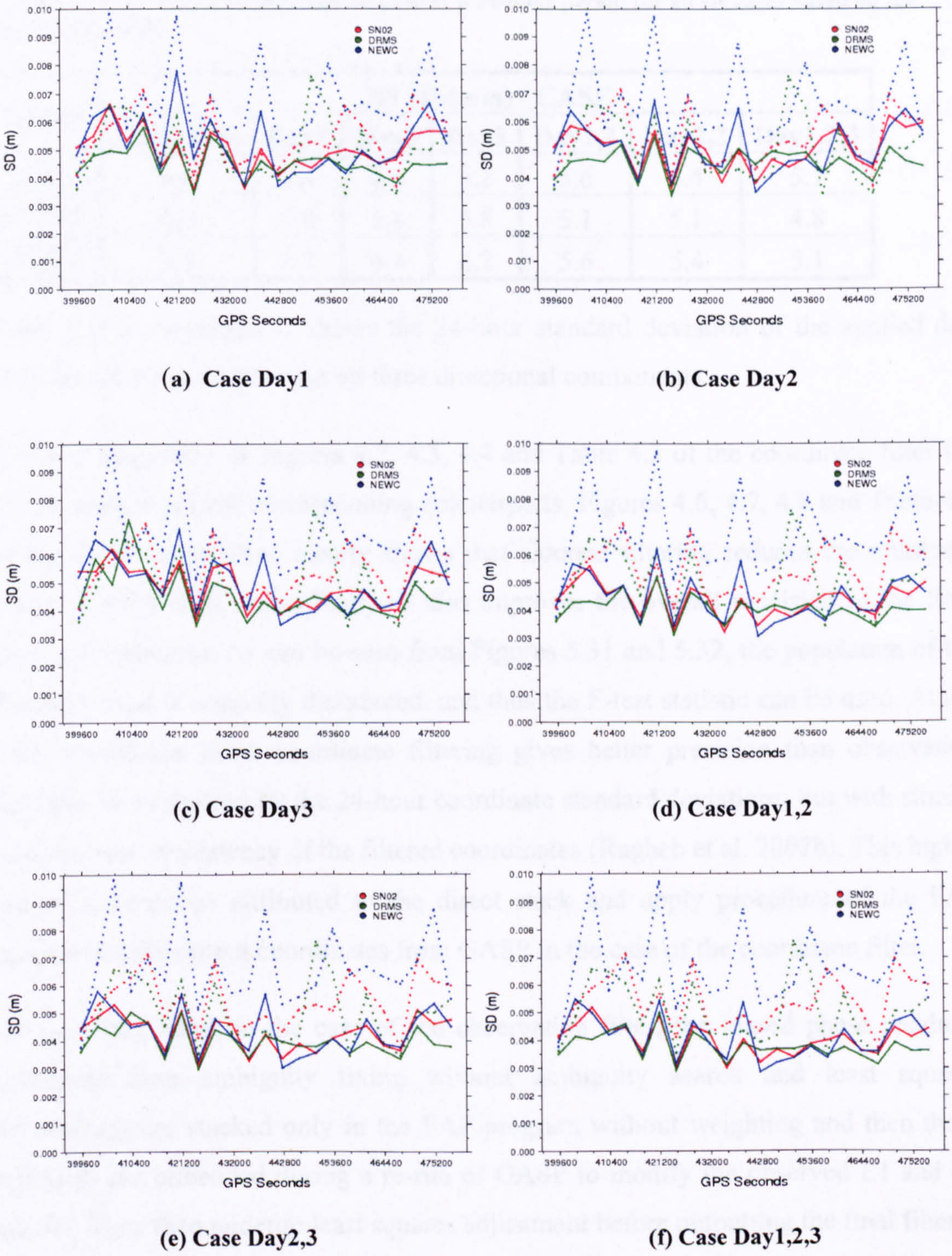

(a) Case Day1

(b) Case Day2

(c) Case Day3

(d) Case Day1,2

(e) Case Day2,3

(f) Case Day1,2,3

Figure 4.8 Hourly Up coordinate standard deviations for all six cases based on the observation filter. Line attributes as before.

Table 4.5 3D 24-hour standard deviation over a 24-hour period for all six cases based on the observation filter.

Station	3D SD (mm) / CASE						
	Unfiltered	Day1	Day2	Day3	Day1,2	Day2,3	Day1,2,3
SN02	6.9	6.4	6.4	6.2	5.6	5.4	5.1
DRMS	6.5	5.8	5.8	5.8	5.1	5.1	4.8
NEWC	9.5	6.7	6.4	6.2	5.6	5.4	5.1

Table C.2 in Appendix C shows the 24-hour standard deviation of the applied day after the observation filter for all three directional components.

A closer inspection of Figures 4.2, 4.3, 4.4 and Table 4.3 of the coordinate filter for all six cases and their corresponding counterparts, Figures 4.6, 4.7, 4.8 and Table 4.5 of the observation filter, clearly shows that sidereal filtering reduces the multipath effect on GPS data. Accordingly, it also improves the overall precision of the final station coordinates. As can be seen from Figures 5.31 and 5.32, the population of the data sets used is normally distributed, and thus the F-test statistic can be used. At the 95% confidence limit, coordinate filtering gives better precision than observation filtering, as evidenced by the 24-hour coordinate standard deviations, but with similar hour-to-hour consistency of the filtered coordinates (Ragheb et al. 2007b). This higher precision could be attributed to the direct stack and apply procedure of the FAP program on the output coordinates from GASP in the case of the coordinate filter.

On the other hand, in the case of the observation filter, the biased phase residuals (obtained from ambiguity fixing without ambiguity search and least squares adjustment) are stacked only in the FAP program without weighting and then those residuals are imbedded during a re-run of GASP to modify the observed L1 and L2 phases. They then undergo least squares adjustment before outputting the final filtered coordinates. In this latter methodology, some errors due to unweighted averaging of biased residuals propagate into the solution before reaching the final outcome, causing a relatively lower precision compared to the first methodology. However, the homogeneities of the hourly coordinate-filtered and observation-filtered coordinate standard deviations (i.e. the variances of the hourly coordinate variances) cannot be distinguished using the F-test statistic with 95% confidence (similar hour-to-hour

consistency), while both are more homogeneous and significant when compared to the unfiltered hourly standard deviations. In other words, either method results in a coordinate time series with more uniform noise characteristics than the unfiltered series, but the degree of uniformity is similar in both filtered cases.

Yet again, confirming all previous results and conclusions, the χ^2 statistic can be extracted from the least squares adjustment results of the GASP re-run in the case of the observation filter through the following expression:

$$\chi^2(v,\sigma)=V^T WV\,, \qquad 4.2$$

where V is the vector of double difference residuals (v) for all satellite pairings in each epoch, while W is the weight matrix of the double difference phase observables, given as a function of the observables formal errors σ. Figures 4.9 and 4.10 illustrates the improvement in the hourly χ^2 mean value and standard deviation after filtering for all six study cases respectively, where they both became more homogeneous after filtering. Once more for verification purposes, Figures D.4, D.5 and D.6 in Appendix D together with Figure 4.11, Table 4.6 and Table C.3 in Appendix C are formed similarly to Figures D.1, D.2, D.3, 4.5, Table 4.4 and Table C.1 respectively, for the application of observation filter methodology using the December_05 data set. From these figures and tables, the same conclusions can be extracted.

4.3.3 Comparison of Computational Efficiency

As previously stated and proven statistically, the coordinate filter gives higher precision than the observation filter. However, one area in which the observation filter is clearly superior is in the CPU time required for filter generation and application. In coordinate filtering (considering the case of stacking 3 days using the April_05 data set **Day1,2,3**), GASP is run once with ambiguity search and least squares adjustment, to output unfiltered coordinates for each of the three "reference" days. This is followed by the stacking of the coordinate residuals in FAP and the application of the filter to the fourth day.

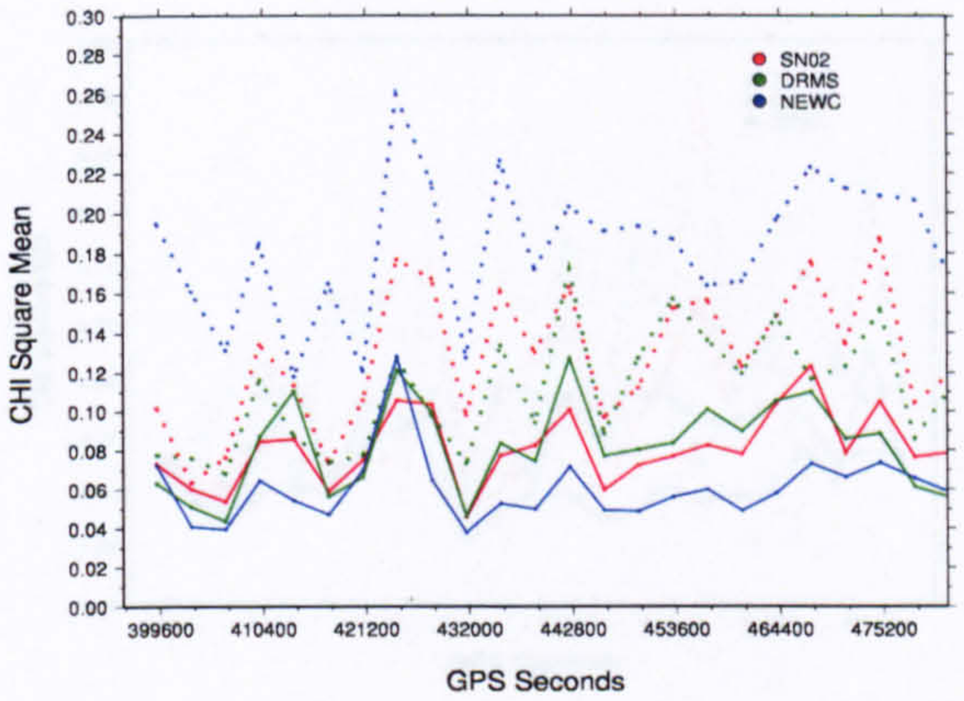

(a) Case Day1

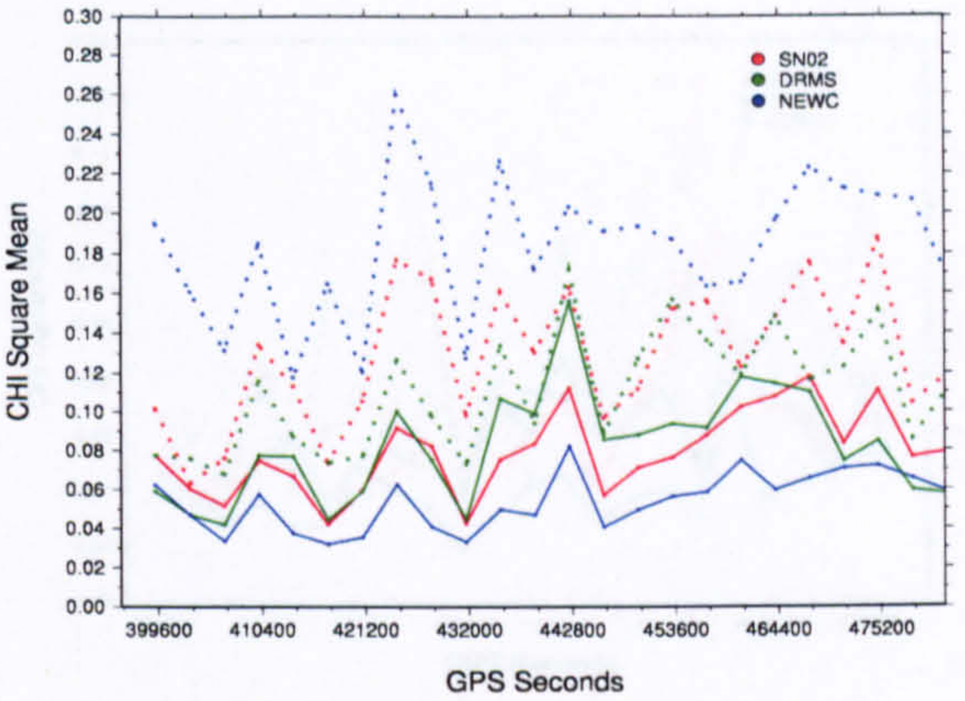

(b) Case Day2

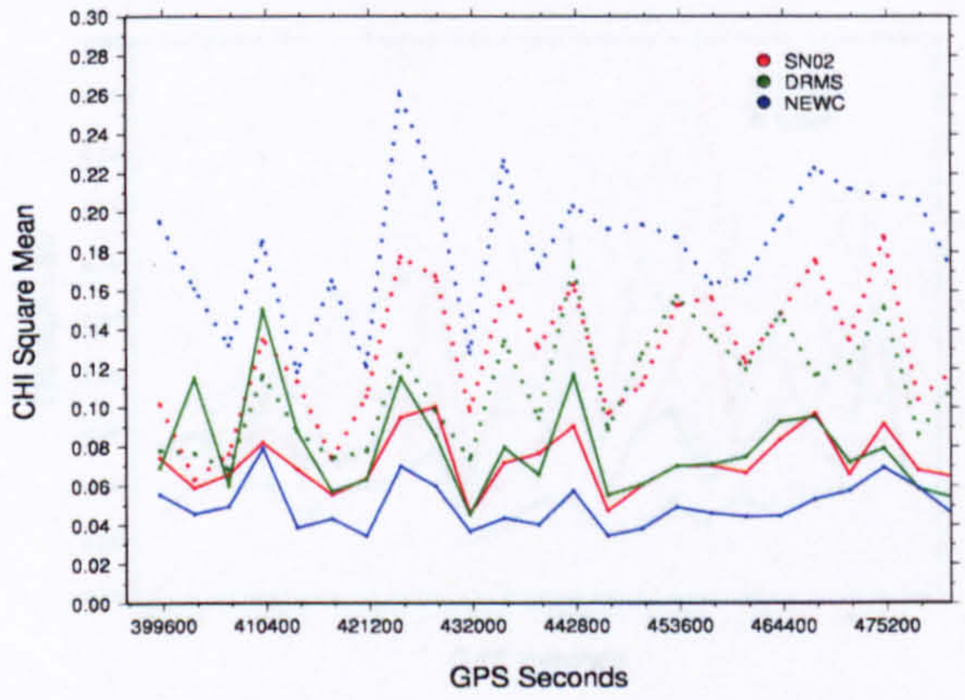

(c) Case Day3

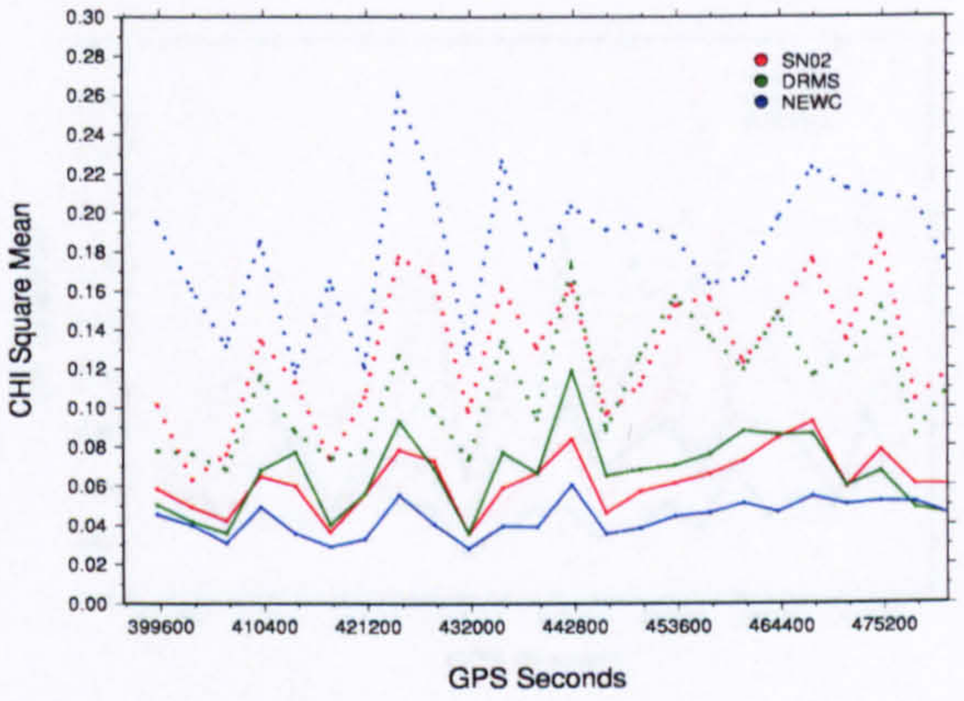

(d) Case Day1,2

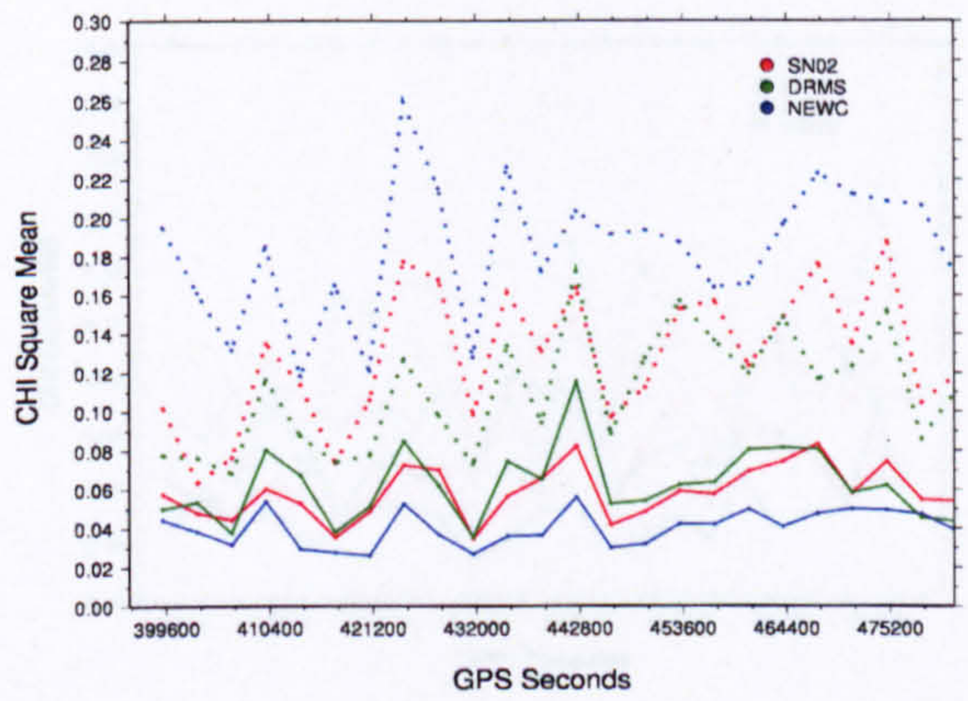

(e) Case Day2,3

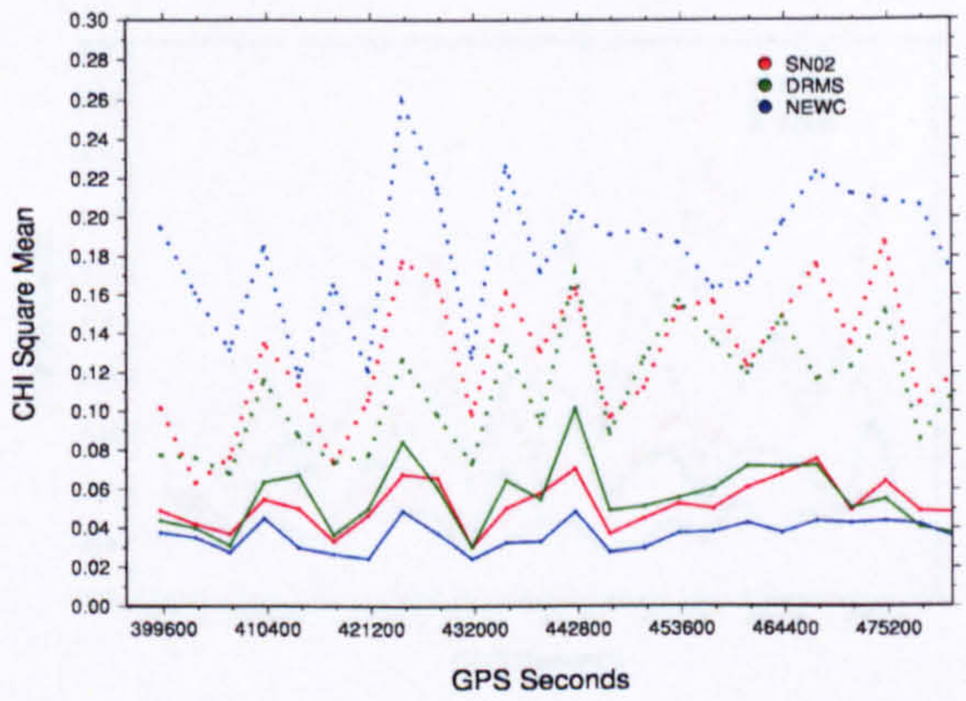

(f) Case Day1,2,3

Figure 4.9 Hourly χ^2 mean values for all six cases based on the observation filter. Line attributes as before.

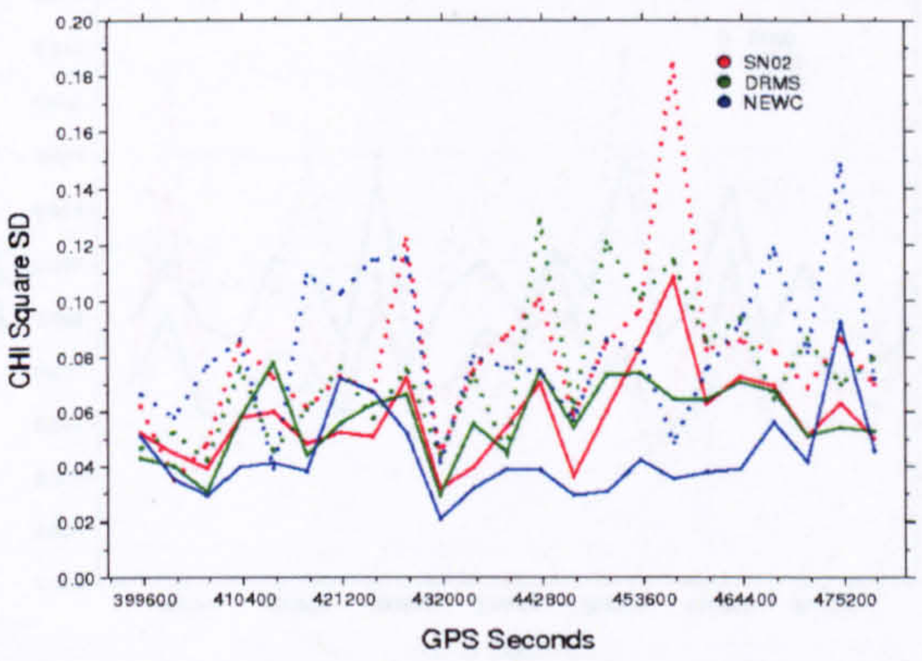

(a) Case Day1

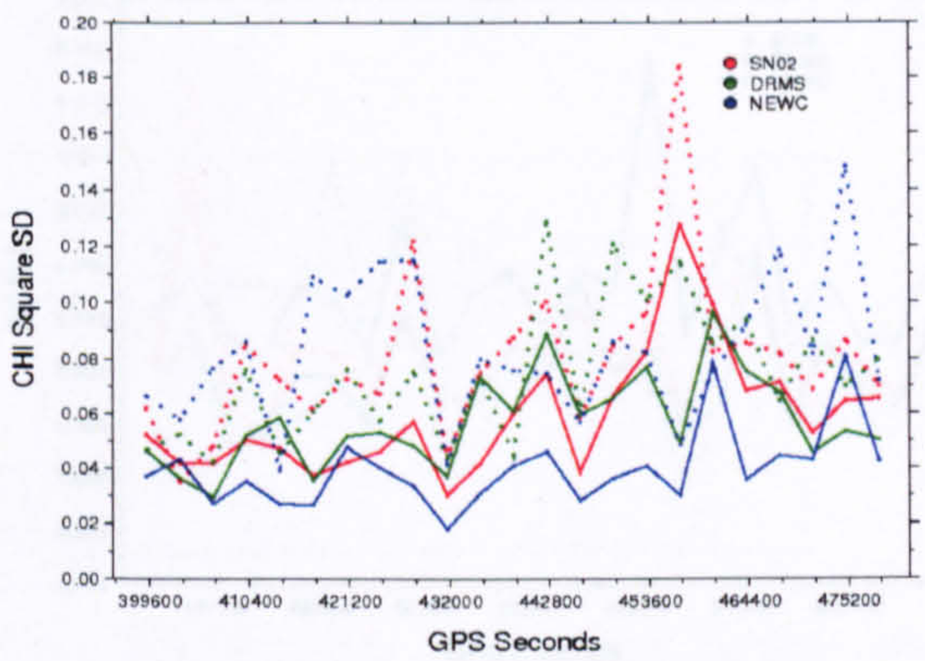

(b) Case Day2

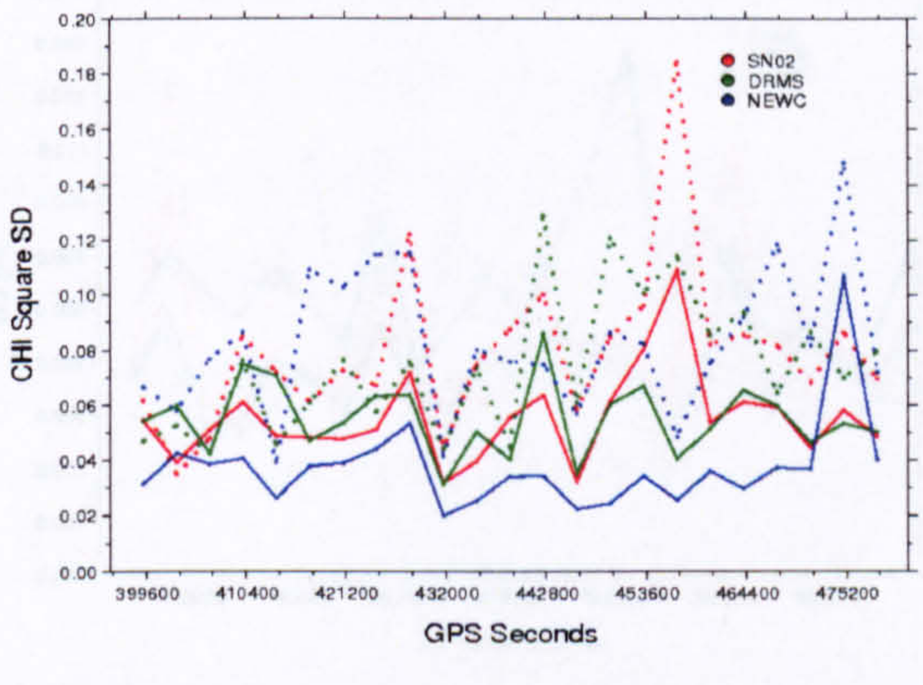

(c) Case Day3

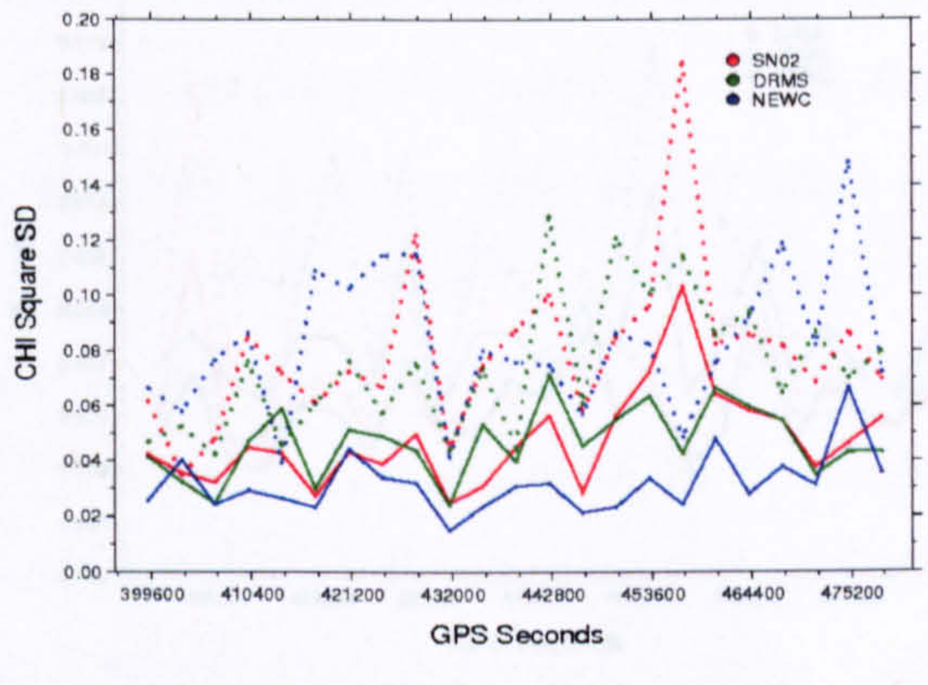

(d) Case Day1,2

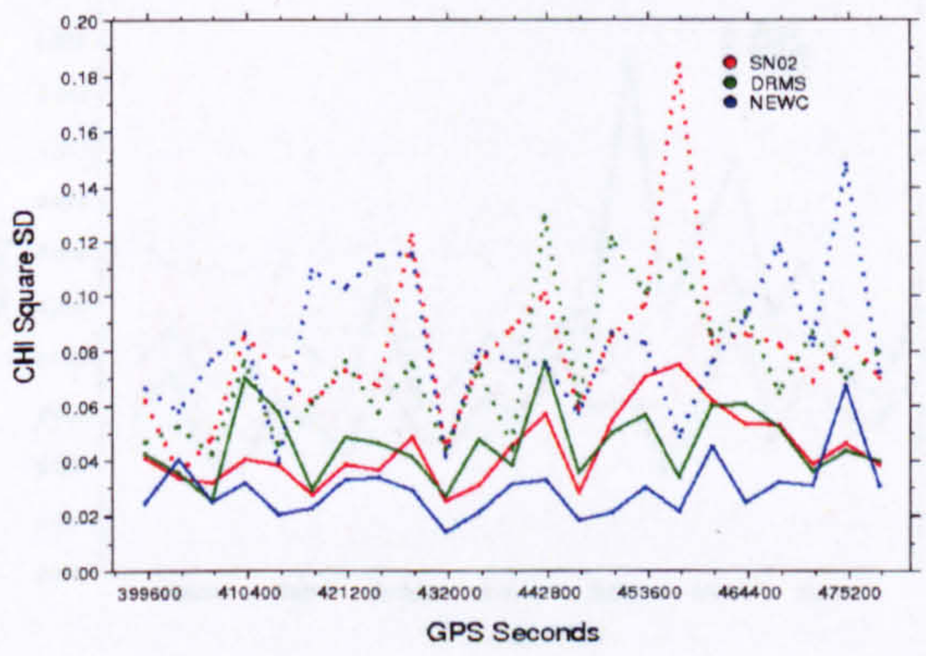

(e) Case Day2,3

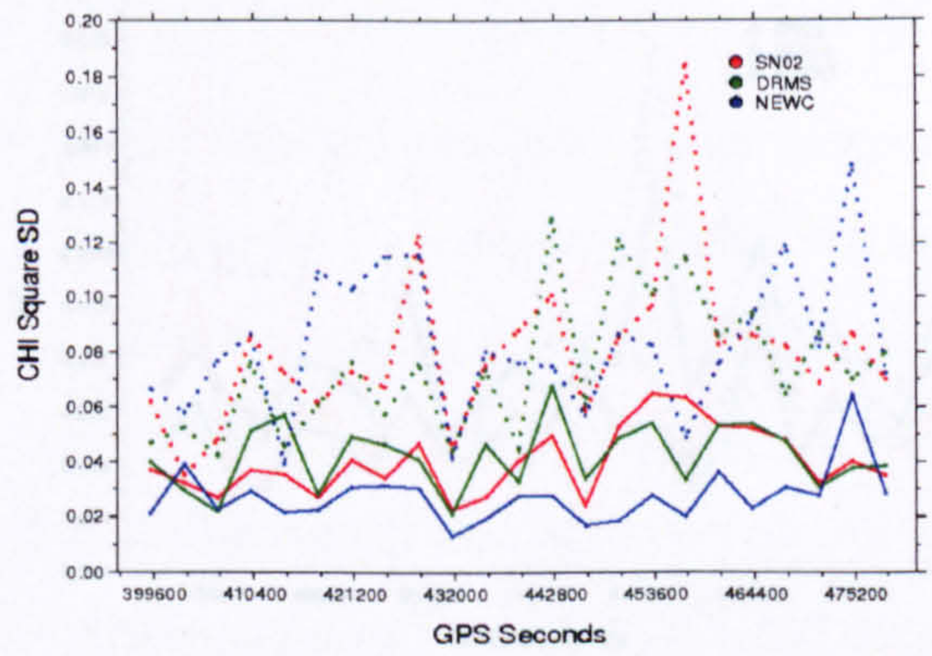

(f) Case Day1,2,3

Figure 4.10 Hourly χ^2 standard deviations for all six cases based on the observation filter. Line attributes as before.

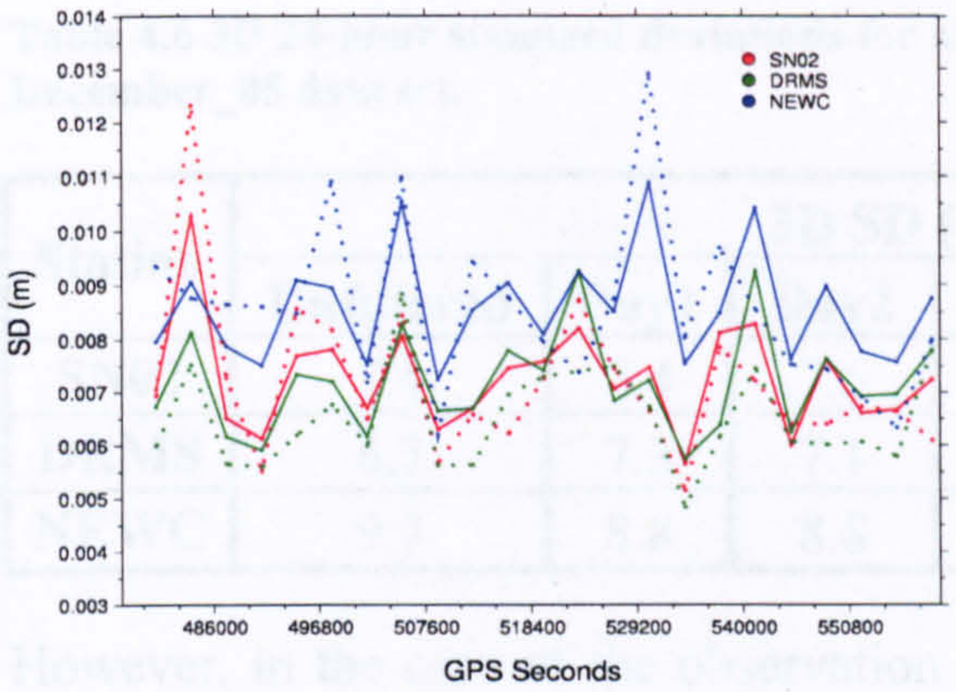

(a) Case Day1

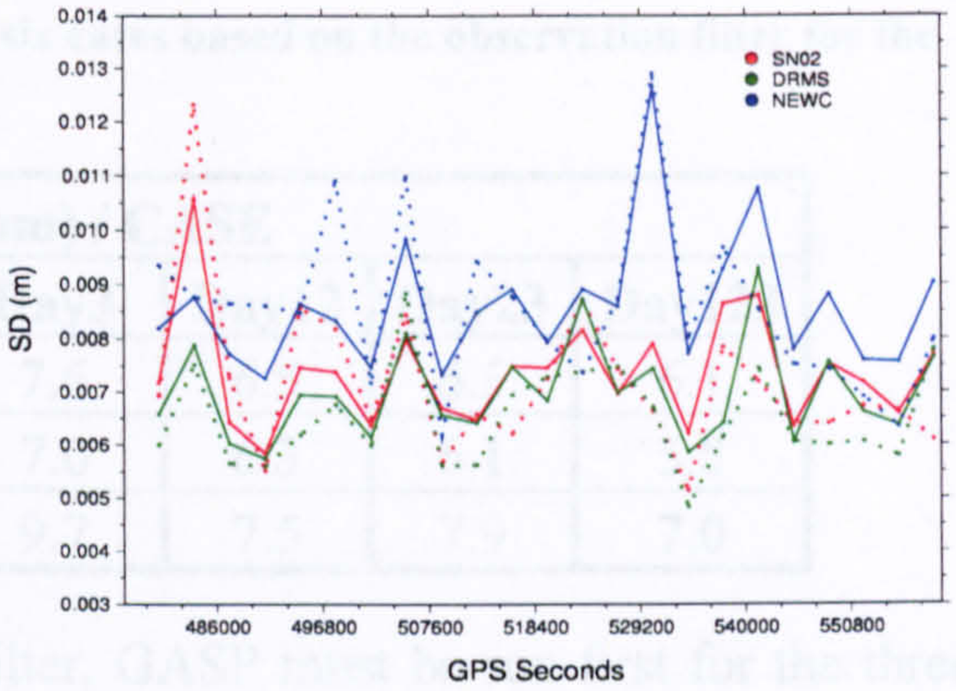

(b) Case Day2

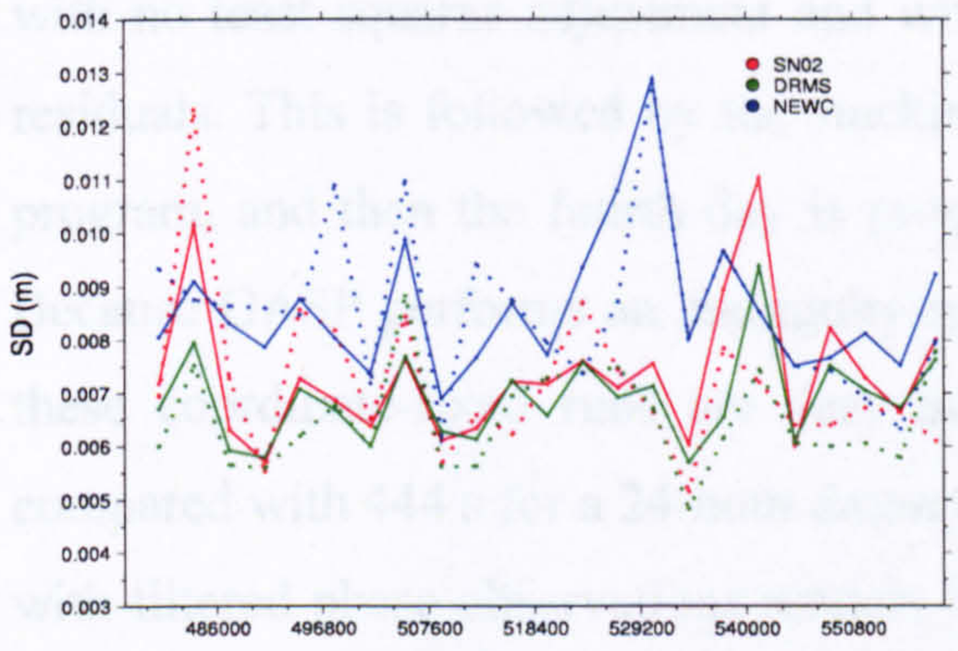

(c) Case Day3

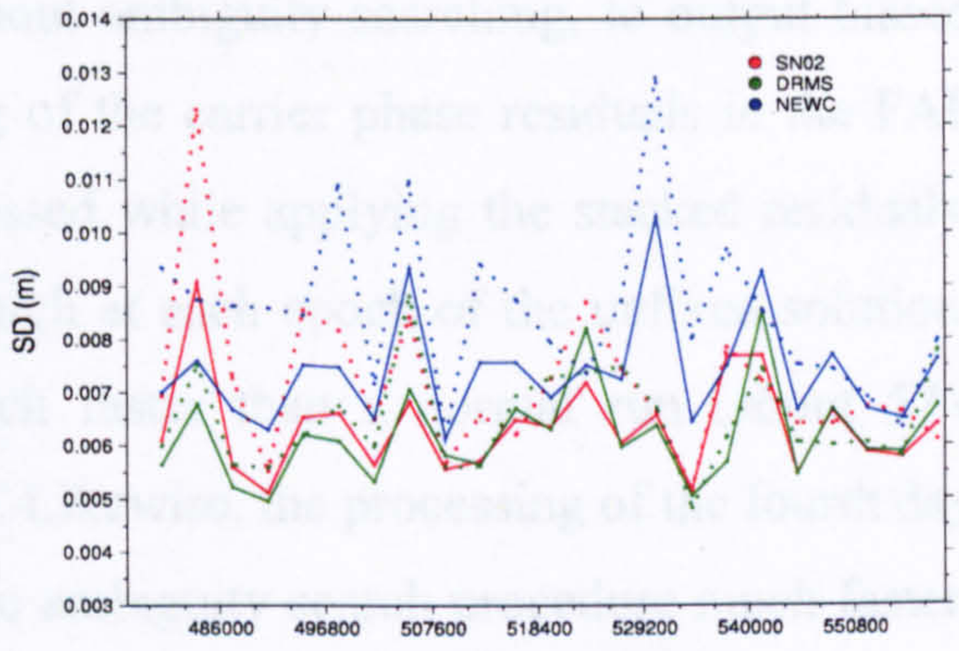

(d) Case Day12

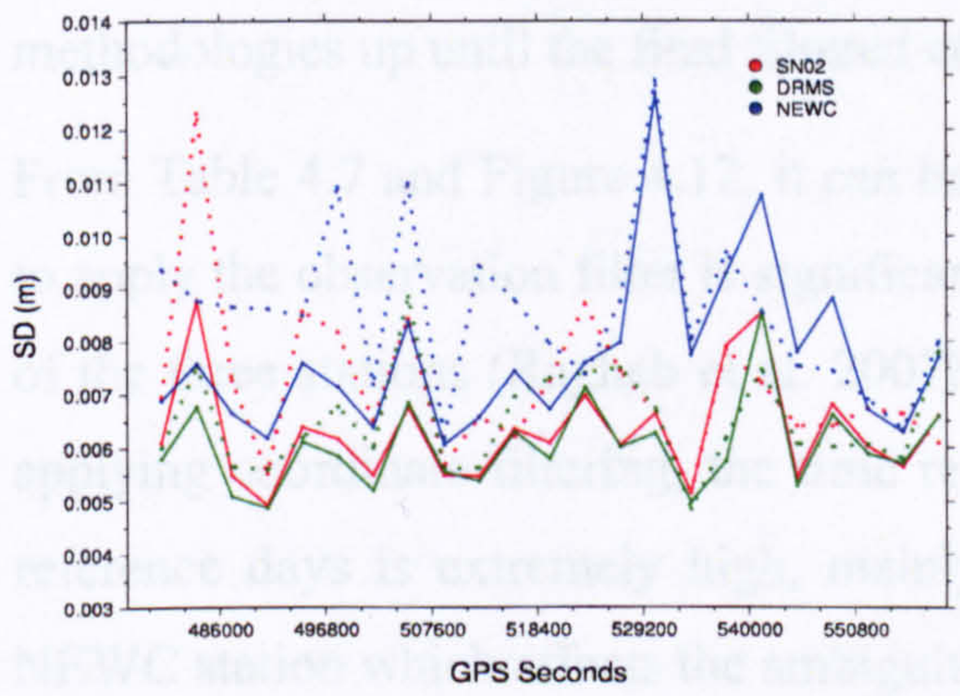

(e) Case Day23

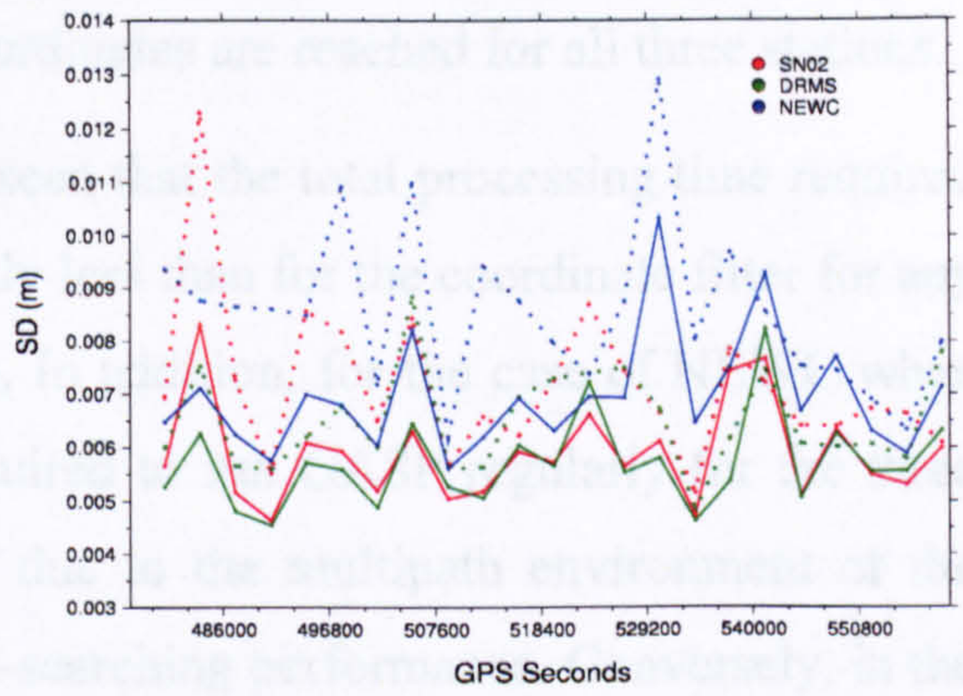

(f) Case Day123

Figure 4.11 3D hourly coordinate standard deviations for all six cases based on the observation filter for the December_05 data set. Line attributes as before.

Table 4.6 3D 24-hour standard deviations for all six cases based on the observation filter for the December_05 data set.

Station	3D SD (mm) / CASE						
	Unfiltered	Day1	Day2	Day3	Day12	Day23	Day123
SN02	7.4	7.4	7.6	7.6	6.5	6.5	6.1
DRMS	6.7	7.3	7.1	7.0	6.3	6.1	5.8
NEWC	9.7	8.8	8.8	9.7	7.5	7.9	7.0

However, in the case of the observation filter, GASP must be run first for the three "reference" days using fixed baseline coordinates, while fixing the ambiguities but with no least squares adjustment and without ambiguity searching, to output biased residuals. This is followed by the stacking of the carrier phase residuals in the FAP program, and then the fourth day is processed while applying the stacked residuals. Because GASP performs an ambiguity search at each epoch of the unfixed solution, these coordinate-fixed runs are very much faster than a normal run (about 57 s compared with 444 s for a 24-hour dataset). Likewise, the processing of the fourth day with filtered phase observations renders the ambiguity search procedure much faster, because acceptable ambiguity values are found within a smaller search volume. Table 4.7 and Figure 4.12 illustrate the times required for each phase of both filtering methodologies up until the final filtered coordinates are reached for all three stations.

From Table 4.7 and Figure 4.12, it can be seen that the total processing time required to apply the observation filter is significantly less than for the coordinate filter for any of the three stations (Ragheb et al. 2007b). In addition, for the case of NEWC when applying coordinate filtering, the time required to run GASP regularly for the three reference days is extremely high, mainly due to the multipath environment of the NEWC station which affects the ambiguity-searching performance. Conversely, in the case of observation filtering, the processing time required to produce final filtered coordinates is almost the same for all three stations regardless of their multipath environment. Again, this confirms the usefulness of sidereal observation filtering to reduce the ambiguity search time during the GASP re-run, even in a high multipath environment.

Note that, although an independent epoch-by-epoch algorithm such as GASP represents an extreme case of computation time reduction, the observation filter

Table 4.7 GASP processing times for each step of both filtering methods for all three stations on a Linux workstation.

Method	Procedure	SN02	DRMS	NEWC
Coordinate Filter	**3 Days processing**	22m 12s	19m 54s	42m 24s
	Processing 4th day and filter application	7m 32s	6m 40s	14m 33s
	Total Time	**29m 44s**	**26m 34s**	**56m 57s**
Observation Filter	**3 Days processing**	2m 51s	2m 59s	2m 36s
	Processing 4th day and filter application	7m 08s	7m 08s	6m 26s
	Total Time	**09m 59s**	**10m 07s**	**09m 02s**

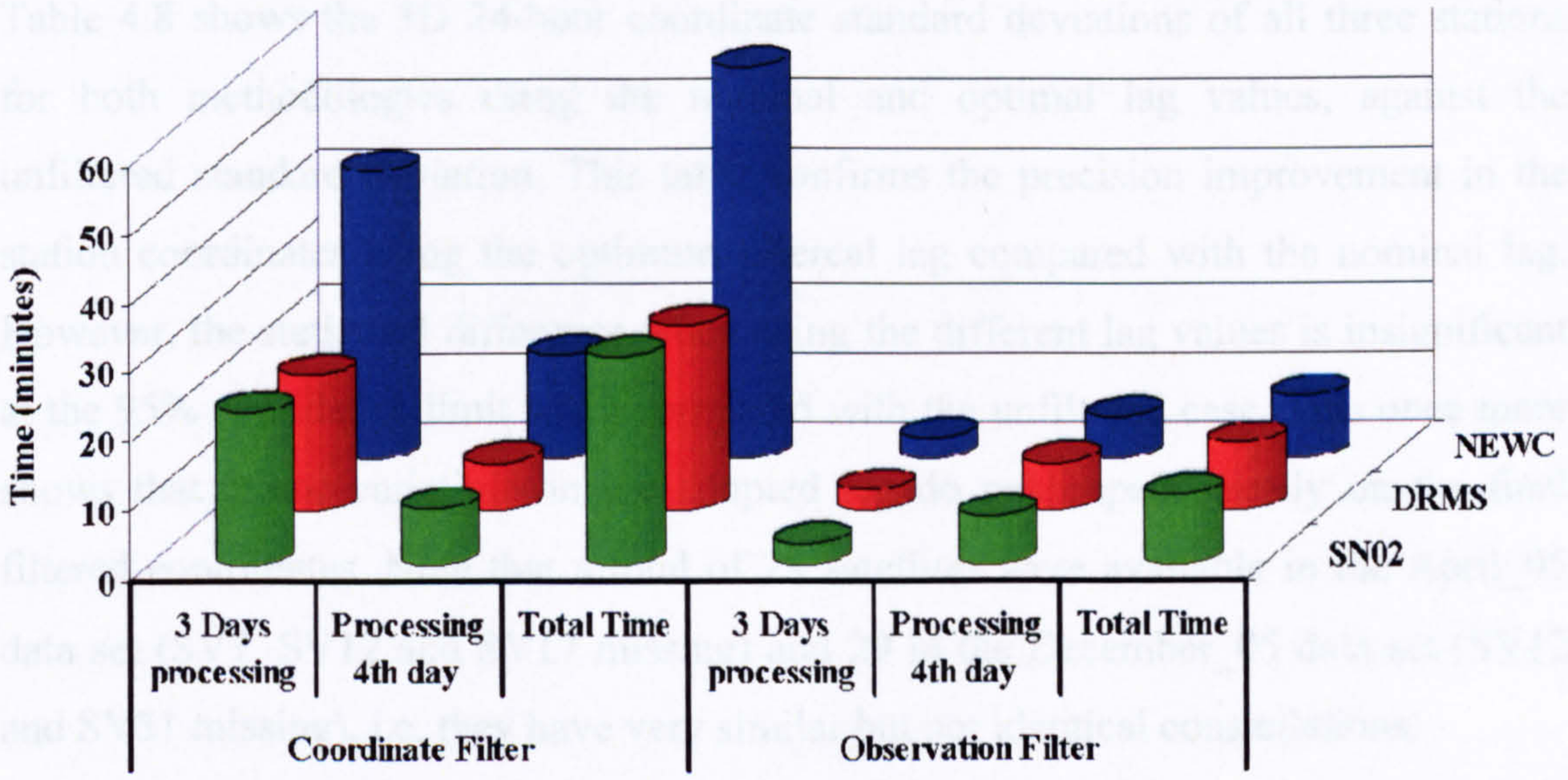

Figure 4.12 A bar chart showing GASP processing times on a Linux workstation for each step of both filtering methods for all three stations.

approach will reduce processing effort to some extent for non epoch-by-epoch methods. This is particularly true in high multipath and reduced-visibility environments, where frequent loss of lock can be expected. As a final remark, the decision whether to use the more precise and homogeneous methodology of coordinate filtering, which takes longer time (especially if an epoch-by-epoch ambiguity searching algorithm is used), or observation filtering with reduced precision, depends on whether coordinate precision or computational time is the over-riding criterion.

4.3.4 Effect of Sidereal Lag Variation

In Chapter 3, it was concluded that slight changes in the optimum value of the lag, or even the use of a constant value, will not affect the efficiency of sidereal filtering, especially for double difference processing. Hence, another important use of the December_05 data set is to prove this conclusion statistically. Coordinate and carrier phase residuals were stacked in 3-day batches, once using the nominal lag of 23h 56m 04s (86164s) and then using the optimal lag of 23h 55m 54s (86154s). These stacked residuals were then applied to the fourth day, from which the 3D coordinate standard deviations could be computed.

Table 4.8 shows the 3D 24-hour coordinate standard deviations of all three stations for both methodologies using the nominal and optimal lag values, against the unfiltered standard deviation. This table confirms the precision improvement in the station coordinates using the optimum sidereal lag compared with the nominal lag. However, the statistical difference when using the different lag values is insignificant at the 95% confidence limit when compared with the unfiltered case. This once more shows that minor variations in the adopted lag do not impact greatly on the final filtered coordinates. Note that a total of 28 satellites were available in the April_05 data set (SV7, SV12 and SV17 missing) and 29 in the December_05 data set (SV12 and SV31 missing), i.e. they have very similar but not identical constellations.

Table 4.8 3D coordinate standard deviations over a 24-hour period, for both methodologies over different lags for the December_05 data set (3-day filter stacking).

Station	3D SD (mm) / Lag / Methodology				
	Unfiltered	23h 55m 54s (Optimal Lag)		23h 56m 04s (Nominal Lag)	
		Coordinate Filter	Observation Filter	Coordinate Filter	Observation Filter
SN02	7.4	5.8	6.1	6.0	6.3
DRMS	6.7	5.4	5.8	5.7	6.1
NEWC	9.7	6.6	7.0	6.9	7.4

4.4 Sidereal Filter Performance

The previous section showed the capability of sidereal filtering, whether using the coordinate or observation filter, in reducing the multipath error and reliably achieving high precision. However, there still exist two main questions that need to be answered in order to demonstrate fully the overall efficiency of sidereal filtering. The first is to determine the optimum number of consecutive days to stack to produce the highest and most consistent precision, after which further stacking will produce similar or even worse precision. Secondly, determining how long a filter established from a previous data set will last when applied to a different data set collected sometime later and yet still yield precision improvement. In other words, it is necessary to determine the filter's lifetime or age during which it can be used to enhance coordinate precision.

4.4.1 Filter Performance Data Collection and Processing

The current investigation is applied using only the two Drummond building DRMN and DRMS stations shown in Figure 3.3. The collection of the first data set used to test filter performance (the March_06 data set) started at 14:21:20 (GPS Time) on Wednesday 22nd of March 2006, with data logged continuously for one month until 14:52:17 (GPS Time) on Friday 21st of April 2006. The same type of receivers and antennae were used as before. Another data set (July_06) was collected on the same two stations for four continuous days starting at 08:42:11 (GPS Time) on Sunday 2nd of July 2006, until 11:42:17 (GPS Time) on Thursday 6th of July 2006. Again, all data collection criteria remained the same.

The RINEX files of the March_06 and July_06 data sets for both stations were processed through GASP, while fixing DRMN as before using rapid precise orbits. The reason for using rapid precise orbits rather than the more precise final orbits is the fact that sidereal lag variability is no longer questioned, as well as comparing sidereal filtering techniques' precision or performance, which required the use of the best available orbits. Here, the efficiency of sidereal filtering with time is being investigated, and thus it is desirable to use quick but still reliable precise orbits,

obtained in near real time. The last day of the March_06 data set was chosen to be the day upon which all different stacked filters will be applied sidereally, in order to investigate the two questions mentioned earlier.

4.4.2 Sidereal Filter Optimum Days Stacking

The search for the optimum number of stacked days was performed using the March_06 data set only. An increasing number of days' coordinate and carrier phase residuals were stacked and applied to form sidereal filters, starting with a one day stack, then two days and so on up to 21 days of stacked residuals. Note that whatever the number of stacked days, all filter stacks are just prior to the applied day mentioned earlier. For each applied filter, the 24-hour standard deviations of the final filtered coordinates are obtained, and then compared to their unfiltered counterparts, through the calculation of the percentage of variance reduction given by Equation 4.1.

As the variance reduction in Easting, Northing and Up coordinates is homogeneous, Figure 4.13 represents the 24-hour variance reduction for all 21 cases in the 3D component, for both filtering methodologies. From this figure, it can be seen that as the number of stacked days increases, the 24-hour variance reduction increases; that is an overall precision improvement. This effect continues until stacking 7 days together, after which the variance reduction starts to decrease, i.e. variance increases, until the total 21 days stacked. That is to say, stacking a week before the applied day will result in the best precision, after which stacking any more days will have lower precision improvement; that is decreasing the overall coordinate precision (Ragheb et al. 2007a). This can be attributed to slight changes in the constellation which will accumulate with stacking increasing number of days and affect the coordinate precision, or due to the fact that the multipath signal is most similar on adjacent days, becoming different as the time separation increases (Agnew and Larson 2007). Table 4.9 shows the minimum standard deviation achieved and percentage variance reduction in Easting, Northing, Up and 3D components, for both filtering methodologies for the optimum number of stacked days (7-day filter).

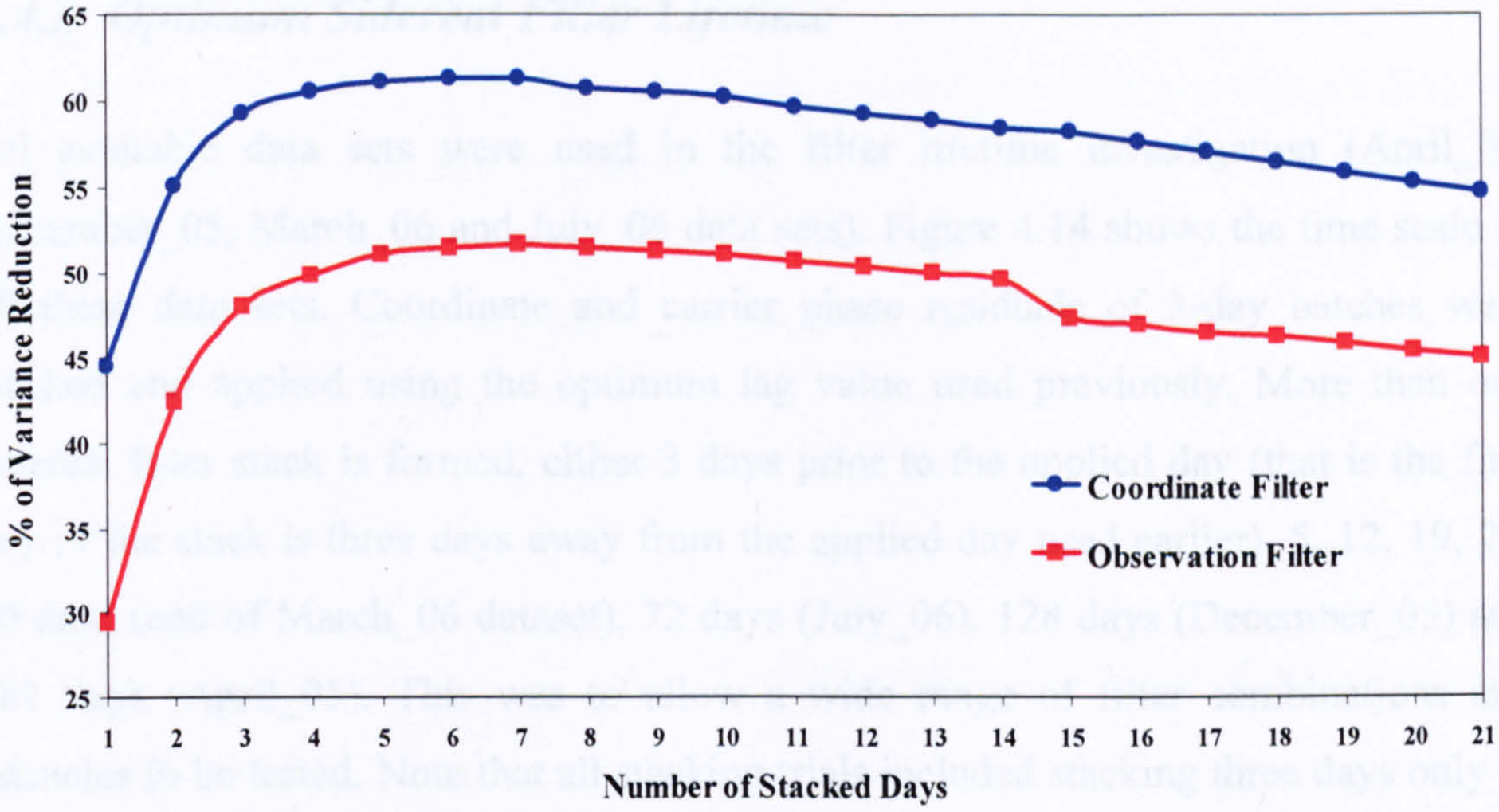

Figure 4.13 Percentage of 24-hour variance reduction of the applied day for both filtering methodologies (optimum stacked filter).

Table 4.9 24-hour standard deviations and variance reductions for the optimum 7-day filter for both filtering methodologies.

Case	Unfiltered	Coordinate Filter		Observation Filter	
	SD (mm)	SD (mm)	δ (%)	SD (mm)	δ (%)
E	2.03	1.35	55.8	1.43	50.4
N	3.39	2.02	64.5	2.29	54.4
U	5.65	3.54	60.7	3.95	51.1
3D	**6.89**	**4.29**	**61.2**	**4.79**	**51.7**

The F-test statistic was again used to test the significance of the results. Except for the first four days where the filter precision increases rapidly, adding one day at a time to the stack does not improve the precision significantly (at the 95% confidence level). All stack sizes of 3 days or more are significantly better than the unfiltered case. Stacking between 5 and 8 days gives practically identical precision. Statistically, the optimum (highest precision) 7-day stack is significantly better than a 3- or 4-day stack, as well as any 10-day or longer stack. The conclusion obtained here is that the 7-day stack is the optimum stacked filter, despite the fact that the 21-day stack still produced precision improvement.

4.4.3 Optimum Sidereal Filter Lifetime

All available data sets were used in the filter lifetime investigation (April_05, December_05, March_06 and July_06 data sets). Figure 4.14 shows the time scale of all these data sets. Coordinate and carrier phase residuals of 3-day batches were stacked and applied using the optimum lag value used previously. More than one sidereal filter stack is formed, either 3 days prior to the applied day (that is the first day of the stack is three days away from the applied day used earlier), 5, 12, 19, 26, 30 days (end of March_06 dataset), 72 days (July_06), 128 days (December_05) and 381 days (April_05). This was to allow a wide range of filter combinations and latencies to be tested. Note that all stacking trials included stacking three days only in order to benefit from and use the April_05, December_05 and July_06 data sets. In addition, the special aim of the July_06 data set was to fill the gap in the lifetime analysis with a stacked filter obtained around two months after the applied day.

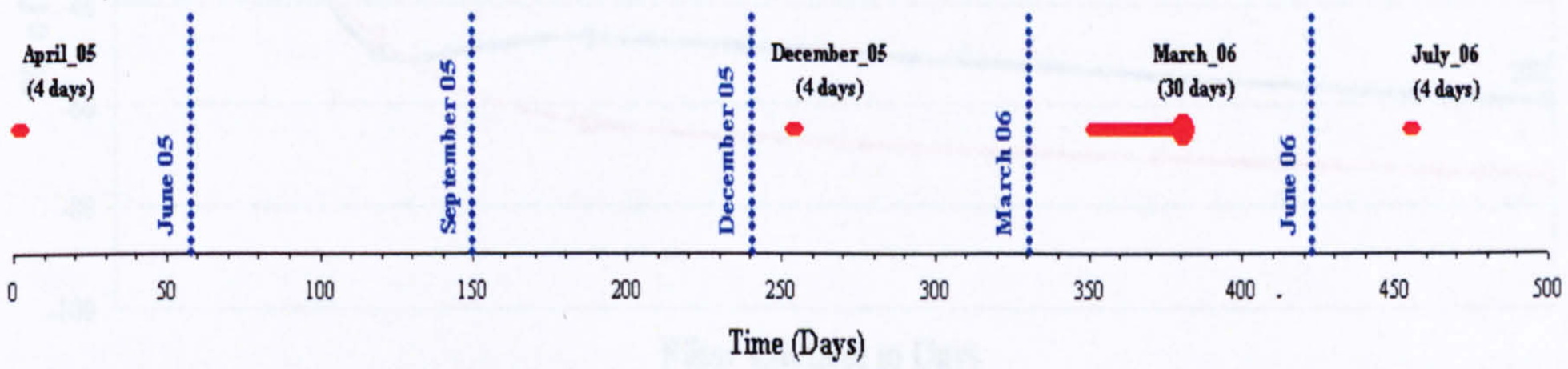

Figure 4.14 Time scale of all used data sets for the sidereal filter lifetime. The filter applied day is marked with a larger symbol. Zero days is set at 4th of April 2005.

Figure 4.15 illustrates the percentage of variance reduction for 3D coordinate components for all filter stacks based on coordinate and carrier phase residual stacking. It is seen that as the time gap between the produced stacked filter and applied day increases, the precision of the applied filter decreases gradually. This occurs until about 30 days from the applied day for the coordinate filter and 23 days for the observation filter, at which time the same precision is achieved as with the unfiltered case. Thus adding further days either after or before the applied day, will produce a lower precision when compared to the case with no filter (Ragheb et al. 2007a). Note that a negative value of variance reduction means the filtered case produced lower precision than the unfiltered one, i.e. the filtered case degraded the precision rather than improving it. More importantly, for the case of the 72-day-old

stack, the observation filter variance reduction follows the same trend as other observation filter stacks — as expected — while in the case of the coordinate filter the variance reduction decreased even more than expected. Accordingly, the produced 72-day-old coordinate stack has a lower variance reduction than the 128-day-old coordinate stack as well as its observation filter stack counterpart.

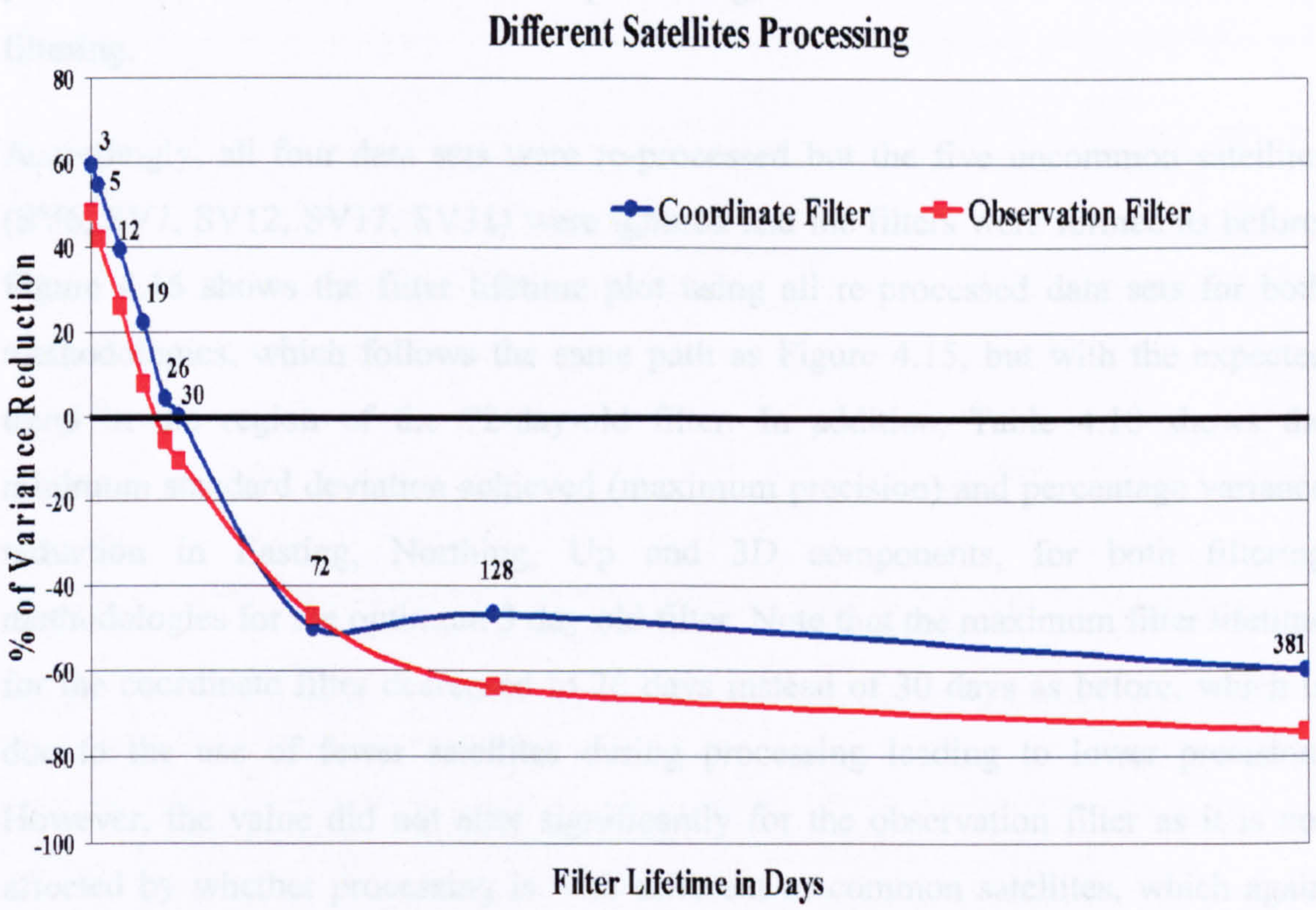

Figure 4.15 Percentage of 24-hour variance reduction of the applied day for both filtering methodologies (different satellites processing). Numbers indicate age of filters.

After the previous investigation, the reason for such illogical behaviour was found to be the processing of the July_06 data set (72-day-old stack) two months later with a different satellite constellation, having SV6 missing. This discrepancy again shows another advantage of the observation filter: in addition to its faster processing time over the coordinate filter, the observation filter was not affected by the change in constellation. During phase residual stacking of the July_06 data set, the filter did not include any satellite double difference pairing of SV6. Thus when it is reapplied while processing the last day of March_06, all residuals of SV6 pairings were not updated or corrected. This was then followed by a full least squares adjustment, which tends to distribute these uncorrected errors.

However, this is not the case in coordinate filtering, as the coordinates of the July_06 data set were processed and stacked without SV6 being involved. These coordinate residuals are then applied directly — without least squares — to the coordinates of the applied day, which had SV6 included during processing. The application of coordinate residuals based on a different constellation and geometry causes a drop in precision due to uncommon satellite processing, which was not seen for observation filtering.

Accordingly, all four data sets were re-processed but the five uncommon satellites (SV6, SV7, SV12, SV17, SV31) were ignored and the filters were formed as before. Figure 4.16 shows the filter lifetime plot using all re-processed data sets for both methodologies, which follows the same path as Figure 4.15, but with the expected trend in the region of the 72-day-old filter. In addition, Table 4.10 shows the minimum standard deviation achieved (maximum precision) and percentage variance reduction in Easting, Northing, Up and 3D components, for both filtering methodologies for the optimum 3 day-old filter. Note that the maximum filter lifetime for the coordinate filter decreased to 26 days instead of 30 days as before, which is due to the use of fewer satellites during processing leading to lower precision. However, the value did not alter significantly for the observation filter as it is not affected by whether processing is with different or common satellites, which again shows the superiority of the observation filter from this point of view.

4.5 Sidereal Filter Conclusions

The use of sidereal filtering minimizes the multipath effect on GPS data and accordingly improves the overall precision of the final station coordinates. Statistically, coordinate filtering gives slightly better precision than observation filtering, but with similar hour-to-hour consistency. However, coordinate filtering requires significantly longer processing times, especially if an epoch-by-epoch ambiguity searching algorithm is used. This may outweigh the relatively small difference in the precision of the final coordinates. In the end, one has to decide whether to use the more accurate and homogeneous method of coordinate filtering,

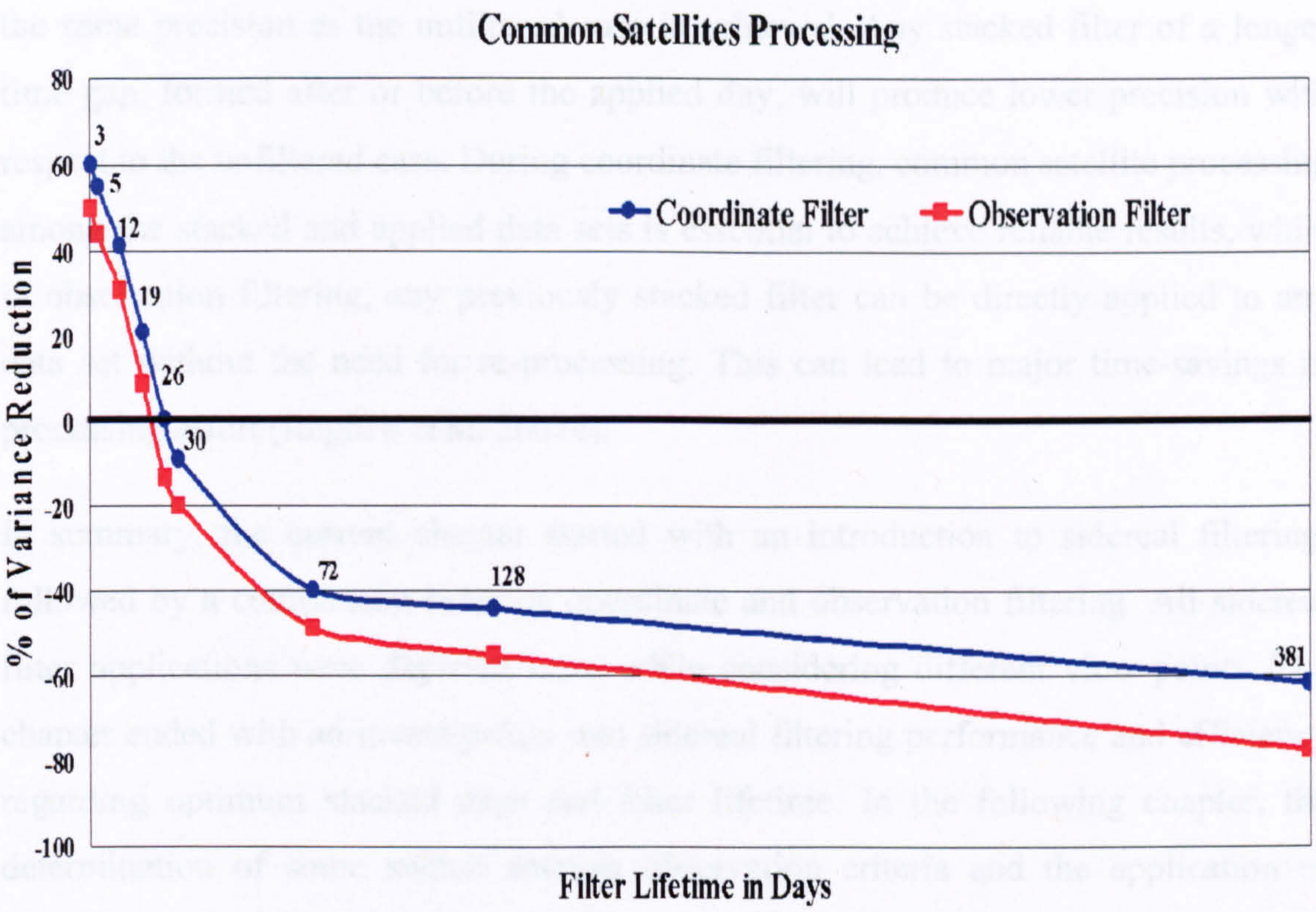

Figure 4.16 Percentage of 24-hour variance reduction of the applied day for both stacking methodologies (common satellites processing).

Table 4.10 24-hour standard deviations and variance reductions for the case of optimum filter age for both filtering methodologies.

Case	Unfiltered	Coordinate Filter		Observation Filter	
	SD (mm)	SD (mm)	δ (%)	SD (mm)	δ (%)
E	2.16	1.45	55.2	1.56	47.8
N	3.53	2.16	62.6	2.44	52.4
U	5.97	3.80	59.6	4.26	49.1
3D	**7.27**	**4.60**	**59.9**	**5.15**	**49.8**

which takes a longer time, or the observation filtering with worse accuracy but less processing time and better robustness to constellation changes (Ragheb et al. 2007b).

Stacking more days will increase the overall precision of the final filtered station coordinates. A 7-day stack results in the best precisions, with 61% variance reduction for coordinate filtering and 52% for observation filtering, after which stacking more days degrades the overall coordinate precision. As the lifetime of any stacked "sidereal" filter increases, the efficiency of the filter decreases up to 30 days difference for coordinate filtering and 23 days for observation filtering, at which point

the same precision as the unfiltered case is achieved. Any stacked filter of a longer time gap, formed after or before the applied day, will produce lower precision with respect to the unfiltered case. During coordinate filtering, common satellite processing among the stacked and applied data sets is essential to achieve reliable results, while in observation filtering, any previously stacked filter can be directly applied to any data set without the need for re-processing. This can lead to major time-savings in processing effort (Ragheb et al. 2007a).

In summary, the current chapter started with an introduction to sidereal filtering, followed by a comparison between coordinate and observation filtering. All sidereal filter applications were depicted next, while considering different view points. The chapter ended with an investigation into sidereal filtering performance and efficiency regarding optimum stacked days and filter lifetime. In the following chapter, the determination of some switch antenna observation criteria and the application of sidereal filter on semi-continuous GPS data are investigated. A brief background is given on the switch multi-antenna array, along with some previous applied studies. As well, the switch dual antenna device adopted in the current research is illustrated. Several switch observation trials are carried out, regarding session observation length, number of epochs to use and the adequate geometry repeat lag. Then, the coordinate filter is applied on periodic GPS data, observed through the developed switch device, while setting different measures of precision and epochs to consider per switch.

GPS SWITCHED ANTENNA ARRAY

5.1 Introduction

Continuous GPS positioning has been commonly utilized in monitoring deformations. However, one of its major drawbacks at present is its high cost due to deployments required throughout the sites to be monitored, especially in projects of large areas and limited budget. When monitoring the deformation of a large number of stations, the overall cost of the whole process will be high due to the usage of multiple, permanently operating GPS equipment required to cover each monitoring station (Chen et al. 2000). Each receiver-antenna setup will include a receiver, antenna, hardware, software, power supply (batteries or mains operated) and additional spare power. Fortunately, cost effective and adequate precision can be achieved using a GPS multi-antenna array system, observing GPS data periodically for each antenna occupying the monitoring station.

In this case, multiple GPS antennae are connected to a main master receiver recording data continuously while switching between antennae periodically. In this set up, one single GPS receiver acts effectively as multiple receivers to monitor multiple stations (Ding et al. 2000). This will, of course, reduce the overall cost of the whole monitoring process significantly, due to the reduction in the number of receivers used, these being replaced by a number of GPS antennae. GPS multi-antenna systems represent an economical and precise technique for deformation monitoring especially for large scale networks (He et al. 2005). In addition, although this technique is used basically for cost minimization, it is also adopted where security and space issues dictate that the installation of many continuous GPS receivers is not feasible (Forward et al. 2001).

This chapter starts with an overview of the general switched antenna array technique, followed by a brief outline of previous multi-antenna array system investigations. The development of the switch device adopted in the current research is described next, after which the test area and data collection process are explained. Then, the investigation for the optimum session observation length regarding precision, reliability and adequacy is illustrated. At the end, the application of sidereal filtering on periodic GPS data is presented in detail.

5.2 Mechanism of Multi-Antenna Array

The switch antenna array system connects multiple GPS antennae to a single GPS receiver. Each antenna is mounted on the required test station, and the periodic observation of each antenna is controlled through a switch mechanism (consisting of multiple input channels and a single output channel). This mechanism could be either manual or controlled via software. The main task of this switch is to allow each antenna sequentially to log its signals to the main receiver for a certain interval of time, thus producing periodic GPS data for a network of monitoring stations (He et al. 2004a). Of course, for relative positioning, another base receiver must be fixed at a station with known coordinates.

The use of the multi-antenna array system should be carefully investigated regarding cost, accuracy and time, as on the other hand, continuously operating GPS receivers have many advantages when compared to episodic positioning, especially in deformation monitoring. One of these advantages is the high temporal resolution, that is the estimation of deformation movements from a short data time span (Forward et al. 2001). Continuous GPS also mitigates systematic errors, as well as the automation of the overall process as it requires less manpower when compared to episodic GPS and thus reduces gross errors and data outliers. It should be mentioned here that short data spans from each antenna are applicable in the current research due to the use of a single epoch approach for ambiguity resolution.

5.3 Previous Multi-Antenna Array Investigations

The concept of a multiple antenna array has been discussed previously in several investigations with a different perspective. One of the earliest investigations in GPS multi-antenna array systems was done by Santerre and Beutler (1993). In their research, multiple antennae were linked to a GPS receiver aiming to improve height determination for baselines of a few kilometres in length. This is done by trying to eliminate relative receiver clock parameters in single difference observations, as well the reduction of the tropospheric error, as they are both highly correlated with baseline height component. With the proposed method, the effect of tropospheric errors becomes smaller, through the introduction of a relative tropospheric zenith delay parameter. Accordingly, the height standard deviation improves by a factor of about three compared to standard GPS data processing.

Forward et al. (2001) developed a GPS switched antenna array system, recording data from different stations quasi-continuously for steep wall deformation monitoring at Mount Keith, Western Australia. The system was automated; all monitoring stations are connected to a computer and processed automatically. The system comprised four antennae located along the open pit deforming mine wall, in addition to two continuously operating reference stations at 1 Hz. Multiple antennae were connected to the master receiver through 300 m long, low-loss coaxial cables fitted with dual frequency amplifiers and lightening protectors. Data were logged for 15 minute periods for each antenna. Then, the data were transferred to the main processing unit through spread spectrum radios, providing real-time positioning. Furthermore, the effect of the cable length on the resultant signal strength and quality degradation was examined here. The project operated continuously for 8 weeks, and with average coordinate precisions for all deformation stations of 4 mm in plan and 10 mm in height being obtained over the whole period, 3D deformations of 2 mm/week were detected. This proposed configuration proved to be viable and a cheaper alternative than using a separate receiver and antenna for each monitoring station.

Chen et al. (2000) and Ding et al. (2000) tested a GPS Multi-antenna System (GMS) to monitor common deformations such as landslides or unstable slopes. This work

used 6 channel GMS switch box employing two antennae only to test the concept. This multi-antenna GPS system has three software components. The first is to switch between antennae, while the second is used for data logging and outputting GPS observations. The last component is responsible for processing, analyzing and managing the GPS data through an application software, with an option of being in fully automatic mode without user assistance. The observation session for each antenna was 16.5 minutes with receiver sampling at 15 seconds, transferring data to a data processing and analysis centre providing real-time or near real-time monitoring. The results obtained reached centimetre precision, which is near to the typical accuracy achieved using conventional GPS surveying systems.

He et al. (2004a, b) used a more developed prototype of GMS with eight channels called GMAS (GPS Multi-Antenna System) for monitoring the Xiaolangdi dam on the yellow river in China. Raw GPS data were collected at three stations using GMAS with a 15 minute switch interval with 20 seconds sampling interval for two hours. Average post processing precision of baselines over the whole observation period reached around 1–2 mm. The same methodology of GMAS was applied in He et al. (2005) on the Xiaowan dam on the Lanchang River in Yunnan province, China, where the use of conventional GPS monitoring methods is limited due to the steep slopes near the arch of the dam. The application included 16 monitoring stations connected to two GPS receivers — eight antennae connected to each receiver — and two base stations with two receivers. The session observation rate was 10 minutes, with a sampling interval of 15 seconds. An overall accuracy of 3 mm in the horizontal direction and 7 mm in the vertical direction were achieved.

Recently, Ding et al. (2007) used GMAS for monitoring landslides over the Heihe reservoir in Xi'an, China as well as monitoring roadside slopes. The technique was tested using five concrete pillars where a three directional moving device was used for simulating various deformations. Then the actual application was performed by setting four switch antennae on the landslide connected to one receiver in addition to another fixed receiver, with five seconds interval and 30 seconds session observation rate. Data logging was divided into three main campaigns, each being 3 hours, getting an average solution every campaign and comparing it to the overall average

coordinates. Roadside slope monitoring was executed using eight switch antennae, again with the same sampling interval and 1 minute session interval. For each antenna, an average coordinate is calculated every 30 minutes, one hour and three hours. For the latter case, an accuracy of ~2 mm can be achieved in all three coordinate components under typical slope site conditions. The authors concluded that the established GMS and its updated version of GMAS were stable, easy to use and operate. They provide cost effective and accurate episodic GPS positioning for deformation monitoring of constructed and natural structures such as dams, slopes and landslides. This can play an important role in decreasing the risk of property damage due to deformations and accordingly save lives.

Note that, all previous trials used different kinds of cable lengths and material for data transfer between the switch antenna and the receiver. As a general requirement, the length of the coaxial cable between the antenna and the switching device should be less than 30 metres, in order to maintain the signal-to-noise ratio to a reasonable threshold. However, longer cables can be used by either fitting the cables with low-noise signal microamplifiers to compensate for the loss of signal strength through the cables, or by using cables of certain materials, which maintain the signal-to-noise ratio, such as a system of fibre-optic cables. In the latter case, commercially available units are used to convert GPS radio-frequency signals into light wave for transmission along a fibre-optic cable and also to convert back into radio-frequency before input to a GPS receiver (Ding et al. 2000). In either case, longer cable lengths can be used reaching up to 1 km (He et al. 2005). On the other hand, data can be either processed on site, or transmitted to a processing centre through mobile phones, radio, internet or using wireless data communication through General Packet Radio Service (GPRS). The latter is very effective especially when transferring large volumes of GPS data to the processing centre (Ding et al. 2007). However, using special kinds of cable length or material is not of concern in the current research as data cables used are considered short in length (20–30 m). In addition, data transferred to receivers are processed on site and thus no special communication is needed for data transmission.

5.4 Development of Dual Antenna Switch Device

The switch device used in the current research is a modified device previously developed and used by Kreutzfeldt (2001). It is originally a dual switch box dealing with one receiver and two antennae, noting that what is applied on two antennae can be expanded to be used with multiple antennae. The box shown in Figure 5.1 contains four connections, two for the two antennae, one connection to the receiver, while the box is connected to the Personal Computer (PC) through a parallel interface. Another serial port can be connected from the receiver to the PC. In addition, the switch box contains a 9–12V Direct Current (DC) power socket, manual switcher and two LED indicators to show which antenna is active. All described connections are schematically shown in Figure 5.2.

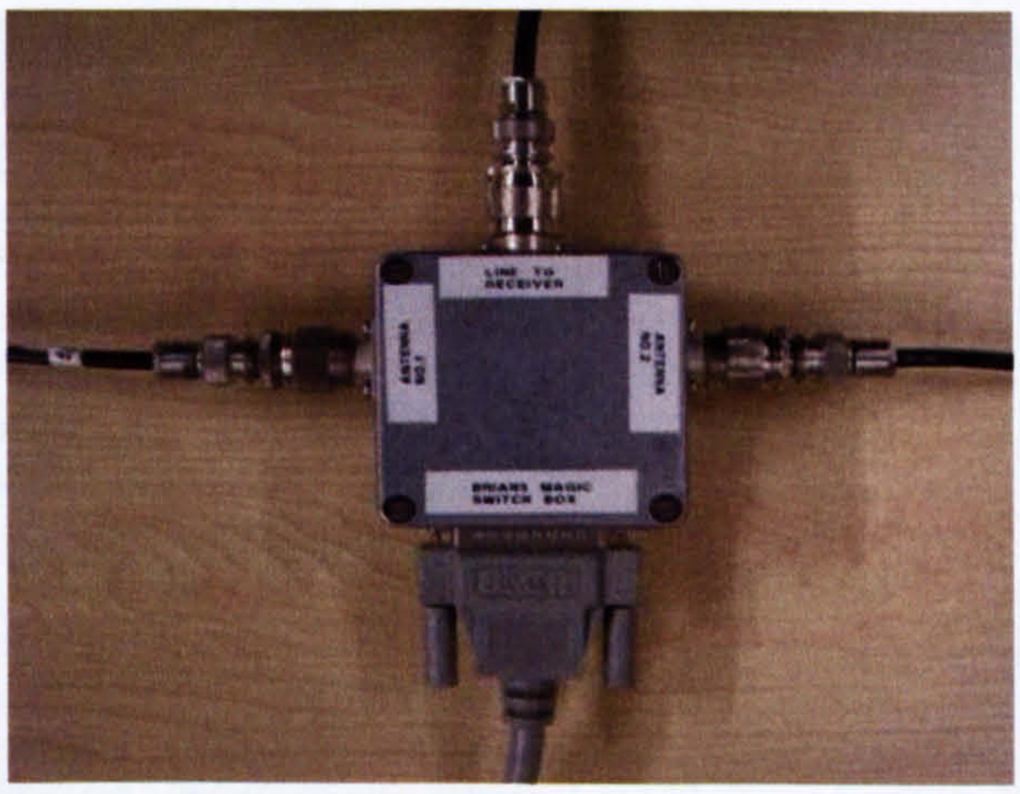

Figure 5.1 The employed switch box.

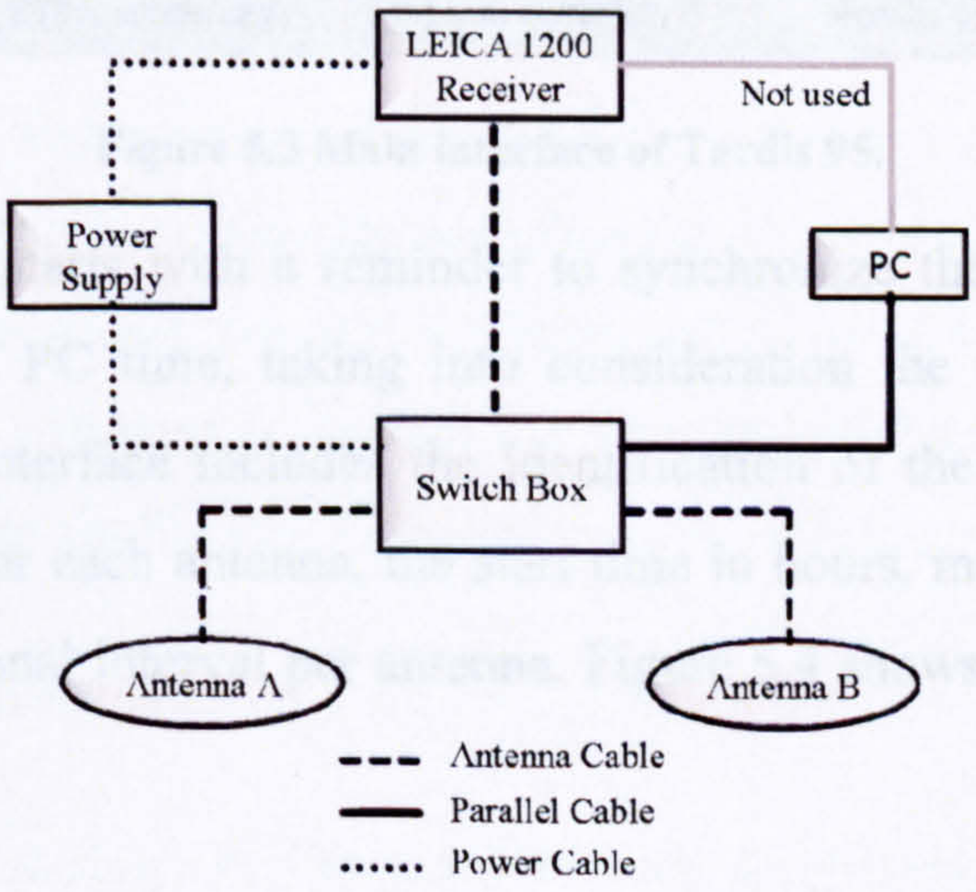

Figure 5.2 Schematic diagram of switch antenna array connections.

Although the switch between the used antennae could be done manually, an updated version of a software written using the Visual Basic language called **R**INEX **A**ntenna **S**witch **p**rogram (**RASP**) is used in order to control the data stream from the receiver to each antenna (Kreutzfeldt 2001). The new modified version of the software is now called **D**ual **A**ntenna **S**witch **P**rogram (**DASP**), dealing with LEICA instead of ASHTECH receivers. An important role of the program is to synchronize the PC clock with the Coordinated Universal Time (UTC) in order to accurately set the switch time relative to GPS time in the RINEX file of each antenna. This is done through logging the PC to the internet and synchronizing the PC clock with a networked timeserver using an independent utility program for Windows called Tardis 95. Figure 5.3 shows the main interface of the Tardis 95 utility program.

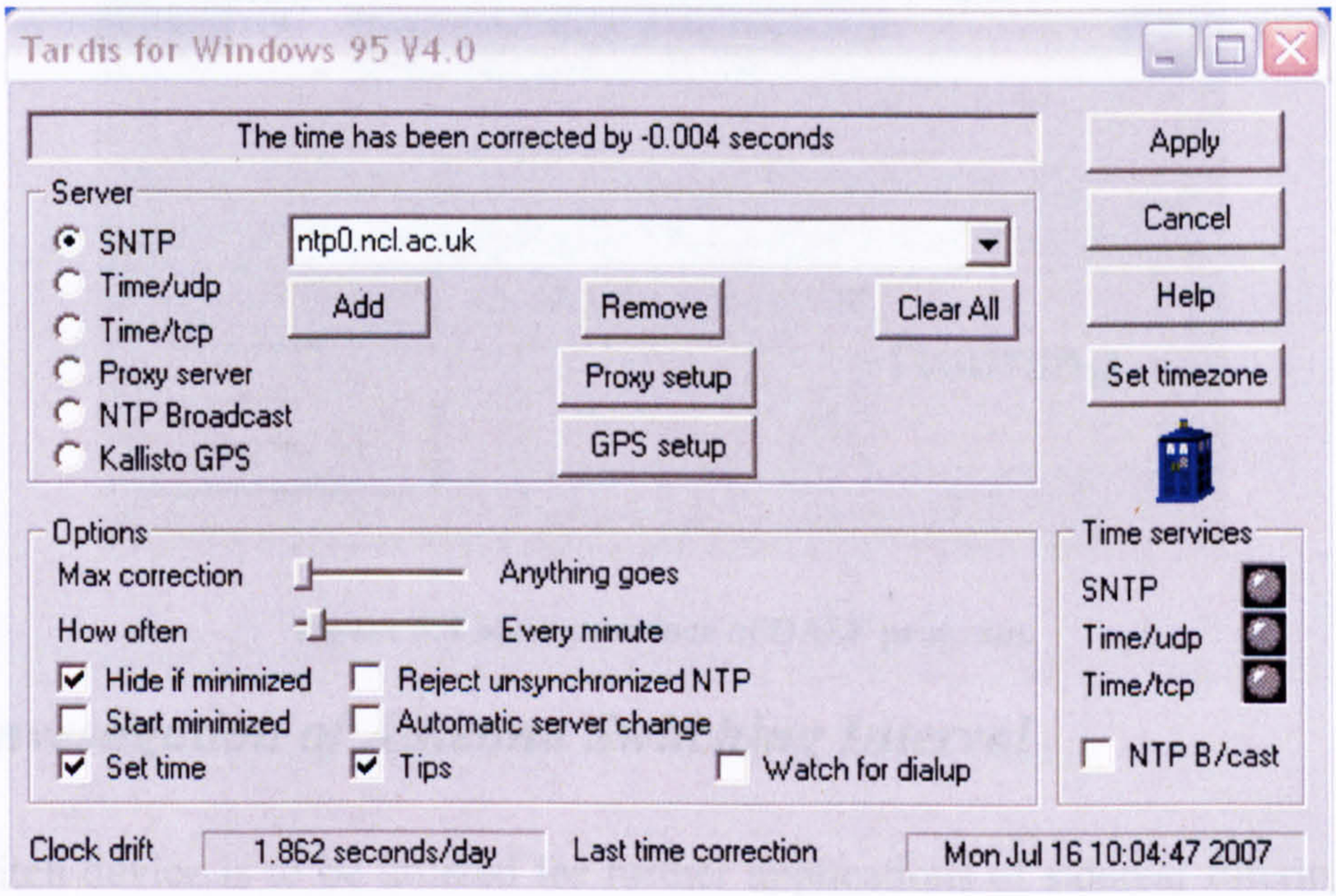

Figure 5.3 Main interface of Tardis 95.

The switch program starts with a reminder to synchronize the program clock with GPS time instead of PC time, taking into consideration the number of GPS leap seconds. The main interface includes the identification of the starting antenna, the number of sessions for each antenna, the start time in hours, minutes and seconds as well as the observational interval per antenna. Figure 5.4 shows the main interface of the DASP program.

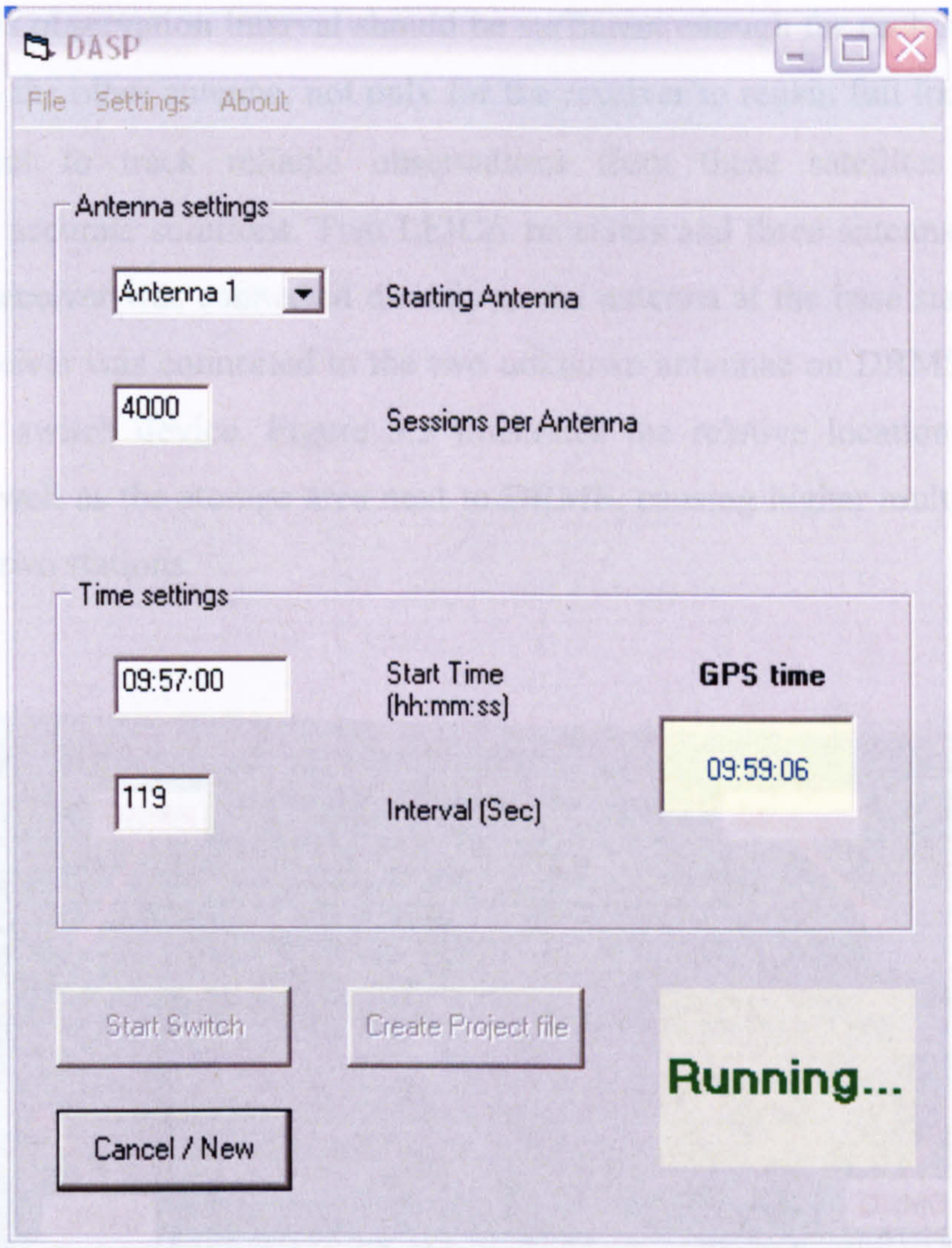

Figure 5.4 Main interface of DASP program.

5.5 *Investigation of Antenna Switching Interval*

The switch device is to be utilized for further applications of sidereal filtering while monitoring structural deformation. Accordingly, several constraints needed to be identified to achieve the best possible organization of the switching operation in a cost-effective and time-saving manner. An important factor to be investigated here is the optimum session observation interval per antenna, producing reliable precision while testing its validity for the application of sidereal filtering.

5.5.1 Data Collection

Three stations on the roof of the Drummond building (DRMN, DRMS and DRME) were chosen for the investigation of the optimum session observation interval for each

antenna. This observation interval should be sufficient enough for each station before switching to the other antenna, not only for the receiver to regain full lock on healthy satellites, but to track reliable observations from these satellites to produce consistently accurate solutions. Two LEICA receivers and three antennae were used, where one receiver was connected directly to the antenna at the base station DRMN. Another receiver was connected to the two unknown antennae on DRMS and DRME through the switch device. Figure 5.5 illustrates the relative location of all three stations, as well as the storage area next to DRME, causing higher multipath relative to the other two stations.

Figure 5.5 Relative location of the three Drummond building stations.

At first, a primary data set was collected normally at DRMS and DRME without switching, in order to compare the multipath environment at the two unknown stations using TEQC (Estey and Meertens 1999). Figures 5.6 and 5.7 represent the MP1 and MP2 RMS values for both stations using 5° and 15° minimum elevation mask angles, respectively. From these two figures, it can be seen that DRME suffers from very high multipath for low and medium elevated satellites, especially when the storage next to the station is involved, which also obstructs satellites in certain parts of the sky. On the other hand, DRMS suffers from relatively lower multipath. Note that an illustration of the multipath environment for DRMN can be seen from Figures 3.6 and 3.7.

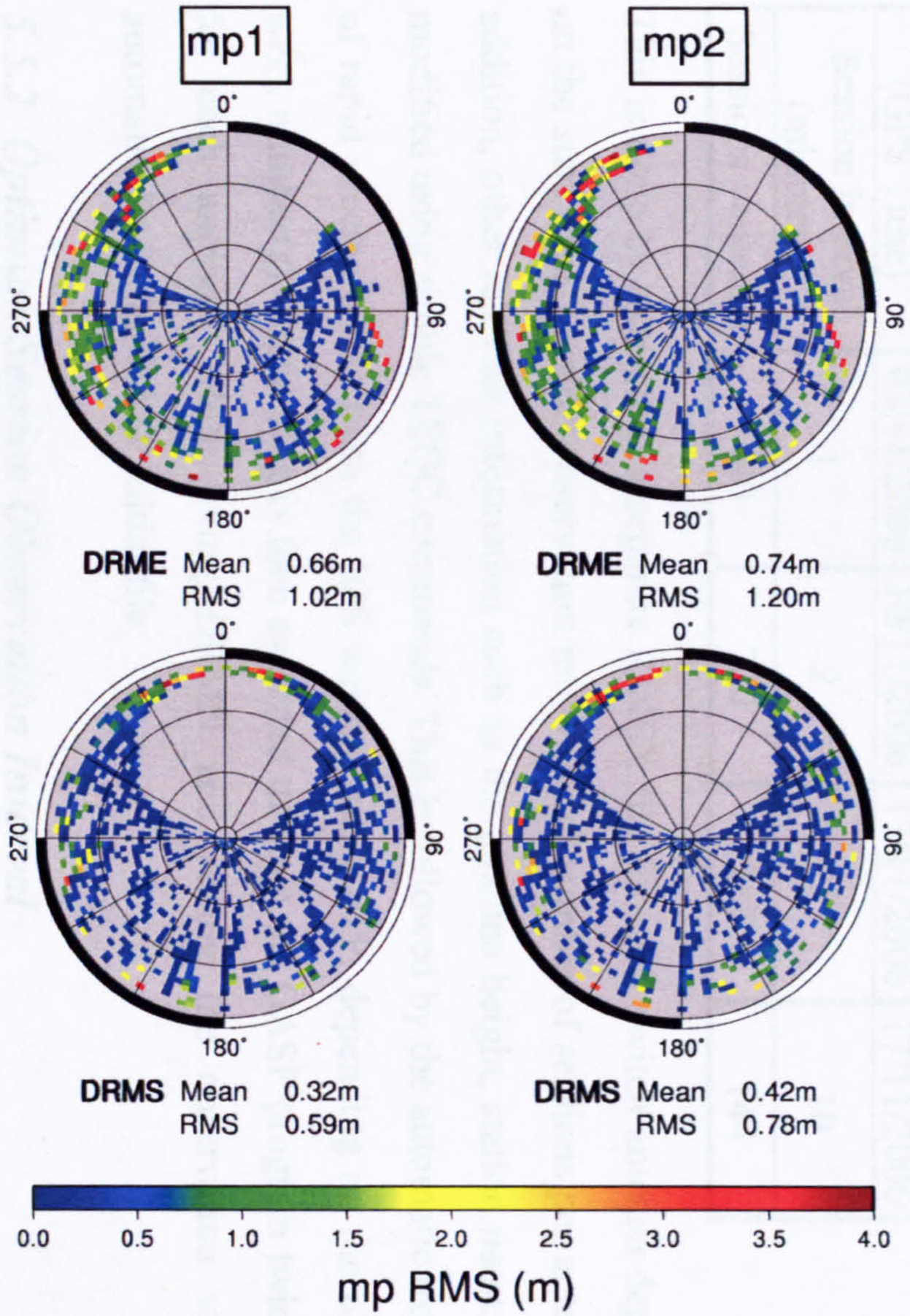

Figure 5.6 Multipath RMS with a 5° elevation mask.

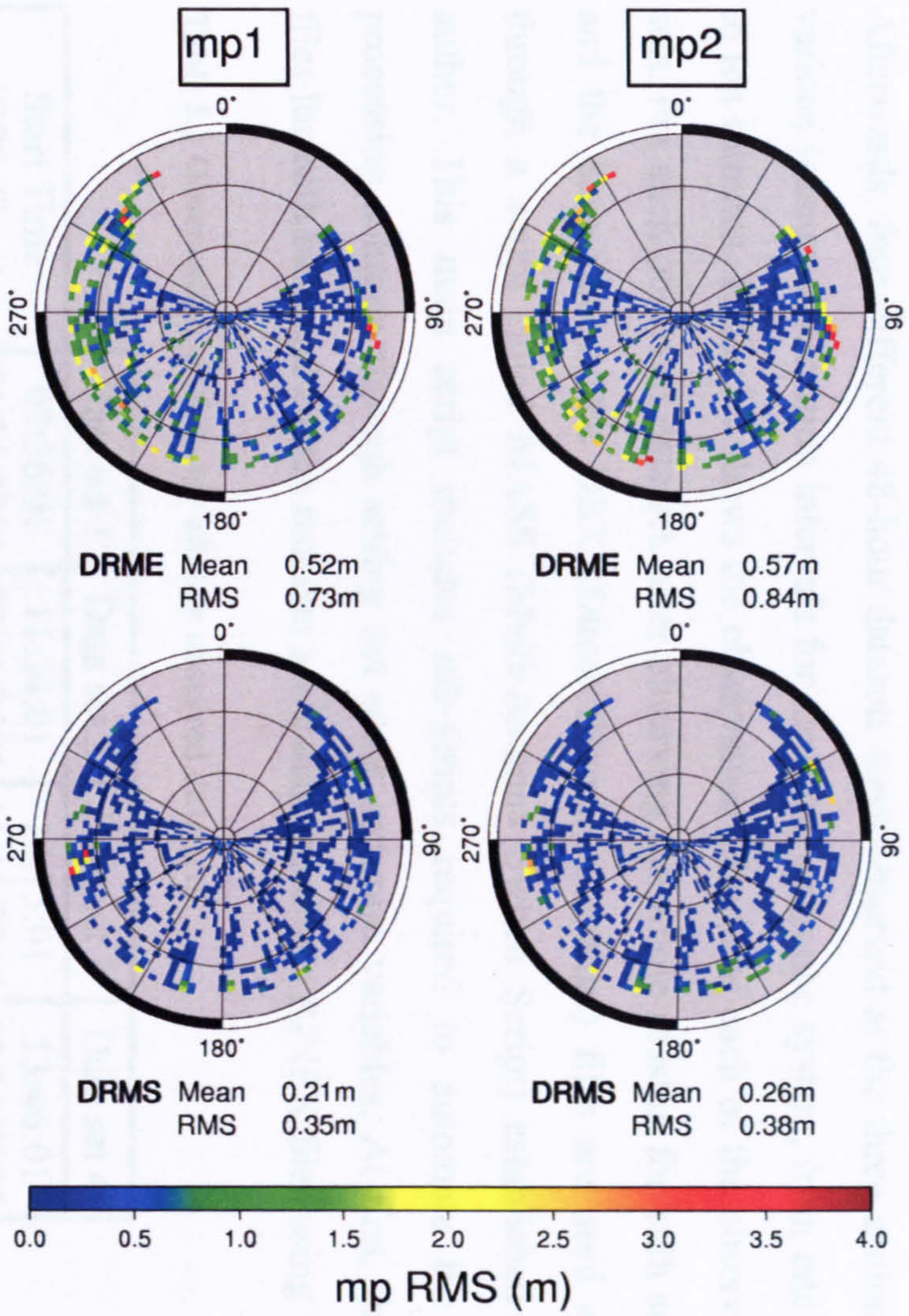

Figure 5.7 Multipath RMS with a 15° elevation mask.

Afterwards, four different 48-hour datasets were observed at the three stations, with various session observation intervals for the multi-antennae system, from one minute to ten minutes. Table 5.1 shows the observation criteria of each of the observed data sets. For each observed data set, after observing the whole session for both antennae and the base station, the DBX (Direct Branch eXchange) files are used and run through a script called **MASS** (Multi-Antenna Switch Script) established by the author. This main script includes sub-scripts required to automate the whole processing solution through setting out some common variables. At first, the DBX files for both base and switch receiver are transformed into RINEX files using TEQC.

Table 5.1 Observation criteria for all four observed data sets.

	Data set 1	Data set 2	Data set 3	Data set 4
Start Time (GPS Time)	09:36:01 01/11/2006	11:34:01 08/11/2006	10:15:01 11/11/2006	13:46:01 15/11/2006
End Time (GPS Time)	09:37:01 03/11/2006	11:36:01 10/11/2006	10:20:01 13/11/2006	13:56:01 17/11/2006
Session Interval (minutes)	1	2	5	10
Sessions / antenna	1440	720	288	144

This is done by extracting a separate RINEX file for each switch antenna depending on the start time, session observation interval and number of sessions per antenna. In addition, other relevant information such as the antenna height, station name, etc. is modified using simple TEQC commands. This is followed by the automatic extraction of rapid precise orbits from the IGS website using FTP, depending on the observed week number(s). Processing is then executed through the GASP program twice, once for each antenna, while fixing DRMN and setting the observation variables automatically in the GASP initial file.

5.5.2 Optimum Session Observation Interval

The main aim here is to investigate the optimum switching time between antennae to produce reliable results. For our investigation here, the main script was run for all available four switching sessions without applying sidereal filtering, in order to determine the optimum session observation time. An automated sub-script is used to

analyse the data and calculate various statistics for each repeating switch interval per antenna. These statistics include the Easting, Northing, Up and 3D discrepancies from the average known coordinates, as well as discrepancy percentiles calculation. Subsequently, all resultant statistics are plotted automatically for each switch session, in addition to the 50^{th}, 95^{th} and 99^{th} discrepancy percentile for each epoch of any switch interval. Figure 5.8a,b shows the 3D discrepancy per each epoch for all switch intervals overlaid upon each other for all switch sessions for both antennae at DRME and DRMS, respectively. Figure 5.9a,b illustrates the 3D discrepancy values which are greater than 50%, 95% and 99% of all switch epochs at any instance.

Looking at Figure 5.8, one can see that the discrepancy of all epochs per switch fluctuates highly among all sessions from tens or sometimes hundreds of metres at the beginning of the switch session up to the centimetre level at the end of the session interval. On the other hand, Figure 5.9 of discrepancy percentiles for all switch intervals for both stations, especially the 50^{th} percentile, indicate that a certain time interval is required in order to achieve centimetre accuracy for 50% of the data, which can be attributed for the utilized receiver hardware. This time interval averages around 40 seconds from the start of the switch interval. Accordingly, the one minute switch interval could not provide a sufficient number of accurate epochs before switching to the other antenna (≈ only 15–20 seconds). This will lead to fewer epochs being provided over the total number of sessions. Therefore, the one minute switch interval will be discarded along with its accompanied analysis and results due to the lack of reliability caused by the small amount of data provided. As a result, more attention will be paid to the two, five and ten minute switch intervals in order to assess the efficiency among them from the precision and applicability point of view. It should be noted here that previous conclusions are mainly cable, receiver and site dependent, and thus may change slightly with the signal-to-noise ratio (SNR) at the receiver, receiver configuration or multipath environment.

In addition, it is well illustrated from the previous figures especially the discrepancy plots, that the collected data is divided among two populations with very little overlap and thus using a certain cut off value to filter the data from outliers will result in a more precise population. For this purpose, the data are filtered to within a certain

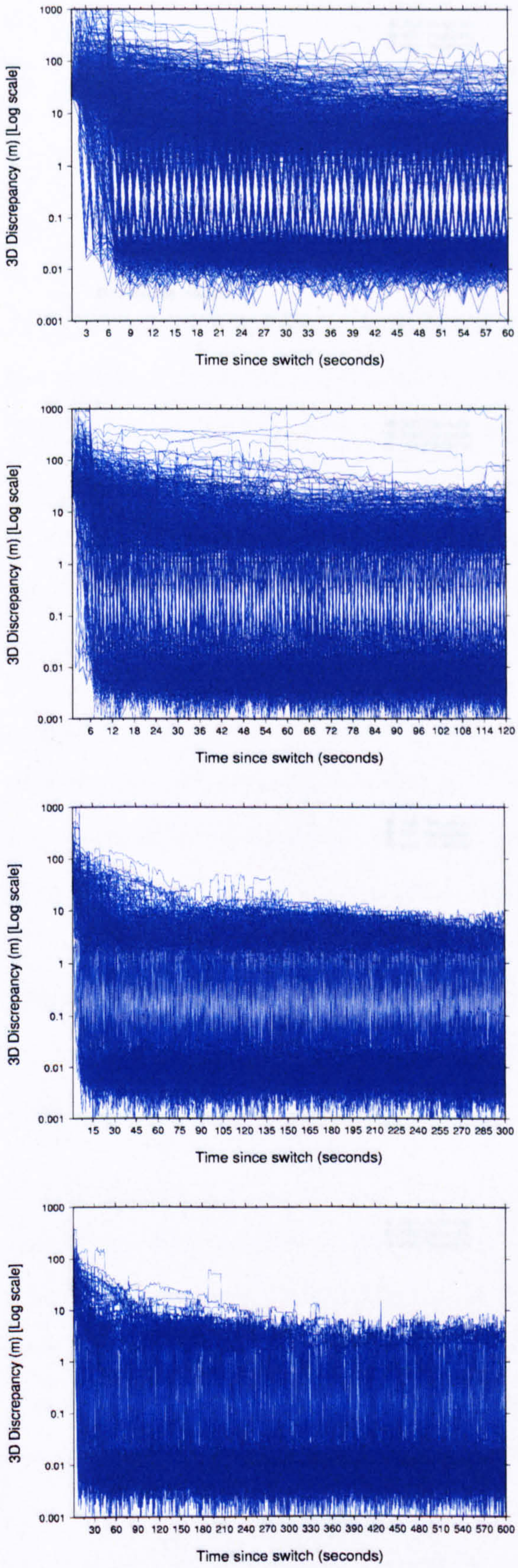

a) DRME

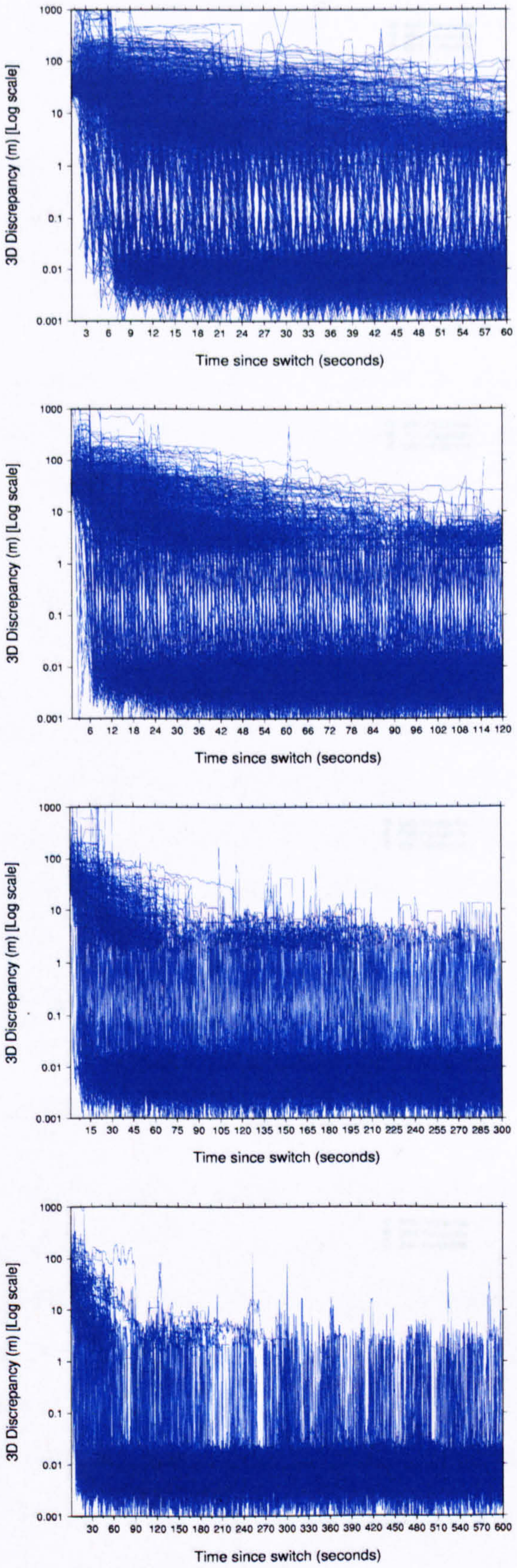

b) DRMS

Figure 5.8 3D discrepancies for all switch intervals. Upper for one minute switch session, then two, five and ten minute. Left for DRME while right for DRMS.

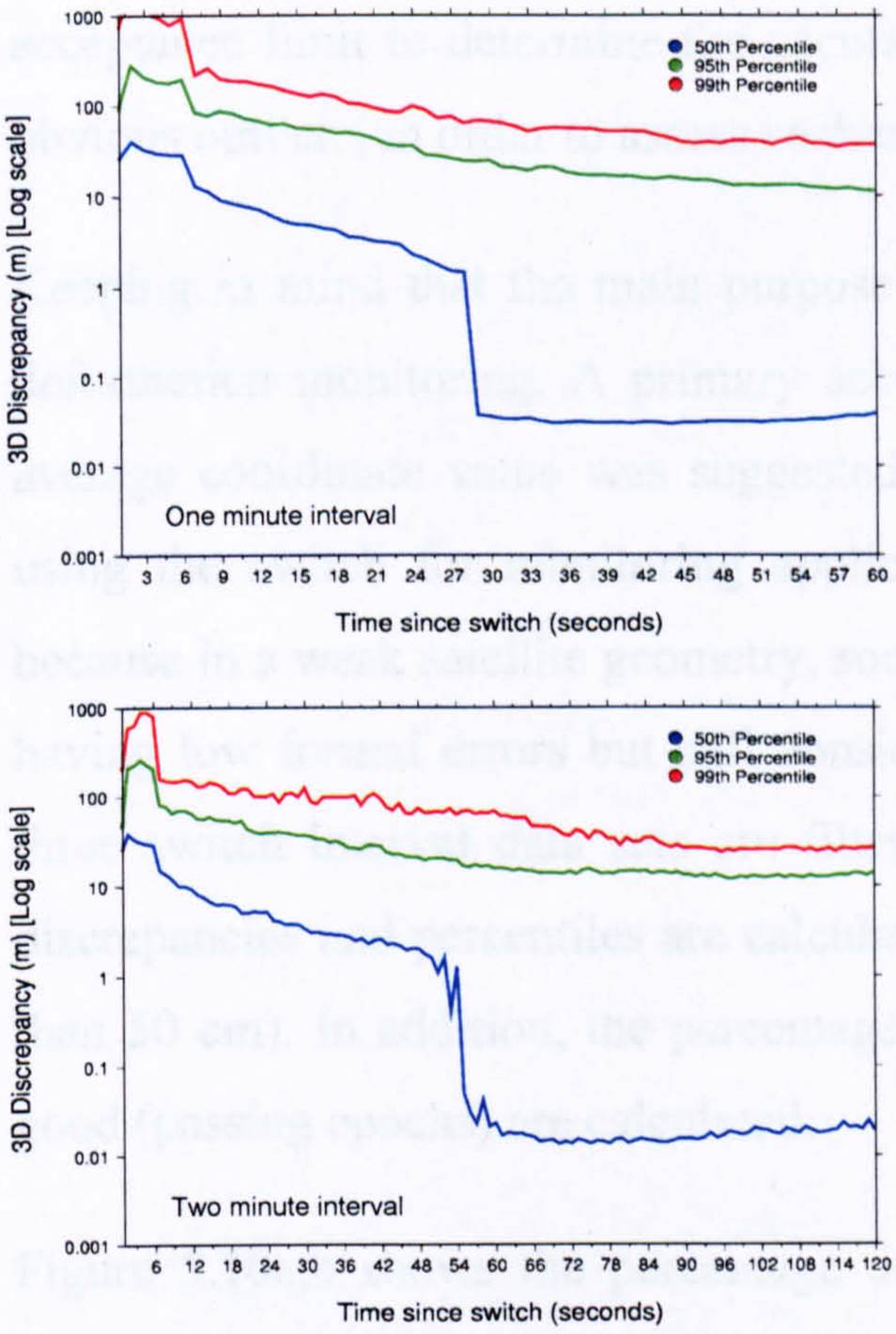

a) DRME **b) DRMS**

Figure 5.9 3D discrepancy percentiles for all switch intervals. Order as before.

acceptance limit to determine the accuracy of the epochs per switch after removing obvious outliers, in order to assess each of the switch intervals used.

Keeping in mind that the main purpose is to use the dual antenna switch array for deformation monitoring. A primary acceptance limit of 50 cm from the long term average coordinate value was suggested to allow for displacements detection when using the switch for monitoring applications. This acceptance limit is necessary, because in a weak satellite geometry, some epochs will pass the AFV threshold while having low formal errors but still considered unreliable. Accordingly, all remaining three switch interval data sets are filtered with this 50 cm limit and then the 3D discrepancies and percentiles are calculated once more for all remaining epochs (less than 50 cm). In addition, the percentages of observed epochs and epochs classed as good (passing epochs) are calculated.

Figure 5.10a,b shows the percentage of observed and passing epochs for the two minute switch interval for both antennae. Again, the multipath environment is well illustrated in this figure where the number of passing epochs for DRMS is greater than those of DRME, indicating higher precision for DRMS. Figures 5.11 and 5.12 are formed in the same manner as Figures 5.8 and 5.9 after removing bad epochs having discrepancies greater than 50 cm. Similarly, Figures 5.13, 5.14 and 5.15 for the five minute switch interval and Figures 5.16, 5.17 and 5.18 for the ten minute switch interval are formed in a similar manner to Figures 5.10, 5.11 and 5.12, respectively.

The discrepancy plots for all switch intervals for both antennae indicate that after removing obvious outliers from the data, the accuracy became more homogeneous around the cm level. Also, looking at the discrepancy percentile plots, 50% reached even the cm level accuracy, while 95% of the data set reached a few centimetres accuracy. This is regardless of the switch interval used. Of course, the exceptions to this are a few epochs after switching from the other antenna, which have worse accuracy due to the transition time required to fully lock on to satellites with reliable observations, which mainly depends on the used receiver hardware.

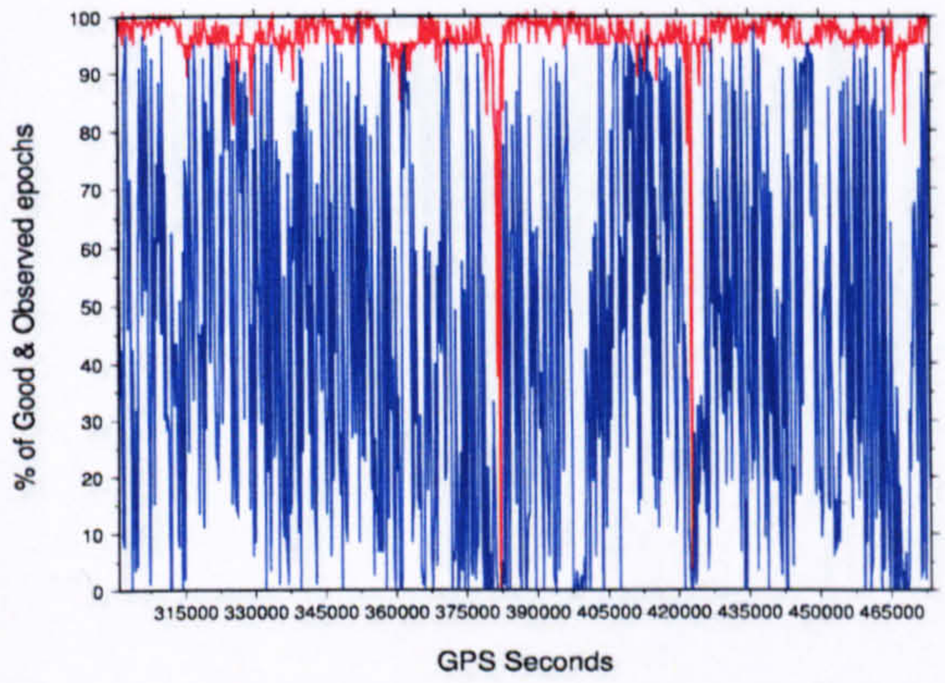

a) DRME

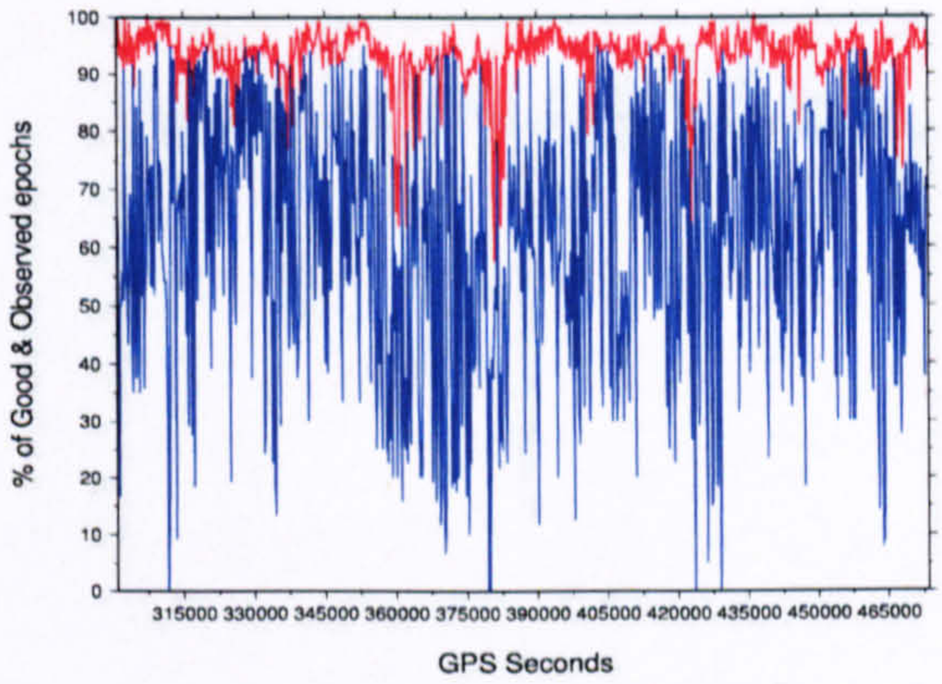

b) DRMS

Figure 5.10 Percentage of passing good epochs (less than 50 cm) and total observed epochs for two minute switch interval. Observed epochs in red. Good epochs in blue.

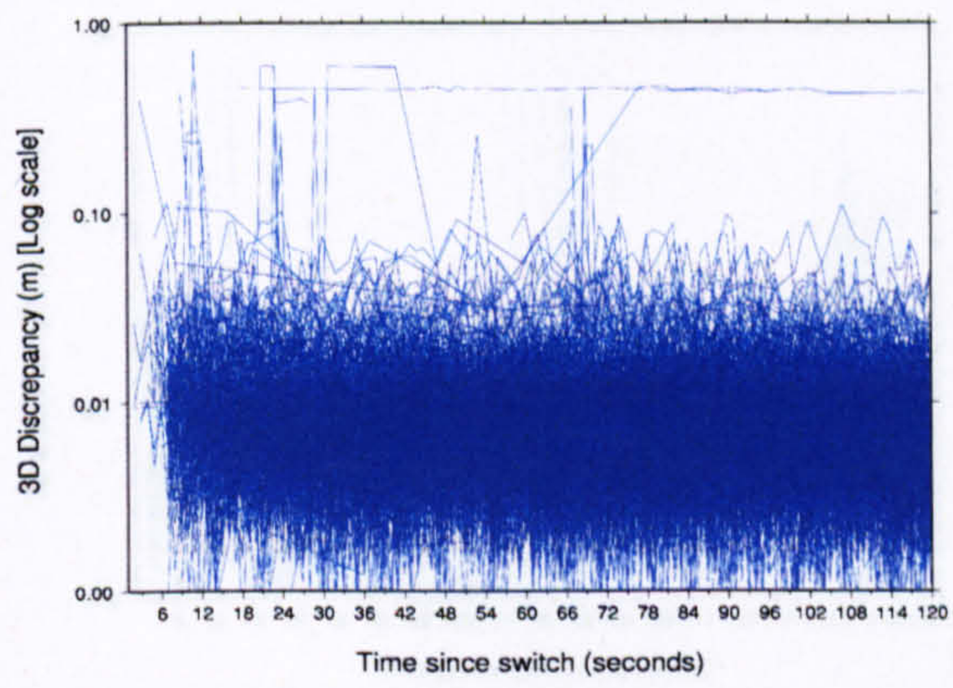

a) DRME

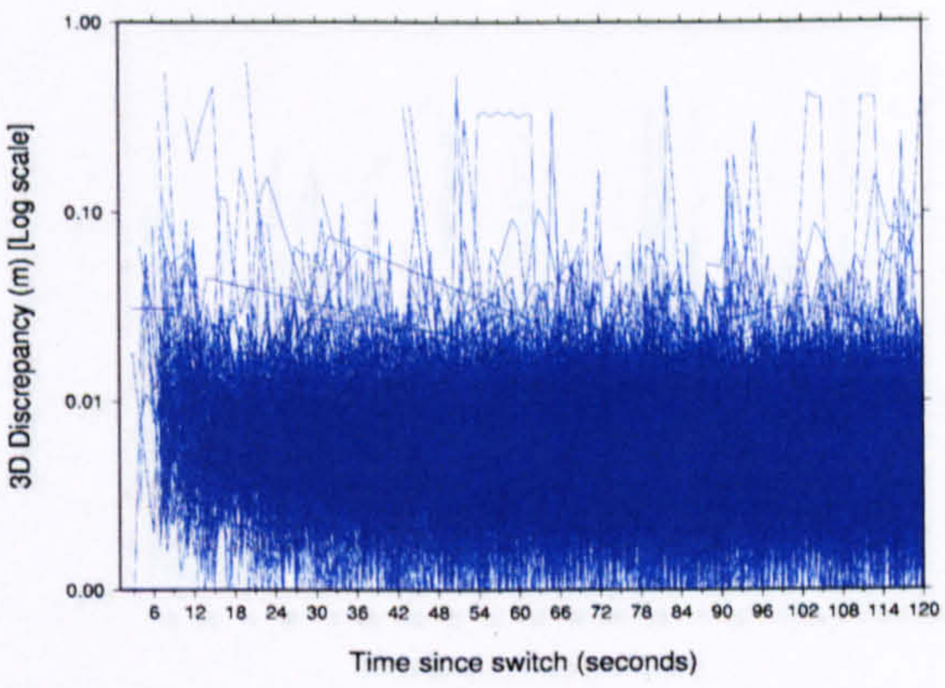

b) DRMS

Figure 5.11 3D discrepancies for all two minute switch sessions after removing epochs > 50 cm.

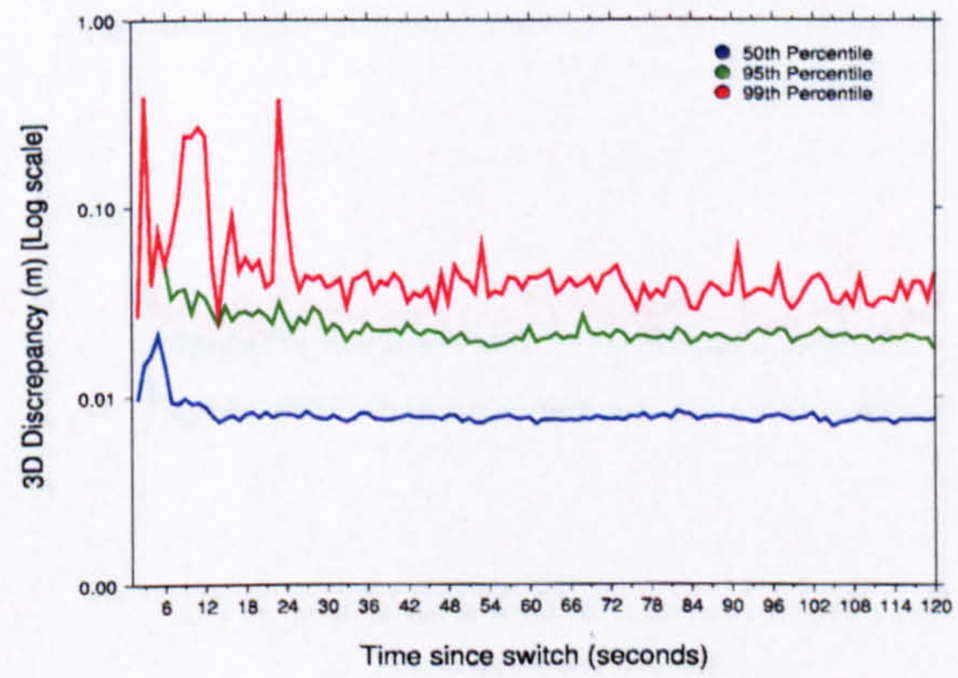

a) DRME

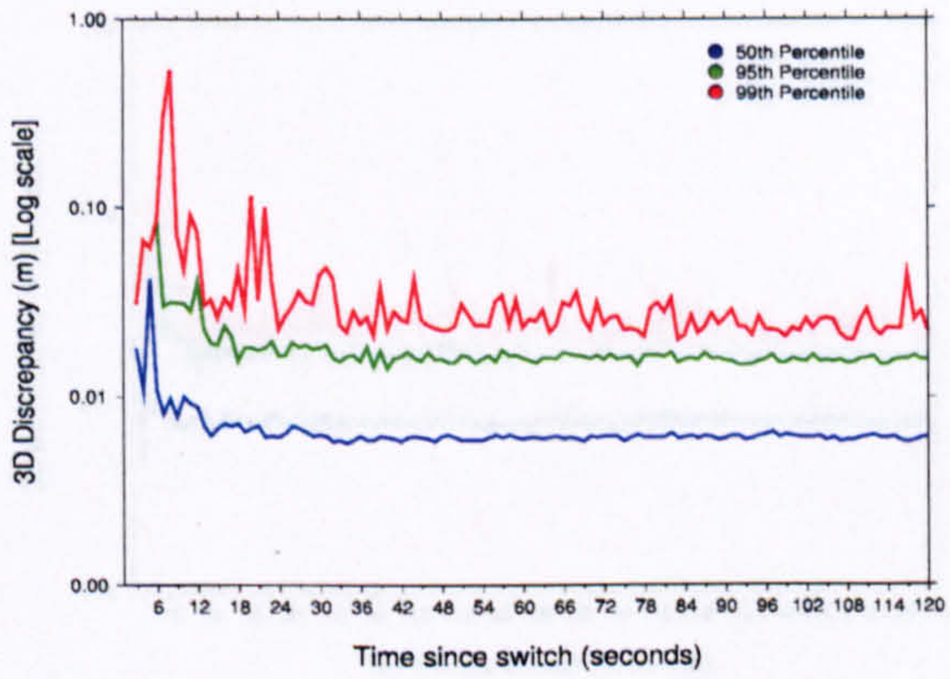

b) DRMS

Figure 5.12 3D discrepancy percentiles for two minute switch interval after removing bad epochs > 50 cm.

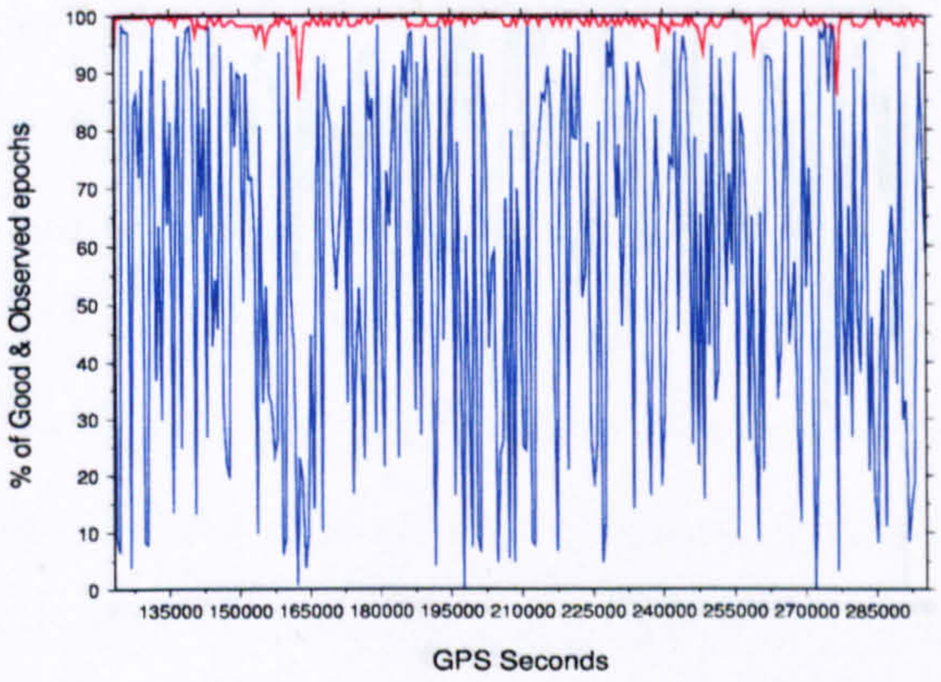

a) DRME

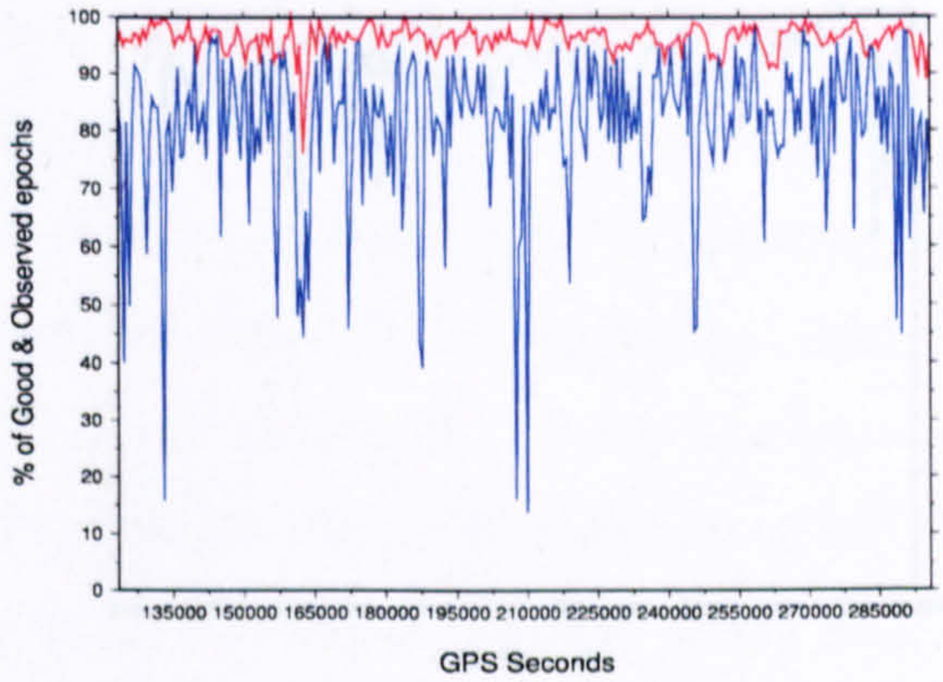

b) DRMS

Figure 5.13 Percentage of passing good epochs (less than 50 cm) and total observed epochs for five minute switch interval. Line attributes as before.

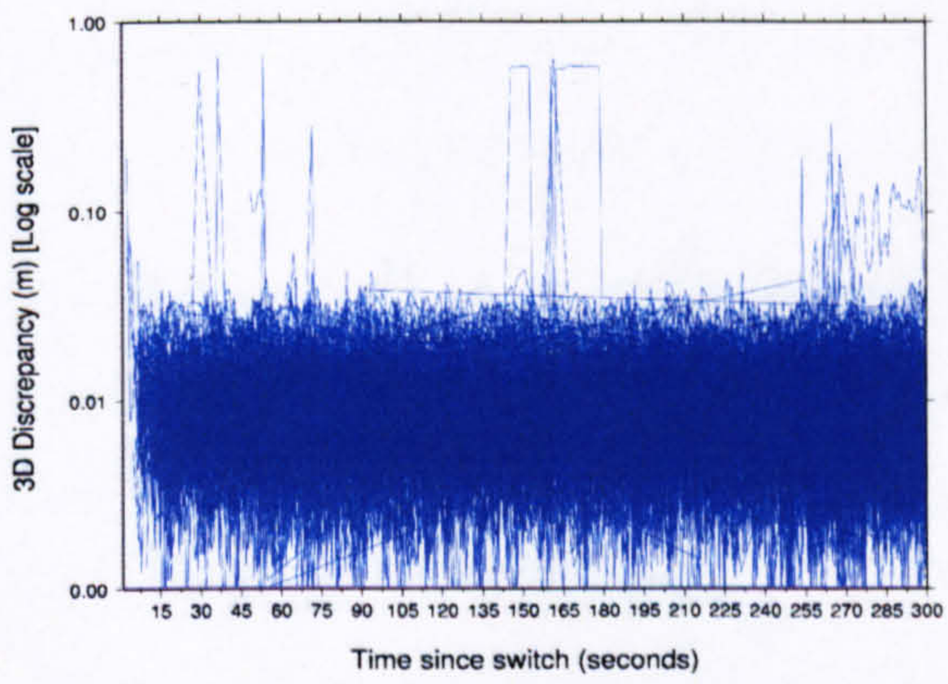

a) DRME

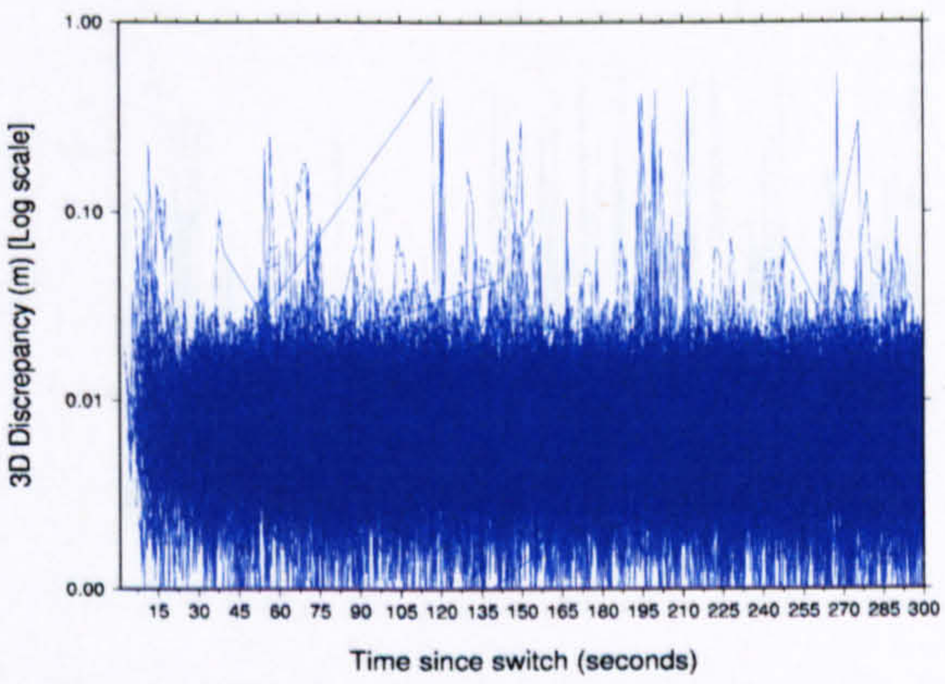

b) DRMS

Figure 5.14 3D discrepancies for all five minute switch sessions after removing epochs > 50 cm.

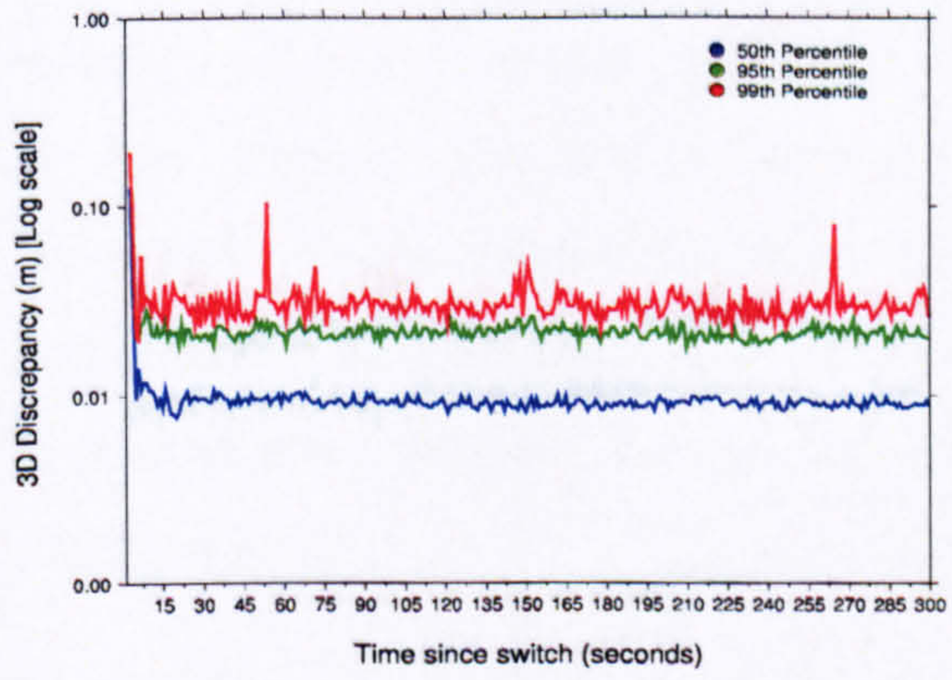

a) DRME

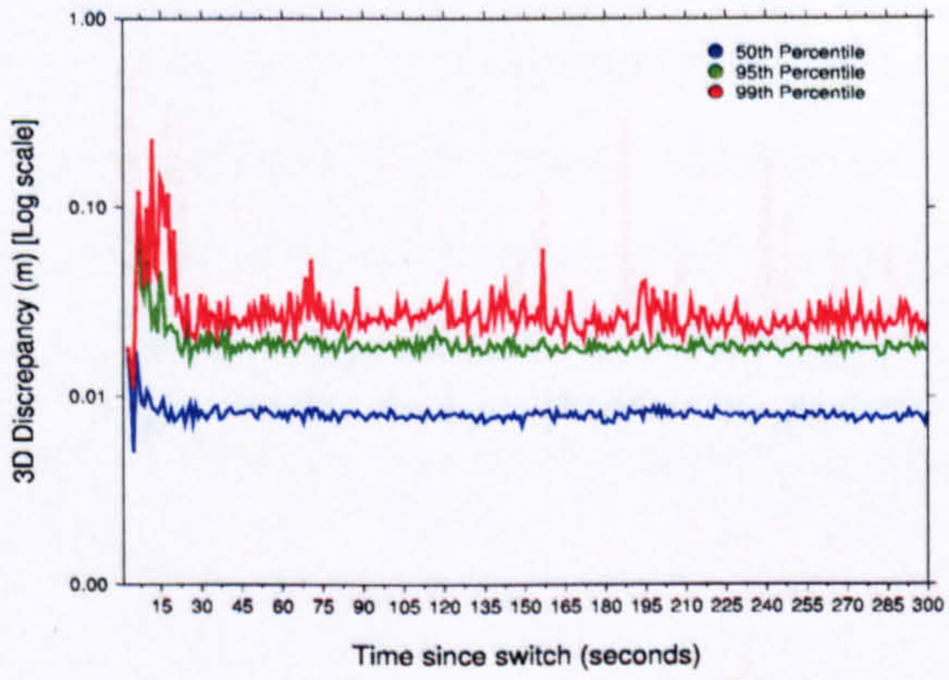

b) DRMS

Figure 5.15 3D discrepancy percentiles for five minute switch interval after removing bad epochs > 50 cm.

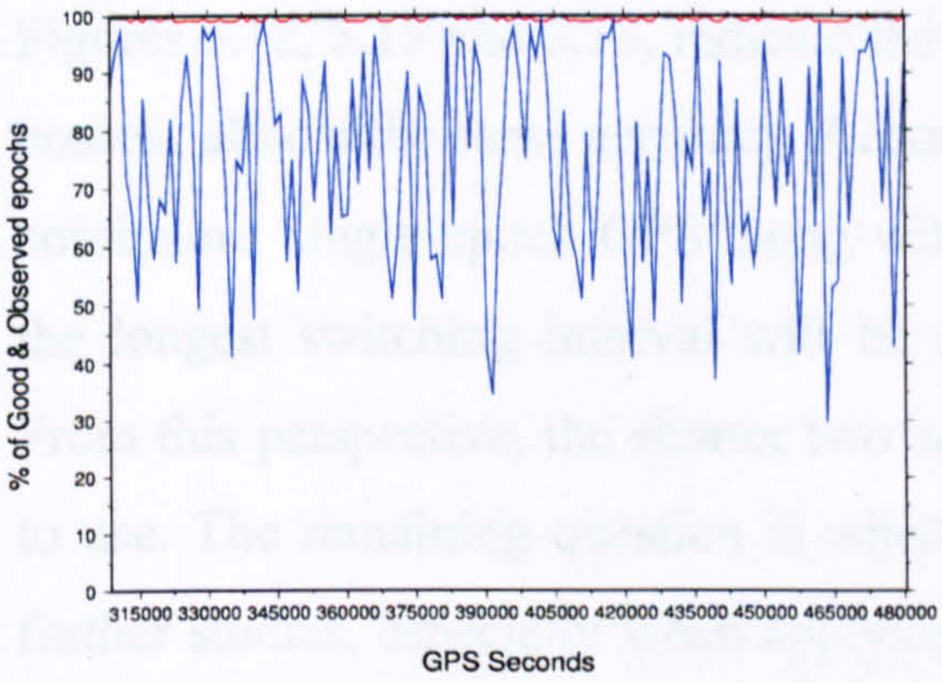

a) DRME

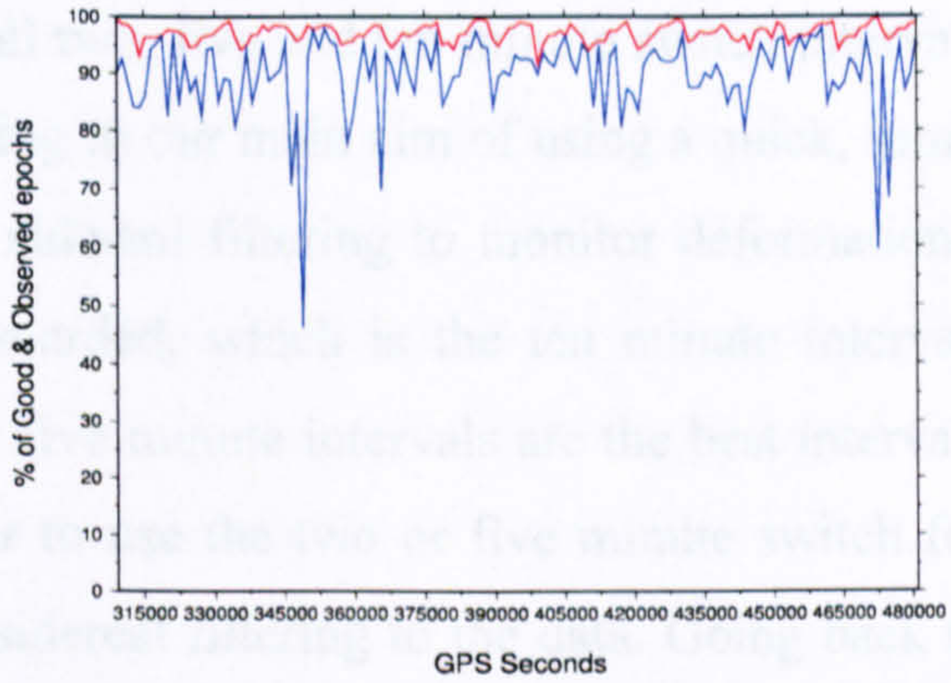

b) DRMS

Figure 5.16 Percentage of passing good epochs (less than 50 cm) and total observed epochs for ten minute switch interval. Line attributes as before.

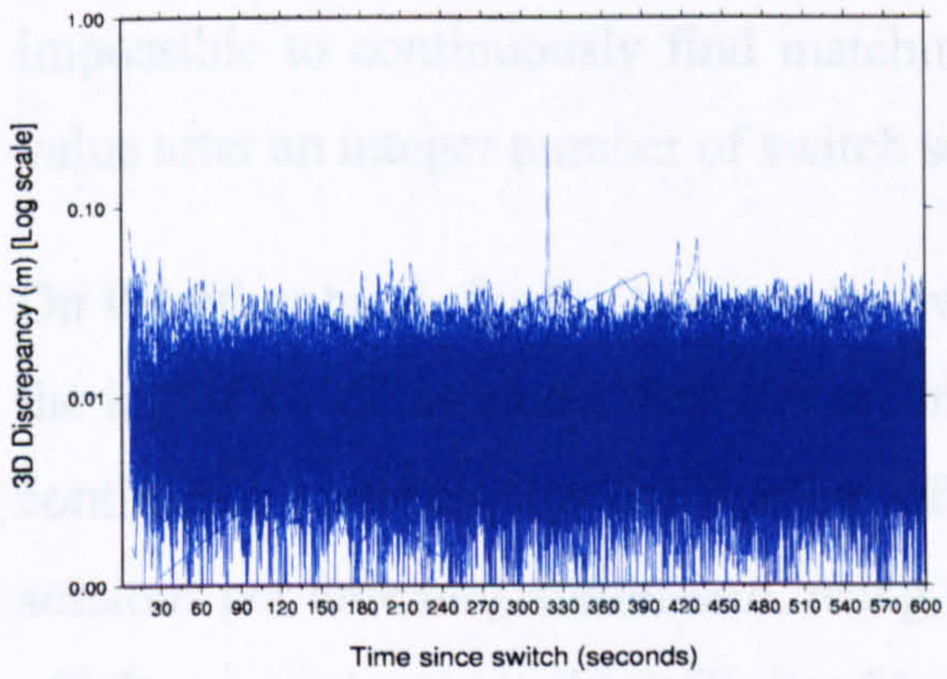

a) DRME

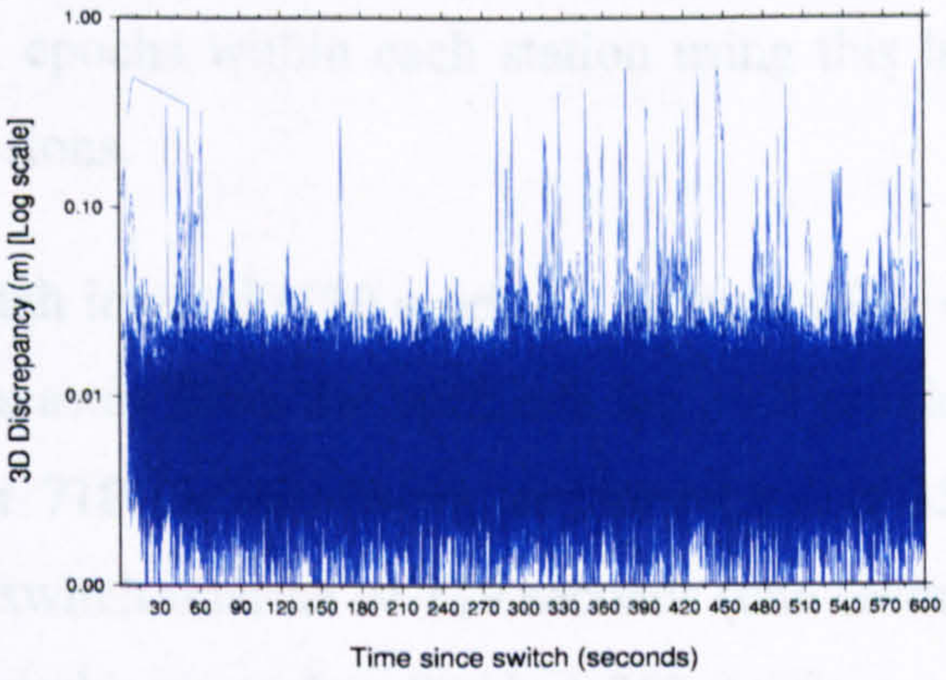

b) DRMS

Figure 5.17 3D discrepancies for all ten minute switch sessions after removing epochs > 50 cm.

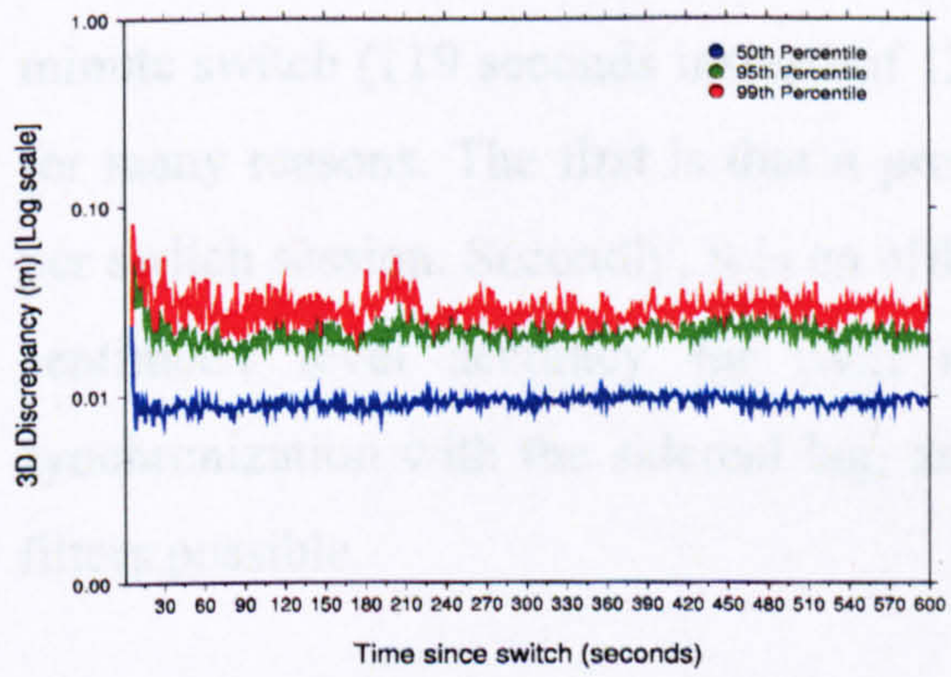

a) DRME

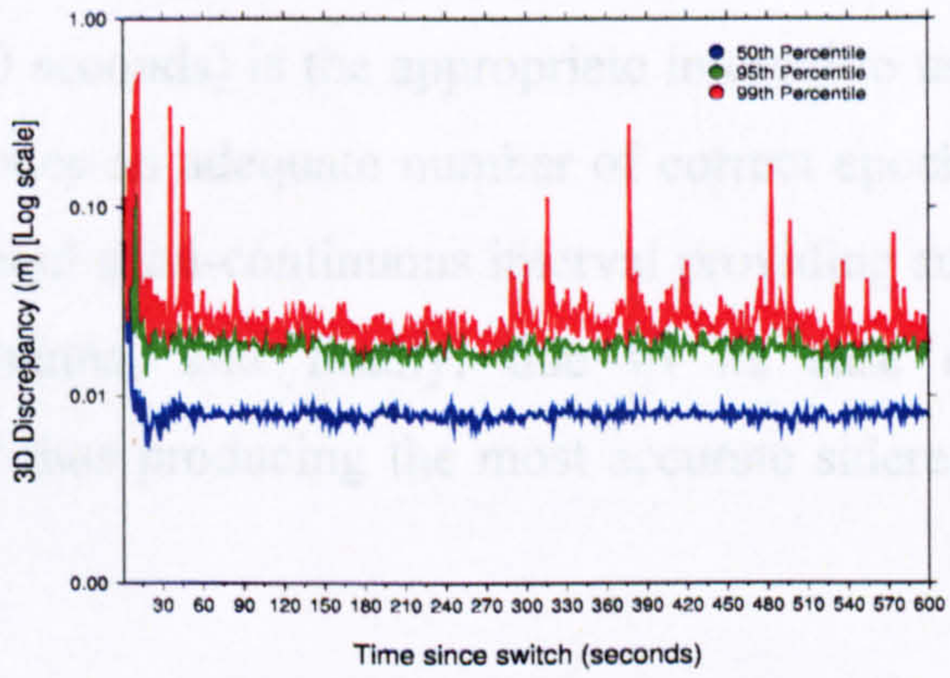

b) DRMS

Figure 5.18 3D discrepancy percentiles for ten minute switch interval after removing bad epochs > 50 cm.

Figures 5.12, 5.15 and 5.18, indicate that all two, five and ten minute switch intervals possess almost the same accuracy. According to our main aim of using a quick, semi-continuous single epoch GPS along with sidereal filtering to monitor deformations, the longest switching interval will be discarded, which is the ten minute interval. From this perspective, the shorter two and five minute intervals are the best intervals to use. The remaining question is whether to use the two or five minute switch for further studies, especially when applying sidereal filtering to the data. Going back to the optimum value of the lag being 86154 seconds (Chapter 3), the five minute switch (300 seconds) cannot be synchronized with this lag value. In other words, by using a 300 seconds switch interval (or even using a range of ± 20 seconds), it will be impossible to continuously find matching epochs within each station using this lag value after an integer number of switch sessions.

On the other hand, for the two minute switch interval (120 seconds), using a value of the lag of 86160 seconds, that is 6 seconds away from the optimum lag, will provide continuous matching epochs starting after 718 overall switch sessions (that is 359 sessions per antenna). Better still, using a switch interval of 119 seconds (one second off the two minute mark), will provide matching epochs after just 362 sessions per antenna with a lag value of 86156 seconds (23h 55m 56s). This lag value is only two seconds off the previously obtained optimum lag. Consequently, the modified two minute switch (119 seconds instead of 120 seconds) is the appropriate interval to use for many reasons. The first is that it provides an adequate number of correct epochs per switch session. Secondly, it is an efficient semi-continuous interval providing sub centimetre level accuracy for each antenna, and finally, due to its ease of synchronization with the sidereal lag, and thus producing the most accurate sidereal filters possible.

5.6 Switched Antenna Sidereal Filter Application

After the determination of the optimum switch session observation interval, it was vital to illustrate the behaviour of the switched data when applying filtered residuals. As shown previously, coordinate filtering gives higher precision than observation filtering (Chapter 4), and thus the former technique is used here for the formation of

coordinate filter residuals. For the two minute switch interval (120 seconds), the residuals of the first day of data for each switch station (≈ 12 hours of data) were applied to the coordinates of the second day of data per station, which are one sidereal lag apart. The most suitable lag is used here which is set to be 86160 seconds (23h 56m 00s). This lag is off the optimum lag by six seconds; however it should not significantly affect the resulting precision, as previously shown in Section 3.5.2.

Another sub-script within the main script MASS is used to automate the whole filter application process by inputting the obtained coordinates from GASP into the FAP program (Chapter 3). The coordinates are stacked and applied depending on the sidereal lag and number of stacked days stated in the main script. After this, the hourly and 24-hr coordinate standard deviations are calculated for all three directional components and 3D, then plotted automatically for the resulting filtered and unfiltered coordinates. This is done while considering several acceptance limits, starting from the previously used 50 cm, and then 40 cm, 30 cm, 20 cm and finally 10 cm, to assess the performance of sidereal filtering using periodic data. Figure 5.19a,b illustrates the hourly filtered and unfiltered coordinate standard deviations after removing any bad epochs having discrepancies greater than 50 cm for DRME and DRMS, respectively. Figures 5.20, 5.21, 5.22 and 5.23 are formed similarly to Figure 5.19, while using an acceptance limit of 40 cm, 30 cm, 20 cm and 10 cm, respectively.

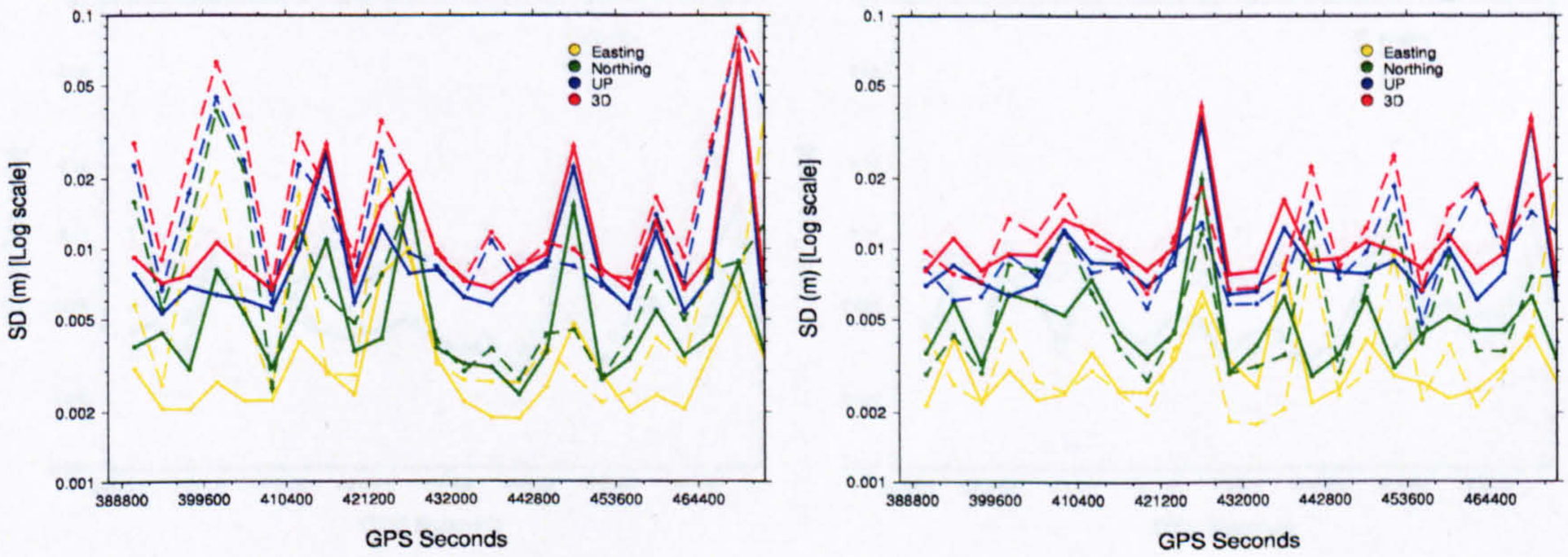

a) DRME **b) DRMS**

Figure 5.19 Hourly coordinate standard deviations using 50 cm limit for accepting epochs. Solid lines for filtered standard deviations. Dashed lines for unfiltered standard deviations.

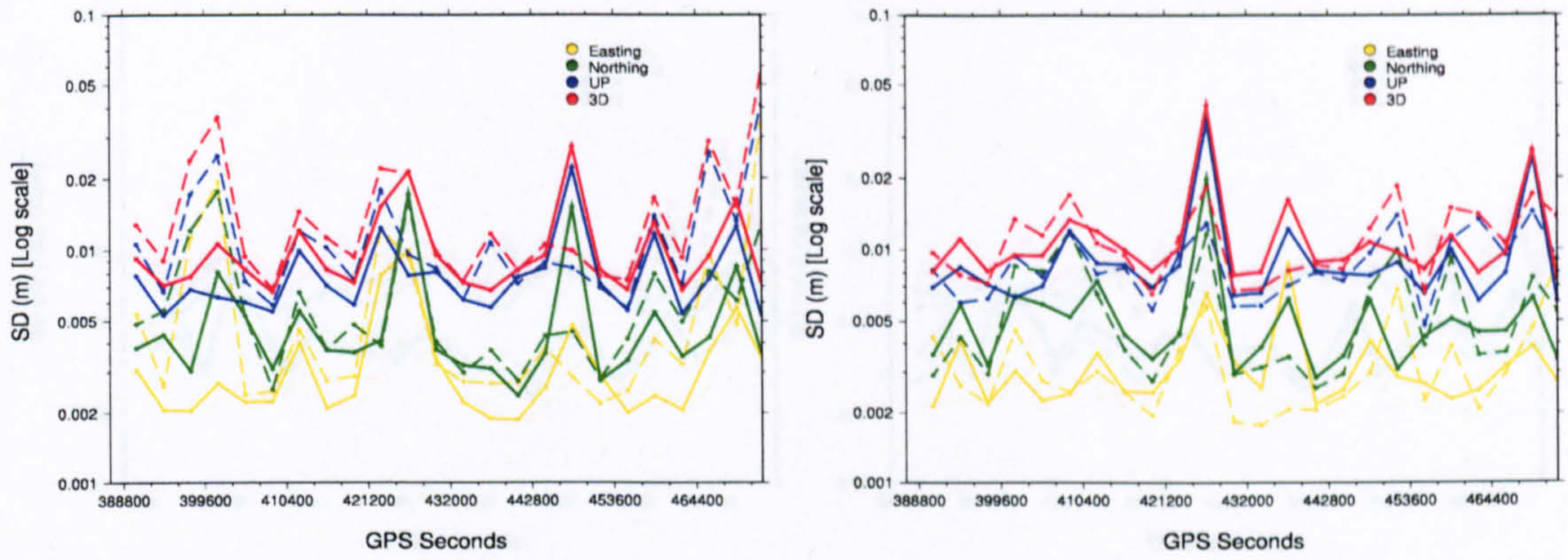

a) DRME b) DRMS

Figure 5.20 Hourly coordinate standard deviations using 40 cm limit for accepting epochs. Line attributes as before.

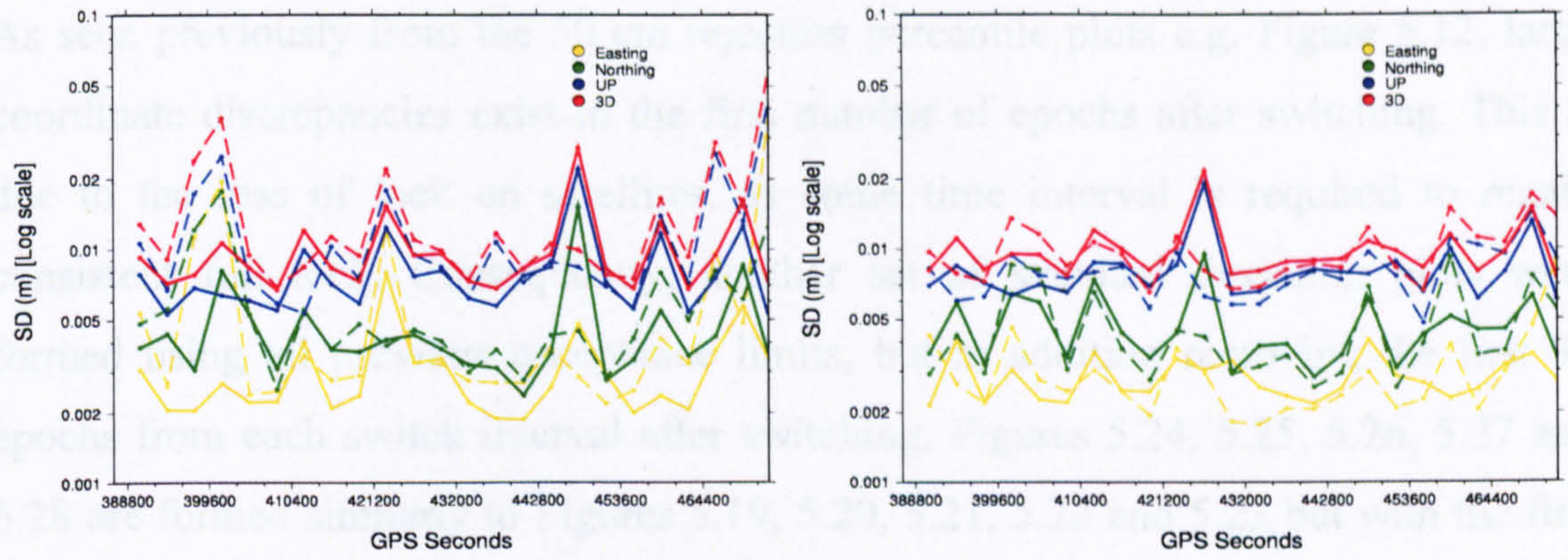

a) DRME b) DRMS

Figure 5.21 Hourly coordinate standard deviations using 30 cm limit for accepting epochs. Line attributes as before.

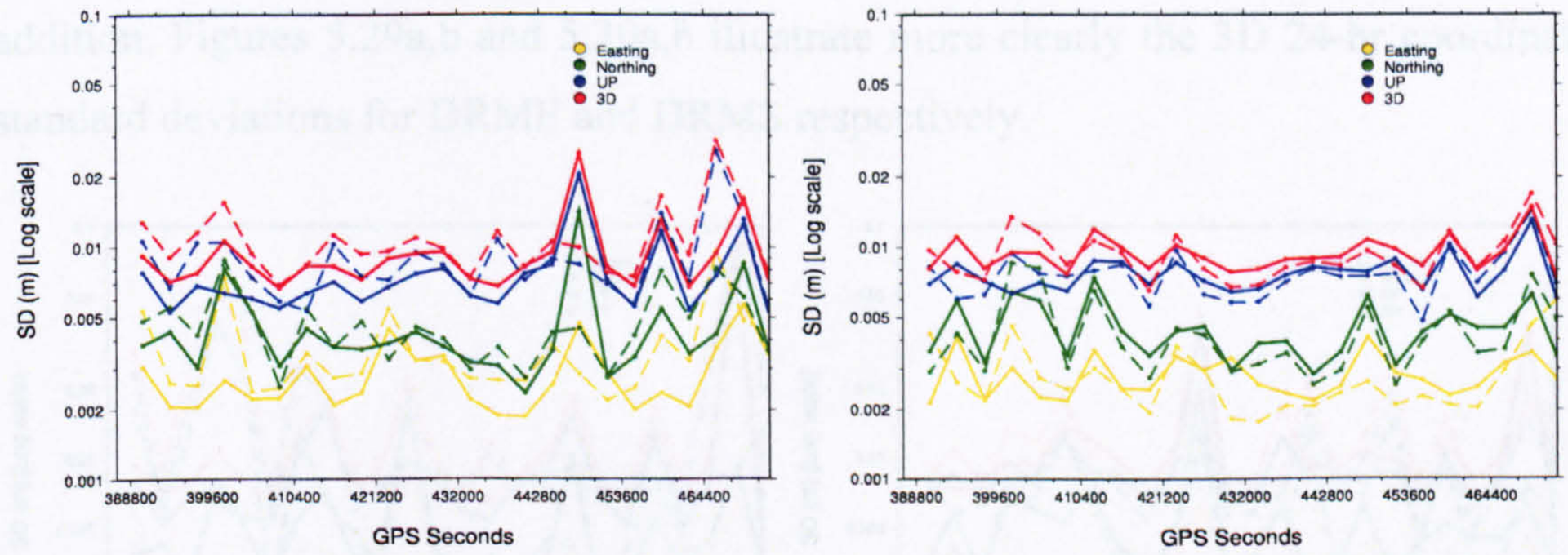

a) DRME b) DRMS

Figure 5.22 Hourly coordinate standard deviations using 20 cm limit for accepting epochs. Line attributes as before.

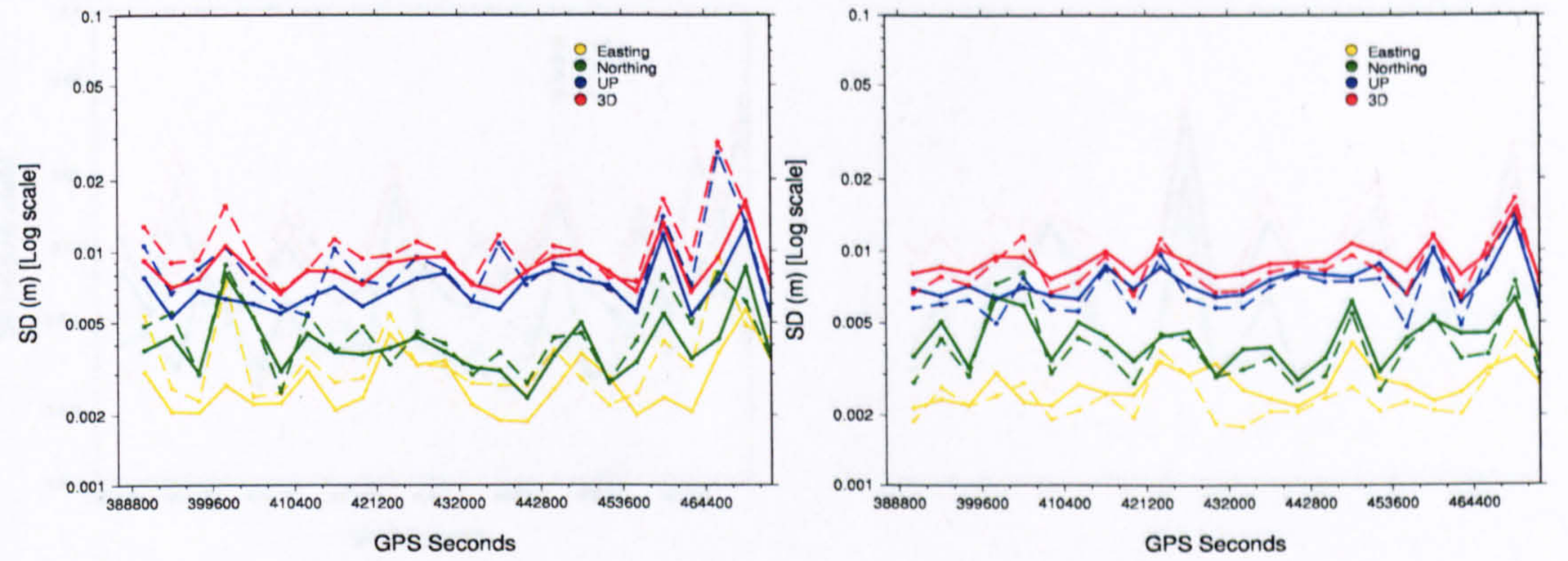

a) DRME **b) DRMS**

Figure 5.23 Hourly coordinate standard deviations using 10 cm limit for accepting epochs. Line attributes as before.

As seen previously from the 50 cm rejection percentile plots e.g. Figure 5.12, large coordinate discrepancies exist in the first number of epochs after switching. This is due to the loss of lock on satellites, as some time interval is required to regain consistent full lock. Consequently, another set of standard deviation plots were formed using all previous acceptance limits, but in addition removing the first 30 epochs from each switch interval after switching. Figures 5.24, 5.25, 5.26, 5.27 and 5.28 are formed similarly to Figures 5.19, 5.20, 5.21, 5.22 and 5.23 but with the first quarter of each session's epochs removed. Summing up, Tables 5.2 and 5.3 show the 24-hr coordinate standard deviations and variance reductions of the applied day for all three directional components, as well as 3D, for DRME and DRMS respectively. In addition, Figures 5.29a,b and 5.30a,b illustrate more clearly the 3D 24-hr coordinate standard deviations for DRME and DRMS respectively.

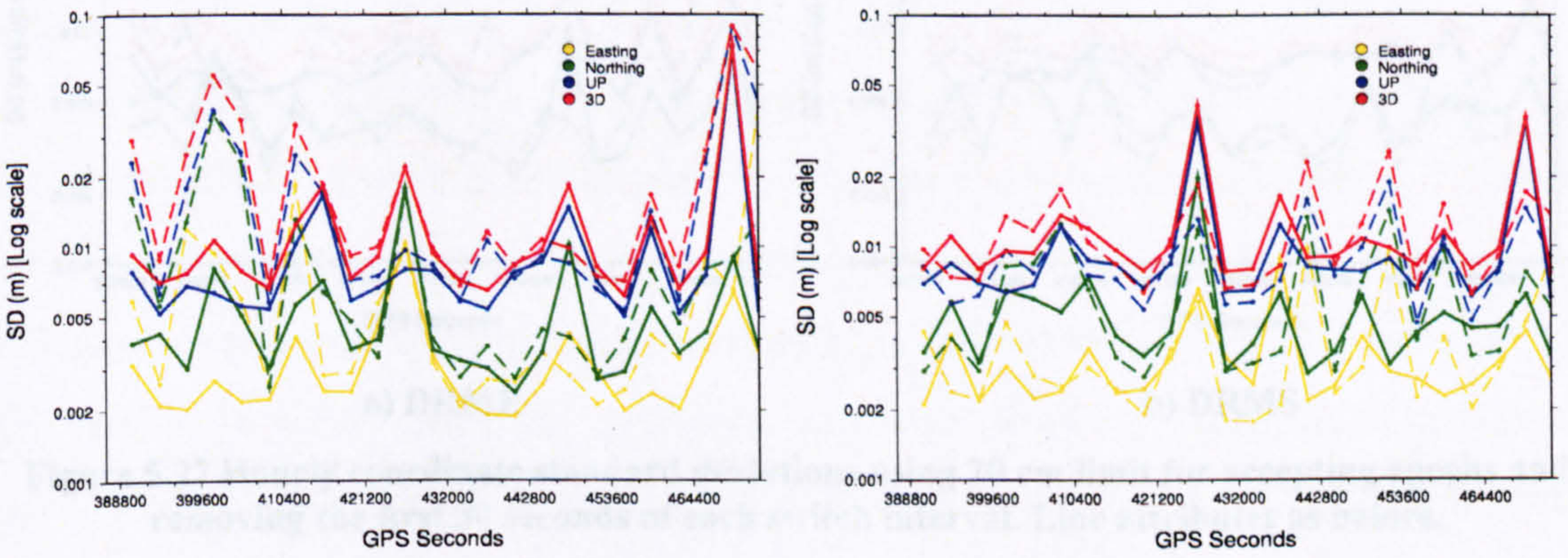

a) DRME **b) DRMS**

Figure 5.24 Hourly coordinate standard deviations using 50 cm limit for accepting epochs and removing the first 30 seconds of each switch interval. Line attributes as before.

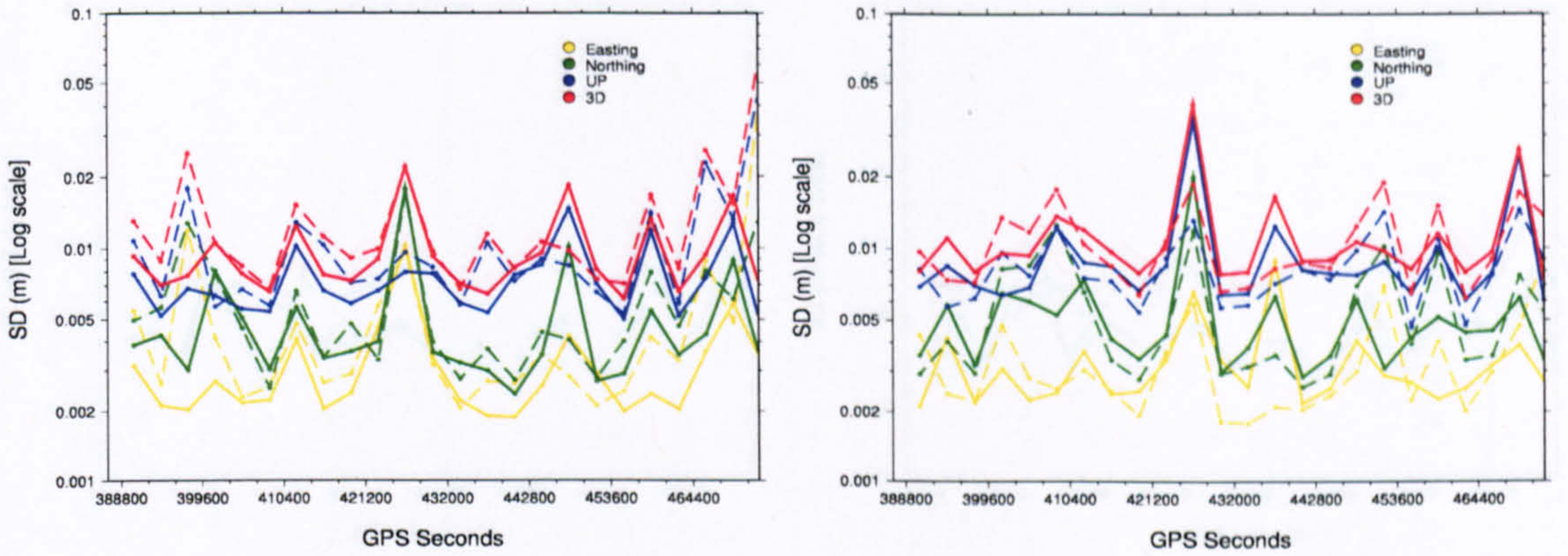

a) DRME b) DRMS

Figure 5.25 Hourly coordinate standard deviations using 40 cm limit for accepting epochs and removing the first 30 seconds of each switch interval. Line attributes as before.

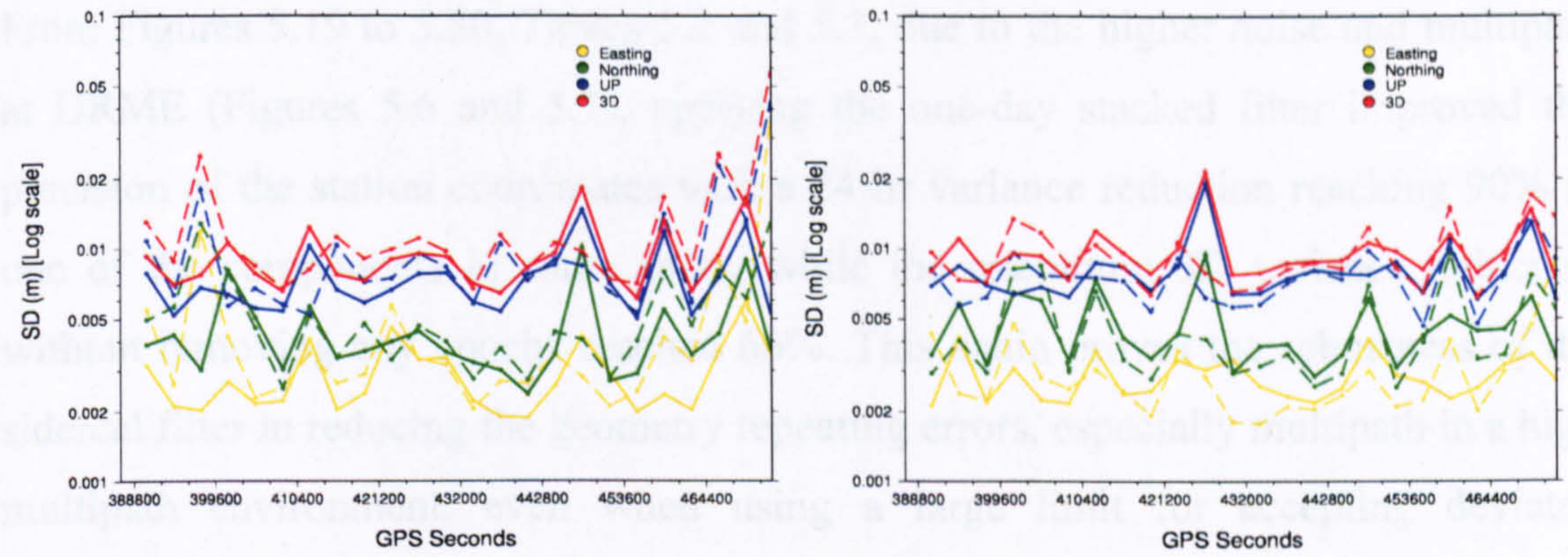

a) DRME b) DRMS

Figure 5.26 Hourly coordinate standard deviations using 30cm limit for accepting epochs and removing the first 30 seconds of each switch interval. Line attributes as before.

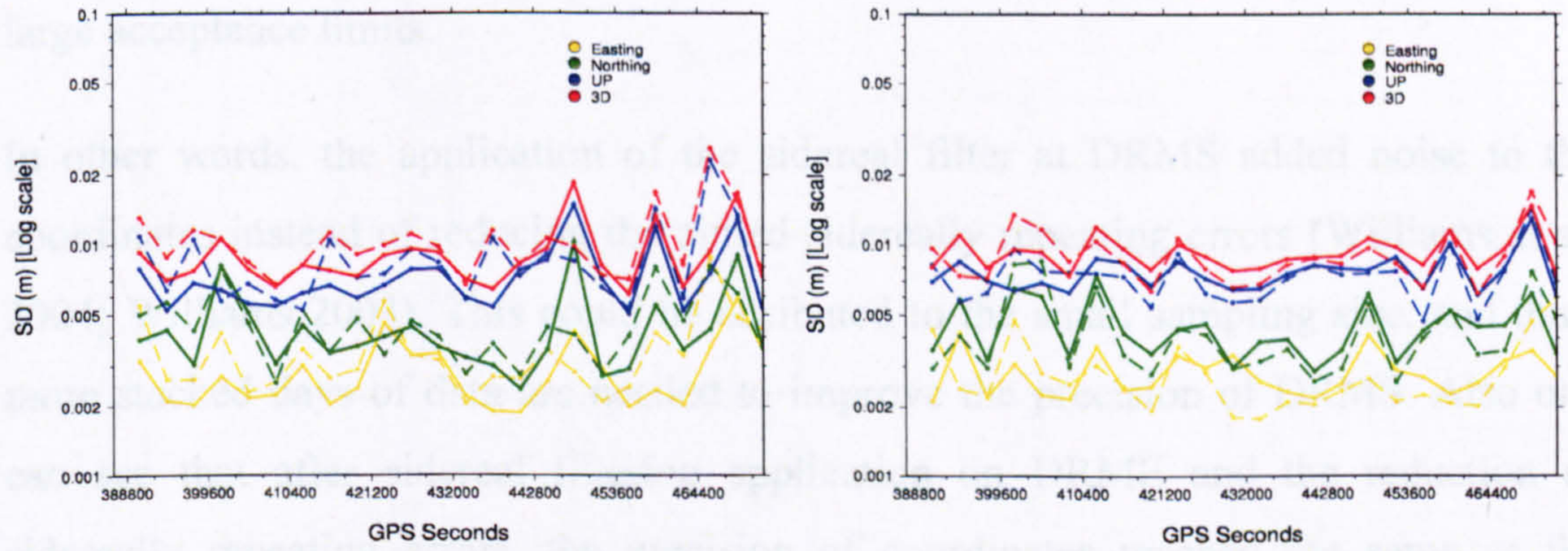

a) DRME b) DRMS

Figure 5.27 Hourly coordinate standard deviations using 20 cm limit for accepting epochs and removing the first 30 seconds of each switch interval. Line attributes as before.

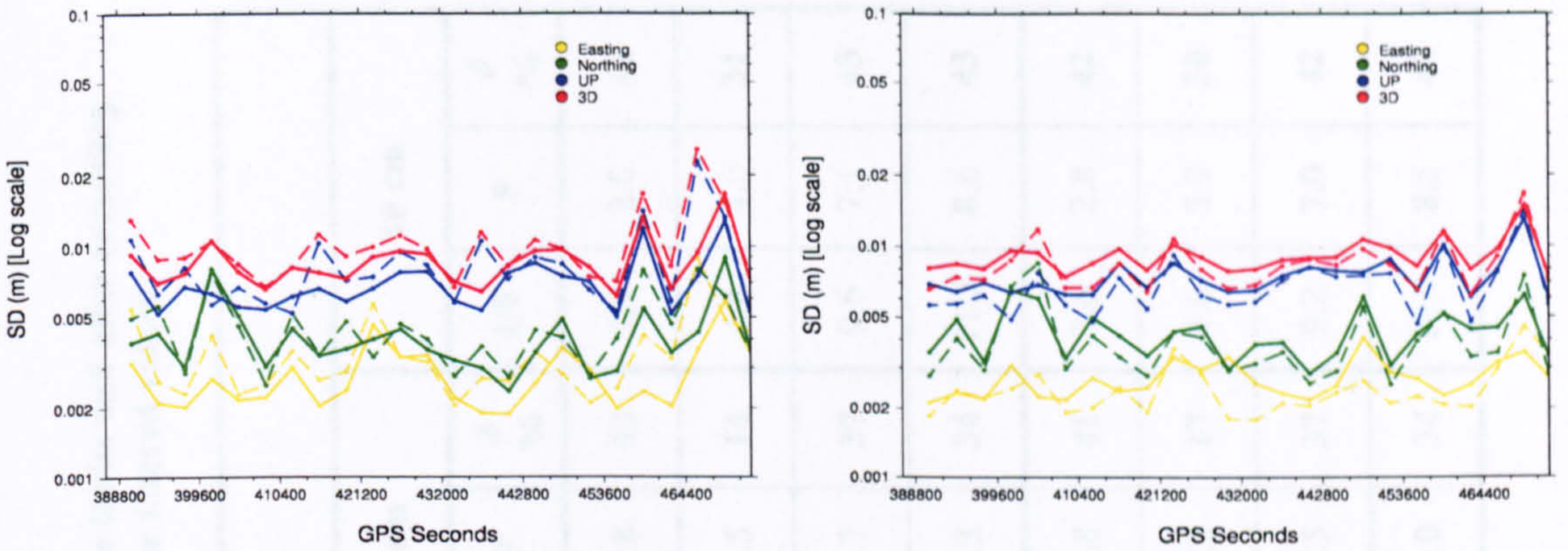

a) DRME **b) DRMS**

Figure 5.28 Hourly coordinate standard deviations using 10 cm limit for accepting epochs and removing the first 30 seconds of each switch interval. Line attributes as before.

From Figures 5.19 to 5.30, Tables 5.2 and 5.3, due to the higher noise and multipath at DRME (Figures 5.6 and 5.7), applying the one-day stacked filter improved the precision of the station coordinates with a 24-hr variance reduction reaching 90% in one of the components in some cases, while the maximum 3D variance reduction without removing any epochs reached 66%. This again proves the robustness of the sidereal filter in reducing the geometry repeating errors, especially multipath in a high multipath environment, even when using a large limit for accepting deviated coordinates. On the other hand, for DRMS, having a relative low multipath environment, applying the one day stacked filter with periodic data did not give much improvement in the precision of the coordinates, especially in the up direction, for large acceptance limits.

In other words, the application of the sidereal filter at DRMS added noise to the coordinates instead of reducing the aimed sidereally repeating errors (Williams et al. 2004; Williams 2003). This could be attributed to the small sampling size, and thus, more stacked days of data are needed to improve the precision of DRMS. Also one can see that after sidereal filtering application on DRME and the reduction of sidereally repeating errors, the precision of coordinates reached the same as the filtered or in some cases the unfiltered precision level of DRMS. As previously concluded, the same level of precision is achieved despite the multipath environment surrounding the station.

Table 5.2 24-hr Easting, Northing, Up and 3D coordinate standard deviations for all cases of acceptance limits and after removing epochs for DRME. (δ) stands for variance reduction, (UF) stands for unfiltered values while (F) stands for filtered values.

CASE	SD (mm)	Acceptance Limits														
		50 cm			40 cm			30 cm			20 cm			10 cm		
		UF	F	δ %	UF	F	δ %	UF	F	δ %	UF	F	δ %	UF	F	δ %
Considering all switch interval epochs	E	10.3	3.6	88	9.3	3.5	86	9.2	3.2	88	3.7	2.8	43	3.7	2.8	45
	N	9.6	6.4	56	6.7	5.8	25	6.2	5.0	35	4.8	4.5	14	4.8	4.0	31
	U	19.3	11.7	63	14.3	8.8	62	14.0	8.8	61	9.7	7.7	37	9.6	7.1	45
	3D	23.9	13.8	66	18.3	11.1	63	17.9	10.6	65	11.5	9.3	34	11.3	8.6	43
Removing first 30 epochs from switch interval	E	10.5	3.4	90	9.5	3.3	88	9.3	2.9	90	3.6	2.8	41	3.6	2.8	42
	N	10.0	5.6	69	6.7	5.3	37	6.2	4.4	49	4.7	4.3	17	4.6	3.9	30
	U	19.8	9.7	76	14.1	7.8	69	13.8	7.8	68	9.4	7.5	37	9.2	7.0	42
	3D	24.5	11.7	77	18.2	10.0	70	17.8	9.4	72	11.1	9.0	34	10.9	8.5	40

Table 5.3 24-hr Easting, Northing, Up and 3D coordinate standard deviations for all cases of acceptance limits and after removing epochs for DRMS. Abbreviations as before.

CASE	SD (mm)	Acceptance Limits														
		50 cm			40 cm			30 cm			20 cm			10 cm		
		UF	F	δ %	UF	F	δ %	UF	F	δ %	UF	F	δ %	UF	F	δ %
Considering all switch interval epochs	E	5.3	3.6	53	3.7	3.6	5	3.3	2.8	27	3.0	2.8	9	2.6	2.7	-10
	N	7.1	6.1	27	6.2	6.1	4	5.0	4.7	11	4.7	4.6	5	4.4	4.3	2
	U	10.5	11.8	-26	9.3	11.5	-51	8.4	8.2	4	8.0	7.7	7	7.5	7.5	-1
	3D	13.8	13.8	0	11.8	13.5	-30	10.3	9.9	8	9.7	9.4	6	9.0	9.1	-1
Removing first 30 epochs from switch interval	E	4.5	3.7	33	3.8	3.7	6	3.4	2.8	29	3.0	2.8	10	2.5	2.7	-11
	N	7.2	6.1	27	6.3	6.1	5	5.0	4.7	12	4.6	4.5	4	4.3	4.3	0
	U	9.7	11.9	-53	8.9	11.6	-71	8.0	8.2	-4	7.7	7.7	2	7.2	7.4	-6
	3D	12.8	13.9	-18	11.5	13.6	-39	10.0	9.8	3	9.5	9.3	3	8.8	9.0	-5

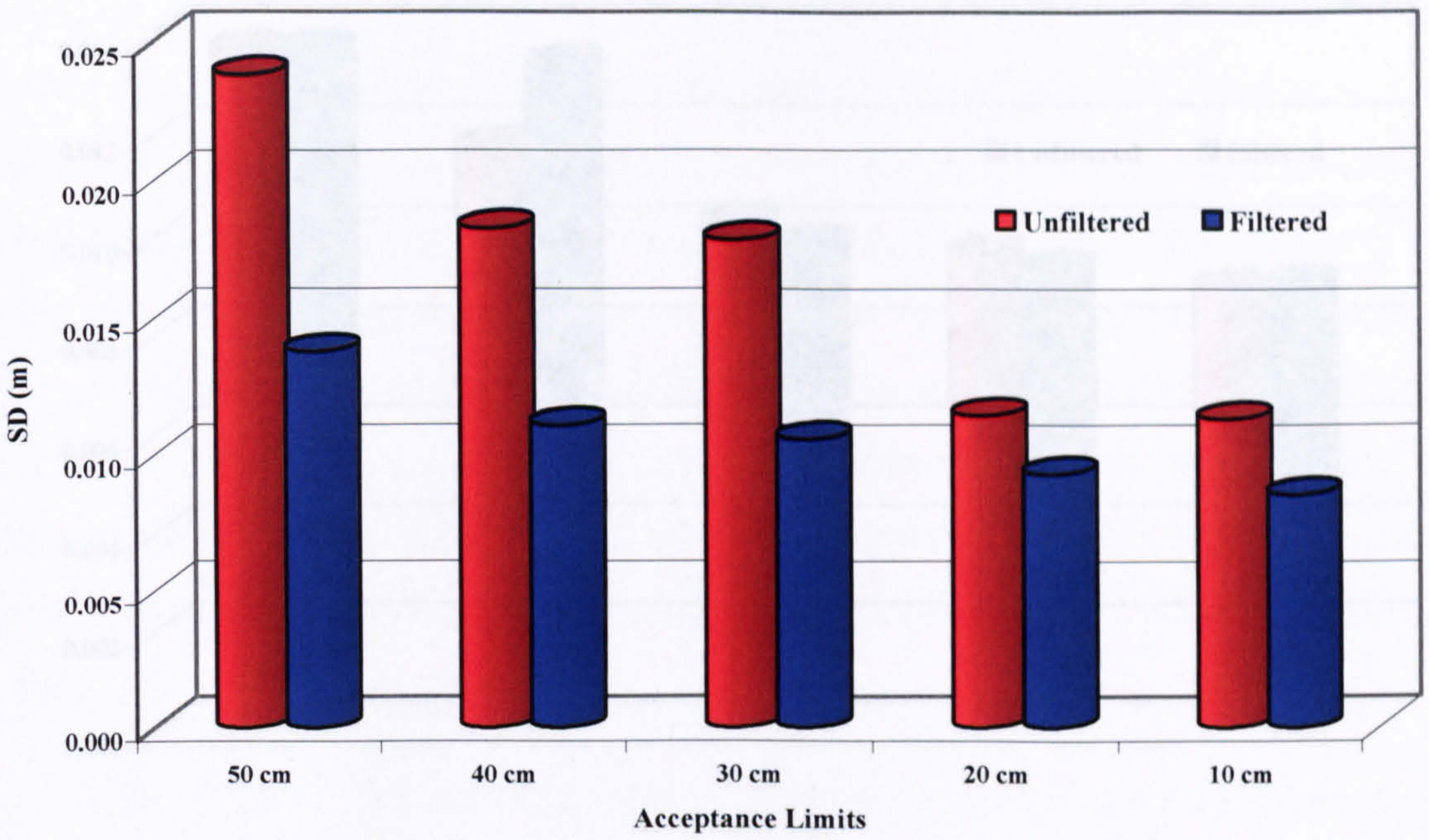

(a)

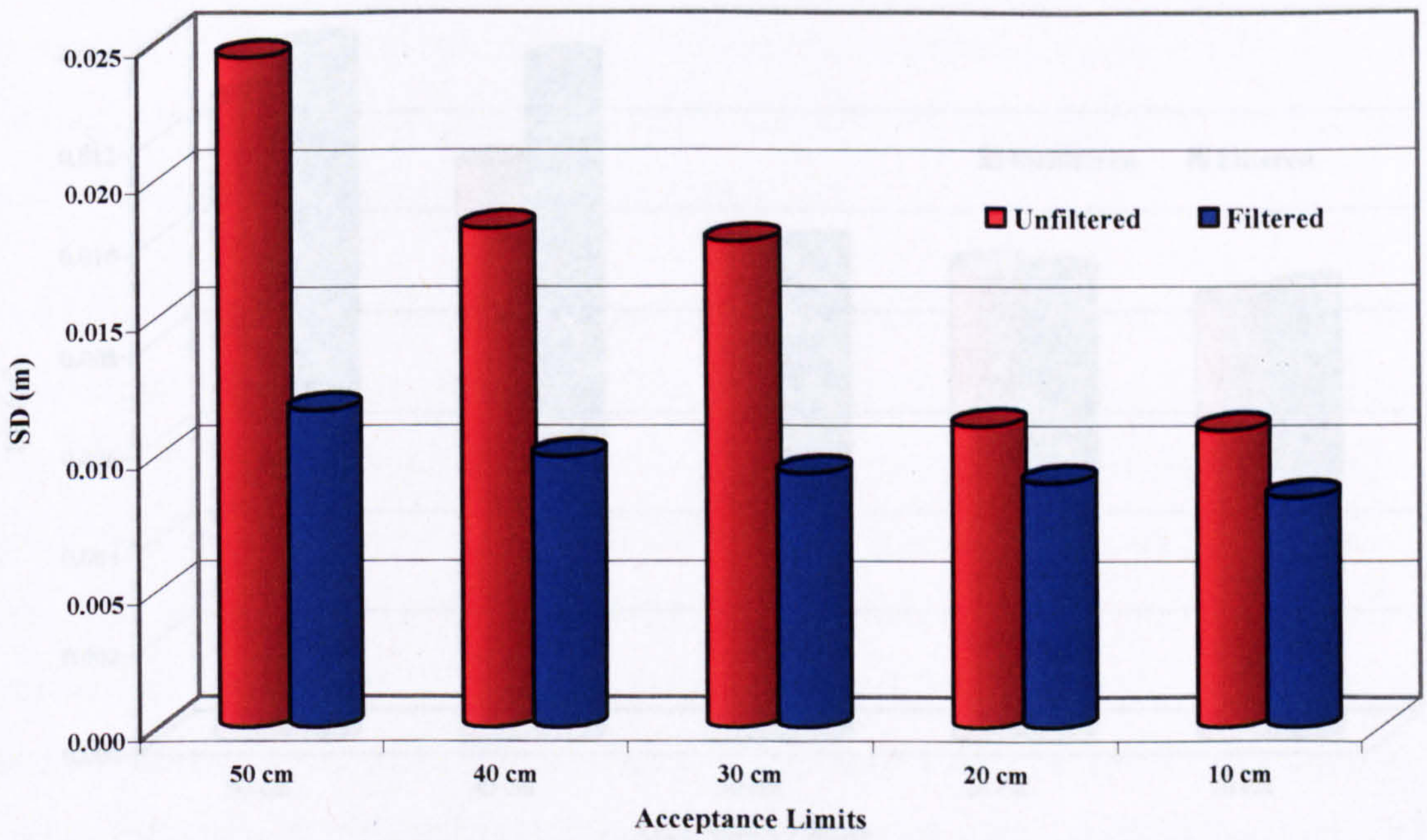

(b)

Figure 5.29 DRME filtered and unfiltered 24-hr 3D coordinate standard deviations for all accepting limits. a) without removing any epochs from the switch session, and b) removing the first 30 seconds from the switch session.

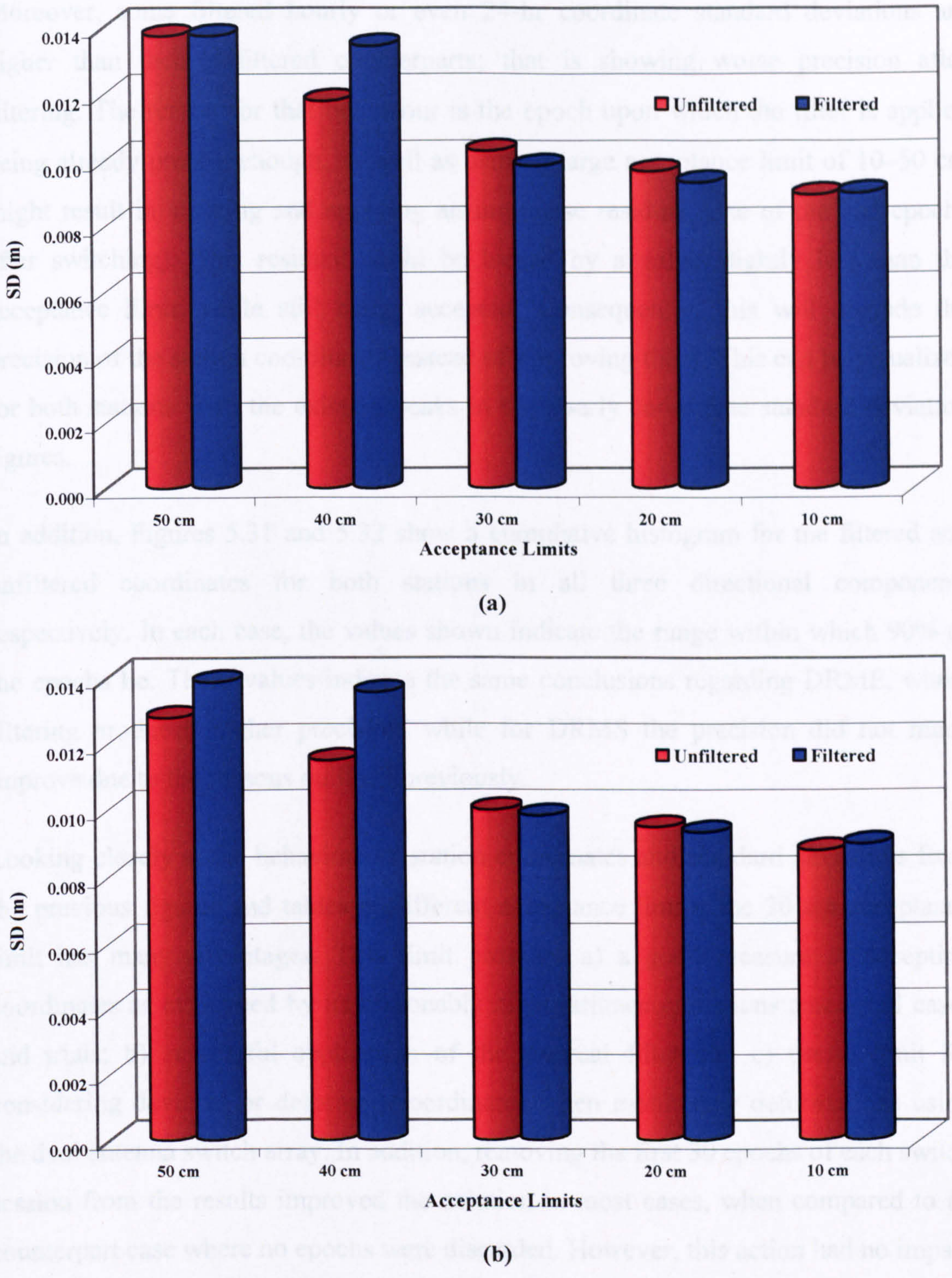

Figure 5.30 DRMS filtered and unfiltered 24-hr 3D coordinate standard deviations for all accepting limits. a) without removing any epochs from the switch session, and b) removing the first 30 seconds from the switch session.

Moreover, some filtered hourly or even 24-hr coordinate standard deviations are higher than their unfiltered counterparts; that is showing worse precision after filtering. The reason for that behaviour is the epoch upon which the filter is applied being already precise enough, as well as using a large acceptance limit of 10–50 cm might result in stacking and applying an imprecise residual (one of the bad epochs after switching). This residual could be biased by a value slightly less than the acceptance limit, while still being accepted. Consequently, this will degrade the precision of the station coordinates instead of improving them. This can be visualized for both stations from the existing peaks in the hourly coordinate standard deviation figures.

In addition, Figures 5.31 and 5.32 show a cumulative histogram for the filtered and unfiltered coordinates for both stations in all three directional components respectively. In each case, the values shown indicate the range within which 90% of the epochs lie. These values indicate the same conclusions regarding DRME, where filtering produced higher precision, while for DRMS the precision did not much improve due to the reasons outlined previously.

Looking closely at the behaviour of station coordinates and standard deviations from the previous figures and tables at different acceptance limits, the 30 cm acceptance limit has many advantages. This limit provides a) a good measure of accepting coordinates as evidenced by its reasonably high variance reductions among all cases and trials; b) successful application of the sidereal filter and c) useful limit for considering deviated or deformed coordinates when monitoring deformations using the dual antenna switch array. In addition, removing the first 30 epochs of each switch session from the results improved the solution in most cases, when compared to its counterpart case where no epochs were discarded. However, this action had no impact in some cases and as it decreased the amount of available data, it was decided to use all switch epochs in future.

Furthermore, comparing the unfiltered standard deviations of both DRME and DRMS, one can see the effect of the multipath environment on the actual station coordinates as first depicted from Figures 5.6 and 5.7. Finally, the sidereal

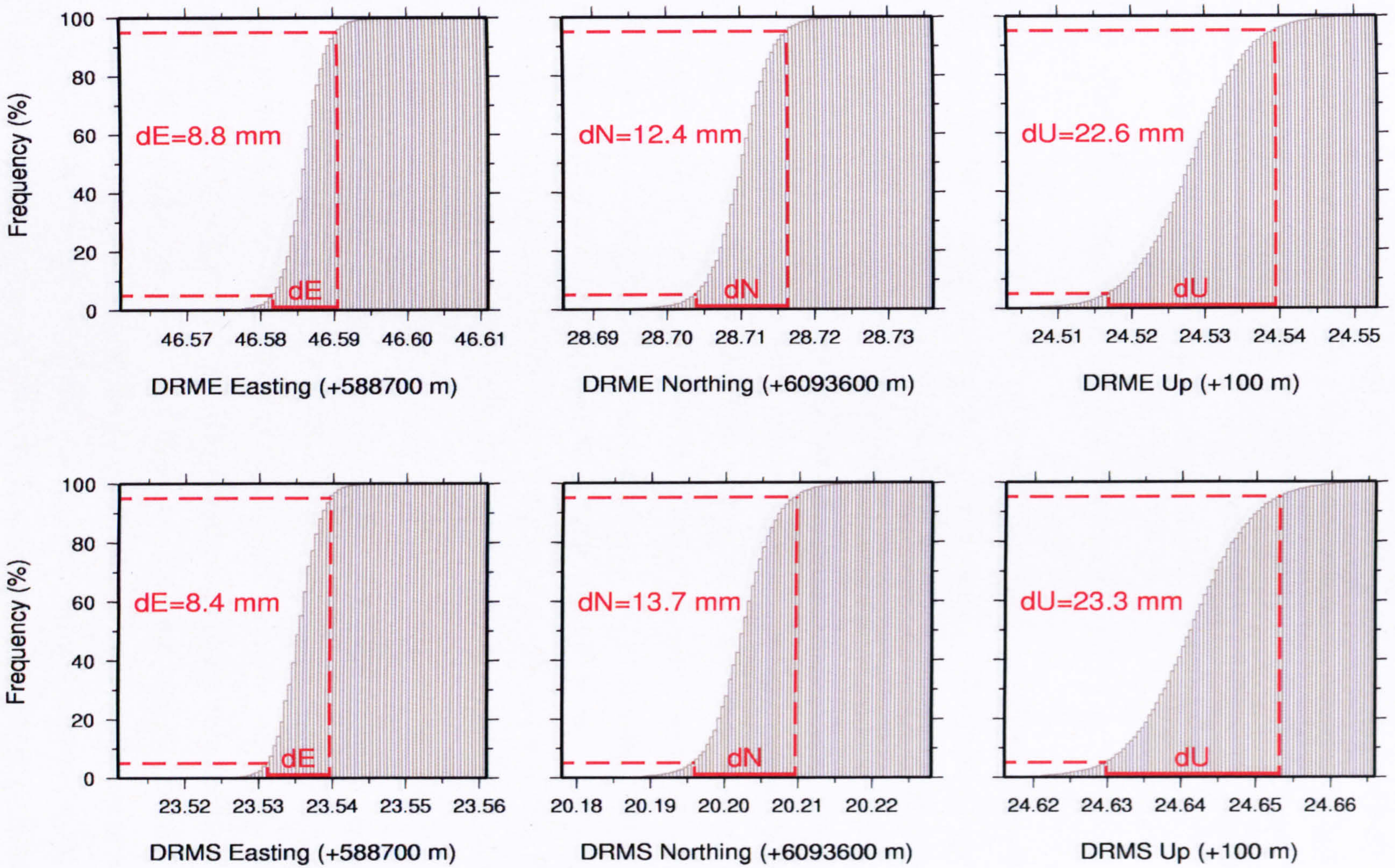

Figure 5.31 Filtered coordinate cumulative histogram for both stations using 50 cm acceptance limit in three directional components. Lower dashed line indicates 5 % frequency. Upper dashed line indicates 95 % frequency.

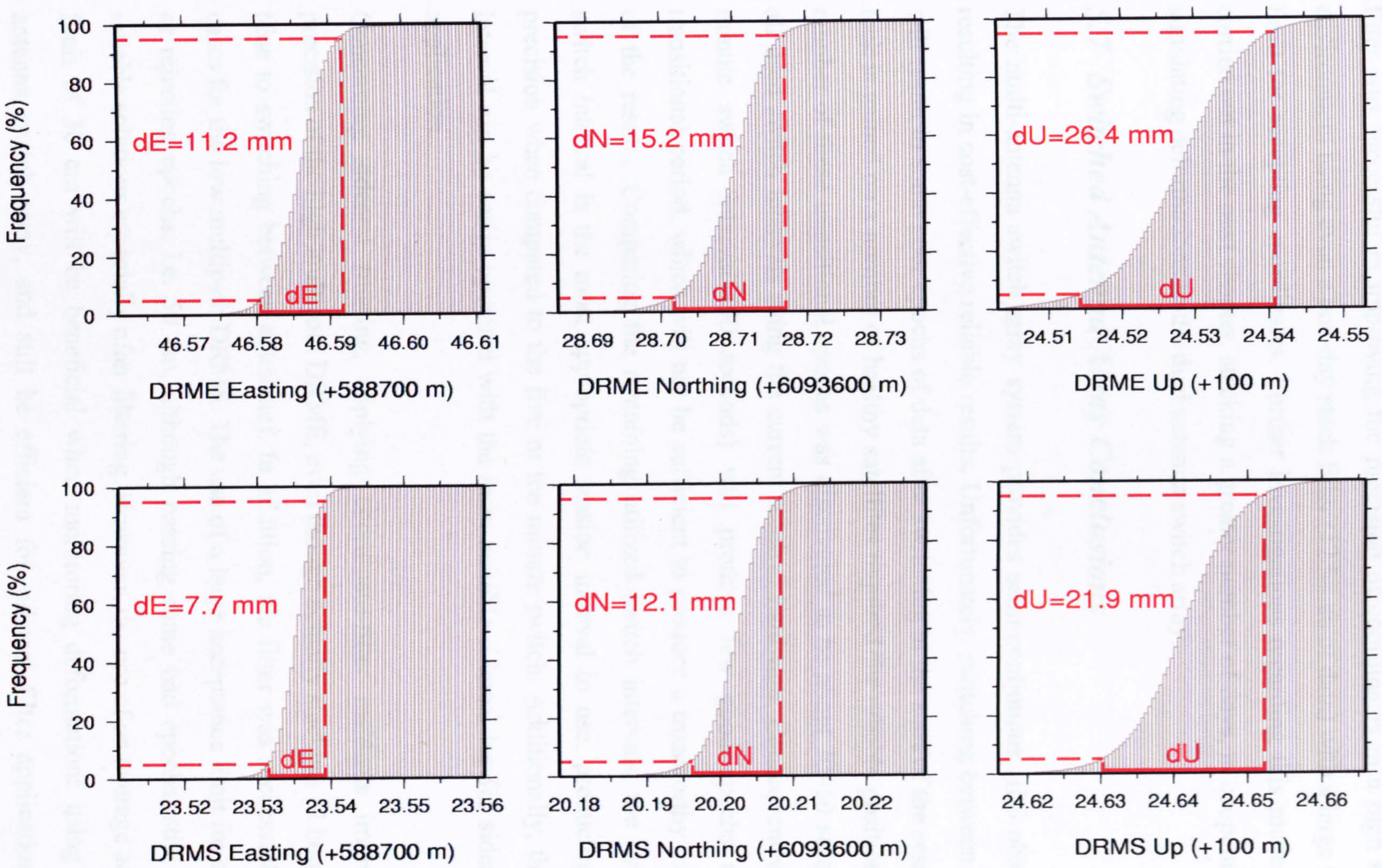

Figure 5.32 Unfiltered coordinate cumulative histogram for both stations using 50 cm acceptance limit in three directional components. Line attributes as before.

filter was successful in improving the precision of coordinates in a high multipath environment using even a one-day stack filter (12 hours of data) with a large tolerance limit for accepting coordinates. Further investigations regarding this matter will be carried out in the next chapter, stacking a greater number of days, in cooperation with simulating deformations to the dual antenna switch array.

5.7 Switched Antenna Array Conclusions

The multi-antenna switch array system provides semi-continuous GPS observations resulting in cost-effective reliable results. Unfortunately, switching between antennae will result in some poor epochs of data after switching at the start of the session until lock is gained on a number of healthy satellites required for reliable positioning. The number of these transitional epochs was discovered to be about 30–50 seconds over all used switch intervals using the current receiver hardware. Consequently, the one minute switch interval (60 seconds) will produce few good epochs after this transitional period, which will not be sufficient to produce a trustworthy assessment of the results. Comparing the remaining utilized switch intervals, the two minute switch interval is the most appropriate session interval to use, producing reliable precision when compared to the five or ten minute switch. Additionally, this switch interval can be easily operated with the most suitable sidereal lag for sidereal filter application.

Concerning sidereal filtering, applying coordinate-filter residuals improved the precision of the high multipath DRME, even though actually stacking 12 hours of data (due to switching between antennae). In addition, the filter was successful in some cases for the low multipath DRMS. The use of a large acceptance limit for approving or rejecting epochs, i.e. 50 cm, although passing some bad epochs, still produced reliable solutions especially after filtering. However, the use of an average acceptance limit of 30 cm will be beneficial when monitoring deformations using the dual antenna switch array, and still be efficient for sidereal filter application. Lastly, removing the first 30 seconds of the switch interval after switching, improved the overall coordinate precision in some of the studied cases. Nevertheless, all switch

session epochs are to be considered, while bad epochs — especially directly after switching — will be rejected through the moderate acceptance limit of 30 cm.

In summary, the multi-antenna array system was fully described here, starting with a brief background, and then the characteristics and advantages of such a system were explained. Different applied investigations using the multi-antenna array system were depicted in brief. Then the dual antenna switch array system used in the research was illustrated. After that, the primary investigation of the optimum antenna switch interval was described in detail, along with an illustration of the applied test area and collected data sets. At the end, the application of the sidereal filter on episodic data was given. Accordingly, in relation to the work done in the current chapter, Chapter six will deal with the application of sidereal filtering with longer switch data sets, while implementing different kinds of displacements of various magnitudes and directions. This will construct a full assessment of the performance of sidereal filtering on deforming semi-continuous GPS data.

DEFORMATION MONITORING USING SIDEREAL FILTER DUAL ARRAY GPS

6.1 Introduction

GPS has proven to be a reliable technique in monitoring different kinds of deformations (see Section 1.1). It is an increasingly utilized technique for performing a deformation monitoring task efficiently. This efficiency can be achieved by carrying out the whole process, a) quickly i.e. identifying the movement in real-time or near real-time in order to act immediately to prevent or at least reduce the impact of disasters, b) with minimum cost, as usually the monitoring process requires multiple stations which in turn involves an amount of costly GPS equipment, and c) precisely such that small as well as large displacements are detected.

Accordingly, reliable and quick deformation monitoring in a cost-effective way, while improving the precision of station coordinates, is the ultimate aim of this chapter. The term quick arises from the use of a single epoch processing technique, while cost-effectiveness can be obtained when observing semi-continuous GPS data through the use of a dual antenna switch array (i.e. two antennae and one receiver, see Chapter 5). Precision improvement is achieved by using the sidereal filter methodology. Consequently, this chapter is a practical application combining these techniques and methodologies together, in order to detect and improve the precision of monitoring structural deformations. At first, a displacement simulation platform is illustrated. Then, the collected data set is explained, followed by some analysis regarding the dual antenna switch array and the implemented multi-directional displacements. After that, the performance of sidereal filtering on semi-continuous GPS data for detecting and improving the precision of deforming station coordinates is discussed.

6.2 Displacement Simulation Platform

Network displacements were implemented in the current research using a purpose-built, rigid and adjustable platform constructed in-house, in order to measure the amount of actual movements. Thus, one can test the success of sidereal filter application with the switched antenna array system in distinguishing these displacements and improving the precision of the final coordinates. The displacement simulation platform shown in Figure 6.1 is a tri-axial platform mounted on a pillar and fixed with a screw bolt and steel ropes to prevent extraneous movement. In addition, some wooden pegs are used to chock the platform on the pillar, as well as ensuring the horizontality of the platform. Each axis movement is controlled separately by a knob connected to a precisely threaded spindle. One complete rotation of the knob in any direction is equivalent to approximately 2 mm. However, for accuracy purposes, any implemented displacement in the horizontal or vertical plane of the platform will be measured by a digital vernier calliper of 0.01 mm accuracy (Figure 6.2). The platform consists of two side flanges upon which GPS antennae can be fixed.

Figure 6.1 Displacement simulation platform.

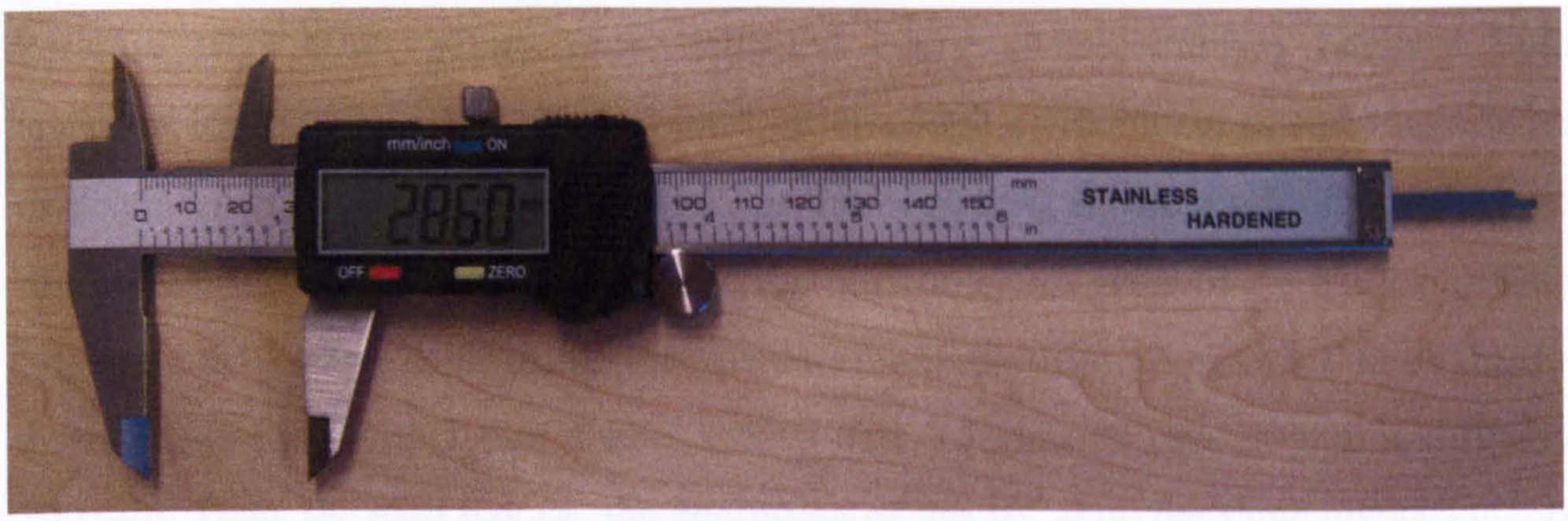

Figure 6.2 Digital vernier calliper used for displacement measurements.

6.3 Switched Data Collection

The switch controlled data set was collected, while mounting two antennae on the displacement platform fixed on DRME (see Figure 5.5), called DRME_A and DRME_B here after (see Figure 6.3). These two antennae are connected to one receiver, while another fixed antenna is set on DRMN connected to a second receiver. Data collection started on 09:52:50 (GPS Time) on Monday 10th September 2007, logging data continuously for DRMN, while switching between the DRME_A and DRME_B antennae, until 17:02:17 (GPS Time) on Wednesday 19th September 2007. The switch interval used is the modified "two minute" switch interval of 119 seconds, as discussed previously in Section 5.5.2. The same type of receivers and antennae were used as before.

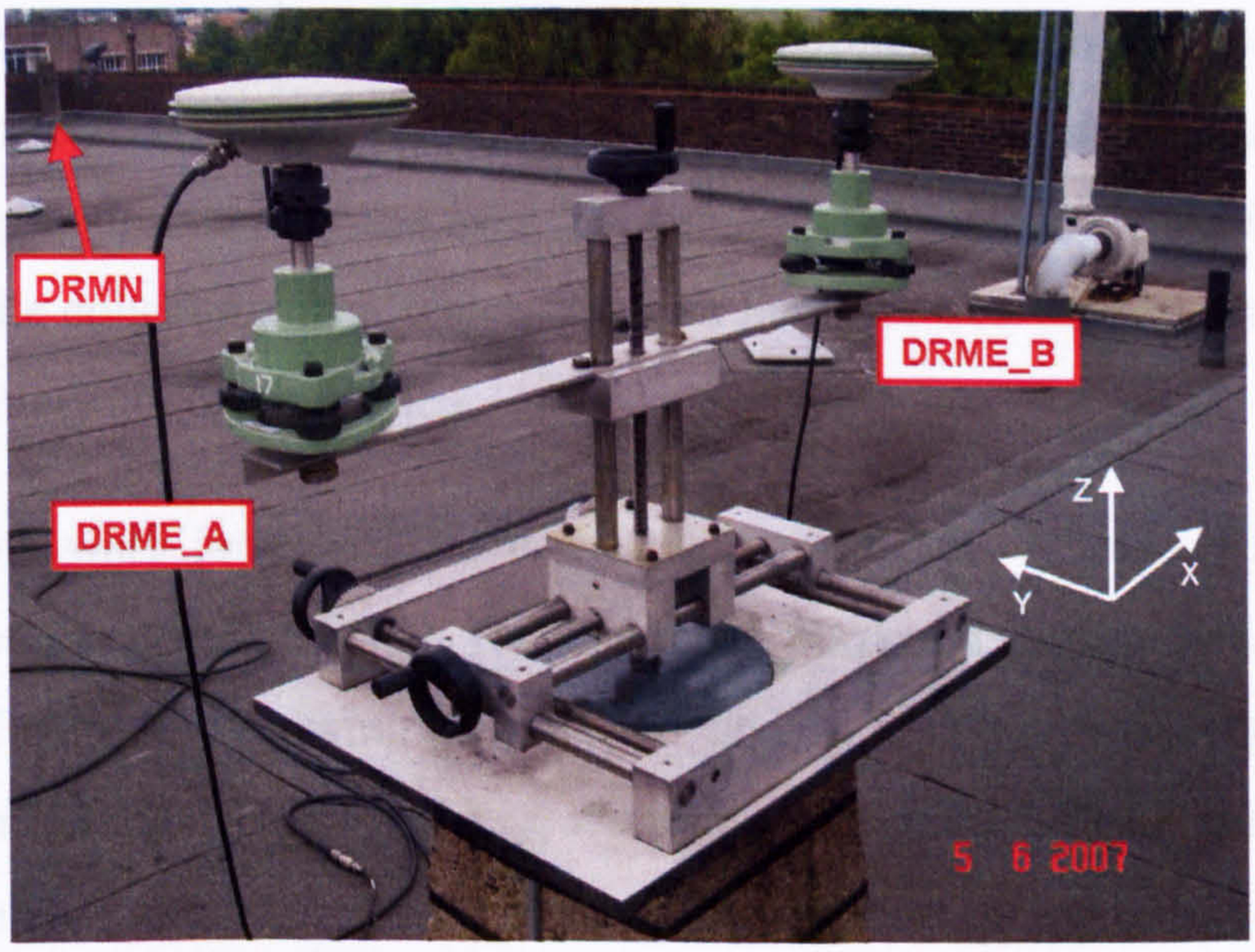

Figure 6.3 DRME A and B antennae mounted on the displacement simulation platform.

Periodic GPS observations were collected every switch interval between both antennae for the first eight sidereal days, after which different types and magnitudes of displacements were applied. At first, in the beginning of the ninth day of the data set, horizontal displacements (relative to the horizontal XY-axes of the platform) were implemented every hour using the displacement platform horizontal knob in X-direction, starting with 1 mm, then 2 mm, 5 mm, 10 mm, 20 mm, 50 mm and finally 100 mm. Then, the next day i.e. the beginning of the 10^{th} day, the same displacements were applied with the same time interval but in the vertical direction (relative to the Z-axis of the platform).

6.4 GPS Processing and Switch Array Analysis

In relation to the research aim mentioned throughout the thesis, of being able to monitor structural deformations in near-real time, the IGS ultra rapid predicted orbits are used here to obtain satellite coordinates. These orbits can be extracted in real time during the monitoring process without the need to wait as in the case for final or rapid precise orbits. IGS ultra rapid half-observed-half-predicted orbits are released four times daily (at 03:00, 09:00, 15:00 and 21:00 UT) containing two days (48 hours) of satellite orbits, named according to the midpoint of the file (00, 06, 12 and 18) respectively. The first half of each file is observed, while the second half is predicted (International GNSS Service 2007). Accordingly, for the optimum use of these files in real time, the first six hours of predicted satellite orbits after the release of each file are extracted e.g. 03:00:00 to 08:59:59 for file 00, and concatenated to their corresponding counterpart of the next file and so on. In this way, satellite orbits are available while collecting data, which can then be processed for real time monitoring and related safety actions if needed.

The GPS data were processed for both antennae DRME_A and DRME_B, while fixing the coordinates of DRMN. For assurance purposes, Figure 6.4a,b are formed similarly to Figure 5.9, showing the 50^{th}, 95^{th} and 99^{th} 3D discrepancy percentiles for DRME_A and DRME_B respectively, without any filtering of bad data with respect to an acceptance limit. This is done of course while considering only the first part of the data set for both antennae without implementing any displacements. From this

figure, 1 cm level of precision is reached for 50% of the data after 48 seconds from switching, for both antennae. This transitional period of unhealthy epochs being an average of what was shown for the two minute switch interval in Section 5.5.2, is achieved similarly for both antennae, which can be attributed to the use of different cables due to a malfunction of the cables used earlier in Chapter 5.

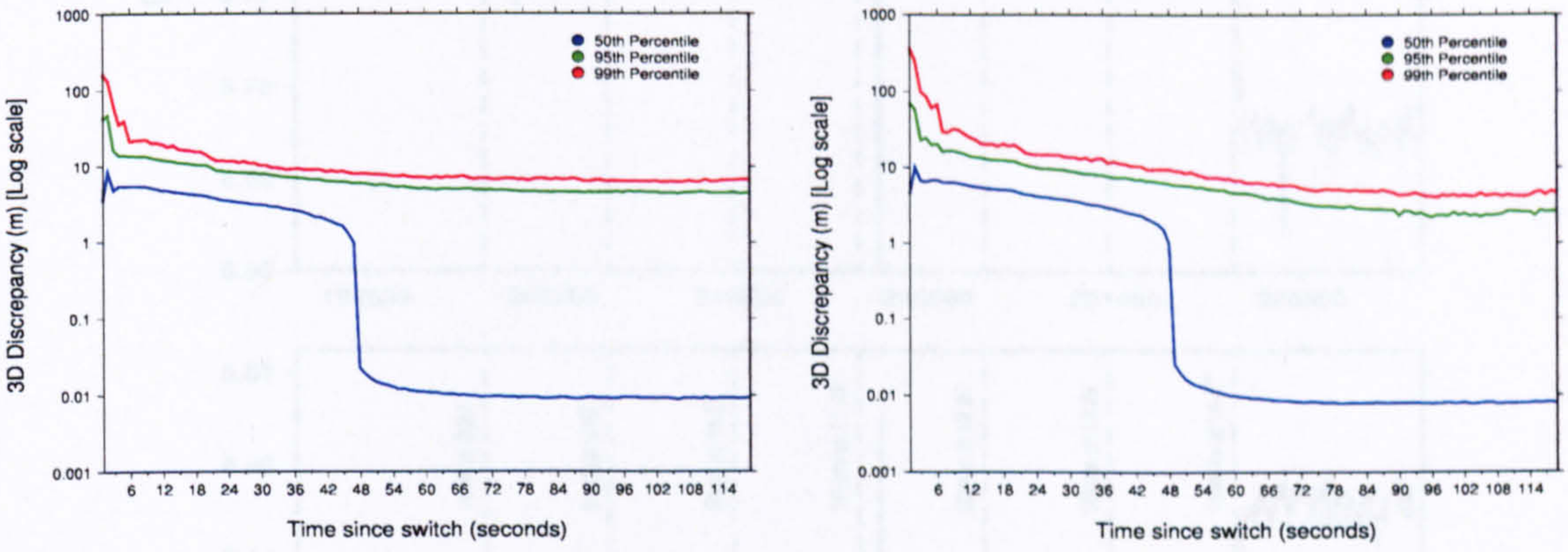

a) DRME_A **b) DRME_B**

Figure 6.4 3D discrepancy percentiles.

On the other hand, Figure 6.5 is formed similarly to 6.4, but filtering the data with a 30 cm acceptance limit (Section 5.7). This figure again shows that similar precision is achieved for both antennae at better than 1 cm level for 50% of all the switched sessions' epochs except for a few epochs after switching from the other antenna.

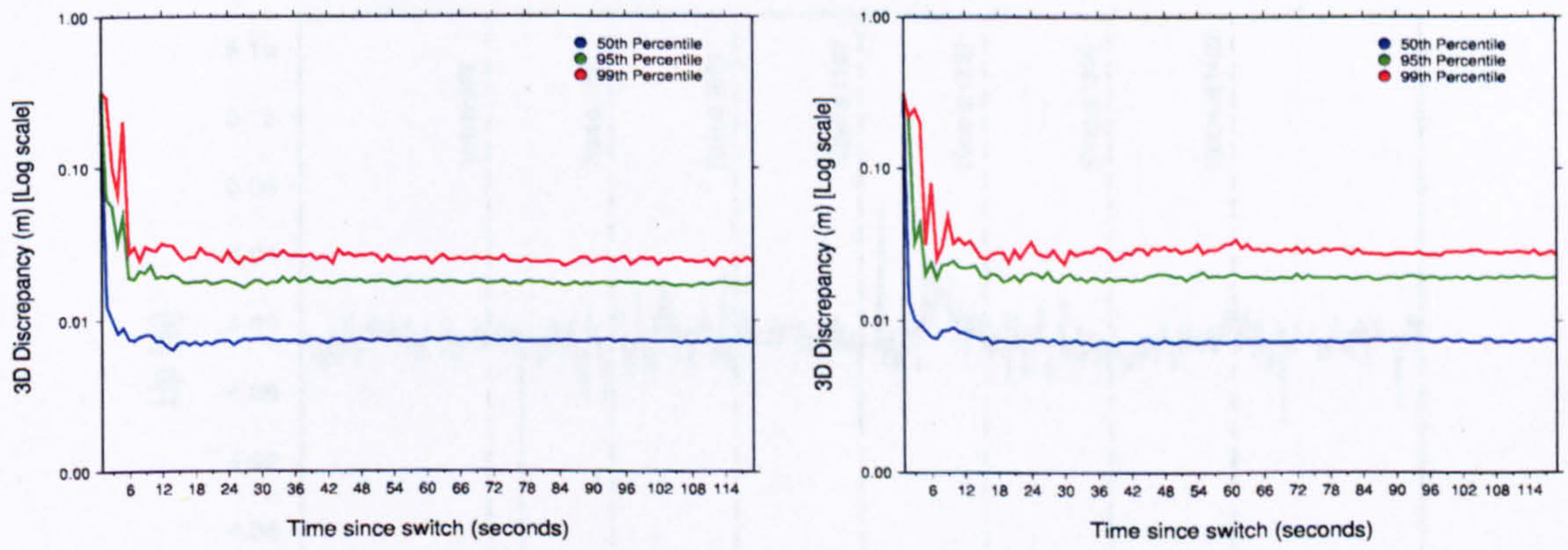

a) DRME_A **b) DRME_B**

Figure 6.5 3D discrepancy percentiles after removing epochs of discrepancies greater than 30 cm.

Figures 6.6 and 6.7 shows the coordinate time series of DRME_A and DRME_B respectively, filtered according to the 30 cm acceptance limit. The time span shown is while applying horizontal displacements of seven different magnitudes, in

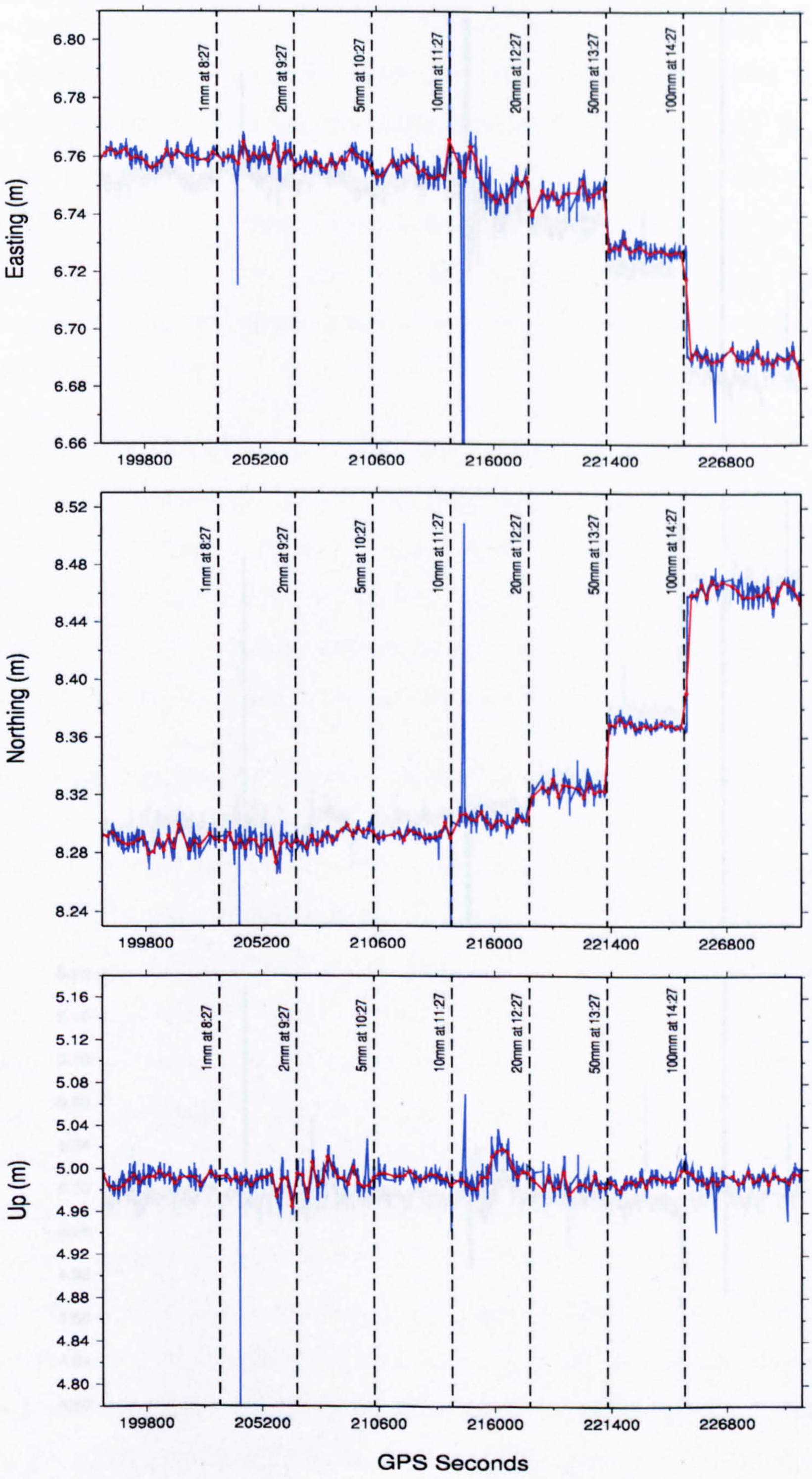

Figure 6.6 DRME_A coordinate time series while applying horizontal displacements. Black dashed lines indicate time of these displacements of different magnitude. Red line shows a 119 seconds box-car filter. Coordinates are plotted relative to a false origin. (GPS week = 1445)

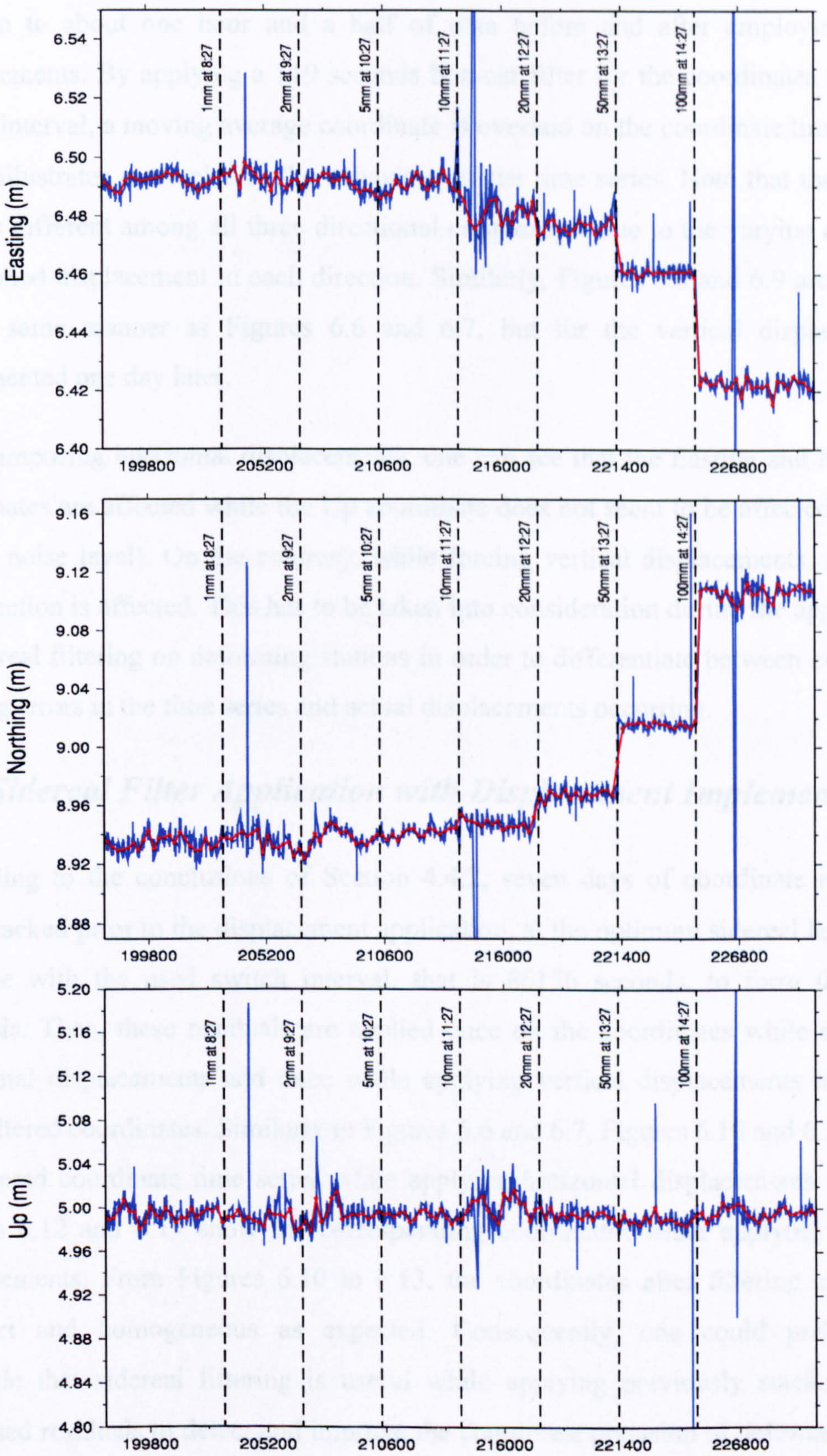

Figure 6.7 DRME_B coordinate time series while applying horizontal displacements. Line attributes, coordinates origin and GPS week as before.

addition to about one hour and a half of data before and after employing these displacements. By applying a 119 seconds box-car filter for the coordinates for each switch interval, a moving average coordinate is overlaid on the coordinate time series, which illustrates more clearly the behaviour of the time series. Note that the Y-axis scale is different among all three directional components due to the varying effect of the applied displacement in each direction. Similarly, Figures 6.8 and 6.9 are formed in the same manner as Figures 6.6 and 6.7, but for the vertical displacements implemented one day later.

While imposing horizontal displacements, one can see that the Easting and Northing coordinates are affected while the Up coordinate does not seem to be affected (with a certain noise level). On the contrary, while forcing vertical displacements, only the Up direction is affected. This has to be taken into consideration during the application of sidereal filtering on deforming stations in order to differentiate between noise and existing errors in the time series and actual displacements occurring.

6.5 Sidereal Filter Application with Displacement Implementation

According to the conclusions of Section 4.4.2, seven days of coordinate residuals were stacked prior to the displacement application, at the optimum sidereal lag that is possible with the used switch interval, that is 86156 seconds, to form the filter residuals. Then, these residuals are applied once on the coordinates while applying horizontal displacements and once while applying vertical displacements to obtain final filtered coordinates. Similarly to Figures 6.6 and 6.7, Figures 6.10 and 6.11 show the filtered coordinate time series while applying horizontal displacements whereas Figures 6.12 and 6.13 show the corresponding coordinates while applying vertical displacements. From Figures 6.10 to 6.13, the coordinates after filtering are more compact and homogeneous as expected. Consequently, one could preliminary conclude that sidereal filtering is useful while applying previously stacked static processed residuals to detect and improve the coordinate precision of deformations in different directions of different magnitudes, especially in our case here of synthesized structural displacements.

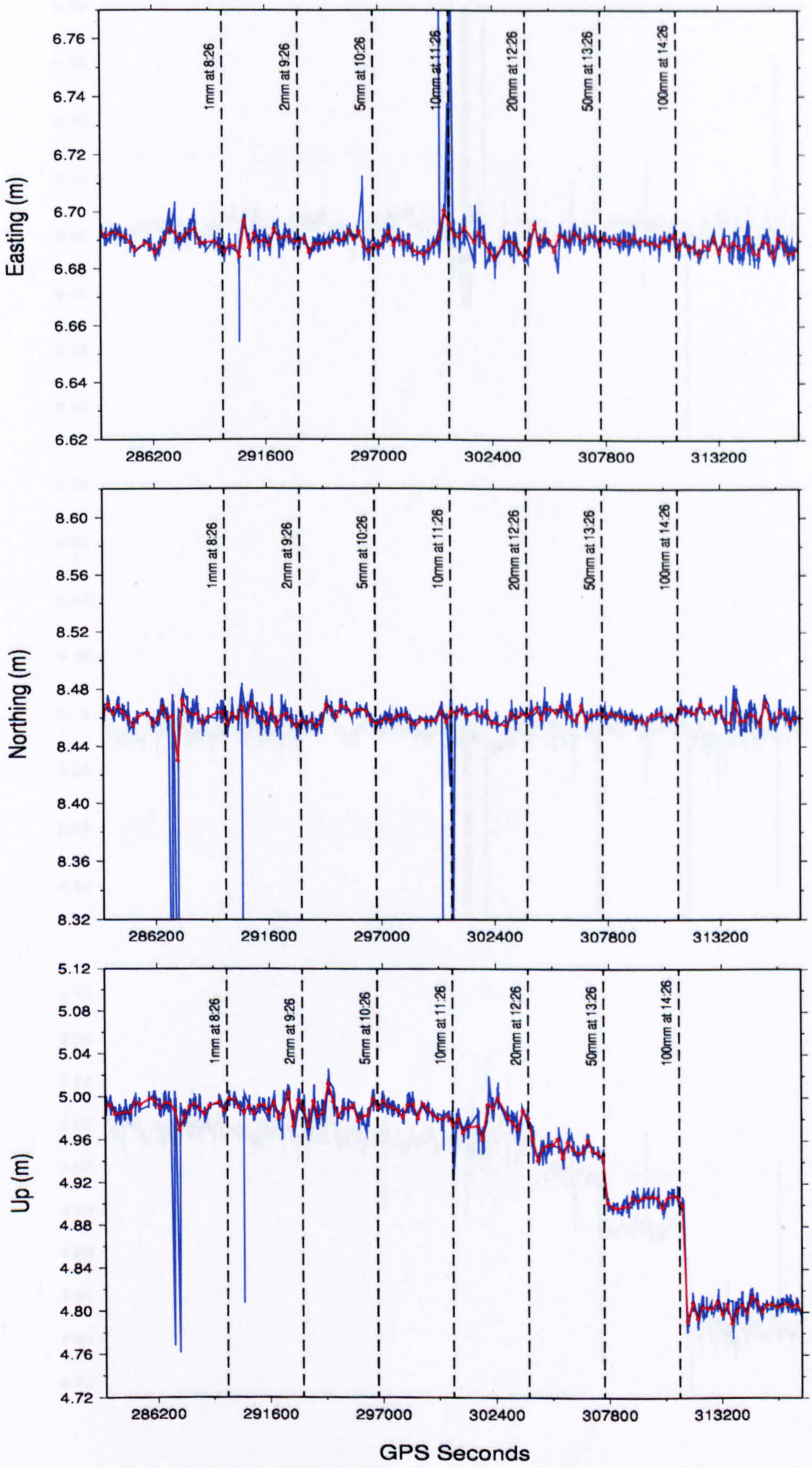

Figure 6.8 DRME_A coordinate time series while applying vertical displacements. Line attributes, coordinates origin and GPS week as before.

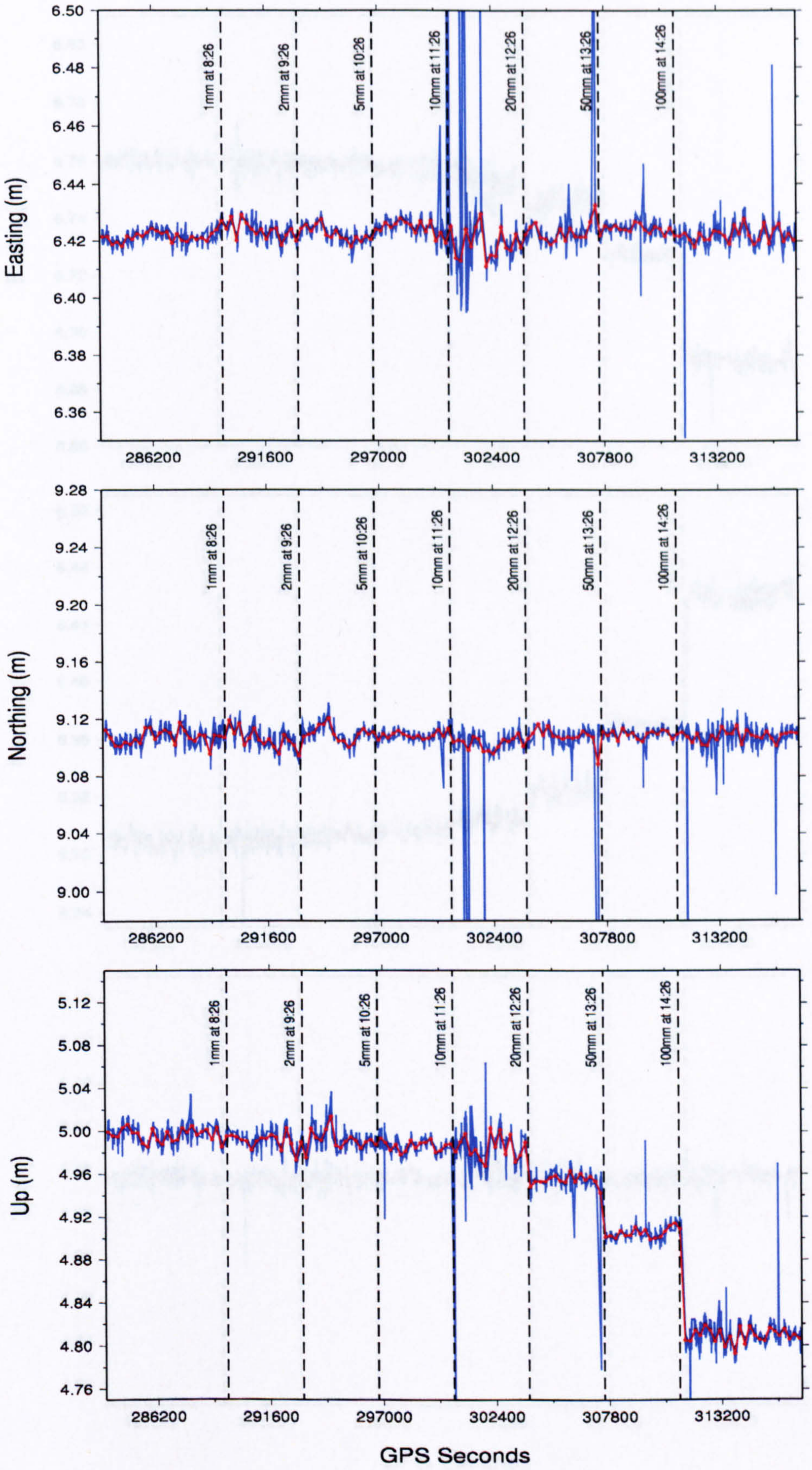

Figure 6.9 DRME_B coordinate time series while applying vertical displacements. Line attributes, coordinates origin and GPS week as before.

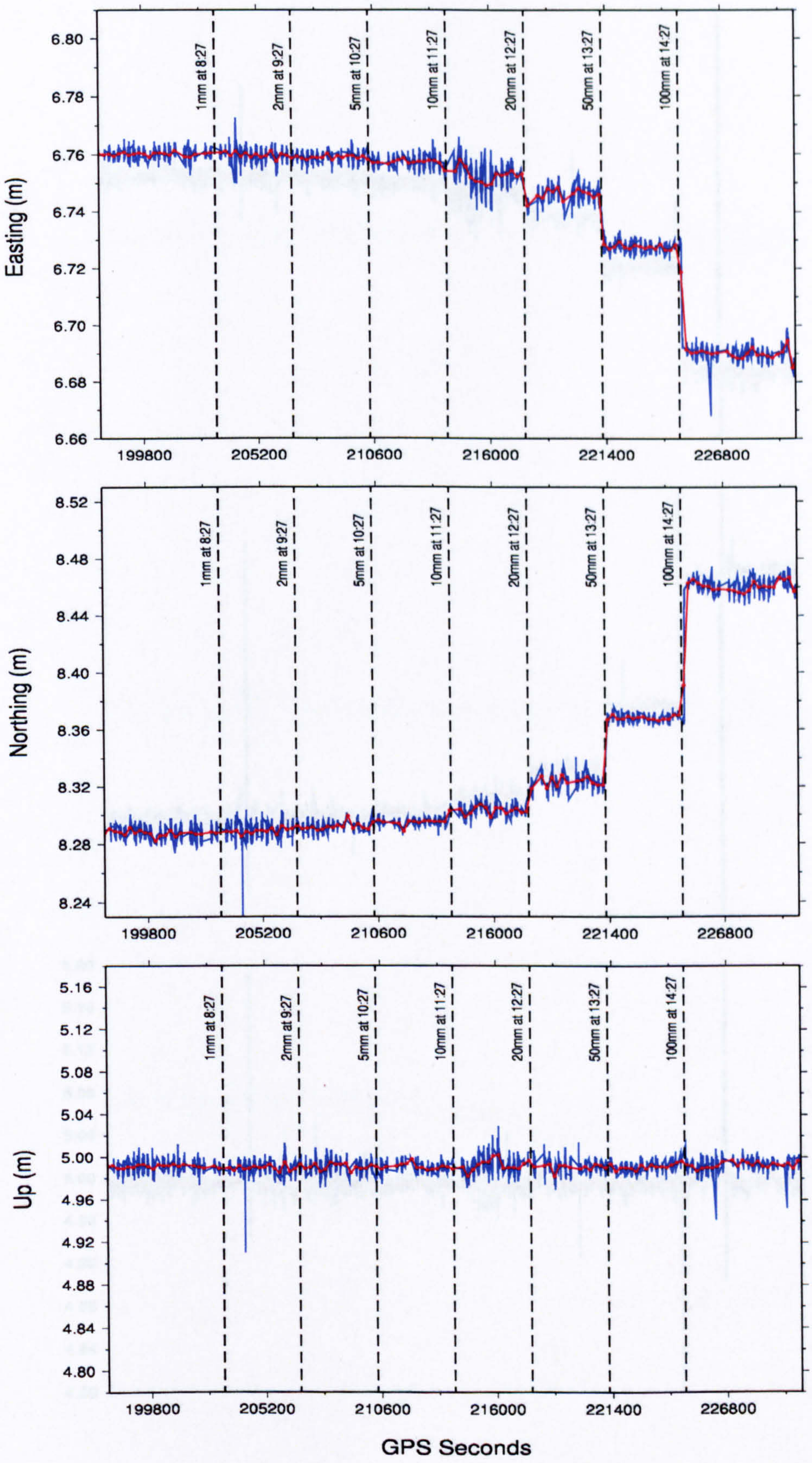

Figure 6.10 DRME_A filtered coordinate time series while applying horizontal displacements. Line attributes, coordinates origin and GPS week as before.

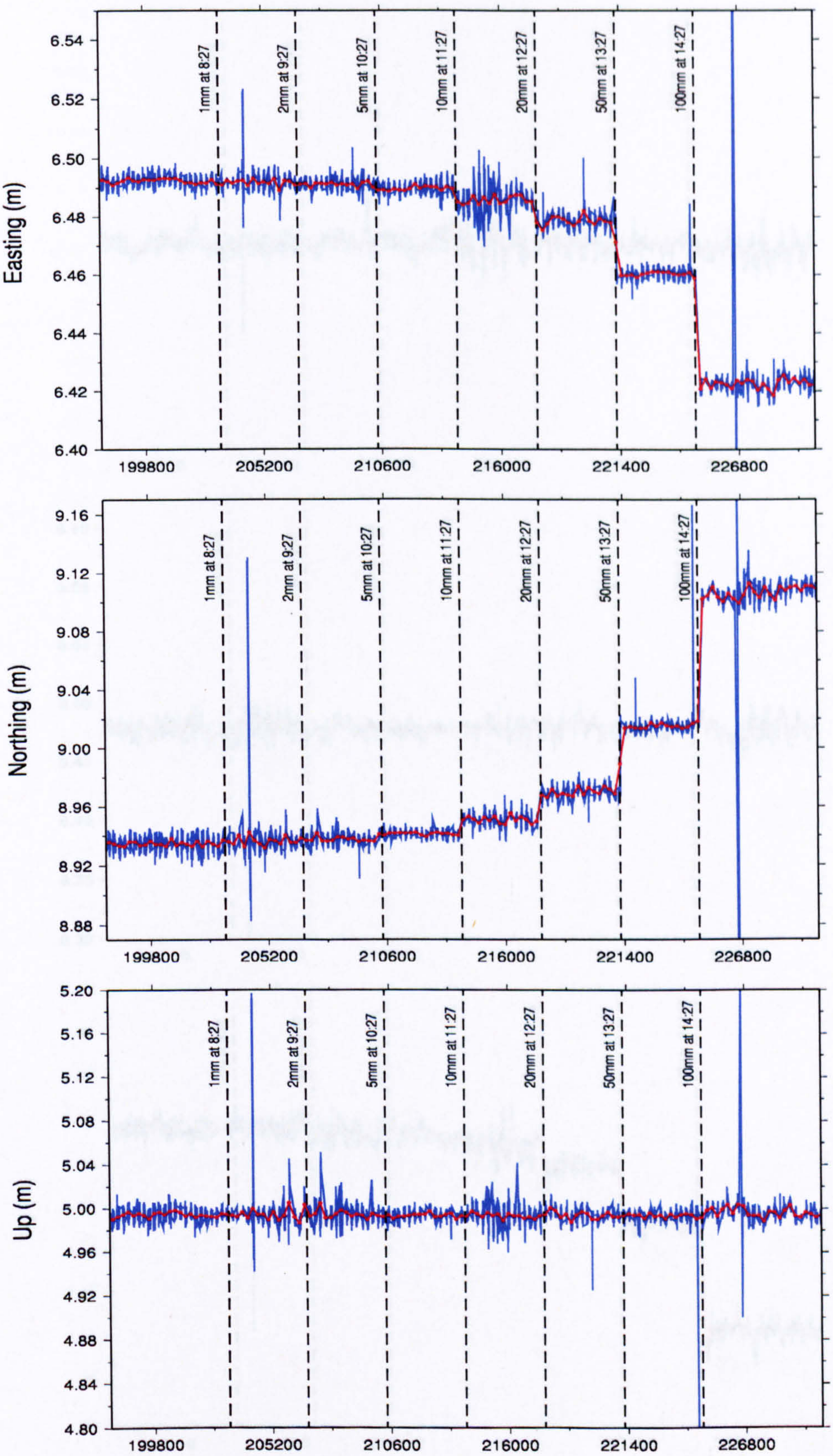

Figure 6.11 DRME_B filtered coordinate time series while applying horizontal displacements. Line attributes, coordinates origin and GPS week as before.

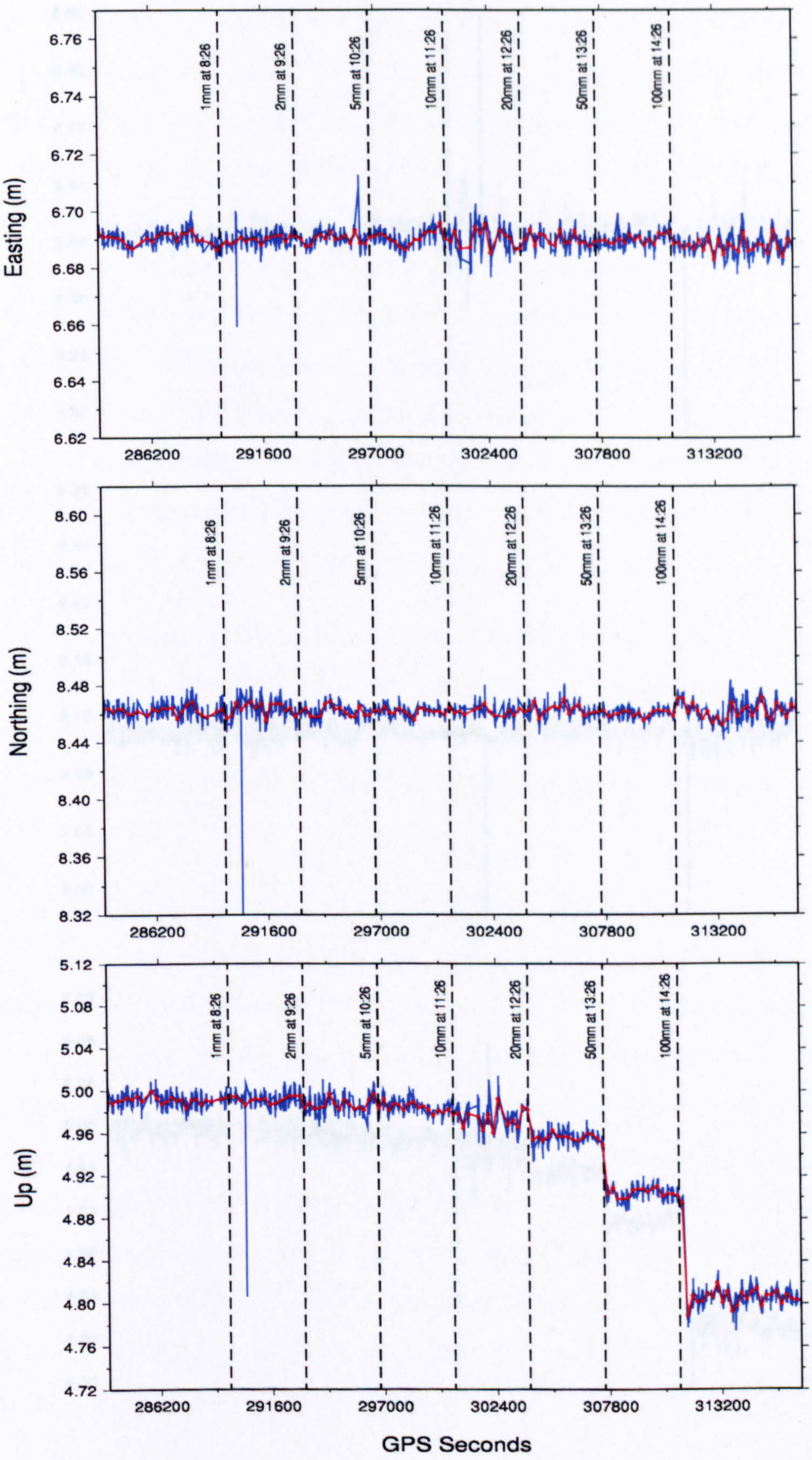

Figure 6.12 DRME_A filtered coordinate time series while applying vertical displacements. Line attributes, coordinates origin and GPS week as before.

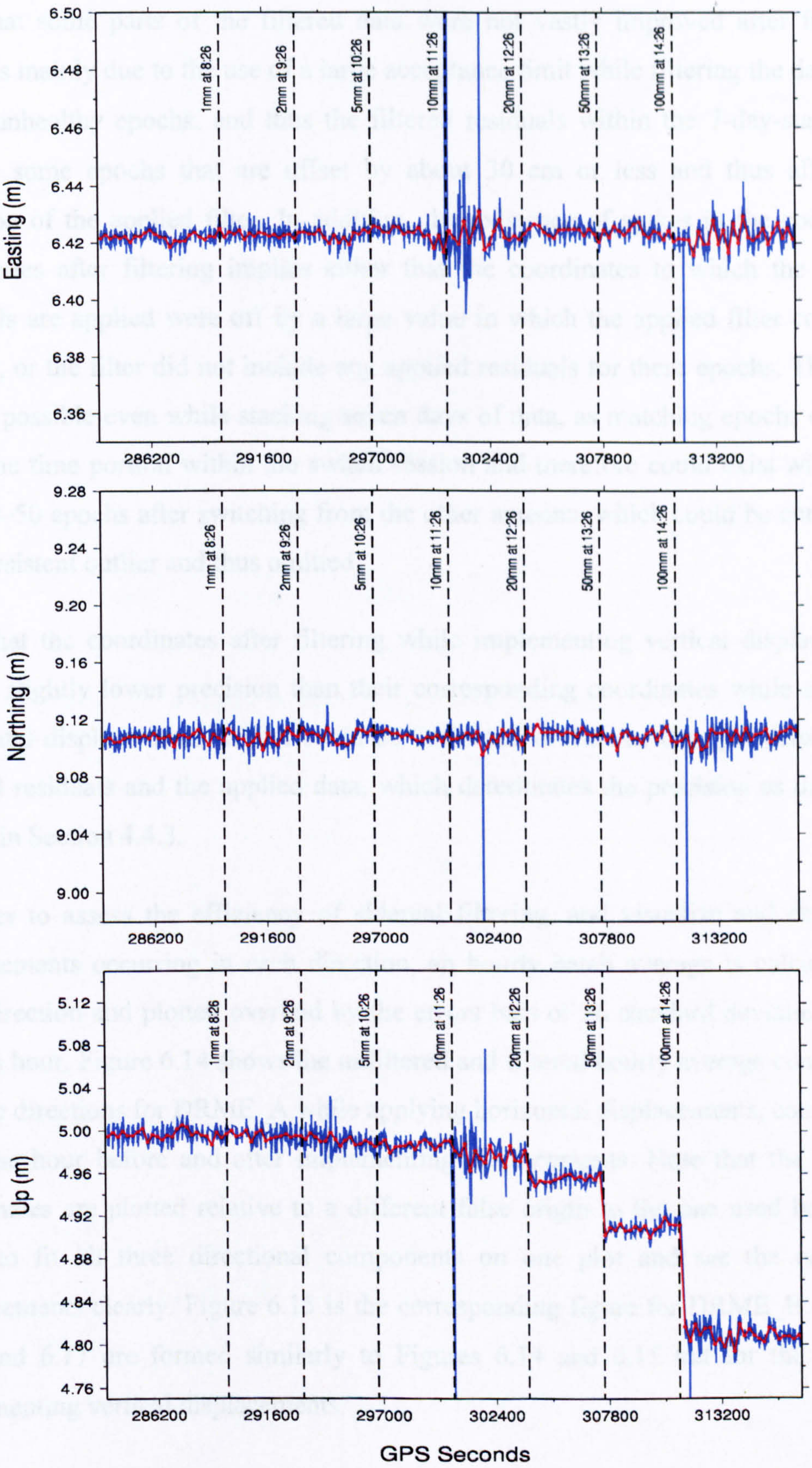

Figure 6.13 DRME_B filtered coordinate time series while applying vertical displacements. Line attributes, coordinates origin and GPS week as before.

Note that some parts of the filtered data were not vastly improved after filtering, which is mainly due to the use of a large acceptance limit while filtering the data from initial unhealthy epochs, and thus the filtered residuals within the 7-day-stack may include some epochs that are offset by about 30 cm or less and thus affect the precision of the applied filter. In addition, the existence of spikes in the coordinate time series after filtering implies either that the coordinates to which the filtered residuals are applied were off by a large value in which the applied filter could not modify, or the filter did not include any applied residuals for these epochs. The latter case is possible even while stacking seven days of data, as matching epochs occur at the same time portion within the switch session and therefore could exist within the first 30–50 epochs after switching from the other antenna, which could be considered as a persistent outlier and thus omitted.

Note that the coordinates after filtering while implementing vertical displacements have a slightly lower precision than their corresponding coordinates while applying horizontal displacements, which could be attributed to the one day gap between the stacked residuals and the applied data, which deteriorates the precision as discussed earlier in Section 4.4.3.

In order to assess the efficiency of sidereal filtering, and visualize and detect the displacements occurring in each direction, an hourly batch average is calculated in each direction and plotted overlaid by the errors bars of 3σ standard deviation limits of each hour. Figure 6.14 shows the unfiltered and filtered hourly average coordinates in three directions for DRME_A while applying horizontal displacements, considering also one hour before and after implementing displacements. Note that the average coordinates are plotted relative to a different false origin to the one used before, in order to fit all three directional components on one plot and see the occurring displacements clearly. Figure 6.15 is the corresponding figure for DRME_B. Figures 6.16 and 6.17 are formed similarly to Figures 6.14 and 6.15 but for the case of implementing vertical displacements.

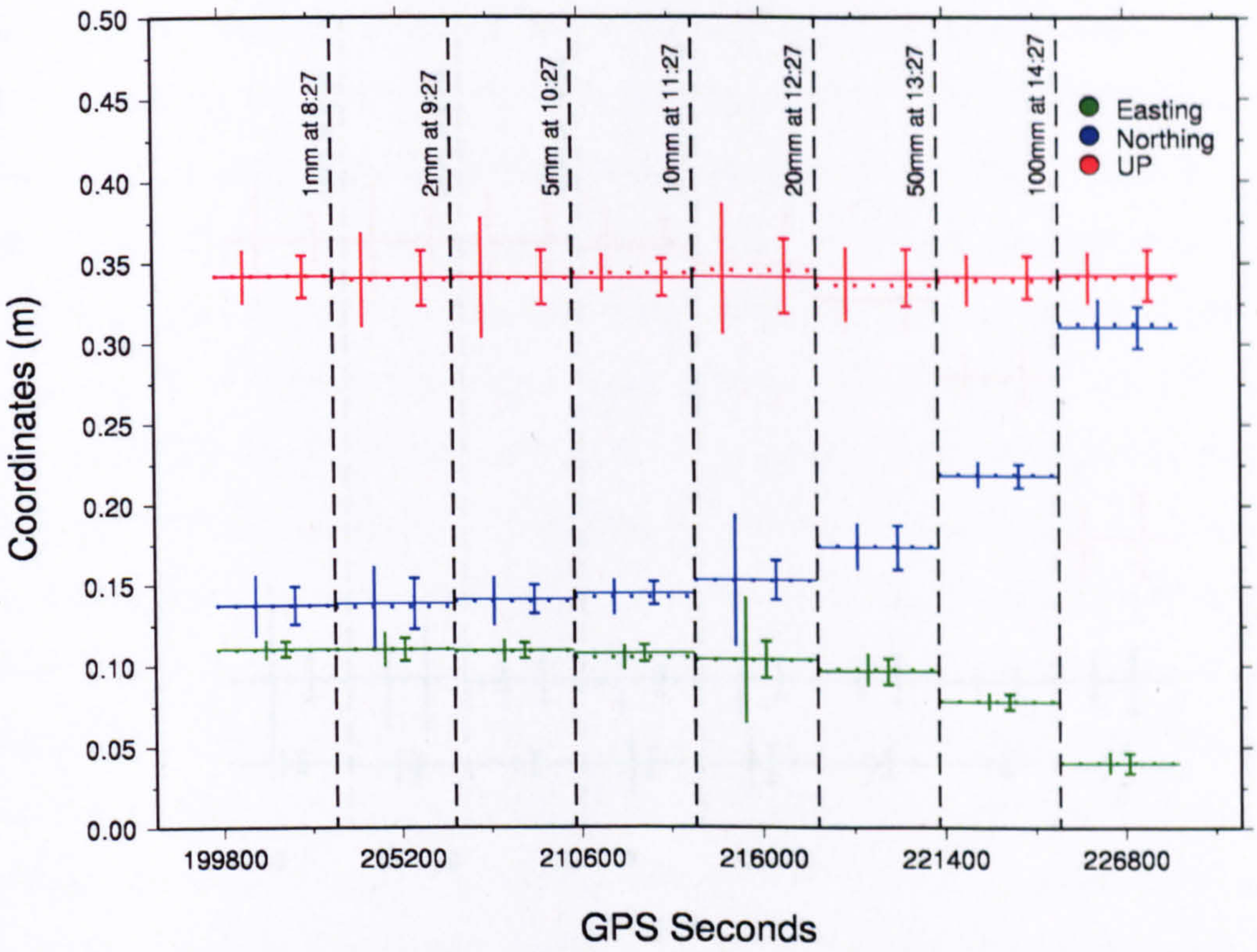

Figure 6.14 DRME_A unfiltered and filtered average hourly coordinates, while applying horizontal displacements. Solid lines and right error bars for filtered coordinates. Dotted lines and left error bars for unfiltered coordinates. Coordinates are plotted relative to a false origin. Error bars show 3σ standard deviation limits. GPS week as before.

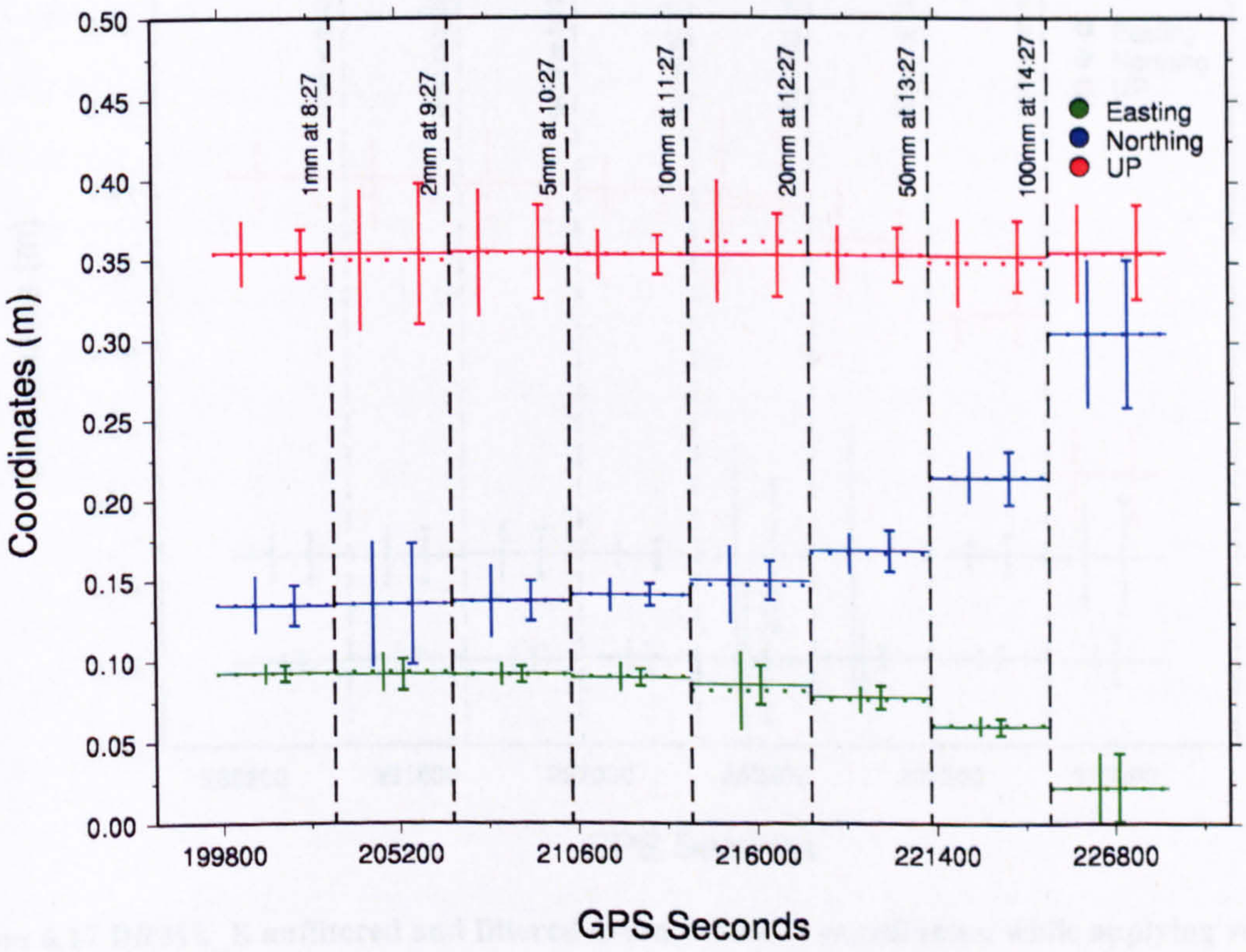

Figure 6.15 DRME_B unfiltered and filtered average hourly coordinates, while applying horizontal displacements. Line attributes, error bars, coordinates origin and GPS week as before.

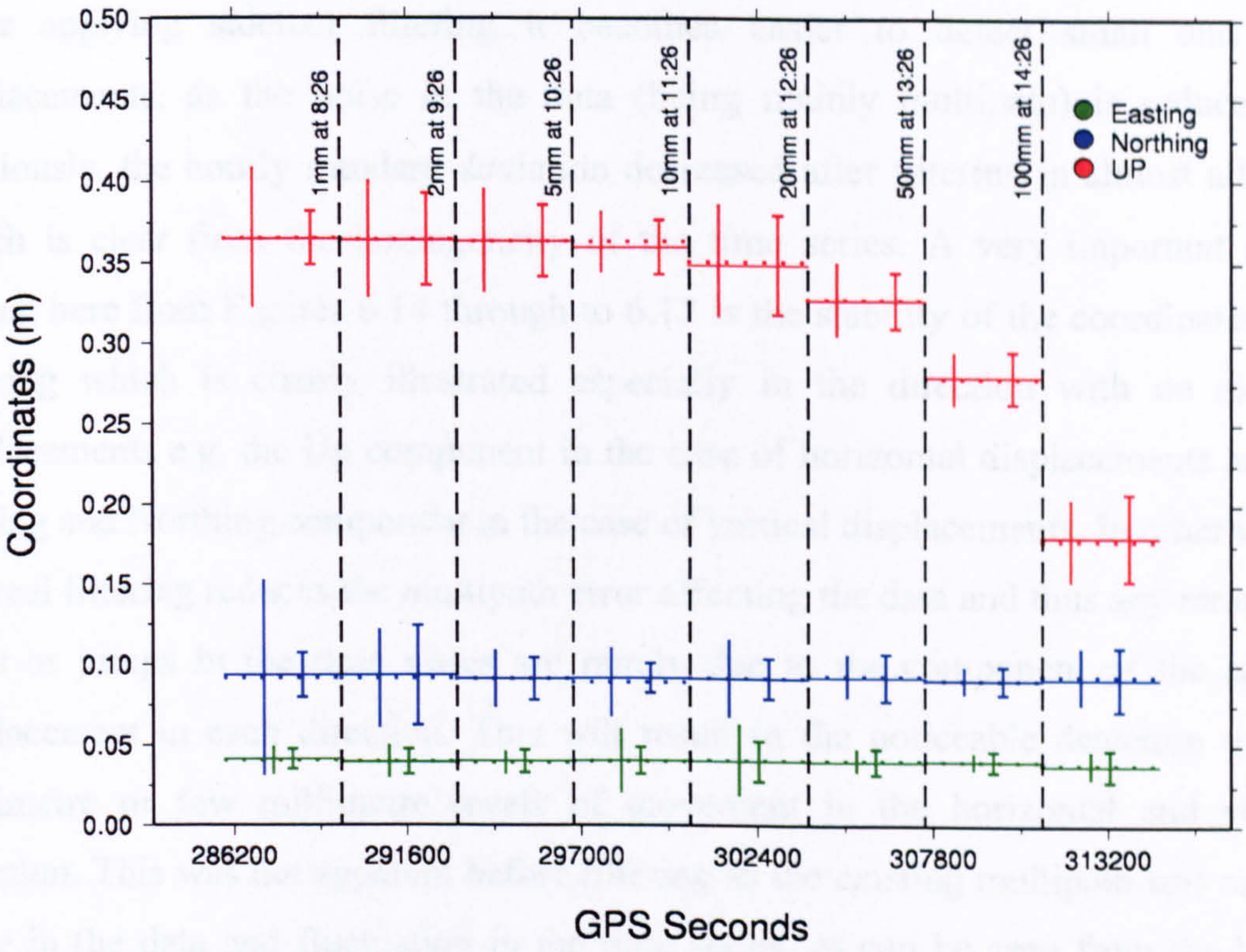

Figure 6.16 DRME_A unfiltered and filtered average hourly coordinates, while applying vertical displacements. Line attributes, error bars, coordinates origin and GPS week as before.

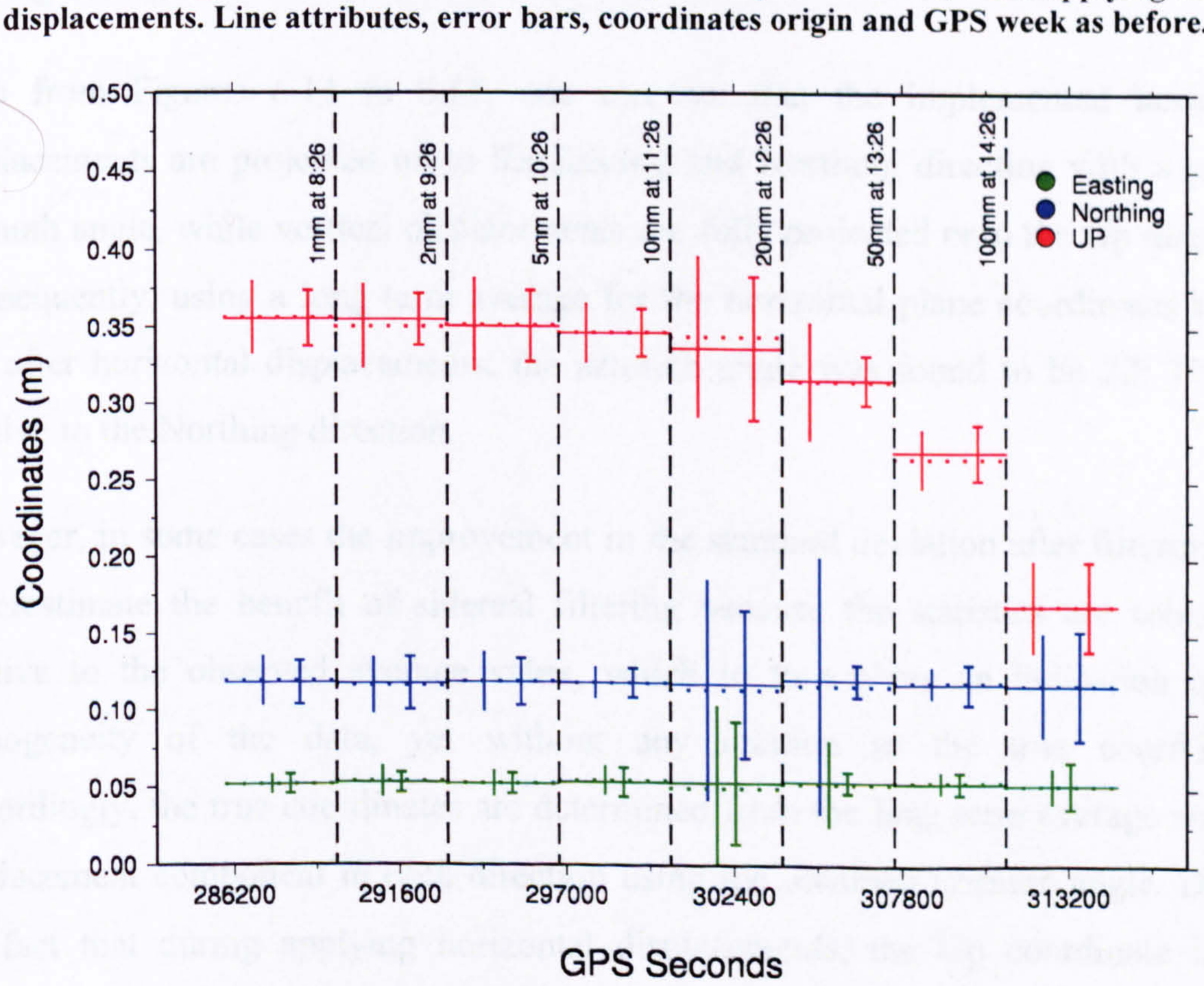

Figure 6.17 DRME_B unfiltered and filtered average hourly coordinates, while applying vertical displacements. Line attributes, error bars, coordinates origin and GPS week as before.

After applying sidereal filtering it becomes easier to detect small and large displacements, as the noise in the data (being mainly multipath) is reduced. As previously, the hourly standard deviation decreased after filtering in almost all cases which is clear from the homogeneity of the time series. A very important aspect arising here from Figures 6.14 through to 6.17 is the stability of the coordinates after filtering which is clearly illustrated especially in the direction with no existing displacements e.g. the Up component in the case of horizontal displacements and the Easting and Northing component in the case of vertical displacements. In other words, sidereal filtering reduces the multipath error affecting the data and thus any remaining steps or jumps in the time series are purely due to the component of the applied displacement in each direction. This will result in the noticeable detection of sub-centimetre or few millimetre levels of movement in the horizontal and vertical direction. This was not apparent before filtering as the existing multipath was causing noise in the data and fluctuation in the time series, as can be seen from the hourly moving average.

Also from Figures 6.14 to 6.17, one can see that the implemented horizontal displacements are projected on to the Easting and Northing direction with a certain azimuth angle, while vertical displacements are fully projected onto the Up direction. Consequently, using a long term average for the horizontal plane coordinates before and after horizontal displacements, the azimuth angle was found to be 22° 17' 37" relative to the Northing direction.

However, in some cases the improvement in the standard deviation after filtering will underestimate the benefit of sidereal filtering because the statistics are calculated relative to the observed average value, which in turn gives an indication of the homogeneity of the data, yet without any relation to the true coordinates. Accordingly, the true coordinates are determined from the long term average and the displacement component in each direction using the obtained azimuth angle. Due to the fact that during applying horizontal displacements, the Up coordinate is not affected, as is the case for the Easting and Northing component while applying vertical displacements, more focus is given to the directional components where displacement exists for both antennae, that is the Easting and Northing component

while applying horizontal displacements and the Up component for vertical displacements.

Figures 6.18 and 6.19 show the true coordinates plotted against the observed unfiltered and filtered coordinates for DRME_A and B respectively, showing the Easting and Northing components for horizontal displacements and the Up component for vertical displacements. In each antenna's component, all epochs are plotted within each hour before, during and after applying different displacement magnitudes, overlaid by the 119 seconds session average and then overlay by the hourly average. In addition, the slope of the best fit to the coordinates as well as the overall RMS of the residuals to the best fit are given for each of the three plotted cases.

From Figures 6.18 and 6.19, as the coordinates are averaged over each session and then over each hour, it can be seen that the RMS of the residuals to the best fit decreases. Additionally, the RMS of the residuals for the filtered coordinates is lower than for the unfiltered coordinates, when comparing all directional components and cases. Figures 6.18 and 6.19 indicate also that sidereal filtering in most cases not only confines the scatter of the coordinates around the average observed value, but also modifies the overall coordinates with minimum fluctuations to the true value. This is again essential especially for monitoring purposes, in order to detect true deformation magnitudes, while reducing sidereally repeating errors which affect the precision of the monitoring process.

According to Figures 6.18 and 6.19, one can reach an overall RMS for the residuals in the horizontal plane of 4.50 mm when considering all epochs, 2.66 mm for the switch sessions' average and 0.61 mm for the hourly average, with an average slope of 0.987 relating the true and observed horizontal coordinates. On the other hand, the RMS for the Up coordinates reaches 7.51 mm for all epochs, 5.45 mm for sessions' average and 0.85 mm for the hourly average, with a 0.993 slope relating the vertical coordinates.

In summary, Tables 6.1, 6.2 and 6.3 show the DRME_A true coordinates for each hour and its corresponding unfiltered and filtered hourly average values, accompanied with the raw and sessions hourly RMS of the residuals to the hourly true coordinates

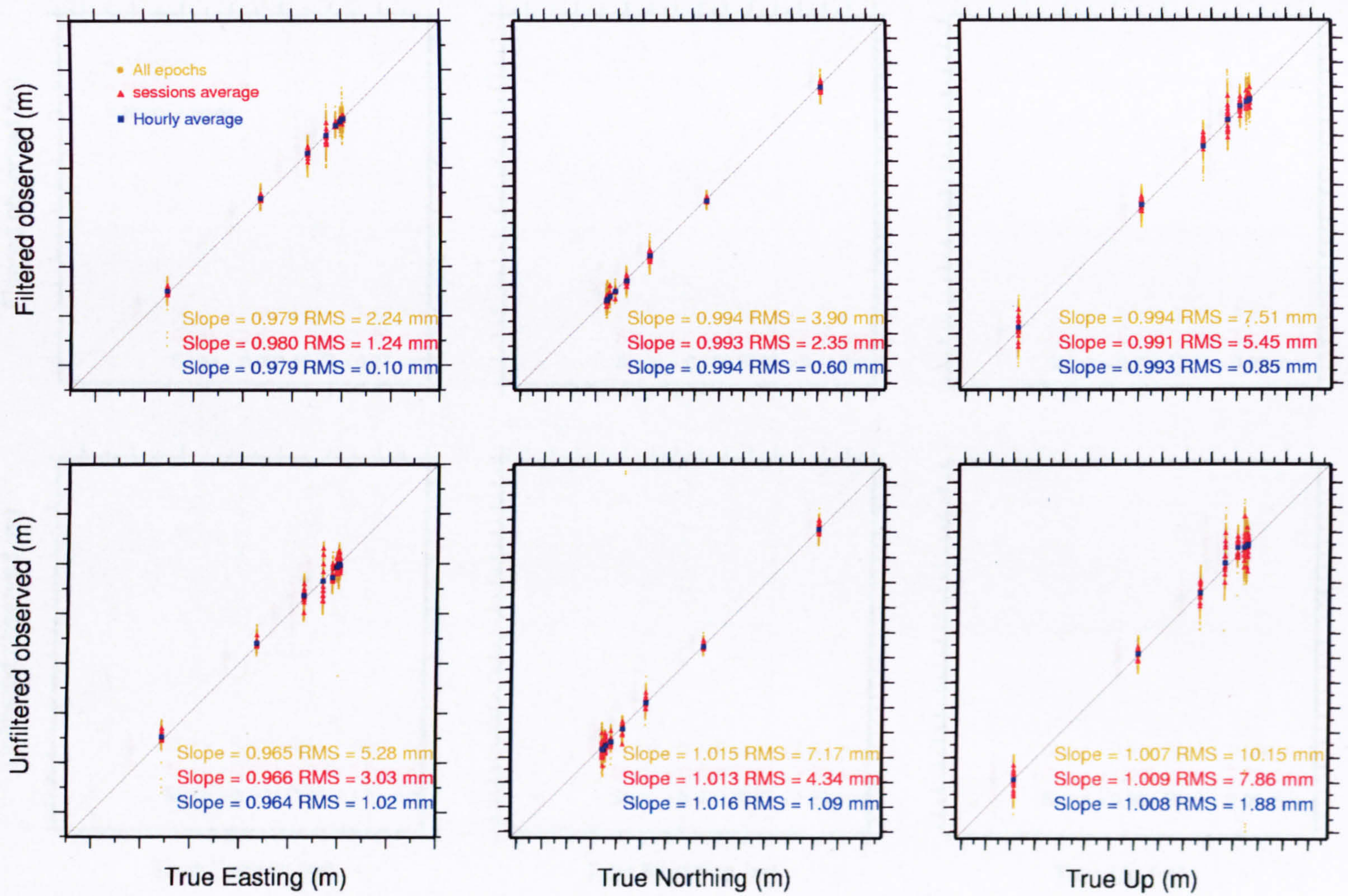

Figure 6.18 DRME_A unfiltered and filtered true versus observed coordinates. Easting and Northing coordinates while applying horizontal displacements on 18/09/2007 and Up coordinates while applying vertical displacements on 19/09/2007. Minor tick marks = 1 cm. Easting scale is double Northing and Up scale. Black line indicates ideal relation.

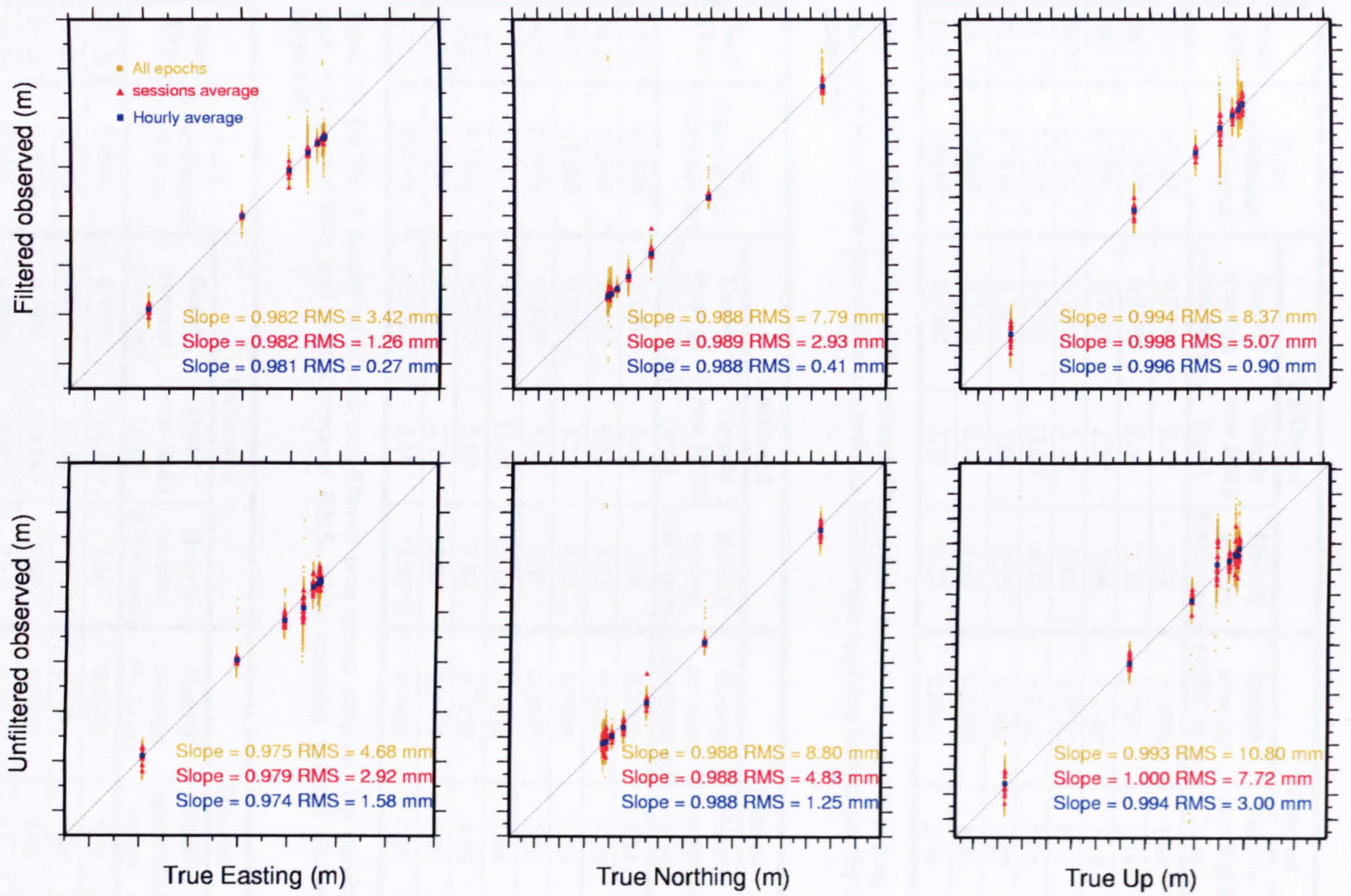

Figure 6.19 DRME_B unfiltered and filtered true versus observed coordinates. Coordinates, tick marks, scale and line attributes as before.

Table 6.1 DRME_A hourly unfiltered and filtered true versus observed Easting coordinates along with hourly raw data and switch sessions RMS, while applying horizontal displacements on 18/09/2007.

Start Time	True Coordinates (+588746 m)	Unfiltered			Filtered		
		Hourly average (+588746 m)	Hourly raw RMS (mm)	Hourly session RMS (mm)	Hourly average (+588746 m)	Hourly raw RMS (mm)	Hourly session RMS (mm)
07:27	0.7602	0.7594	2.17	1.96	0.7600	1.61	0.67
08:27	0.7598	0.7598	3.51	2.32	0.7597	2.34	0.97
09:27	0.7591	0.7587	2.37	1.98	0.7589	1.58	0.60
10:27	0.7572	0.7544	3.77	3.06	0.7572	1.71	0.59
11:27	0.7534	0.7531	13.00	6.22	0.7532	3.76	2.33
12:27	0.7458	0.7472	3.66	2.95	0.7460	2.67	1.76
13:27	0.7268	0.7279	2.15	1.45	0.7276	1.76	1.07
14:27	0.6889	0.6904	2.71	2.22	0.6901	2.40	1.56

Table 6.2 DRME_A hourly unfiltered and filtered true versus observed Northing coordinates along with hourly raw data and switch sessions RMS, while applying horizontal displacements on 18/09/2007.

Start Time	True Coordinates (+6093628 m)	Unfiltered			Filtered		
		Hourly average (+6093628 m)	Hourly raw RMS (mm)	Hourly session RMS (mm)	Hourly average (+6093628 m)	Hourly raw RMS (mm)	Hourly session RMS (mm)
07:27	0.2880	0.2867	6.48	5.76	0.2870	4.01	2.29
08:27	0.2889	0.2857	9.18	5.76	0.2880	5.35	1.93
09:27	0.2908	0.2894	5.28	4.74	0.2906	3.03	2.27
10:27	0.2954	0.2920	5.07	4.57	0.2945	2.56	2.26
11:27	0.3047	0.3025	13.91	5.32	0.3028	4.44	3.15
12:27	0.3232	0.3239	5.00	3.84	0.3232	4.58	3.19
13:27	0.3694	0.3686	2.79	2.09	0.3678	2.87	1.83
14:27	0.4619	0.4623	5.19	4.03	0.4600	4.78	3.63

Table 6.3 DRME_A hourly unfiltered and filtered true versus observed Up coordinates along with hourly raw data and switch sessions RMS, while applying vertical displacements on 19/09/2007.

Start Time	True Coordinates (+124 m)	Unfiltered			Filtered		
		Hourly average (+124 m)	Hourly raw RMS (mm)	Hourly session RMS (mm)	Hourly average (+124 m)	Hourly raw RMS (mm)	Hourly session RMS (mm)
07:26	0.9900	0.9902	14.39	7.36	0.9901	5.53	3.82
08:26	0.9890	0.9894	12.16	7.54	0.9892	9.80	3.57
09:26	0.9870	0.9884	10.84	9.58	0.9883	7.40	4.86
10:26	0.9820	0.9880	8.63	7.45	0.9845	6.05	4.38
11:26	0.9720	0.9759	12.23	11.19	0.9735	10.30	9.64
12:26	0.9520	0.9524	7.70	6.30	0.9519	6.52	4.93
13:26	0.9020	0.9033	5.67	4.52	0.9041	5.80	4.46
14:26	0.8020	0.8027	8.62	7.02	0.8049	9.51	8.30

for the considered Easting, Northing and Up directions respectively. Similarlily, Tables 6.4, 6.5 and 6.6 are formed for the DRME_B coordinates. Again, from Tables 6.1 through to 6.6, one can see that the sessions residuals RMS are lower than the raw data in each hour, as well as in most cases, sidereal filtering shifting the hourly average coordinates closer to the true value, which is an indication of an accuracy improvement in the coordinates within each hour, which is then verified from the reduction in the RMS of the residuals to the true coordinates. Accordingly, successful monitoring of deformations can be achieved using sidereal filtering in high multipath environments, with a precision better than 5 mm in the horizontal plane and 8 mm in the vertical plane.

In relation to the forgoing discussion, note that some parts of the data for DRME_A or DRME_B are still noisy even after filtering which can be due the use of a large acceptance limit or the effect of adding noise being greater than the reduction of the sidereally repeating error or even the instability of the antenna, as both antennae are not fixed on pillars but on the flanges of the moving platform, which could be affected by many factors e.g. wind.

6.6 Deformation Monitoring Conclusions

The combined method of instantaneous GPS processing, applying sidereal filtering to periodic GPS data, was successful in detecting horizontal and vertical displacements in simulated near-real time, to the millimetre level. The applied technique improves the precision of deforming coordinates, reaching to a precision better than 5 mm and 8 mm in the horizontal and vertical plane respectively. Despite rejecting coordinates with greater than ± 30 cm discrepancies while forming the filter, the efficiency of this combined technique is still evident from the more precise results obtained after filtering for most of the data set. Better results can be obtained using a tighter acceptance limit as shown earlier in Section 5.6, however this may affect the temporal resolution.

Even though using switched antenna GPS data, which in turn results most of the time in the loss of about 45 seconds at the start of each switched session, based on the used

Table 6.4 DRME_B hourly unfiltered and filtered true versus observed Easting coordinates along with hourly raw data and switch sessions RMS, while applying horizontal displacements on 18/09/2007.

Start Time	True Coordinates (+588746 m)	Unfiltered			Filtered		
		Hourly average (+588746 m)	Hourly raw RMS (mm)	Hourly session RMS (mm)	Hourly average (+588746 m)	Hourly raw RMS (mm)	Hourly session RMS (mm)
07:27	0.4927	0.4922	2.11	1.73	0.4924	1.62	0.75
08:27	0.4923	0.4930	4.03	2.82	0.4916	3.28	1.20
09:27	0.4916	0.4915	2.34	1.95	0.4915	1.75	0.80
10:27	0.4897	0.4900	3.04	2.72	0.4895	1.74	0.64
11:27	0.4859	0.4817	9.13	5.61	0.4856	4.08	1.30
12:27	0.4783	0.4766	3.22	2.83	0.4784	2.42	2.30
13:27	0.4593	0.4607	2.51	1.64	0.4601	1.93	1.03
14:27	0.4214	0.4223	7.33	2.59	0.4221	7.18	1.69

Table 6.5 DRME_B hourly unfiltered and filtered true versus observed Northing coordinates along with hourly raw data and switch sessions RMS, while applying horizontal displacements on 18/09/2007.

Start Time	True Coordinates (+6093628 m)	Unfiltered			Filtered		
		Hourly average (+6093628 m)	Hourly raw RMS (mm)	Hourly session RMS (mm)	Hourly average (+6093628 m)	Hourly raw RMS (mm)	Hourly session RMS (mm)
07:27	0.9344	0.9348	6.00	4.46	0.9342	4.18	1.57
08:27	0.9353	0.9352	13.05	5.25	0.9354	12.53	2.83
09:27	0.9372	0.9366	7.60	6.47	0.9370	4.17	1.51
10:27	0.9418	0.9407	3.64	3.07	0.9408	2.55	1.32
11:27	0.9511	0.9475	8.85	4.68	0.9506	4.10	2.27
12:27	0.9696	0.9677	4.61	6.22	0.9694	4.29	5.44
13:27	1.0158	1.0158	5.36	1.70	1.0149	5.54	1.79
14:27	1.1083	1.1051	15.71	5.95	1.1050	15.71	5.15

Table 6.6 DRME_B hourly unfiltered and filtered true versus observed Up coordinates along with hourly raw data and switch sessions RMS, while applying vertical displacements on 19/09/2007.

Start Time	True Coordinates (+124 m)	Unfiltered			Filtered		
		Hourly average (+124 m)	Hourly raw RMS (mm)	Hourly session RMS (mm)	Hourly average (+124 m)	Hourly raw RMS (mm)	Hourly session RMS (mm)
07:26	0.9934	0.9959	8.37	6.58	0.9954	6.42	5.12
08:26	0.9924	0.9901	9.51	7.25	0.9946	6.03	3.94
09:26	0.9904	0.9914	10.23	8.84	0.9906	7.77	3.77
10:26	0.9854	0.9863	6.60	4.74	0.9864	5.30	3.62
11:26	0.9754	0.9836	19.29	14.26	0.9760	15.61	7.17
12:26	0.9554	0.9548	12.81	4.64	0.9558	5.35	3.28
13:26	0.9054	0.9048	6.40	4.46	0.9090	7.01	5.65
14:26	0.8054	0.8088	10.57	7.76	0.8089	10.37	8.02

hardware, displacements were detected with an acceptable precision especially after improving this precision through sidereal filtering. This implies the usefulness of this combined technique not only to monitor horizontal or vertical deformations in near-real time, but with reduced error even in a high multipath environment. Accordingly, the adopted methodology accomplished the required target of monitoring deformations using a quick, cost-effective and precise GPS technique.

In summary, the current chapter started with a description of the simulation moving platform, and then the collected data sets and applied displacements were explained. The orbits and processing technique employed were shown next, followed by analysis of the effects of the switched antenna array. The chapter concluded with the application of sidereal filtering for monitoring deformations and improving the precision of station coordinates using semi-continuous GPS data. The next chapter will include a brief summary of the work done throughout the whole thesis, followed by the main conclusions and related recommendations.

SUMMARY, CONCLUSIONS AND RECOMMENDATIONS

This chapter gives a brief summary of the topics discussed in the current research followed by the main conclusions based on the results obtained. The chapter ends with a series of recommendations which could be extracted from the conclusions, as well as discussions of some issues and approaches which are not addressed here and thus may be suitable for future work.

7.1 Summary

The current research aims to improve GPS positioning in three different aspects. The first is to use a fast processing software utilizing single epoch positioning, the second to reduce the effect of multipath error on the resulting coordinate precision, and finally to minimize the cost of GPS positioning used for monitoring structural deformations. Quick ambiguity resolution is advantageous especially when monitoring deformations in real time or near-real time. On the other hand, multipath error caused by reflection of GPS signals from nearby surfaces to the receiver is considered one of the major errors among sidereally repeating errors that will hinder precise GPS positioning. In addition, the high running cost of continuous GPS positioning play an important role in the choice of the deformation monitoring technique.

In the current research, a single epoch ambiguity resolution technique is used to solve for the integer phase ambiguity. This methodology is implemented through a GPS processing software called GASP. This program operates in a double difference mode, adopting the Ambiguity Function Method to solve for the unknown phase

ambiguities at each epoch independently from the previous or next epoch. This is advantageous because there is no necessity for static initialization, as well as being free of cycle slips.

As GPS satellites are designed to orbit the earth twice a day (half of one sidereal day), the geometry constellation of the satellite will nominally repeat every sidereal day. At first, an investigation was undertaken to study the actual error repeat interval, called here "sidereal lag", using the autocorrelation among station coordinates or carrier phase residuals. Given that the GPS receiver's environment remains essentially static, as the satellite geometry repeats in the sky, sidereally dependent errors will repeat as well, especially the most dominant multipath error. Accordingly, coordinate residuals "coordinate filter" or carrier phase residuals "observation filter" were stacked over several days at the optimum "sidereal lag", in order to reduce as much as possible the sidereally repeating errors. This analysis was not only based on the improvement in coordinate precision, but on the processing time required to produce such filtered coordinates as well. During these investigations, a comparison between the optimum obtained sidereal lag and the known nominal one was undertaken, again from the coordinate precision point of view.

After sidereal filter investigations at the coordinate or observation level, further sidereal filter studies were required in order to investigate two main factors. As several days can be stacked to produce a sidereal filter, the first study examined the optimum number of consecutive days to stack and apply while producing the best possible final filtered precision for station coordinates. In contrast, the second study considers the relation between the lifetime or age of any previously stacked filter versus the improvement in coordinate precision after filtering. In other words, how long any filter will last in order to still produce improvement in the coordinate precision when applied.

Several previous applications discussed the use of periodic GPS data especially for monitoring different kinds of deformations using the most economic and cost effective approach possible. This can be achieved efficiently by using a switched multi-antenna array, in which multiple antennae are connected to one receiver, while

logging data from each antenna every epoch for a specific period of time. Switching between antennae could be done manually or automatically. The current research uses a dual antenna switch device operated by a Visual Basic program to switch between two antennae. However, it was first vital to carry some investigations regarding the optimum observation length per antenna before switching to the other one. This was done while seeking the best possible precision, efficiency and compatibility with the optimum sidereal lag, for the possibility of adapting this technique for use with sidereal filtering. After the determination of this optimum session observation length, sidereal filtering was applied to periodic GPS data.

At the end, the dual antenna switch array was used in conjunction with the GASP single epoch processing software, while applying sidereal filtering in order to monitor known horizontal and vertical deformations, as well as improving the stability and precision of the deforming stations' coordinates. Deformations were implemented manually through a platform built in-house.

7.2 Conclusions

Based on the work performed throughout the thesis, a number of conclusions can be extracted from the obtained results. The following are the main conclusions:

1. The longer the window size used for sidereal lag determination e.g. 10-hours, the more consistent and steady the obtained lag value will be. However, a shorter window will still produce a usable value of the lag but with higher fluctuations with autocorrelation within 97 % of the longer-term optimum value (Section 3.5.2).

2. For double difference processing, the best possible lag to use in order to stack coordinate or phase residuals is 23h 55m 54s, i.e. 86154 in GPS seconds, that is 10 seconds earlier than the known nominal lag, in agreement with Choi et al. (2004); Axelrad et al. (2005); Agnew and Larson (2007). This optimum lag is stable over at least eight months period including satellite constellation changes (Figures 3.24 and 3.25).

3. Using a lag value other than the optimum obtained lag within a range of ± 5 seconds does affect the final coordinate precision, when double difference processing is adopted.

4. The multipath environment will affect the determination of the optimum lag. The higher the multipath, the less homogeneity and consistency of the lag throughout the data set (Figures 3.9 through to 3.11).

5. Sidereal filtering enhances the precision of station coordinates by reducing the effect of sidereally repeating errors especially multipath (Figure 4.1). Using a three-days-stack-filter, a daily 3D variance reduction of 50% and 73% is achieved in a low multipath environment (DRMS) and high multipath environment (NEWC) respectively (Table 4.3).

6. Coordinate filtering (based on the stack of coordinate residuals) gives slightly higher precision of 73% in 3D daily variance reduction in a high multipath environment, compared to observation filtering (based on the stack of double difference carrier phase residuals) of 71% variance reduction (Tables 4.3 and 4.5), yet they both give similar hour to hour consistency (Ragheb et al. 2007b).

7. Observation filtering takes shorter processing time — approximately one third — to achieve final filtered coordinates when compared to coordinate filtering, especially if a single epoch ambiguity resolution technique is adopted (Section 4.3.3). The higher the multipath environment, the longer time required to process the GPS data in coordinate filtering, which is not the case in observation filtering. This is due to the effect of multipath on the ambiguity search algorithm in the GASP software when running regularly in the fixed-base mode.

8. Stacking more days' residuals improves the overall coordinate precision, which remains valid until the optimum case of stacking seven days' residuals (Figure 4.13). In this case, a 3D daily variance reduction of 61% in the coordinates is achieved in a low multipath environment e.g. DRMS (Table 4.9), after which the coordinate precision drops with the increase in number of stacked days. In other words, stacking seven consecutive days' residuals prior to the applied day

produces the best possible precision for station coordinates. On the other hand, although stacking 7 days and more (until 21 days-stack) produced lower precision, they still all possess better precision when compared to the case where no filter is applied.

9. Considering stacking 3-day batches, as the time gap between any previously stacked filter and the applied day increases — the filter lifetime or "age" — the coordinate precision decreases. This continues until 23 days for observation filtering and 30 days for coordinate filtering (Figure 4.15). At this stage, similar precision to the unfiltered case is achieved, and thus applying any filter of longer age will worsen the coordinate precision rather than improving it (Ragheb et al. 2007a).

10. Although sidereal filtering is efficient in most applied cases, noise is still added along with the filtered residuals. Consequently, in particular instances, such as low multipath environments or weak multipath signals, the noise becomes the dominant error, which leads to the degradation of the efficiency of sidereal filtering.

11. During sidereal filter application of data sets of different satellite constellation, the observation filtering technique is the more robust technique to use, as common satellite processing between the stacked and applied data is unnecessary. On the contrary, for coordinate filtering common satellite processing is essential to achieve consistent results. This will save a great deal of time in re-processing of data, in order to apply the filter with common satellite constellation (Figure 4.15).

12. The switched multi-antenna array provides semi-continuous GPS data in a cost effective manner, due to the use of multiple antennae and one receiver, and thus reducing the number of used receivers. However, during switching between antennae, a certain transitional time ranging between 30–50 seconds is required after switching, in order to gain full lock back on satellites with reliable observations. This transitional period depends on several factors, mainly the

receiver hardware used. Accordingly, some bad epochs will occur at the start of each switch session (Figure 5.9).

13. According to this loss of lock after switching, the one minute switch interval does not provide adequate number of good epochs per switch interval per antenna. Hence, the optimum session observation length per antenna is two minutes, possessing similar precision to the five and ten minute switch intervals but with many advantages. Simply, the two minute switch interval offers a short session length, while providing adequate sub-centimetre level of accuracy for station coordinates. In addition, this interval can be easily synchronized with the optimum sidereal lag with some modifications for the optimum application of sidereal filtering. The first is to use a lag value of 86156s, that is two seconds away from the optimum lag — which will not have a major effect on the final filtered coordinates as stated before — and the second is to use a session length of 119 seconds instead of the proper two minute interval (120 seconds), which was then called the modified two minute switch interval in this thesis (Section 5.5.2). However, the above modifications depend on several factors such as: the cable length and material, receiver and antenna type, receiver firmware or the signal-to-noise-ratio (SNR) at the receiver, as well as the environmental conditions e.g. multipath.

14. Applying coordinate filtering on semi-continuous GPS data improved the coordinate precision of station coordinates, with higher efficiency in higher multipath environments, reaching to 65% variance reduction in daily 3D coordinates with a moderate acceptance limit (Table 5.2).

15. Using a large acceptance limit for epochs to be used in the filter e.g. 50 cm, although allowing the use of some bad epochs, still produced reliable results in coordinate filtering of the data. In addition, a 30 cm acceptance limit will provide a balance between maintaining a large acceptance limit to allow for monitoring different magnitudes of deformations, as well as being able to distinguish between good and poor epochs to a certain extent. However, deformations

occurring with magnitudes greater than the acceptance limit will be considered as outliers to be omitted, and thus will not be detected e.g. landslides.

16. Although the first 30–50 epochs after switching mostly proved to be unhealthy epochs, forming the filter while disregarding those epochs did not greatly improve the precision of station coordinates. This implies the use of all switch session epochs as they are, in which unhealthy ones will be removed through the adopted acceptance limit.

17. As sidereal filtering reduces sidereally repeating errors, mainly multipath, the coordinates after filtering before and after deformations are more stable, which makes it easier to differentiate between existing noise and occurring deformations, especially in the coordinate direction where the applied deformation has no component (Figures 6.14 through to 6.17).

18. The combined technique used in the current research adopting single epoch switched dual array GPS utilizing sidereal filtering was successful in monitoring horizontal and vertical deformations to the sub-centimetre or even the sub-millimetre level. The filtered horizontal plane coordinates were related to their true value counterparts with a slope of 0.987. The associated average rms for the residuals for the total considered epochs, 119 seconds average and hourly average is 4.50 mm, 2.66 mm and 0.61 mm respectively. For the filtered vertical plane coordinates, the slope of the observed/true relation was 0.993 while their residuals' RMS was 7.51 mm, 5.45 mm and 0.85 mm respectively (Figure 6.18).

19. The use of sidereal filtering in the combined technique improved the coordinate precision of deforming stations, reaching to 5 mm precision in the horizontal plane and 8 mm in the vertical plane, based on the average of hourly RMS values (Tables 6.1 to 6.6).

Looking at the above conclusions in a wider perspective, the current research provides useful methodologies to implement in various applications. One could obtain an average value of the geometry repeat interval using a short data set, which can be considered constant over a long period, followed by a stack and apply procedure of

coordinate or carrier phase residuals, depending on the governing factor being precision or processing time. Thus, this will in turn, end up with a more precise set of station coordinates with reduced multipath effect. This precision can be enhanced by increasing the number of stacked days up to seven days. In addition, in the longer term, sidereal filtering is still applicable while producing precision improvement even with a lengthy time gap between the stacked filter and the applied data reaching up to one month, depending on the type of stacked residuals, without sometimes even the need for common number of satellites between used data during processing.

Using semi-continuous instead of continuous GPS data, through the employment of a switched multi-antenna array, proved to be beneficial in supplying adequate and reliable data using a short session length, which can be further augmented through synchronization with sidereal filtering. And finally, integrating both methodologies of sidereal filtering and switched multi-antenna array, will present a cost-effective and precise technique suitable for monitoring slow occurring deformations to the sub-centimetre or millimetre level, while recovering the stability of the deforming stations through the improvement of station coordinate precision.

7.3 Recommendations and Future Work

This research recommends the use of a large window size (8–12 hours) for the determination of the optimum sidereal lag using autocorrelation. The average optimum repeat lag to use to filter the coordinates from sidereally repeating errors is 23h 55m 54s, while adopting double difference processing. This lag value appears stable and usable over time, without the need for further testing. From the precision point of view, coordinate filtering is the optimal sidereal filtering technique to use. Alternatively, from the processing time point of view, observation filtering is the more efficient sidereal filtering technique. The choice of whether to use the former or latter technique will depend on the overriding criteria of any project.

Stacking more days' residuals will increase the overall coordinate precision, with a maximum of seven consecutive days to gain best possible precision. In addition, it is not recommended to apply any previously stacked sidereal filter on any data set with a

time gap of 30 days if using coordinate filtering or 23 days if using observation filtering, as the resulting coordinates will be worse than the case where no filter applied.

When adopting the switched antenna array, switching between antennae every two minutes (exactly 119 seconds) or a multiple thereof is considered the most efficient, due to its rapidity, accuracy, as well as its suitability with sidereal filter application. Finally, the adopted combined technique of single epoch switched dual array GPS using sidereal filtering presents a quick, precise and economical system, which will provide a possible capability of near-real time monitoring of slow moving deformations. Consequently, this will in turn make the whole system useful for minimizing the severity of disasters.

On the other hand, while the current research covered many aspects regarding sidereal lag determination, filter application, switch multi-antenna array and deformation monitoring, there still exist some viewpoints and research aspects which might be considered for further investigation. The following is a list of some of these suggestions.

At first there would be some suggested enhancements to the GPS GASP processing software for a more efficient performance:

- Adopting a methodology in GASP for the rejection of observations from a specific or a number of satellites, based on the final position obtained, i.e. the usage of the best combination of available satellites aiming for the most precise solution.

- As the current GASP software is restricted for short baselines less than 25 km (Corbett 1994; Al-Haifi 1996), further investigations could be undertaken to use the GASP software for longer baselines processing. For example one could consider the implementation of different types of ionospheric models, the use of a more robust tropospheric model with temporal constraints, as well as considering the effect of ocean tide loading and solid earth tides.

- GASP operates in a single epoch processing mode and thus each epoch is treated independently from the preceding epoch. However, one should look into the application — optionally — of Kalman filtering, through the use of any processed good epoch data in the subsequent epoch, which could result in reducing the search size and required search time, in addition to improving the accuracy of the final outcome. This could be examined while using GASP in a static environment or more importantly in semi-static or even a kinematic environment.

- The updated GASP software deals only with GPS satellites. Accordingly, further modifications are required to enhance the software to process GLONASS satellites as well, which will boost the performance and the accuracy of the final output due to the increase in number of available satellites. This will of course ease the inclusion of satellites of other GNSS systems in the future such as Galileo, CNSS and QZSS.

Some other recommendations are given concerning sidereal filtering:

- Regarding any sidereal filter lifetime, it was seen that as the filter lifetime increases, the precision of the filtered data decreases (because of adding noise instead of reducing sidereally repeating errors). An effective investigation would be to not use a fixed value of the sidereal lag regardless of the filter age. On the contrary, change the lag value in order to suit any applied filter depending on its age, or in other words reducing the effect of adding noise while still reducing these errors of which the majority is multipath. The choice of the appropriate lag to use could be examined through the autocorrelation methodology. As a result, one could apply any previously formed filter on any data set, with no lifetime restriction and without degrading the precision of the final station coordinates.

- Further studies could be carried out on how applying sidereal filtering using carrier phase residuals could assist in the ambiguity resolution of the GPS processing software. In other words, how can carrier phase residuals contribute in the reduction of the search size and time, required to obtain final set of correct integer ambiguities.

- During weighting the coordinates while forming the coordinate stack, one could use the formal errors of the coordinates along with a Gaussian weighting as function of time, to produce more efficient weighted stacked coordinate residuals. For the observation filter, higher weights could be given to stacked carrier phase residuals when applied in the re-run of the GASP program, compared to unfiltered residuals. Considering both filtering methodologies, older stacked residuals could be given less weight than newly formed stacked residuals according to the time separation between the filtered residuals and the applied data.

Finally, further recommendations are presented regarding the switched antenna array and the use of the combined single epoch dual antenna switch array adopting sidereal filtering for monitoring deformations:

- Some useful research could be undertaken to study the relations between cable length and type, receiver and antenna type, multipath environment, and the time required for the receiver to lock back onto appropriate number of satellites with reliable observations after switching from the other antenna. This could be extended to study their effects on the switch session length and number of unhealthy epochs.

- As the extracted conclusions for the switched antenna array are general, then the dual antenna switch array GPS technique can be expanded to be used with multiple antennae to monitor more points, especially when monitoring a large structure or area using different deformation test points.

- This combined technique is ideal to be used for slow moving deformations, where deformations occurring at periods greater than double the switch interval. However, it can also be expanded to be used for monitoring rapid structural deformations e.g. strong wind forces or seismic forces due to earthquakes, but with data gaps in the time series which may affect the temporal resolution of the whole process.

- Pre-assessment investigations into the structure under study concerning the most influential deformations will give an idea of the expected magnitude of deformations. Thus, one could use a more suitable limit for accepting epochs while stacking and applying residuals during sidereal filtering and therefore further improving the precision of station filtered coordinates.

REFERENCES

Agnew D. and Larson K. (2007). Finding the Repeat Times of the GPS Constellation. GPS Solutions, **Vol.11** (1): pp.333–336.

Al-Haifi Y. (1996). Short Range GPS Single Epoch Ambiguity Resolution. PhD Thesis, Department of Surveying, University of Newcastle upon Tyne, Newcastle upon Tyne, UK.

Ali R. (2003). High Accuracy Real-Time Engineering Monitoring using Low-Cost GPS Equipment. PhD Thesis, Civil Engineering Department, Faculty of Engineering, Mattaria-Helwan University, University College London.

Axelrad P., Comp C. and MacDoran P. (1996). SNR-based Multipath Error Correction for GPS Differential Phase. IEEE Transactions on Aerospace and Electronic Systems, **Vol. 32** (2): pp.650–660.

Axelrad P., Larson K. and Jones B. (2005). Use of the Correct Satellite Repeat Period to Characterize and Reduce Site-Specific Multipath Errors. Proceedings of the 18th International Technical Meeting of the Satellite Division of the Institute of Navigation, ION GNSS 2005, Long Beach Convention Centre, Long Beach, California, USA, pp.2638–2648.

Barker B., Betz J., Clark J., Correia J., Gillis J., Lazar S., Rehborn K. and Straton J. (2000). Overview of the GPS M-Code Signal. Technical Paper at the MITRE Corporation.

Barnes J. (2000). Real Time GPS and Multipath: Characterisation and Improved Least Squares Modelling. PhD Thesis, Department of Geomatics, University of Newcastle upon Tyne, Newcastle upon Tyne, UK.

Barnes J., Rizos C., Wang J., Meng X., Cosser E., Dodson A. and Roberts G. (2003). The Monitoring of Bridge Movements using GPS and Pseudolites. Proceedings of the 11th FIG Symposium on Deformation Measurements, Santorini, Greece.

Bilich A. and Larson K. (2007). Mapping the GPS Multipath Environment using the Signal-to-Noise Ratio (SNR). Radio Science, **Vol. 42** (RS6003).

Bock Y., De Jonge P., Honcik D., Bevis M., Bock L. and Wilson S. (2001). Epoch-By-Epoch Positioning Applied to Dam Deformation Monitoring at Diamond Valley Lake, Southern California. The 10th FIG International Symposium on Deformation Measurements, Orange, California, USA.

Bock Y., Nikolaidis R., De Jonge P. and Bevis M. (2000). Instantaneous Geodetic Positioning at Medium Distances with the Global Positioning System. Journal of Geophysical Research, **Vol. 105** (B12): pp.28223–28253.

Cannon J. (1998). Mitigation of Static Carrier-phase Multipath Effects using Multiple Closely-spaced Antennas. Proceedings of the 11th International Technical Meeting of the Satellite Division of the Institute of Navigation, ION GPS-98, Nashville Convention Centre, Nashville, Tennessee, USA, pp.1025–1034.

Chen A., De Lorenzo D., Enge P., Xingxin Gao G. and Lo S. (2007). GNSS over China: The Compass MEO Satellite Codes. Inside GNSS, July/August 2007.

Chen D. (1993). Fast Ambiguity Search Filter [FASF]: A Noval Concept for GPS Ambiguity Resolution. Proceedings of the 6th International Technical Meeting of the Satellite Division of the Institute of Navigation, ION GPS-93, Salt Palace Convention Centre, Salt Lake City, Utah, USA, pp.781–787.

Chen Y., Ding X., Huang D. and Zhu J. (2000). A Multi-antenna GPS System for Local Area Deformation Monitoring. Earth Planets and Space, **Vol. 52**: pp.873–876.

Choi K., Bilich A., Larson K. and Axelrad P. (2004). Modified Sidereal Filtering: Implications for High-rate GPS Positioning. Geophysical Research Letters, **Vol. 31** (L22608).

Cohen C. and Parkinson B. (1991). Mitigating Multipath Error in GPS-based Attitude Determination. Guid Control Adv Astronaut Sci, 53: pp.53–68.

Corbett S. (1994). GPS Single Epoch Ambiguity Resolution for Airborne Positioning and Orientation. PhD Thesis, Department of Surveying, University of Newcastle upon Tyne, Newcastle upon Tyne, UK.

Corbett S. (1993). GPS for Attitude Determination and Positioning in Airborne Remote Sensing. Proceedings of the 6th International Technical Meeting of the Satellite Division of the Institute of Navigation, ION GPS-93, Salt Palace Convention Centre, Salt Lake City, Utah, USA, pp.789–796.

Counselman C. and Gourevitch S. (1981). Miniature Interferometer Terminals for Earth Surveying: Ambiguity and Multipath with Global Positioning System. IEEE Transactions on Geosciences and Remote Sensing, **Vol. G-19** (4): pp.244–252.

Crosetto M., Arnaud A., Duro J., Biescas E. and Agudo M. (2003). Deformation Monitoring using Remotely Sensed Radar Interferometric Data. Proceedings of the 11th FIG Symposium on Deformation Measurements, Santorini, Greece.

Cross P. (1990). Advanced Least Squares Applied to Position-Fixing. Working Paper No. 6, School of Surveying, University of East London, UK.

De Jonge P., Bock Y. and Bevis M. (2000). Epoch-by-Epoch Positioning and Navigation. Geodetics Inc., La Jolla, CA, USA.

Ding X., Chen Y., Huang D., Zhu J., Tsakiri M. and Stewart M. (2000). Slope Monitoring using GPS: A Multi-Antenna Approach. GPS World, **Vol. 11** (3): pp.52–55.

Ding X., Dai W., Yang W., Zhou X., Lam J., Zhang Q. and Wang L. (2007). Application of Multi-Antenna GPS Technology in Monitoring Stability of Slopes. Strategic Integration of Surveying Services, FIG Working Week 2007, Hong Kong SAR, China.

El-Rabbany A. (2006). Introduction to GPS: The Global Positioning System. Second Edition, Artech House Inc, Massachusetts.

Elósegui P., Davis J., Jaldehag R., Johansson J., Niell A. and Shapiro I. (1995). Geodesy using the Global Positioning System: The effects of signal scattering on estimates of site position. Journal of Geophysical Research, **Vol. 100** (B7): pp.9921–9934.

Enge P. (2003). GPS Modernization: Capabilities of the New Civil Signals. Invited Paper at the Australian International Aerospace Congress, Brisbane, Australia.

Erickson C. (1992). An Analysis of Ambiguity Resolution Technique for Rapid Static GPS Surveys using Single Frequency Data. Proceedings of the 5th International Technical Meeting of the Satellite Division of the Institute of Navigation, ION GPS-92, Albuquerque Convention Centre, Albuquerque, New Mexico, USA, pp.453–462.

Erol S., Erol B. and Ayan T. (2004). A General Review of the Deformation Monitoring Techniques and a case study: Analysing Deformations using GPS/Levelling. 20th ISPRS Congress "Geo-Imagery Bridging Continents", Istanbul, Turkey.

Estey L. and Meertens C. (1999). TEQC: The Multi-Purpose Toolkit for GPS/GLONASS Data. GPS Solutions (pub. by John Wiley & Sons) **Vol. 3** (1): pp.42–49.

Eueler H. and Goad C. (1991). On Optimal Filtering of GPS Dual Frequency Observations without using Orbit Information. Journal of Geodesy, **Vol. 65** (2): pp.130–143.

Eueler H. and Landau H. (1992). Fast GPS Ambiguity Resolution OTF for Real-Time Applications. The 6th International Geodetic Symposium on Satellite Positioning, Ohio State University, Columbus, Ohio, USA.

Fontana R., Cheung W., Novak P. and Stansell T. (2001). The New L2 Civil Signal. Proceedings of the 14th International Technical Meeting of the Satellite Division of the Institute of Navigation, Salt Palace Convention Centre, Salt Lake City, Utah, USA, pp.617–631.

Forward T., Stewart M., Penna N. and Tsakiri M. (2001). Steep Wall Monitoring using Switched Antenna Arrays and Permanent GPS Networks. The 10th FIG International Symposium on Deformation Measurements, Orange, California, USA.

Frei E. and Beutler G. (1990). Rapid Static Positioning based on the Fast Ambiguity Resolution Approach "FARA", Theory and First Results. Manuscripta Geodaetica, **Vol. 15**: pp.325–326.

Gen-you L., Yao-zhong Z. and Rong-sheng Z. (2005). A New Approach of Single Epoch GPS Positioning for Landslide Monitoring. ACTA SEISMOLOGICA SINICA, **Vol. 18** (4): pp.427–434.

Genrich J. and Bock Y. (1992) Rapid Resolution of Crustal Motion at Short Ranges with the Global Positioning System. Journal of Geophysical Research, **Vol. 97** (B3): pp.3261–3269.

Georgiadou Y. and Kleusberg A. (1988). On Carrier Signal Multipath Effects in Relative GPS Positioning. Manuscripta Geodaetica, **Vol. 13** (3): pp.172–179.

Gledan J. (2004). Development of Low Cost Strategies for Deformation Monitoring. PhD Thesis, School of Civil Engineering and Geosciences, University of Newcastle upon Tyne, Newcastle upon Tyne, UK.

GPS-QZSS Technical Working Group (2007). Interface Specification for QZSS: About QZSS. Retrieved September 2007 from http://qzss.jaxa.jp/is-qzss/qzss_e.html.

Gunasingam R. (2003). Single Epoch Ambiguity Resolution using Low-Cost GPS Receivers. MPhil Thesis, School of Civil Engineering and Geosciences, University of Newcastle upon Tyne, Newcastle upon Tyne, UK.

Haji G. (1990). The Multipath Simulator: A Tool Toward controlling Multipath. Proceedings of the 2nd Symposium on GPS Applications in Space, Hanscom Air Force base, MA, USA, pp.229–243.

Hatch R. (1990). Instantaneous Ambiguity Resolution, in Kinematic Systems in Geodesy Surveying and Remote Sensing. Banff, Canada.

He X., Sang W., Chen Y. and Ding X. (2005). Steep Slope Monitoring: GPS Multiple Antenna System at Xiaowan Dam. GPS World, November: pp.20–25.

He X., Yang G., Ding X. and Chen Y. (2004a). Application and Evaluation of a GPS Multi-antenna System for Dam Deformation Monitoring. Earth Planets Space, **Vol. 56**: pp.1035–1039.

He X., Yang G., Ding X. and Chen Y. (2004b). Development of GPS Multi-antenna Switch for Deformation Monitoring. The 2004 International Symposium on GNSS/GPS, Sydney, Australia.

Hill C. and Sippel K. (2002). Modern Deformation Monitoring: A Multi Sensor Approach. 12th International Federation of Surveyors (FIG), Washington, DC, USA, pp.1–12.

Hofmann-Wellenhof B., Lichtenegger H. and Collins J. (2001). GPS: Theory and Practice. 5th Edition, Springer-Verlag Wien, New York, USA.

International GNSS Service (2007). IGS Product Availability. Retrieved September 2007 from http://igscb.jpl.nasa.gov/components/prods_cb.html.

Johnson B. (1997). Geodetic Applications in GPS. Nordic Geodetic Commission, Sweden.

Kaplan E. and Hegarty C. (2006). Understanding GPS: Principles and Applications. Second Edition, Artech House Inc, Massachusetts.

Kreutzfeldt H. (2001). RASP Description and Switch Box Investigation. Report, Newcastle University, Newcastle, UK.

Lachapelle G., Cannon E. and Lu G. (1992). Ambiguity Resolution On The Fly. A Comparison of P-Code and High performance C/A-Code Receiver Technologies. Proceedings of the 5th International Technical Meeting of the Satellite Division of the Institute of Navigation, ION GPS-92, Albuquerque Convention Centre, Albuquerque, New Mexico, USA, pp.1025–1032.

Larson K., Bilich A. and Axelrad P. (2007). Improving the precision of high-rate GPS. Journal of Geophysical Research, **Vol. 112** (B05422).

Lau L. and Cross P. (2007). Development and Testing of a New Ray-tracing Approach to GNSS Carrier-phase Multipath Modelling. Journal of Geodesy, **Vol. 81** (11): pp.713–732.

Lau L. and Mok E. (1999). Improvement of GPS Relative Positioning Accuracy by using SNR. Journal of Surveying Engineering-ASCE, **Vol. 125** (4): pp.185–202.

Lavrakas J. (2007). GNSS in the Year 2017. GPS World, **Vol. 18** (5): pp.14–20.

Leica Geosystems (2007). Leica SmartStation: Total Station with Integrated GNSS/GPS. Retrieved August 2007 from http://www.leica-geosystems.com/corporate/en/products/total_stations/lgs_8276.htm.

Leica Geosystems (2005). Leica Geo Office Surveying & Engineering Software. Retrieved February 2005 from http://www.leica-geosystems.com/corporate/en/products/software/lgs_4611.htm.

Leick A. (2004). GPS Satellite Surveying. Second Edition, John Wiley & Sons Inc, New York.

McGraw G. (2006). How can Dual Frequency Code and Carrier Measurements to be Optimally Combined to Enhance Position Solution Accuracy? Inside GNSS, July/August 2006.

Meng X. (2002). Real-time Deformation Monitoring of Bridges Using GPS/Accelerometers. PhD Thesis, Institute of Engineering Surveying and Space Geodesy, The University of Nottingham, UK.

National Geodetic Survey (2005). GPS Antenna Calibration. Retrieved April 2005 from http://www.ngs.noaa.gov/ANTCAL/index.shtml.

Neilan R., Zumberge J., Beutler G. and Kouba J. (1997). The International GPS Service: A Global Resource for GPS Applications and Research. Proceedings of the 10th International Technical Meeting of the Satellite Division of the Institute of Navigation, ION GPS-97, Kansas City Convention Centre, Kansas City, USA, pp.883–890.

Niell A. (1996). Global Mapping Functions for the Atmosphere Delay at Radio Wavelengths. Journal of Geophysical Research, **Vol. 101** (B2): pp.3227–3246.

Nikolaidis R., Bock Y., De Jonge P., Shearer P., Agnew D. and Van Domselaar M. (2001). Seismic Wave Observations with the Global Positioning System. Journal of Geophysical Research, **Vol. 106** (B10): pp.21897–21916.

NIST/SEMATECH (2005). E-Handbook of Statistical Methods. Retrieved May 2005 from http://www.itl.nist.gov/div898/handbook/.

Ogaja C., Rizos C. and Han S. (2000). Is GPS Good Enough for Monitoring the Dynamics of High-Rise Buildings? Trans Tasman Surveyors, Queenstown, New Zealand, pp.150–164.

Ogaja C., Rizos C., Wang J. and Brownjohn J. (2001). Toward the Implementation of On-line Structural Monitoring using RTK GPS and Analysis of Results using the Wavelet Transform. The 10th International Federation of Surveyors (FIG), Working Group 6, Deformation Measurements and Analysis, Orange, California, USA, pp.284–293.

Partyka J. (2007). Modernization Fits and Starts: SA, III, IIF, IIR-M. GPS World, **Vol. 18** (10): pp.16–17.

Penna N. and Stewart M. (2003). Aliased tidal signatures in continuous GPS height time series. Geophysical Research Letters, **Vol. 30** (23): pp.2184.

Philippov V., Sutiagin I. and Ashjaee J. (1999). Measured Characteristics of Dual Depth Dual Frequency Choke Ring for Multipath Rejection in GPS Receivers. Proceedings of the 12th International Technical Meeting of the Satellite Division of the Institute of Navigation, ION GPS-99, Nashville Convention Centre, Nashville, Tennessee, USA, pp.793–796.

Pratt A. (1991). Mathematical and Physical Modelling of Multipath Interference. Proceedings of the 4th International Technical Meeting of the Satellite Division of the Institute of Navigation, ION GPS-91, Albuquerque Convention Centre, Albuquerque, New Mexico, USA, pp.1013–1020.

Pullen S. and Enge P. (2004). A Civil User Perspective on Near-term and Long-term GPS Modernization. Proceedings of Japan GPS/GNSS Symposium, Tokyo, Japan.

Radovanovic R. and Teskey W. (2001). Dynamic Monitoring of Deforming Structures: GPS Versus Robotic Tachometry Systems. The 10th International Federation of Surveyors (FIG) International Symposium on Deformation Measurements, Orange, California, USA.

Ragheb A., Clarke P. and Edwards S. (2007a). Coordinate-space and Observation-space Filtering Methods for Sidereally Repeating Errors in GPS: Performance and Filter Lifetime. Proceedings of the National Technical Meeting 2007, Catamaran Resort Hotel, San Diego, California, USA: pp.480–485.

Ragheb A., Clarke P. and Edwards S. (2007b). GPS Sidereal Filtering: Coordinate- and Carrier-phase-level Strategies. Journal of Geodesy, **Vol. 81** (5): pp.325–335.

Ray J. (2000). Mitigation of GPS Code and Carrier Phase Multipath Effects using a Multi-antenna System. PhD Thesis, Department of Geomatics Engineering, University of Calgary, Calgary, Alberta, Canada.

Remondi B. (1991). Kinematic GPS Results without Static Initialization. Proceedings of the 47th Annual Meeting of the Institute of Navigation, Washington, D.C., pp. 87-111.

Remondi B. (1984). Using the Global Positioning System (GPS) Phase Observable for Relative Geodesy: Modelling, Processing and Results. PhD Thesis, Centre for Space Research, University of Texas, Austin, USA.

RICOH (2007). Geo-Imaging. Retrieved August 2007 from www.ricohsolutions.com/geo.

Rizos C. (2007). Principles and Practice of GPS Surveying. Satellite Navigation and Positioning Lab, University of New South Wales. Retrieved September 2007 from http://www.gmat.unsw.edu.au/snap/gps/gps_survey/principles_gps.htm.

Roberts G., Meng X. and Dodson A. (2001a). The use of Kinematic GPS and Triaxial Accelerometers to Monitor the Deflections of Large Bridges. The 10th International Federation of Surveyors (FIG), Working Group 6, Deformation Measurements and Analysis, Orange, California, USA, pp.268–275.

Roberts G., Meng X. and Dodson A. (2001b). Data Processing and Multipath Mitigation for GPS/Accelerometer Based Hybrid Structural Deflection Monitoring System. Proceedings of 14th International Technical Meeting of the Satellite Division of the Institute of Navigation (ION GPS-2001), Salt Palace Convention Centre, Salt Lake City, Utah, USA, pp.473–508.

Rutledge D., Gnipp J. and Kramer J. (2001). Advances in Real-Time GPS Deformation Monitoring for Landslides, Volcanoes and Structures. The 10th FIG International Symposium on Deformation Measurements, Orange, California, USA.

Saastamoinen J. (1973). Contribution to the Theory of Atmospheric Refraction Part II: Refraction Corrections in Satellite Geodesy. Journal of Geodesy, **Vol. 47** (1): pp.13–34.

Saastamoinen J. (1972). Contribution to the Theory of Atmospheric Refraction. Journal of Geodesy, **Vol. 46** (3): pp.279–298.

Santerre R. and Beutler G. (1993). A Proposed GPS Method with Multi-Antennae and Single Receiver. Journal of Geodesy, **Vol. 67** (4): pp.210–223.

Satirapod C. and Rizos C. (2005). Multipath Mitigation by Wavelet Analysis for GPS Base Station Applications. Survey Review, **Vol. 38** (295): pp.2–10.

Schofield W. (2001). Engineering Surveying: Theory and Examination Problems for Students. Fifth Edition, Butterworth-Heinemann, Oxford, UK.

Schupler B. and Clark T. (1991). How different antennas affect the GPS Observable. GPS World, **Vol. 2** (11): pp.32–36.

Teferle N., Bingley R., Dodson A., Apostolidis P. and Staton G. (2003). RF Interference and Multipath Effects at Continuous GPS Installations for Long-term Monitoring of Tide Gauges in UK Harbours. Proceedings of the 16th International Technical Meeting of the Satellite Division of the Institute of Navigation, ION GPS/GNSS 2003, Oregon Convention Centre, Portland, Oregon, USA, pp.2082–2092.

Teunissen P. (1993). Least Squares Estimation of the Integer GPS Ambiguities. Invited Lecturer, Section IV Theory and Methodology, IAG General Meeting, Beijing, China.

US Coast Guard (2007). GPS Modernization. Retrieved October 2007 from http://www.navcen.uscg.gov/gps/modernization/.

US Coast Guard (2006). CGSIC General Information. Retrieved December 2006 from http://www.navcen.uscg.gov/cgsic/.

US Geological Survey (2007). Two-color EDM. Retrieved August 2007 from http://earthquake.usgs.gov/research/deformation/twocolor/.

US Army Corps of Engineers (2003). Engineering and Design - NAVSTAR Global Positioning System Surveying. Engineer Manual, Department of the Army, Washington, DC, USA, EM 1110-1-1003.

US Army Corps of Engineers (2002). Structural Deformation Surveying. Engineer Manual, Department of the Army, Washington, DC, USA, EM 1110-2-1009.

Van Dierendonck A. and Braasch M. (1997). Evaluation of GNSS Receiver Correlation Processing Techniques for Multipath and Noise Mitigation. Proceedings of the National Technical Meeting 1997, Loews Santa Monica Beach Hotel, Santa Monica, California, USA, pp.207–216.

Williams S. (2003). The effect of Coloured Noise on the Uncertainties of Rates Estimated from Geodetic Time Series. Journal of Geodesy, **Vol. 76** (9–10): pp.483–494.

Williams S., Bock Y., Fang P., Jamason P., Nikolaidis R., Prawirodirdjo L., Miller M. and Johnson D. (2004). Error Analysis of Continuous GPS Position Time Series. Journal of Geophysical Research, **Vol. 109** (B03412).

Zheng D., Zhong P., Ding X. and Chen W. (2005). Filtering GPS Time Series using a Vondrak Filter and Cross-validation. Journal of Geodesy, **Vol. 79** (6–7): pp.363–369.

GASP INITIAL FILE

```
Input Data
Base receiver Observation file name:              /.../DRMN/DRMN0940.05o
Unknown receiver Observation file name:           /.../DRMS/DRMS0940.05o
Output file name:                                 /.../OUTPUT/DRMS_OUT940
XYZ output file name:                             /.../XYZout/DRMS_XYZ940
NEU output file name:                             /.../NEUout/DRMS_NEU940
Phase output file name:                           /.../PHASEout/DRMS_PH940
Satellite Pairing file name:                      /.../SAT/DRMS_DD940
Use SP3 Precise Orbit? (Y/N):                     Y
Precise orbit file:                               /.../PRECISE/igs1317.sp3
Apply Antenna PCV Correction? (Y/N):              Y
Fixed Receiver PCV file name:                     /.../PCVC/Leica_AX1202
Moving Receiver PCV file name:                    /.../PCVC/Leica_AX1202
Apply Phase Residuals Filter? (Y/N):              Y
Filtered Phase Residuals file name:               /.../FILTER/DRMS_FL_RES
Optimum Sidereal Lag (Seconds):                   86154
Fix coordinates of Unknown Point? (Y/N):          N
Fixed Coordinates of Base Point:                  3666.. -10329.. 124.5..
Ignore Specific Satellites? (Y/N)(No.)(SVs): Y  04   07 12 17 31
Base receiver (S)tatic or (M)oving:               S
Unknown receiver (S)tatic or (M)oving:            M
Search Size:                                      5
Reduce search range (Y/N):                        N
Limit of Maximum Search Size:                     8
Limit of Maximum AFV (%):                         95
Apply Coordinates Continuation (Y/N):             Y
Start time (Seconds or DD/MM/YY Hr:Min:Sec): 3/12/2004 11:00:00
Stop time (Seconds or DD/MM/YY Hr:Min:Sec):  3/12/2004 11:00:15
Use code for approx positions (Y/N):              Y
Code solution (P1,P2,C1,P3,P5):                   C1
AFM threshold (%):                                90
Epoch interval:                                   1
Elevation Angle Value:                            5
Average Geodetic Undulation (m):                 -45

Output Data

Lat/Lon/Ht (Y/N):                                 Y
X/Y/Z (Y/N):                                      Y
E/N/h (Y/N):                                      Y
Number of satellites (Y/N):                       Y
Number of Trial positions (Y/N):                  Y
```

GASF INITIAL FILE

```
Input File Name:                                    /../GASF/SN02.xyz
Output File Name:                                   /../GASF/SN02.out
Time of Start Epoch (Seconds):                      223200
Number of Sidereal Lag Increase:                    60
Total Number of Processed Epochs:                   7200
Minimum Sidereal Lag Period (Seconds):              86130
Tolerance limit for Standard Deviation (m):         0.1
Steps of increasing Sidereal Lag (Seconds):         1
Tolerance Limit for Epoch Coordinates (m):          0.2
Approximate Coordinates (X Y Z):    3667115.02 -103500.04  5200148.86
```

SIDEREAL FILTER TABLES

Table C.1 24-hour coordinate standard deviations in three directions for all six cases based on the coordinate filter for the December_05 data set.

Station	SD (mm)	CASE						
		Unfiltered	Day1	Day2	Day3	Day1,2	Day2,3	Day1,2,3
SN02	E	2.2	2.1	2.1	2.1	1.8	1.8	1.7
	N	3.7	3.5	3.4	3.5	3.1	3.0	2.9
	U	6.0	5.7	5.7	5.9	5.0	5.0	4.7
DRMS	E	1.9	2.0	2.0	1.9	1.7	1.7	1.6
	N	3.3	3.3	3.2	3.2	2.8	2.8	2.6
	U	5.5	5.5	5.4	5.3	4.7	4.6	4.4
NEWC	E	2.9	2.3	2.3	2.3	2.1	2.1	2.0
	N	4.5	3.8	3.8	3.7	3.4	3.5	3.2
	U	8.1	6.5	6.5	6.4	5.7	5.9	5.5

Table C.2 24-hour coordinate standard deviations in three directions for all six cases based on the observation filter for the April_05 data set.

Station	SD (mm)	CASE						
		Unfiltered	Day1	Day2	Day3	Day1,2	Day2,3	Day1,2,3
SN02	E	2.3	2.1	2.1	2.0	1.9	1.8	1.7
	N	3.3	3.1	3.1	3.0	2.7	2.7	2.5
	U	5.6	5.2	5.2	5.0	4.5	4.4	4.1
DRMS	E	1.9	1.8	1.8	1.8	1.6	1.6	1.5
	N	3.3	2.9	2.9	2.8	2.6	2.5	2.4
	U	5.3	4.7	4.7	4.7	4.1	4.1	3.9
NEWC	E	2.9	2.3	2.0	2.0	1.8	1.7	1.6
	N	4.3	3.1	3.1	2.8	2.6	2.5	2.4
	U	8.0	5.5	5.3	5.2	4.6	4.5	4.2

Table C.3 24-hour coordinate standard deviation in three directions for all six cases based on the observation filter for the December_05 data set.

Station	SD (mm)	CASE						
		Unfiltered	Day1	Day2	Day3	Day1,2	Day2,3	Day1,2,3
SN02	E	2.2	2.2	2.3	2.3	2.0	2.0	1.8
	N	3.7	3.7	3.8	3.8	3.3	3.3	3.0
	U	6.0	6.0	6.1	6.1	5.3	5.3	4.9
DRMS	E	1.9	2.2	2.1	2.1	1.9	1.8	1.7
	N	3.3	3.6	3.5	3.5	3.1	3.0	2.8
	U	5.5	5.9	5.8	5.7	5.2	5.0	4.8
NEWC	E	2.9	2.6	2.6	2.6	2.2	2.3	2.1
	N	4.5	4.2	4.4	4.4	3.7	3.9	3.5
	U	8.1	7.3	7.2	8.2	6.1	6.5	5.8

SIDEREAL FILTER FIGURES

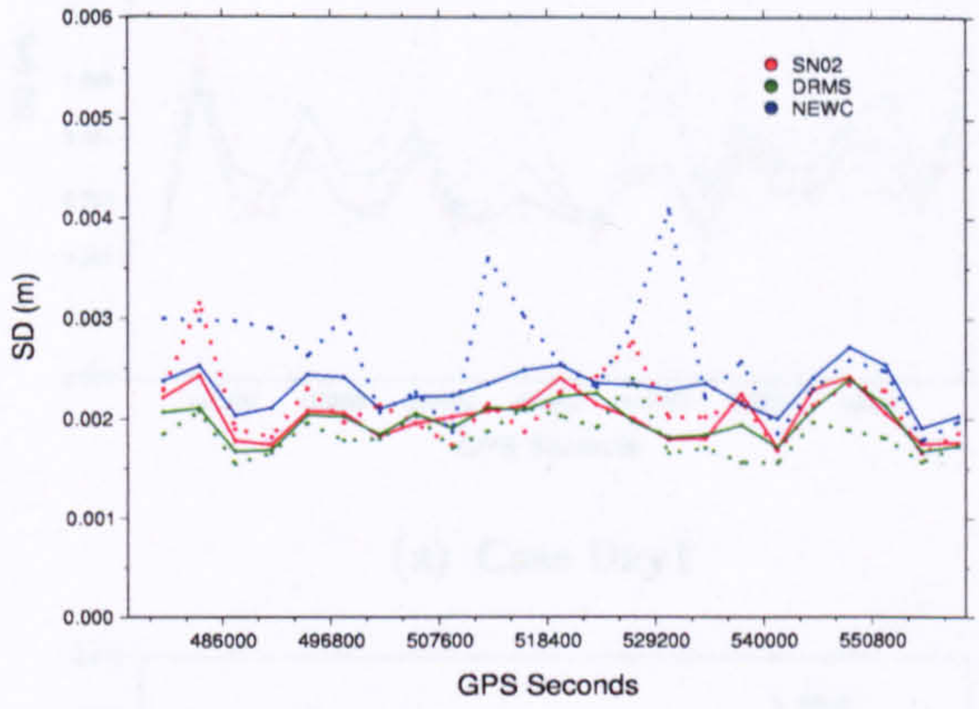

(a) Case Day1

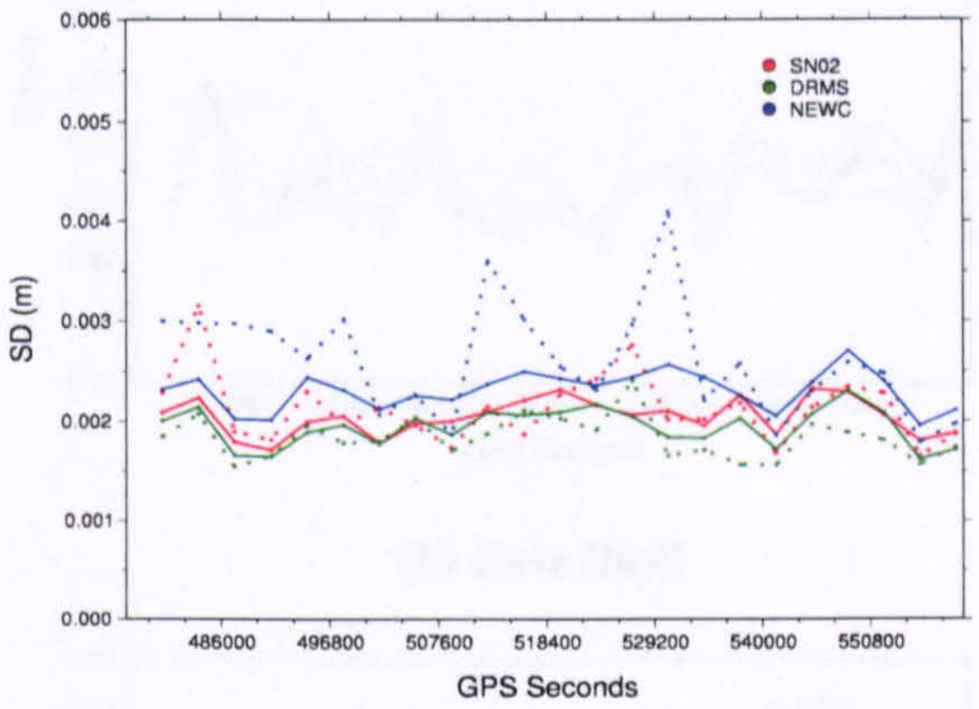

(b) Case Day2

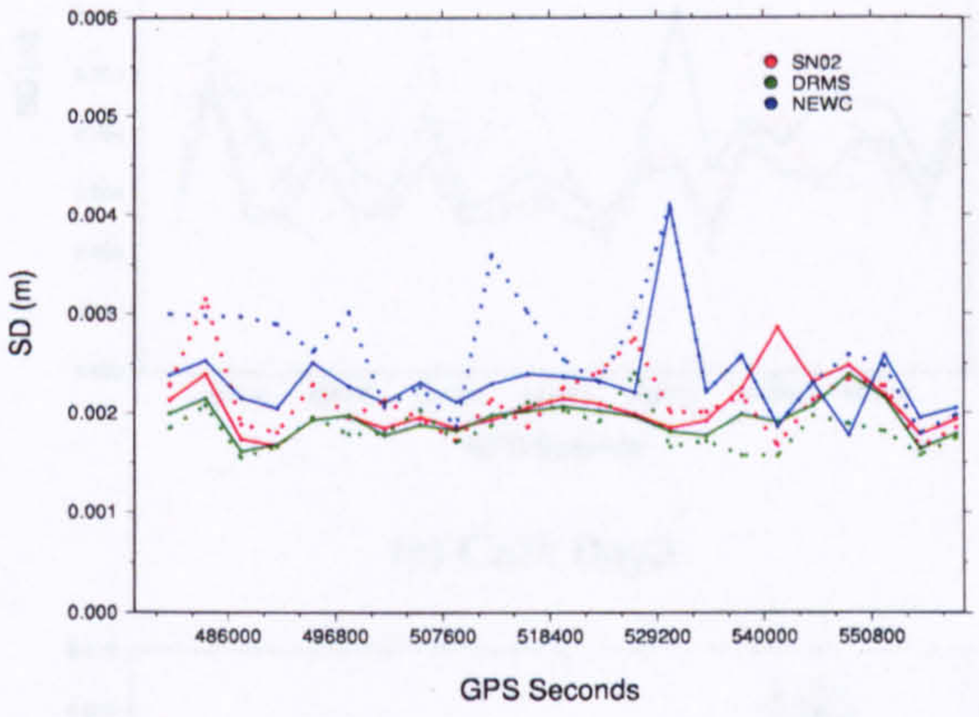

(c) Case Day3

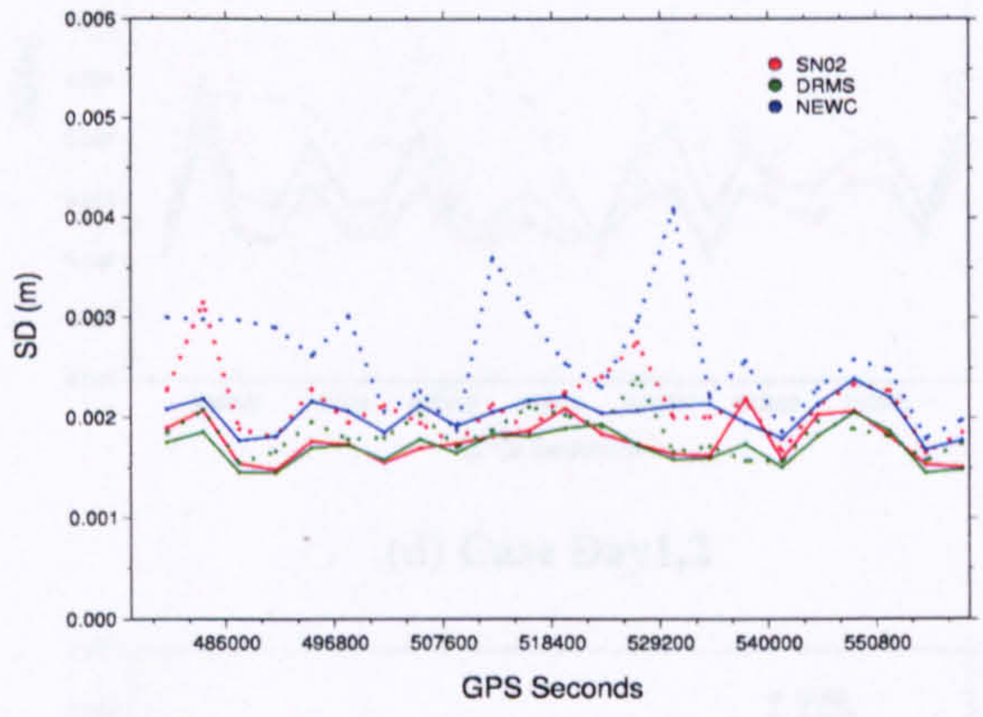

(d) Case Day1,2

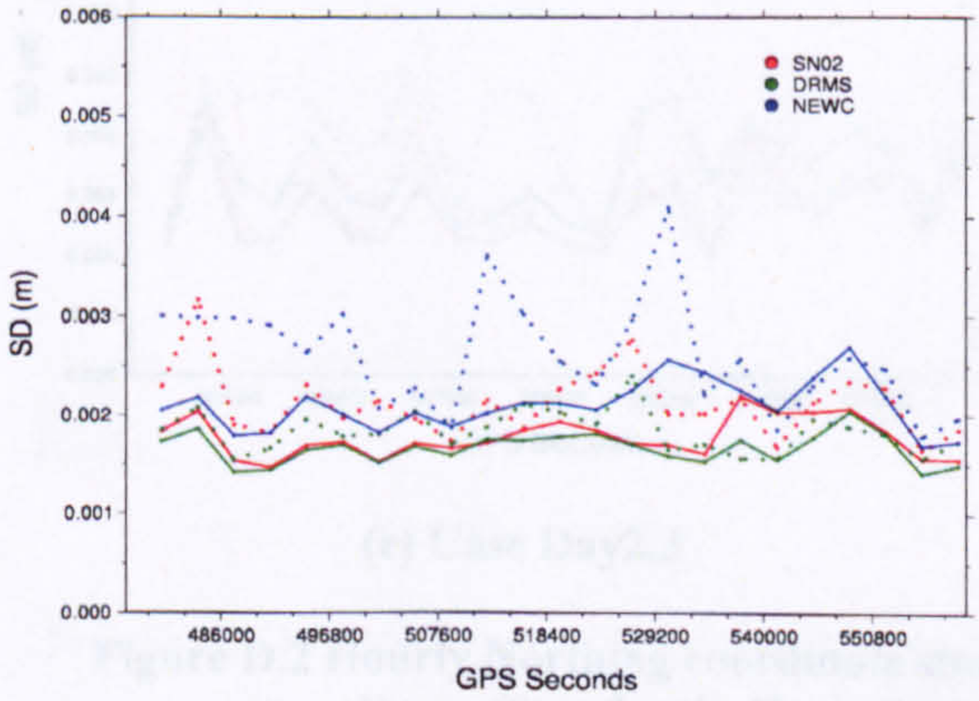

(e) Case Day2,3

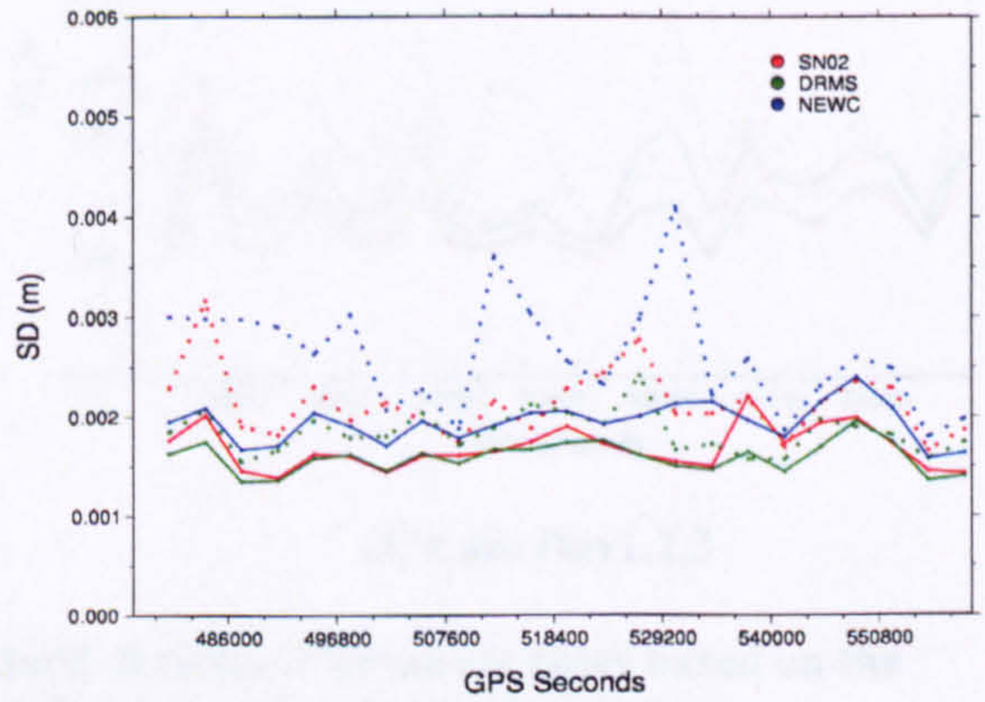

(f) Case Day1,2,3

Figure D.1 Hourly Easting coordinate standard deviations for all six cases based on the coordinate filter for the December_05 data set. Line attributes as before.

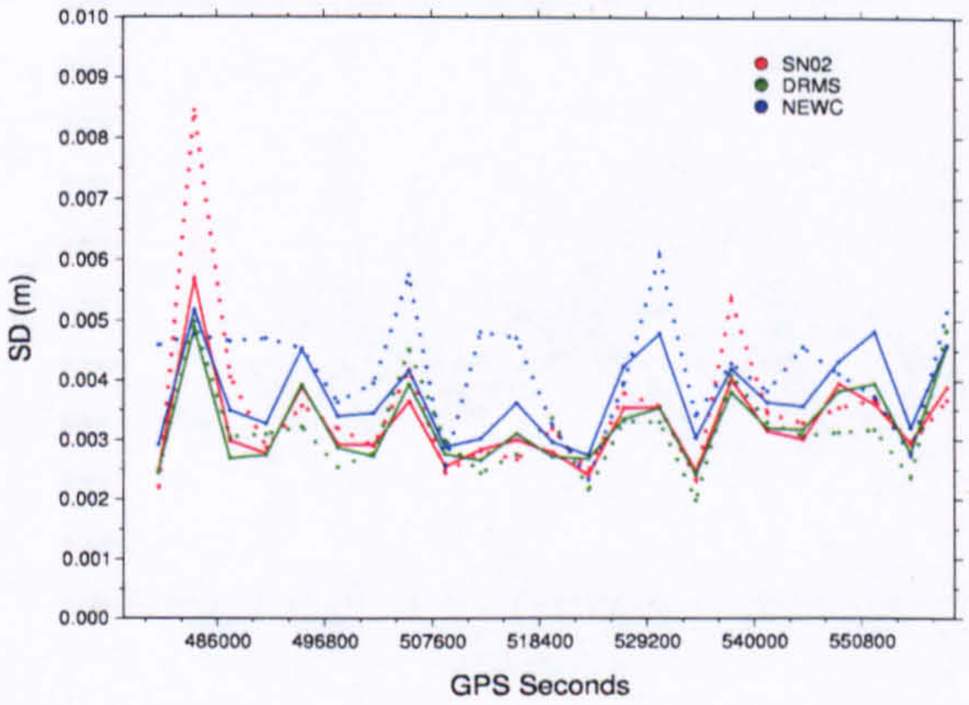

(a) Case Day1

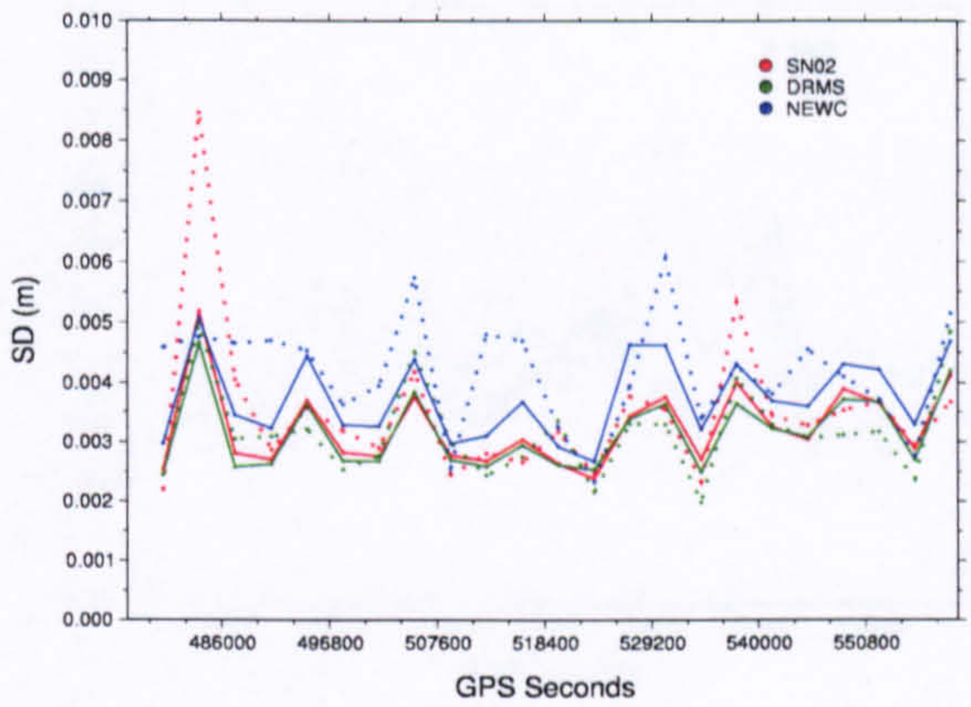

(b) Case Day2

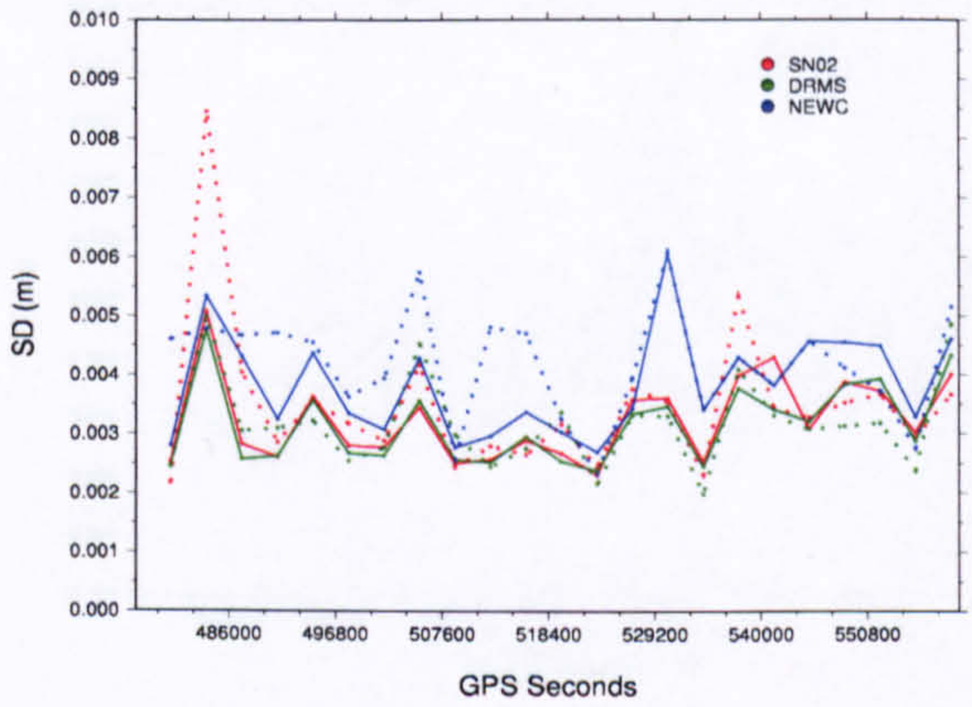

(c) Case Day3

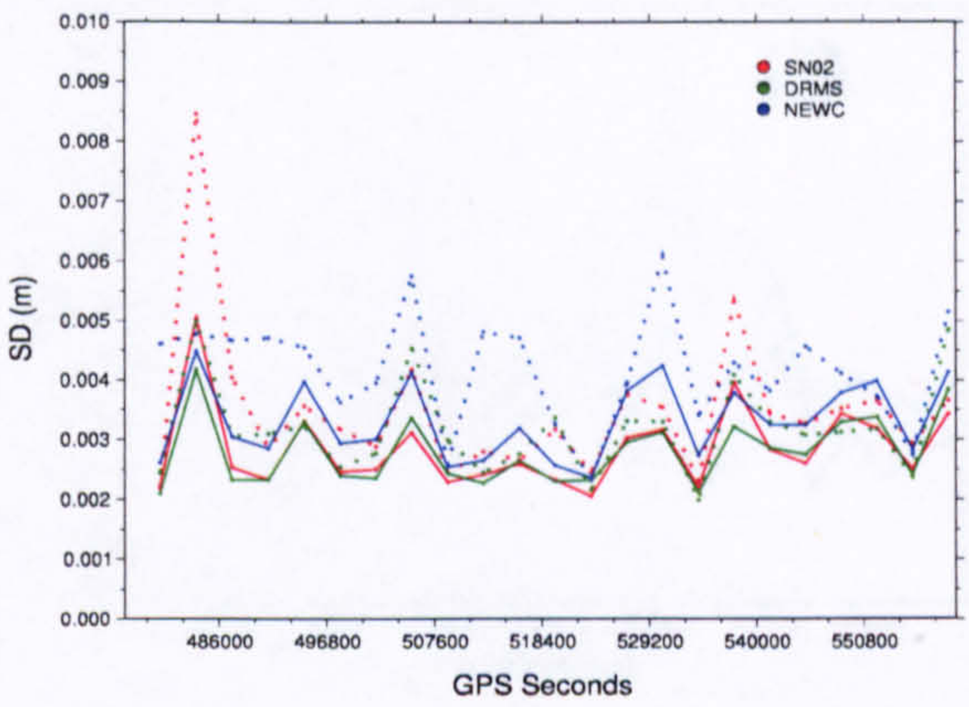

(d) Case Day1,2

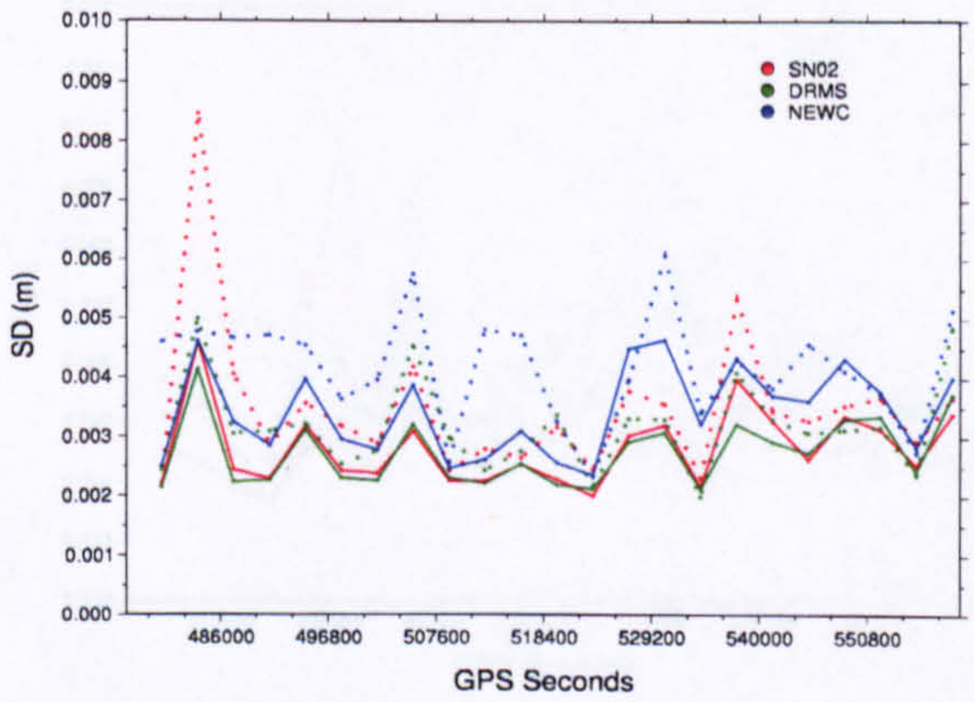

(e) Case Day2,3

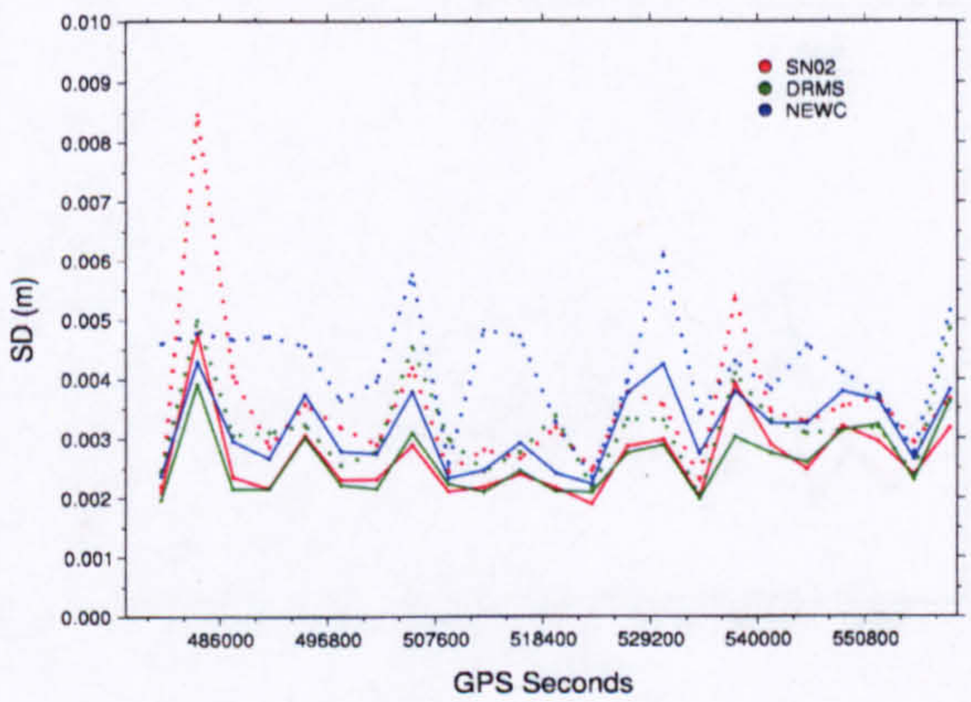

(f) Case Day1,2,3

Figure D.2 Hourly Northing coordinate standard deviations for all six cases based on the coordinate filter for the December_05 data set. Line attributes as before.

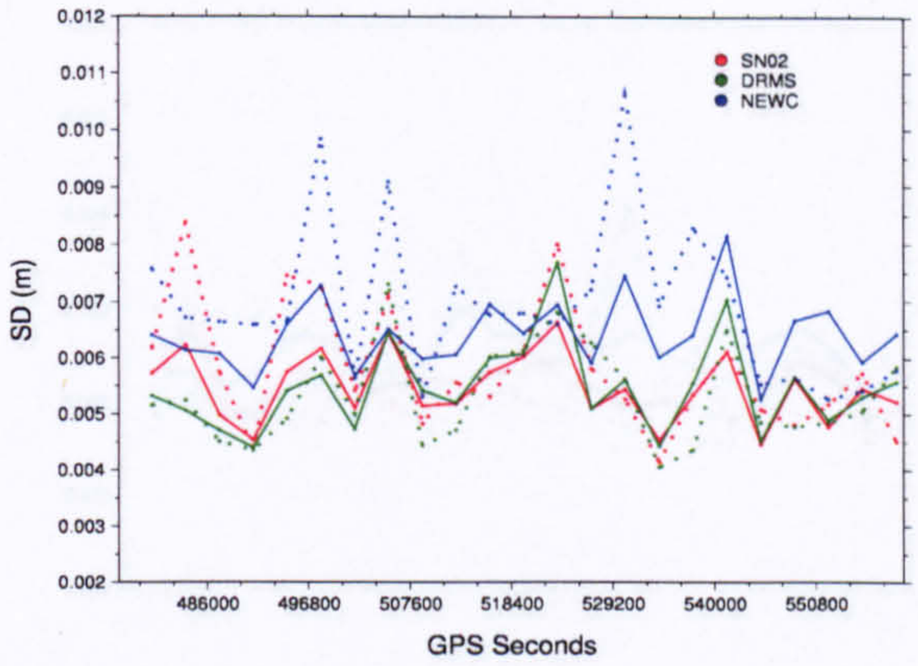

(a) Case Day1

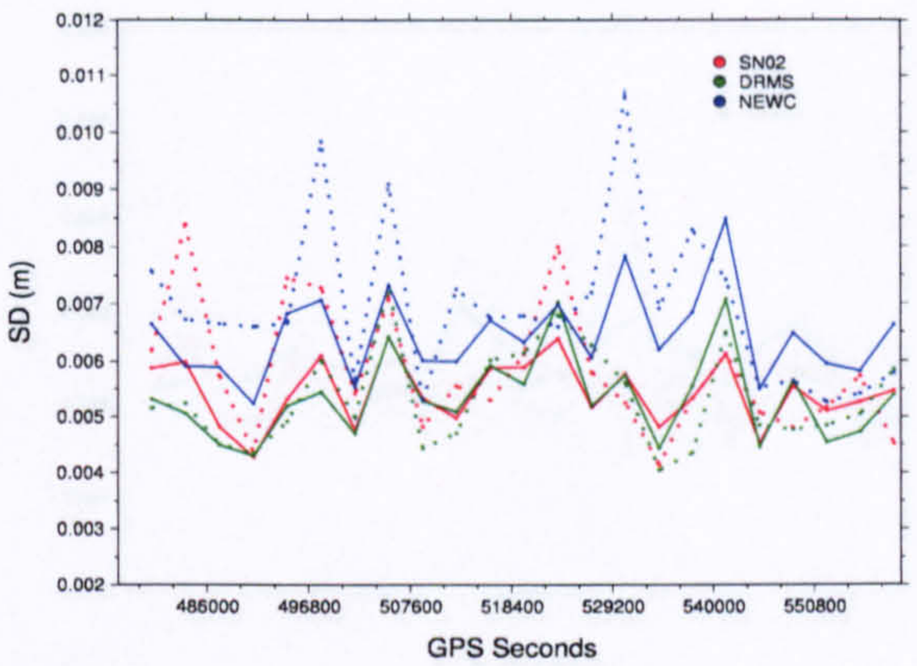

(b) Case Day2

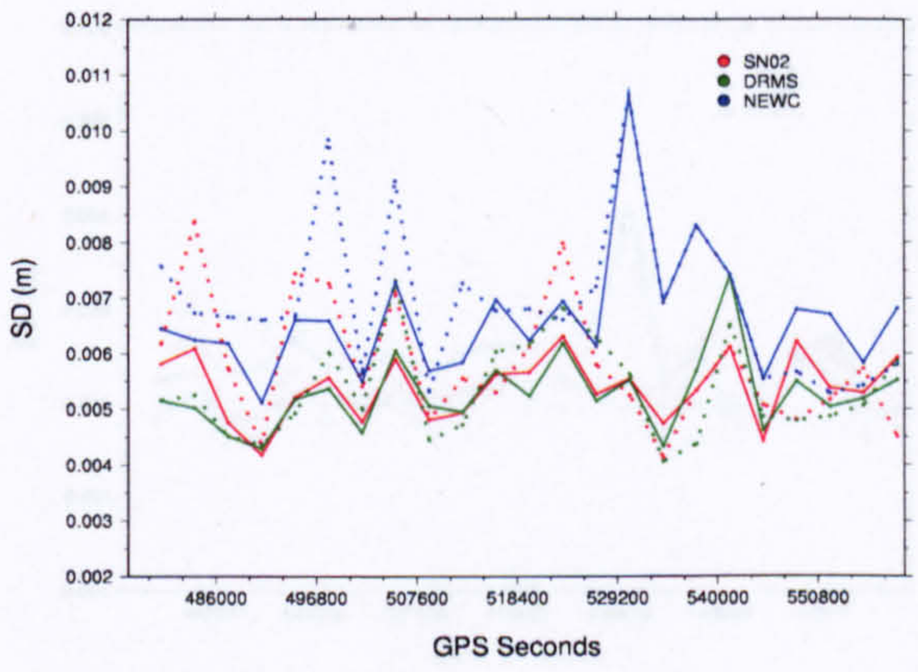

(c) Case Day3

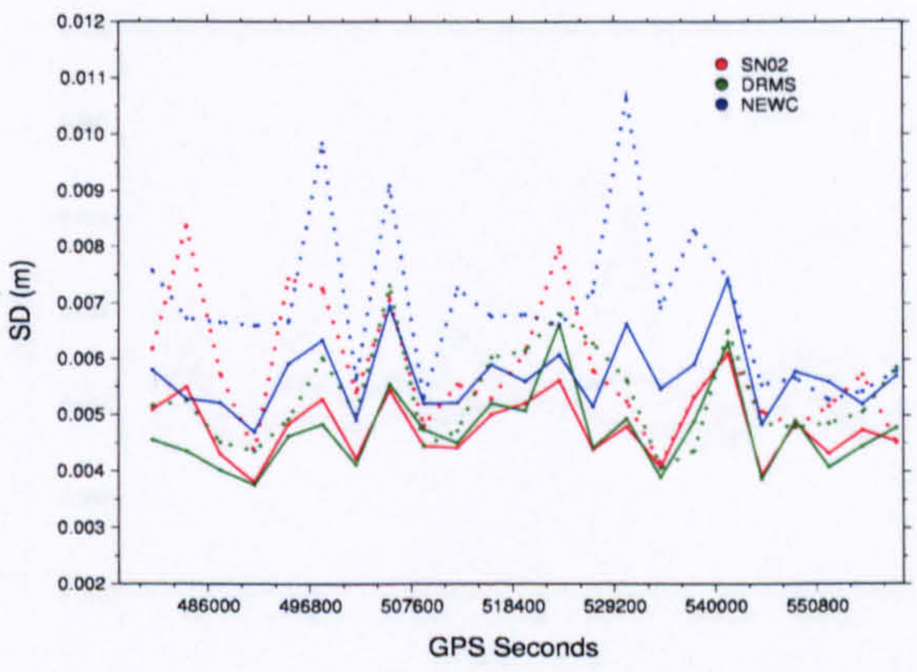

(d) Case Day1,2

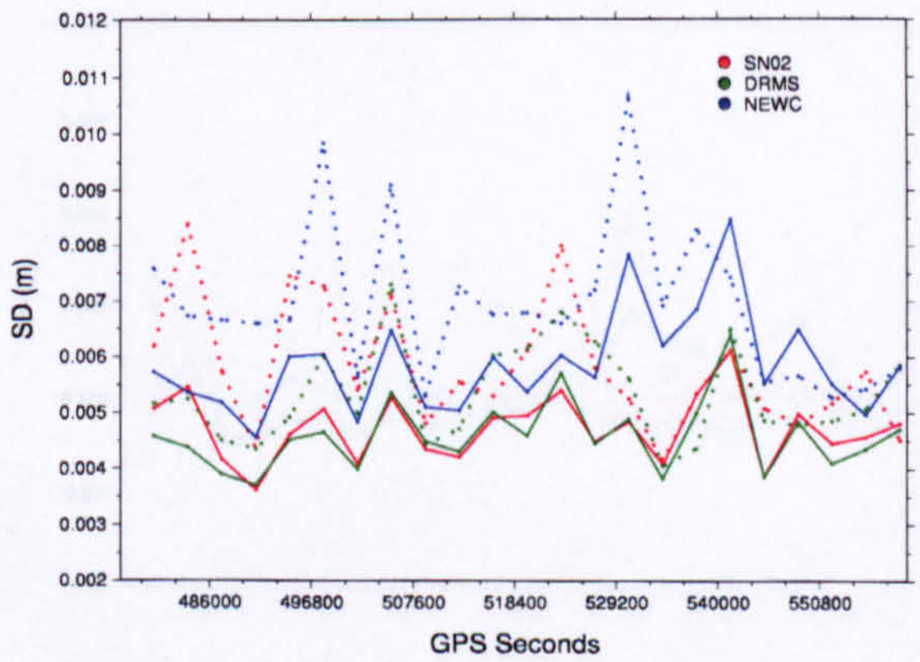

(e) Case Day2,3

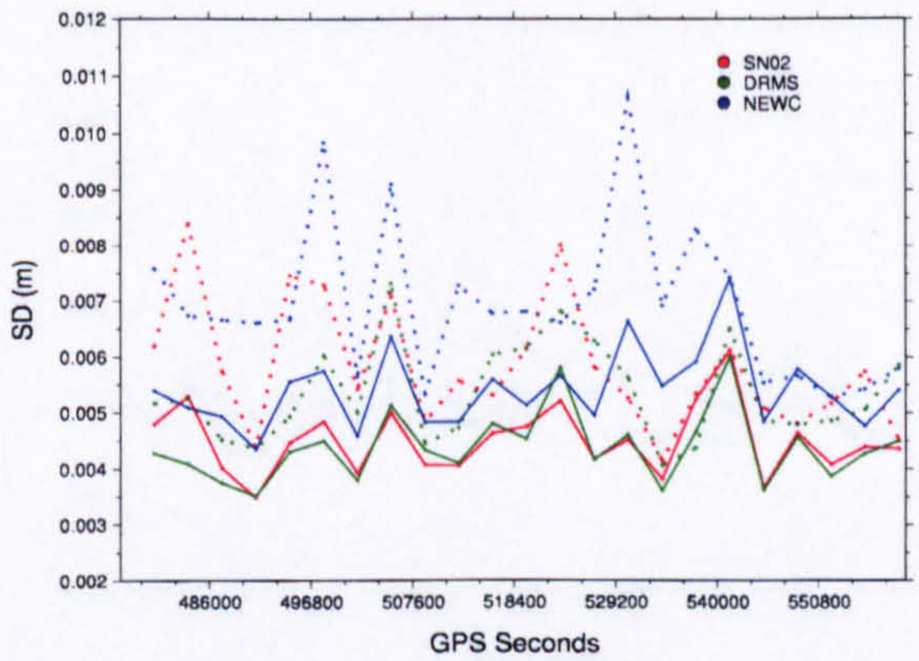

(f) Case Day1,2,3

Figure D.3 Hourly Up coordinate standard deviations for all six cases based on the coordinate filter for the December_05 data set. Line attributes as before.

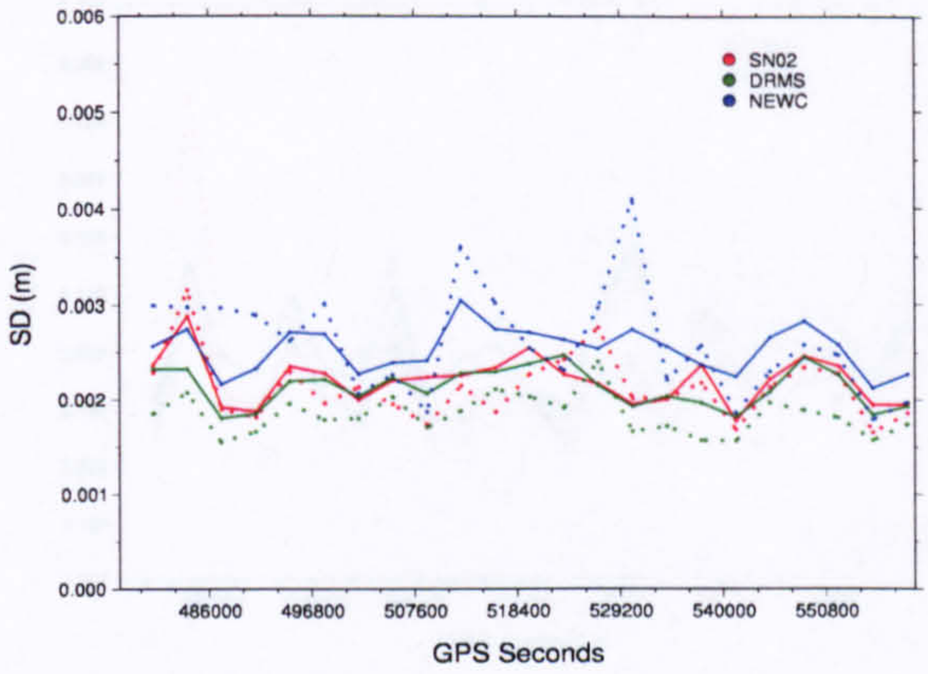

(a) Case Day1

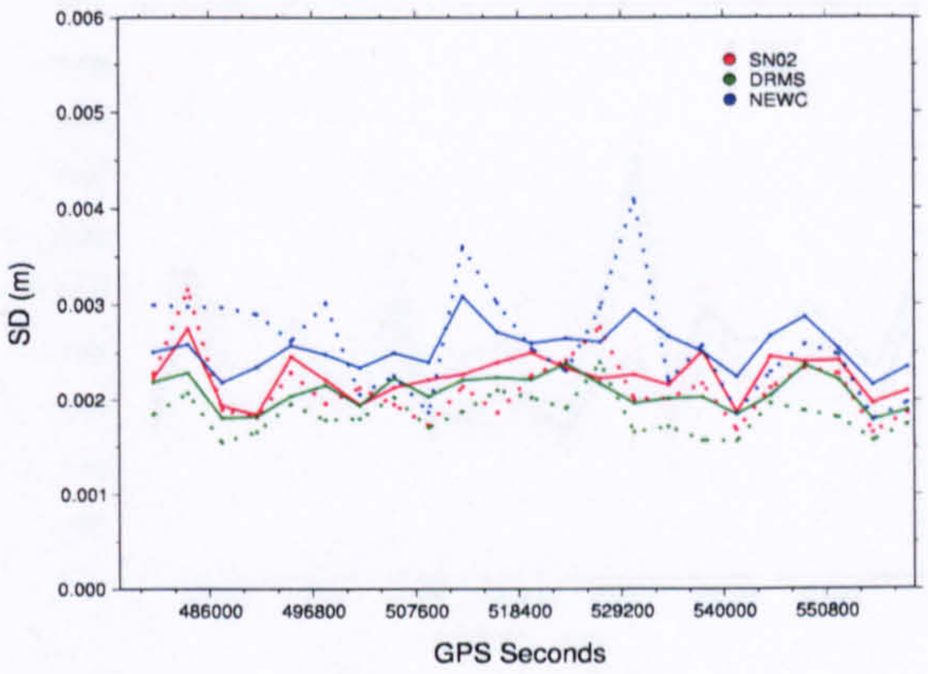

(b) Case Day2

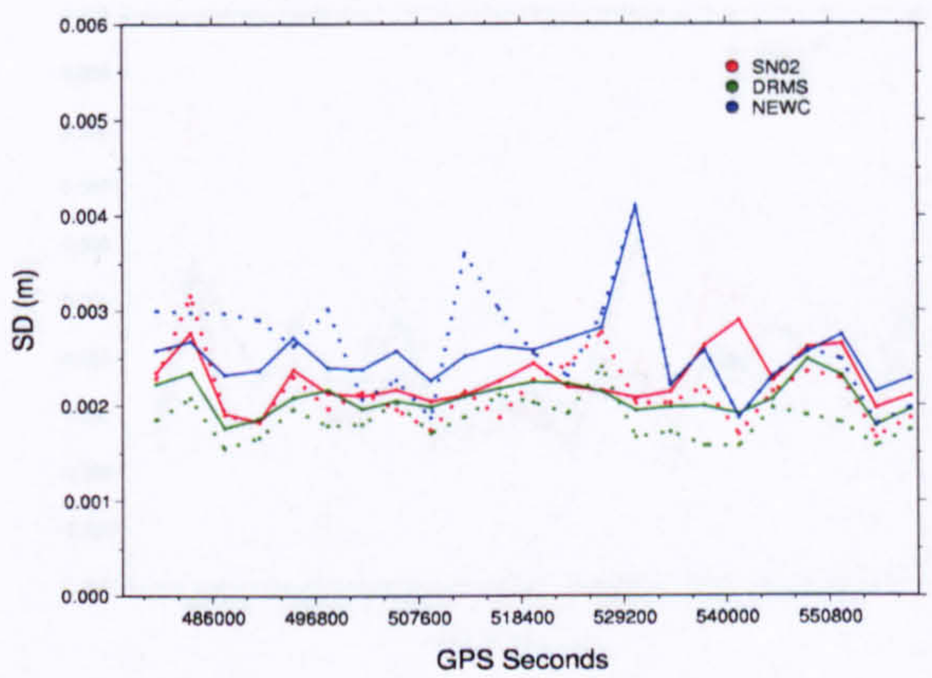

(c) Case Day3

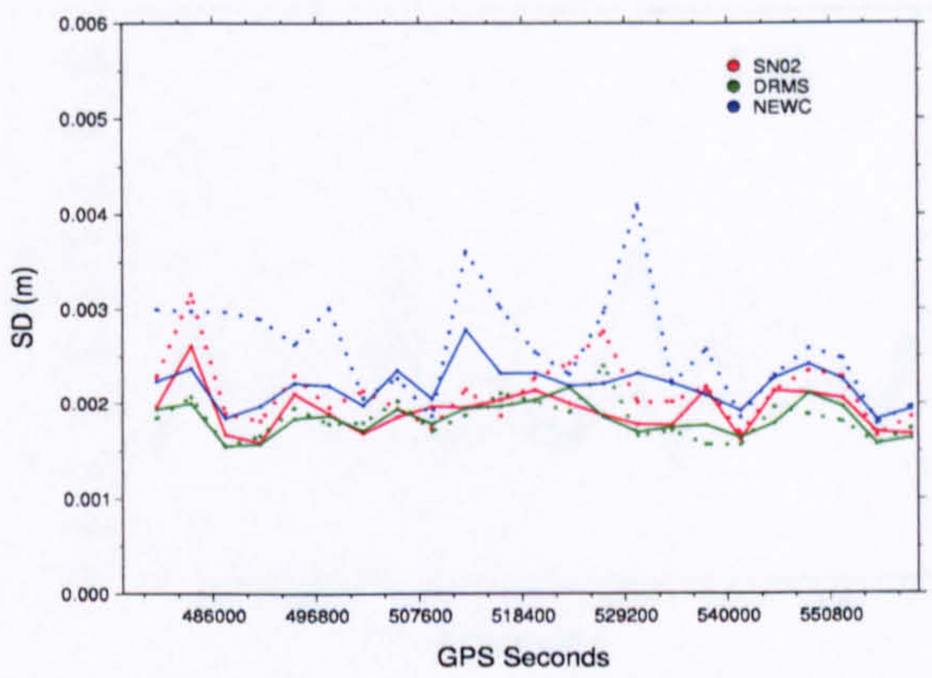

(d) Case Day1,2

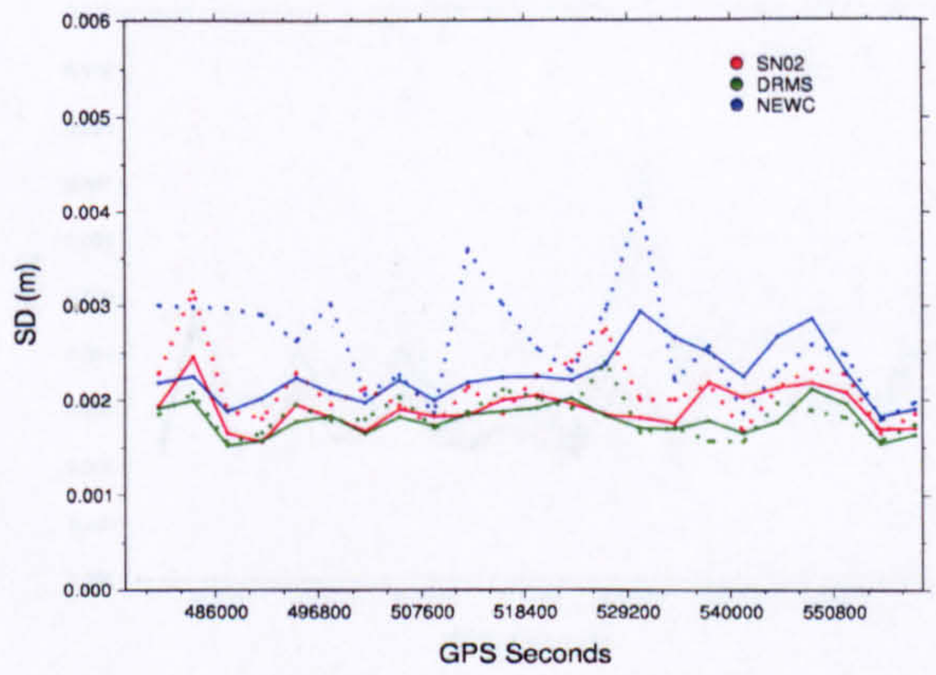

(e) Case Day2,3

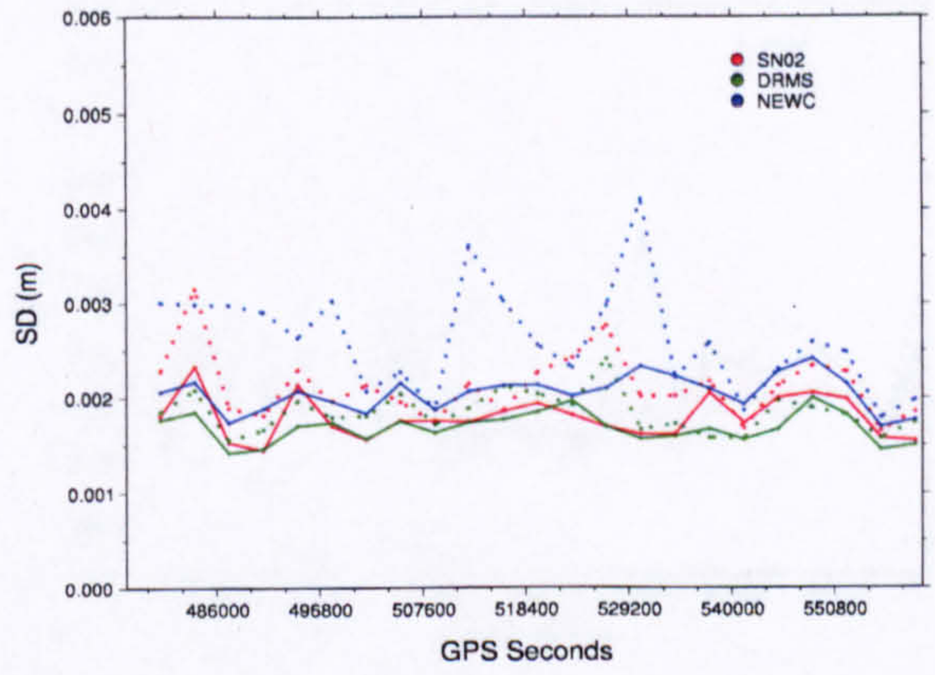

(f) Case Day1,2,3

Figure D.4 Hourly Easting coordinate standard deviations for all six cases based on the observation filter for the December_05 data set. Line attributes as before.

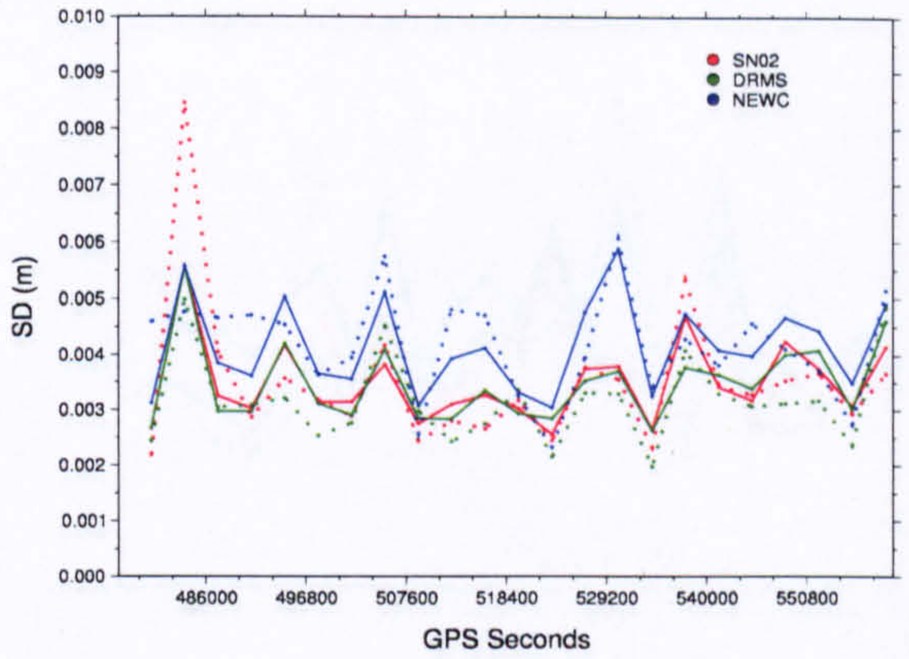

(a) Case Day1

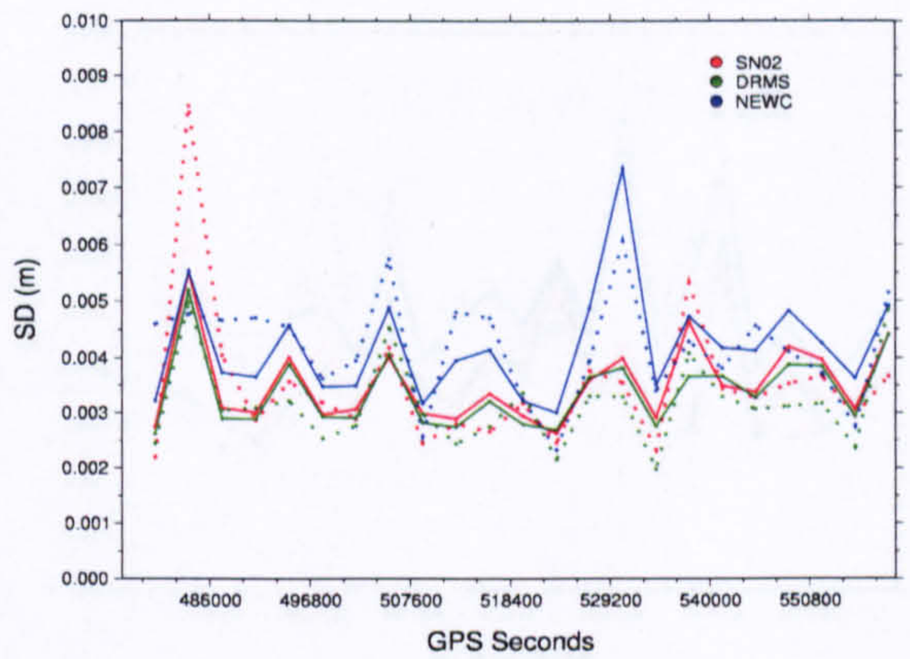

(b) Case Day2

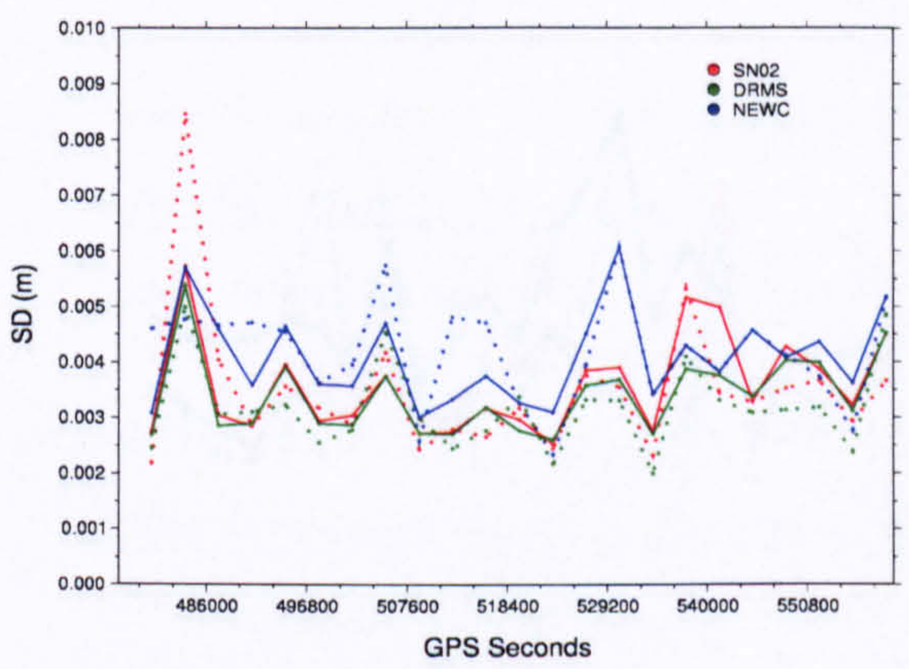

(c) Case Day3

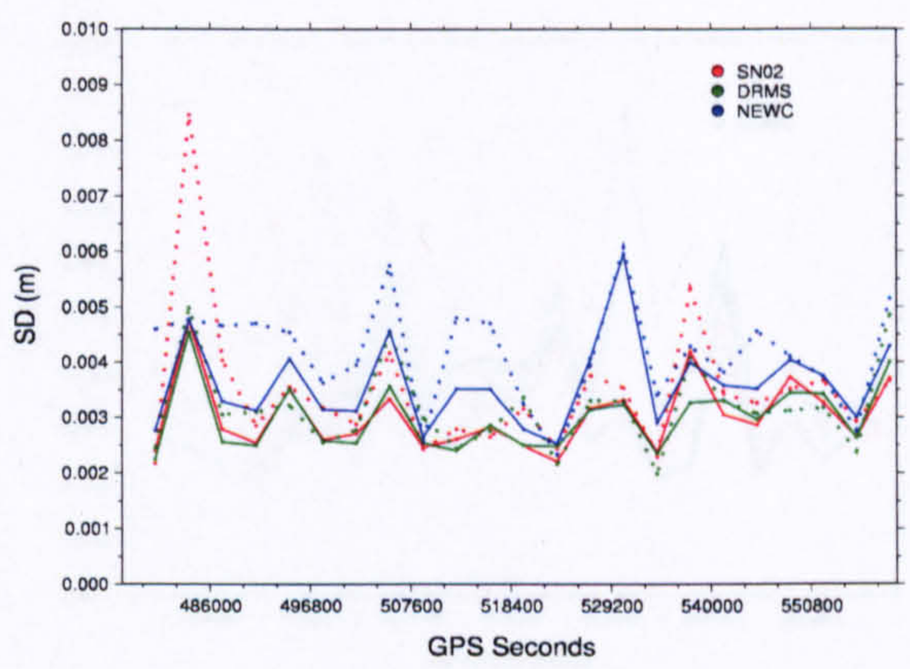

(d) Case Day1,2

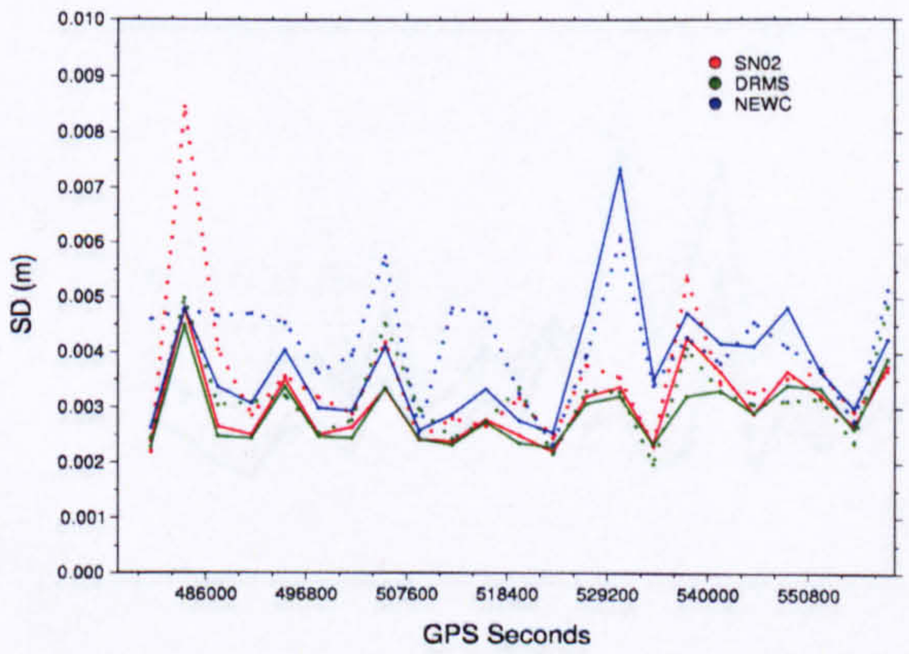

(e) Case Day2,3

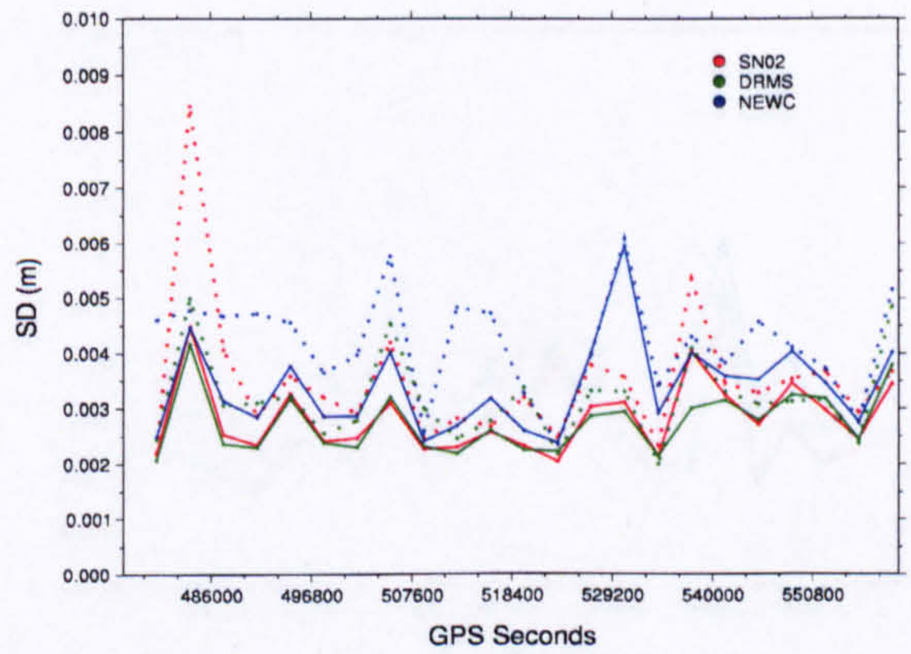

(f) Case Day1,2,3

Figure D.5 Hourly Northing coordinate standard deviations for all six cases based on the observation filter for the December_05 data set. Line attributes as before.

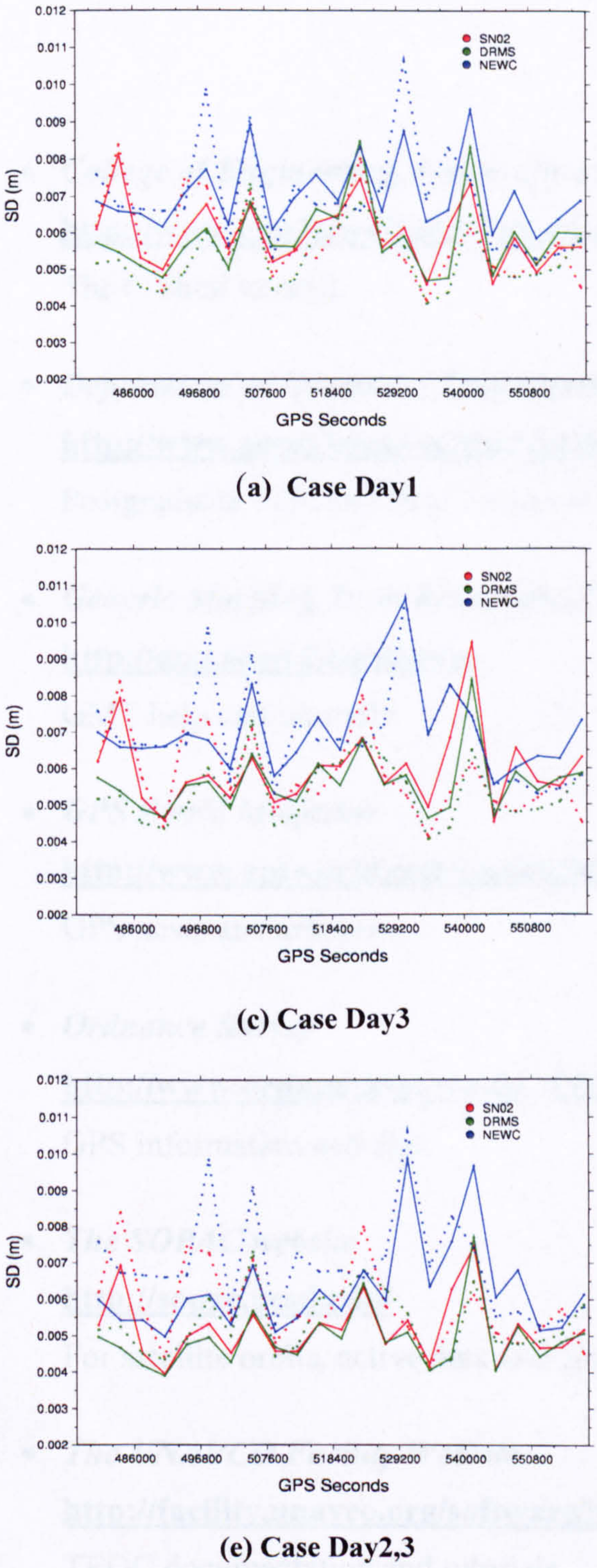

(a) Case Day1

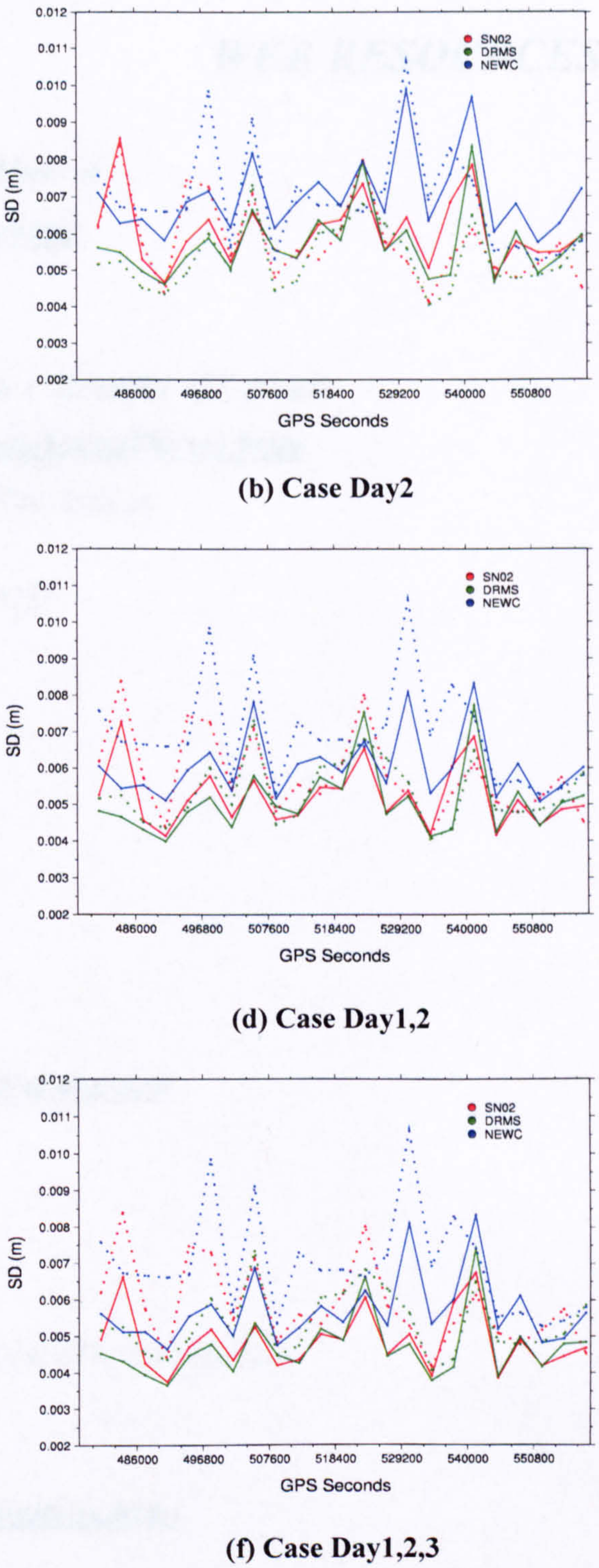

(b) Case Day2

(c) Case Day3

(d) Case Day1,2

(e) Case Day2,3

(f) Case Day1,2,3

Figure D.6 Hourly Up coordinate standard deviations for all six cases based on the observation filter for the December_05 data set. Line attributes as before.

WEB RESOURCES

- ***College of Engineering, University of Hawaii***

  http://www.eng.hawaii.edu/Tutor/csh.html

  The C Shell tutorial

- ***Department of Geomatics Engineering, University of Calgary***

  http://www.geomatics.ucalgary.ca/links/GradTheses.html

  Postgraduate MSc and PhD Theses in PDF format

- ***Generic Mapping Tools homepage (GMT)***

  http://gmt.soest.hawaii.edu/

  GMT help and tutorials

- ***GPS World Magazine***

  http://www.gpsworld.com/gpsworld/

  GPS news and articles

- ***Ordnance Survey***

  http://www.ordnancesurvey.co.uk/oswebsite/gps/

  GPS information and data

- ***The SOPAC website***

  http://sopac.ucsd.edu/

  For satellite orbits, active data and general GPS information

- ***The UNAVCO Facility Website***

  http://facility.unavco.org/software/teqc/teqc.html

  TEQC documentation and tutorials

- ***The Wikipedia Free Encyclopedia***

  http://en.wikipedia.org/wiki/GPS

  Scientific terms and definitions